MATHEMATICAL MODELING OF WILDFIRE DYNAMICS

By

Kevin Del Bene

A Thesis Submitted to the Graduate

Faculty of Rensselaer Polytechnic Institute

in Partial Fulfillment of the

Requirements for the Degree of

DOCTOR OF PHILOSOPHY

Major Subject: MATHEMATICS

Approved by the
Examining Committee:

_____
Donald Drew, Thesis Adviser

_____
Donald Schwendeman, Member

_____
Ashwani Kapila, Member

_____
Assad Oberai, Member

Rensselaer Polytechnic Institute
Troy, New York

September 2013
(For Graduation December 2013)

CONTENTS

LIST OF FIGURES

ACKNOWLEDGMENT

If you would have told me, I wouldn't have believed...and I still cannot believe where I have come from and where I am today. This thesis the the culmination of several years of my life, and couldn't have done it without the help and support of many people.

Dr. Drew, the countless hours of meeting with me and listening to my outrageous ideas have helped me to become the mathematician you see within this work. I couldn't have done this without your help, and your ideas and advice carry with them the countless years of wisdom and experience that I could only hope to possess. Thank you so much.

I also want to thank my committee for helping me achieve my goals and guiding me in the right direction. The questions that have been asked always keep me thinking, ever bettering my work.

Rensselaer Polytechnic Institute has given me opportunities that I never would have imagined possible. One such opportunity is the Accelerated BS/PhD program. Dr. Siegmann and Dr. Wait, your help and support has provided me the means necessary to navigate the program, allowing the completion of all three degrees in six years.

My graduate career was made possible by NSF through the Graduate Research Fellowship Program, and I want to thank NSF for providing me the means necessary to attend graduate school.

My family has provided me the support I needed during times of setbacks. Dad, although you may not understand my work, that didn't stop you from trying to provide insight and advice. The support has been never ending, and I hope you are proud. Krista, I love you. I am sorry for the nights I have been stressed, and for the many more stressful days as I begin to finalize this thesis. You have been the one who has believed in me the most. I hope I have shown you that when you put your mind to anything, it can be achieved.

My officemates in AE 316W, both past and present, have provided the comic

relief and distractions necessary to stay sane throughout this process. Thank you to Peter for being a wonderful sounding board by telling me "I don't know, but I'm pretty sure you can't do that" whenever I had a question. It really did help.

I want to thank all of those who never believed in me and doubted my abilities to succeed. You have provided me the extra motivation to prove you wrong.

Grandpa, I wish you were here to see this day. You are one of the reasons I came to RPI. You knew I was special before anyone else could see it. You will forever be in my heart.

ABSTRACT

Wildfires continue to pose a long-standing threat in our society. In this thesis, I derive and solve a fluid dynamics model to study a specific type of wildfire, namely, a two-dimensional flow around a rising plume above a concentrated heat source modeling a fire line. This flow assumes a narrow plume of hot gas rising and entraining the surrounding air. The surrounding air is assumed to have constant density and is irrotational far from the fire line. The flow outside the plume is described by a Biot-Savart integral with jump conditions across the position of the plume. The plume model describes the unsteady evolution of the mass, momentum, energy, and vorticity inside the plume, with sources derived to model mixing in the style of Morton et al. [55].

The fire in the above plume model is taken to be a stationary point source fire with properties calculated from the fire model. The effects of fire dynamics are modeled using a control volume derivation to write equations for total density, fuel density, oxygen density, and energy. This fire model allows the fire to propagate, where the plume and fire models are coupled through the point source fire and ambient air flow, allowing for a feedback mechanism between the two models. The derivation and implementation of the fire model are extended to investigate the situations of slope driven fires. The results show that the models presented in this thesis are capable of capturing the complex dynamics present in a wildfire. Specifically, the models address the complex interaction of the fire and fire plume with the surrounding air, fuel layer, and topography.

CHAPTER 1
Introduction

1.1 Introduction

Fire is a phenomenon that has likely mesmerized people since it was discovered thousands of years ago. Fire has also influenced, or been used in such inventions as the light bulb, steam power, and several other household items most of us take for granted. Unfortunately, many people also discover the true power of fires when they burn out of control. Houses, buildings, and even historic cities (The Great Chicago Fire [60, 62]) have been reduced to a pile of ashes in a fraction of the time it took to build them. Unfortunately, the advance of technology is a double-edged sword; buildings have been made safer and the safety of all people involved on a fire scene remains the top priority, but technology has also changed the fuel that is most commonly involved in fires. What were once rooms full of wood and organic matter are now rooms full of plastics and man-made products. These "new" materials carry several times the energy density that the "old" materials possessed [7, 33, 35] and in turn, make the fires faster, stronger, and more deadly [24, 36, 41]. Firefighters have had to adopt new techniques for fighting the fires [33, 68], as well as new technology to keep themselves, and the tools they use, safe [12, 16, 22, 27, 37]. While it appears that these advances are specific to commercial and residential use, the technology that has been developed for these fires can be used for fighting wildfires as well.

Most people are familiar with the common natural disasters (hurricanes, tornadoes, mudslides, earthquakes, etc.), but few people really consider fire as a natural disaster. Most wildfires are a natural disaster that many people overlook, or do not think about until one "hits home;" however, if you ask anyone who lives in a high risk area, they certainly know what the risks are. These extremely powerful forces of nature have the ability to devastate large areas with huge amounts of heat, smoke, and flame. The high risk of these fires breaking out over the years has prompted the media to become heavily involved in publicizing the issues and hardships associated with these disasters. One such example is the television personality Smokey the

Bear and his "Only You can Prevent Wildfires" campaign. Aside from cartoons advising children to be more cautious, national news media have been covering stories of large wildfires that impact broad areas and a huge number of people. Ascribing a cause to these massive blazes is difficult since many variables contribute to fires. Most of the time, drought conditions contribute in some way. These dry conditions await an ignition event, which could be a careless act involving a spark or fire, a stray lightning strike, or arson.

Once these fires start, no matter the cause, if they are not contained right away, they become extremely difficult to control once they spread. Unfortunately, wildfires have the amazing ability to spread at rapid speeds and jump the gaps of roads, rivers, and firefighting efforts. From the view of firefighters, many variables influence the propagation of the fire and these variables are out of their control. These variables are often factors that aid in the spread of the fire and sometimes halt all firefighting efforts. One important factor is the weather, whether it be heat, wind, rain, or drought. Weather can change within seconds, which means the fire can change directions and behavior just as quickly. Indeed, these factors can be something as simple as the topography of the land. Inclines coupled with wind in the correct direction can greatly increase the speed at which the fire moves and the size of the area affected [17, 20, 39, 43, 48].

Fire only exists in the presence of the fire tetrahedron: fuel, oxygen, heat, and chemical chain reaction. Without one piece of the tetrahedron, the fire will be extinguished; firefighters use this fact when formulating a plan of attack to extinguish the fire. Solid fuel is converted to gas fuel using large amounts of heat through the chemical process pyrolysis [30, 42]. Wildfires transfer this heat energy through conduction, convection, radiation, and the transport of embers.

Wildfires cannot, and should not be completely prevented; in fact, certain types of fires are instrumental in renewal of plant life. Small controlled wildfires are often used to clear underbrush, reducing the size of the fuel layer, and promote the growth of new plants, especially in national parks. The chemical processes involved in fire release carbon dioxide and ash, which are nutrients that help plants grow [3]. In addition to plant growth, wildfires can also be used to control the advance

of insects and plant disease. Wildfires do have helpful uses, but once the fires get out of control, these benefits are far outweighed by the devastating damage. Many times, these fires have gotten out of hand, resulting in the burning of large areas of land. In essence, stopping all fires, large or small, could be adding fuel to the fire, literally. Suppressing fires allows underbrush to build up in areas, increasing the fuel bed for future fires. After such buildups, fires can grow in size and cost, and become more dangerous.

When all factors involved in a wildfire are considered, fighting these fires sounds hopeless. When a blaze burns out of control, the effects are long reaching. Not only are woods and animal habitats in peril, but homes and lives of people living in the area are also affected. The fires cause unimaginable amounts of damage, not only monetary, but emotional, societal, and environmental as well. This would include the natural resources that are lost in fires, and cultural resources (historical buildings, etc.) as well. An example of decisions that may impact such resources would be deciding to divert a fire away from a structure. This decision could end up costing natural and cultural resources worth more than the structure itself, just like stopping a fire today will result in higher fuel loads and a larger fire tomorrow. In addition to damage, the cost of maintaining equipment and personnel and the actual effort to suppress the wildfire costs several billion dollars annually [32, 71, 75]. This cost is born by taxpayers, not only in high risk areas, but all over the country.

Wildfires are an issue not only in the United States, but around the world; several of the articles used here as references highlight global studies. Fires have been known to occur on all continents except for Antarctica, so accurate insight into the inner workings of wildfires could benefit people around the world. Specifically here in the United States, impacts of wildfires can be seen in both direct and indirect economic costs.

Every fire has its own personality, drastically affecting the amount of money associated with each event. It needs to be noted that the costs discussed in the financial responsibility reports (reviewed in the following paragraphs) [5, 18, 71] do not include the cost of devastation and damage in the areas affected, not to mention the emotional toll, loss of business to the area, and loss of natural resources. If these

types of damages were able to have an associated dollar amount, the overall figures discussed in these cost reviews would be much higher than reported.

Most costs reviewed and reported here are federal costs. In today's bureaucratic world, jurisdiction is a large issue, especially when it comes time to split the costs to each participating level of government. The cost analysis presented here outlines the federal spending for the large fires in which federal resources were part of the suppression effort. As mandated by Congress, an independent panel is required to review the costs and decisions leading to the costs for all wildfires with federal suppression cost exceeding ten million dollars to determine if the US Forest Service made the most cost effective decisions during the incident. Two of the costs analysis papers reviewed here are reports from this independent panel review from 2008 and 2009 [5, 18], and the last is a full USDA Forest Service report for 2010 [71].

In 2008, twenty-two fires were reviewed [18]; as mandated, each individual fire cost over ten million dollars in federal suppression costs. Not surprisingly, most fires were located on the west coast or in the central portion of the United States. The federal suppression costs of these twenty-two fires was six hundred eighty-three million dollars, which topped the five hundred forty-eight million dollars used to suppress the fires reviewed in 2007. Although, the number of acres burned and number of fires was less in 2008 when compared to 2007. In 2008, one fire alone cost over one hundred twenty million dollars and burned for almost 100 days. The cost of suppression in 2008 was the largest federal cost total since the reviews were mandated by Congress in 2004. The large fires reviewed account for twenty percent of the acres burned but thirty-eight percent of the cost, enforcing the fact that the largest fire is not necessarily the most expensive. Even more proof of this is the fact that the largest fire in 2008 occurred in Texas and cost less than ten million dollars in suppression costs. In 2008 there were seventy-eight thousand fires reported, and these fires burned a total of 5.3 million acres. In the short term trends between 2007 and 2008, the amount of fires and the total acres burned is decreasing, but the number of fires with federal suppression costs exceeding ten million dollars is increasing.

In 2009, six large fires were reviewed in the report [5]. The total suppression costs of all fires was about one hundred ninety million dollars. The cost, acreage burned and duration widely varied depending on the different factors discussed below. As with previous trends in 2008, many large fires occurred on the west coast of the United States, resulting in much of the data being collected from this geographical area. In 2010, there were almost seven thousand wildfires reported to the USDA Forest Service (in total, not just those costing over ten million dollars in suppression costs) [71], which burned about three hundred twenty thousand acres and cost nine hundred million dollars in suppression costs. There were more acres burned in 2010, but the number of fires reported was fewer as compared to 2009.

To get an idea of the amount of money available for use towards suppression costs, in 2010 the US forest service was funded by the Departments of Interior, Environment and the Related Agencies Appropriations Act which provided over $2.1 billion in funding. There was also a reserve fund provided by the appropriations bill for $413 million. This money is used for the challenges of budgeting fire suppression and to allow the quick response during fire seasons. All together the US Forest Service had $2.5 billion at their disposal during 2010 [71].

There are two different types of costs associated with a cost analysis of a given fire considered in the large fire cost analysis papers reviewed here [5]. Direct costs for example, are the costs accrued by transporting personnel, aircraft, and equipment to fight the fire. Indirect costs for example, would be the costs accrued by transporting personnel, supplies, catering, camp crew, etc. which support the fire-fighting operation. This includes the cost of all living necessities for the sometimes large number of people involved in the operation, and the incident command itself. On average for large fires, the percentage of direct costs is about sixty-eight percent, and the percentage of indirect costs is thirty-two percent [5]. The costs listed above for yearly totals include both indirect and direct costs.

When considering individual fires, the cost is highly dependent on the personality of the fire, the weather, the strategy employed by the incident commander, the terrain, the type of fuel, the resources available to fight the fire, jurisdiction issues, private property obstacles, public pressure, etc. Firefighter safety is the top priority

when on a fire scene. Unfortunately, this necessary priority carries a heavy cost burden. Decisions need to be made differently when considering the people who risk their lives to put the fire out. For example, it may be deemed unsafe for firefighting efforts to continue due to any of the factors listed above. A possible outcome of the suspension of such efforts could result in the growth of the fire, and in the long run, a higher cost to regain the lost progress.

Making firefighter safety the highest priority on a fire ground has had a large impact on line of duty deaths. In 2010 wildfire firefighter fatalities has decreased from the numbers in 2009. The largest cause of fatalities continues to be aviation accidents, accounting for twenty of the thirty-two fatalities in a five year period. The second largest cause of fatalities was burnovers (when firefighters or fire vehicles are caught in an advancing fire line), which accounted for twenty-two percent of the total number of fatalities. These two causes combined accounted for over eighty-five percent of all fatalities in 2010 [71].

Steep slopes and fuel type largely influence how quickly the fire spreads. In addition to this, thick fuel beds make it extremely difficult to find all hot spots. The fire could burn within the fuel layer, virtually undetected over large areas, surfacing in what seems like random areas. This burn pattern is extremely difficult to track and suppress. Access to the fire line also impacts the actions taken for fighting the fire. Different equipment needs to be used if ground apparatus cannot be used, and costs rise steeply when aerial rigs are used. Fires which have a large amount of smoke visible for large distances are known to cost more, and catch the public's eye nationally. With such large fires, media participation only helps to apply pressure from the community on the incident command to take actions to suppress the fire, even if it isn't the action needed. Members of the community are not supportive when a fire burns for a long time, creating smoke and altering everyday life. Aside from pressure from the community, political pressures also have a large influence in actions taken by the incident command.

The public's perception is that fighting a fire from the air seems like the most logical method to stop the advancement of a roaring blaze, but contrary to this, it may not be. The cost of aircraft in firefighting efforts drives up the overall cost of the

fire more rapidly than any other piece of equipment. Of the fires reviewed in 2008, fourteen percent of the total cost of suppression was attributed to aviation resources, although the percentage depends greatly on the role aviation took in suppressing the fire [18]. Additionally, the effectiveness per cost of the equipment is disputed by people in charge of the operations, even during today's fires. There have been cases where incident commanders have ordered the use of aircraft to fight the fire solely on demand from the public, even though it was known there would be no positive effect from the operation [5]. This was done because the aircraft is widely assumed to be the most effective means of fighting wildfires, and keeping the public outlook positive was most important at the time. An example of this political pressure has taken place in the Los Angeles Basin. Due to the large number of people in the area, and several media outlets, the fires drew significant public attention. This attention places pressure on the people in charge, and causes them to make fiscally irresponsible decisions, including the use of aerially delivered flame retardant when it is known that there will be little to no effect [5]. In other areas this has occurred to the point that aerial operations were conducted just so that it could be filmed and shown on television to keep public outlook favorable, even though the people in charge knew little, if any, of the material dropped would reach the ground [18]. This is not always the case, and in some fires, the use of aircraft has been pivotal in some suppression efforts.

Despite the high risk of fire, residents continue to build homes in the wildland-urban interface (WUI). This greatly impacts the decisions that need to be made during fire incidents. There are many more factors that need to be considered when dealing with fires in the WUI, and delegation of resources becomes more and more complicated. The presence of buildings in the area of a fire commits people and apparatus to protect these buildings, taking away from forming a fire line; this is called structure protection [5, 18, 71]. In areas that are prone to many fires, taking away resources from stopping the fire to protecting houses may allow the fire to spread, and eventually burn longer and in a larger area. In the long-term, the overall cost of suppressing the fire would increase. This might explain why suppression costs in California are much higher than other locations around the

country. In California, the fires occur in areas that are more urban, thus making the fire far more complex. There are more buildings that need to be accounted for, and worried about. Coupling this complex behavior with high fuel loads, the situation and costs can get out of control very quickly.

Residential and commercial firefighting often lend hands to wildfire techniques. One example of this is the use of infrared cameras, both handheld [27] and mounted to aircraft [5]. This helps find fire spots within fuel layers not easily seen from the ground and without the thermal camera. In one instance aircraft mounted infrared cameras were used to aid firefighters on the ground in navigating through thick smoke [5]. It allowed a clear view of the fire front, and even provided visibility to the aircraft, allowing firefighting efforts to continue.

Over the past two decades, there has been a dramatic increase in extreme behavior of the wildfires, the risk to firefighters, loss of property and homes, and cost. This type of trend calls for a more strategic response to address the rising challenges to fighting the fires. A strategy for fighting fires depends greatly on the landscape, local topography, and other factors listed above. Attempting to devise a global strategy is difficult, because each area has its own climate, fuel characteristics, and weather patterns. A localized strategy should also be able to engage the community, work with its members, and make the overall area more resistant to future fires [71]. This community involvement may include on site twenty-four hour information centers to ease public pressure, or even public service announcements like Smokey the Bear.

The Smokey the Bear campaign has been around for many years. In 2009, the campaign received more than fifty-four million dollars, and in just the first half of 2010, it received over twenty-one million dollars [71]. This shows the support and positive results the public service announcement has obtained over the past years. Overall, an adaptive strategy should consider the individual pieces of the fire management, especially the response and bureaucratic policy, minimizing the political red tape allowing for an efficient response and suppression.

Considering all aspects of fires, factors influencing their behavior, and trends in the past years, it is no surprise that large fires have been getting more complex

and dangerous. Although, with careful planning and training, the people in charge can make fiscally responsible decisions, helping to reduce the cost of suppressing the fires.

Kaval [32] surveyed people in high risk areas as to how they perceived a threat of wildfires burning their property. Surprisingly, most participants accurately identified the threat. Another question in the study explored the option of paying additional money to help reduce the risk of wildfires in their area. The results show that residents were willing to pay some amount to help prevent the wildfires. Kaval proposes one way to reduce the risk of wildfires is to thin fuels by removing underbrush and small vegetation creating an area called a defensive zone [48]. By understanding more about how wildfires work, through modeling, other methods can be developed to reduce the risk. This understanding could spur better preventative measures and predictive models.

Modeling wildfires can benefit many different people, from the residents in the area, to the firefighters who risk their lives trying to get the fires under control. Predictive models can be used to create early warning systems to give residents in high risk areas the chance to evacuate when a wildfire does occur. In addition to early warning systems, predictive models can be used to assist in firefighting efforts. The aid of predictive models can give firefighters the opportunity to modify their techniques to become more efficient and even allow them to develop new methods. It is apparent that fighting normal fires is dangerous, so any insight into making firefighting efforts more efficient will likely save lives. To understand the complex mechanisms that cause the fire plume to rise and entrain ambient air, models need to account for the fire plume itself and its interaction with the surrounding area.

In this thesis, I present and analyze a model of wildfires that is based on breaking the problem down into core components; these parts consist of a fire, the fire plume, and the surrounding atmosphere. The hope is that this simplified model requires less computational cost while still allowing for an accurate understanding of the interactions between the plume, the fire, and the ambient air. The model will include ideas and equations used to describe a flag flapping in the wind [1], creating a novel model that allows for a plume to react more accurately to external forces.

This approach will be discussed more in Section 1.4. Applications of this model will be used to analyze the interactions between the atmosphere, propagation of fire through different media, and fires effected by topography.

1.2 Previous Works–Plume and Plume Propagation

Several agencies have made significant efforts in modeling wildfires, including the National Institute of Standards and Technology (NIST), the Department of Agriculture Forestry Service (USDA), and the Department of Energy (DOE). The following sections will review several categories of papers which take different approaches to modeling fire, whether it is wildfires or not. These categories include systems obtained by the reduction of the Navier-Stokes equations, fully physical solution methods, some using Lagrangian particles, and reactive plume models.

1.2.1 Techniques Involving Reduction of the Navier-Stokes Equations

The Navier-Stokes equations are an extremely versatile set of equations that can describe the motion of any fluid flow given the right conditions. In essence, all models reviewed here were derived from the Navier-Stokes equations, or equivalently, conservation laws. Several assumptions can be made depending on the type of flow being studied. Rehm and Baum [63] make an assumption about the rate at which heat is added to the system of a thermally driven plume, while Morton et al. [55] assume a very specific form of velocity and buoyancy force. In contrast, Riahi [64] uses multiple axisymmetric plumes in the numerical domain. These assumptions, while very different and applied in different types of systems, help to reduce the difficult non-linear Navier-Stokes equations down to a more manageable set of equations that can be easily solved numerically. Several more papers are reviewed in [28], where the core equations are derived from the conservation laws.

Morton et al. [55] use the Navier-Stokes equations to explore the interactions of heated bodies with ambient air. The particular interest involves the fluid velocity and temperature in close proximity to heat sources. Unlike previous works, Morton et al. discuss the effects of a thermally buoyant plume rising though a thermally stratified atmosphere. Verified by experiments, Morton et al. make the assumption

that the rate of entrainment at the boundary of the plume is proportional to the vertical velocity at any given height of the plume. Additionally, the authors make an assumption that the velocity and buoyancy force, at any given height, have a top-hat profile. The authors call the type of flow studied in the paper "maintained sources," a category under which a fire falls. One large difference in the formulation of the problem is that they consider a three-dimensional, axisymmetric plume, whereas here, consideration involves a two-dimensional line fire. Equations concerning the conservation of momentum, volume, and energy are derived and solved for uniform fluid under the top-hat profile assumption. In stratified fluid, the plume entrains cool ambient air, causing it to ultimately stall. As the plume stalls, it spreads out horizontally creating the familiar shape of a plume. Morton et al. list entrainment parameters from experiments which will be useful in creating the entrainment model for this work.

Whereas Morton et al. described heated bodies, Rehm and Baum [63] describe a system of equations which describe the motion of a thermally driven plume. The process used is to write the Navier Stokes equations with a heat source term, which represents the fire. Then, the system of equations is non-dimensionalized and a small parameter δ, whose magnitude represents heating rate of the system, is introduced. Here, $\delta \ll 1$ represents a rapid addition of heat to the system, which is characteristic in laser applications, and $\delta \gg 1$ corresponds to slow heat addition to the system, which is characteristic in controlled fires. Obviously, the interest here is on $\delta \gg 1$. The dependent variables are expanded in powers of δ such that there is a balance between pressure terms and convective terms. Rehm and Baum consider room fires, and the equations are tailored toward this result. In the scenario described therein, the pressure in the room builds until a window breaks or a flashover occurs. One notes that the derivation valid for room fires is not realistic for wildfire, however the method of perturbation expansions will be adopted for this work.

Riahi [64] takes an approach that uses multiple plumes in the numerical domain. Each plume is assumed to be subject to the same conditions and form. The plumes are assumed to be axisymmetric, circular plumes that rise from a heated horizontal surface. Raihi uses equations derived from the Navier-Stokes equations

in cylindrical coordinates, where convection is time averaged. The equations are non-dimensionalized and scaled according to asymptotic limits to assure fundamental balances are maintained. Raihi assumes the Rayleigh number is large, allowing for an asymptotic expansion of the dependent variables. A two-dimensional assumption is made so that a stream function can be introduced, allowing the calculation of volume flux. One notes that the Boussinesq approximation is used in conjunction with the axisymmetric plume. However, while these are valid approximations, they are not the focus of this work.

1.2.2 Direct Numerical Solutions

The Navier-Stokes equations can be numerically solved directly using a computational fluid dynamics code (CFD). There are several CFD codes that are commonly used and one can use different "add-ons" to more fully understand the solution. One of these "add-ons" is Lagrangian particles or elements that can be used to trace particle paths. Not only is this a good way to visualize the flow, but it is also a way to keep track of how much fuel is being consumed and when the fuel is expended. Baum et al. [14], Baum & McGrattan [13], and Mell et al. [49] use direct numerical solutions to describe fires with very different characteristics.

NIST has spent a considerable amount of time and resources in developing several realistic models to predict many different types of fires. Several of the papers described in this section have been developed by NIST.

An important development is the Fire Dynamics Simulator (FDS) model. An early version of FDS was reviewed by Ma and Quintiere [40], where several different types of fires are examined. I will discuss a later version of this model [47] in this section. It must be understood that results from the model presented in this thesis will not appear as physically complete as the results from the FDS model. This is due to the fact that many people over several years have been involved in the development and improvement of FDS. Particularly visualization of the simulations from the FDS model are complex, and there are several sub-models used in the FDS model to account for physical phenomenon and visualizations alone.

Baum et al. [14] take an approach to modeling fire plumes similar to the one

I will present in the coming chapters. Although the specialization of Baum et al.'s work is for large aviation hangers, the methodology is a reassuring sign that my approach is valid. The authors use large eddy simulation (LES) and CFD codes to visualize the flow. Large eddy simulation is a solution method in which the smallest size of vortices is assumed to be the size of the mesh. Vortices smaller than the mesh are subject to viscous effects and are dissipated. Mathematically, Baum et al. begin with a paradigm similar to the one used in this thesis: a thermally buoyant plume rising from a heat source. The flow is assumed to be at low Mach number; thus an incompressible, or nearly incompressible assumption can be employed. The authors start with the Navier Stokes equations with a time dependent average pressure and take a perturbation expansion in temperature and density. Additionally, an adiabatic lapse rate gives a definition of pressure in terms of reference, hydrostatic, and perturbation pressure. The model uses Lagrangian elements to track fuel and smoke particles throughout the flow. This actively models the process of propagation by ember transport, which is a focus of this paper. The solution of the problem involves an FFT-based solver, where the reduced system is solved directly. This solution process differs greatly from the one I will present. The computation cost of a direct method is far greater than what is considered in this work. I will introduce a method that will involve reducing the system of equations to a manageable set that can be solved nearly analytically.

Baum & McGrattan have also adapted their work for large industrial outdoor fires [13]. Again, this is a different application in which ideas may be adapted to aid the work I am conducting. The authors note that wildland fires have low heat release per unit area of fuel, but a large area over which the fire can spread. Although the application is not wildland fires, the authors provide insight into the amount of energy released and the fuel consumption rate associated with such fires. The authors take special care in how they model the stratified atmosphere. The assumption is made that pressure is comprised of two different pieces, a stratified hydrostatic pressure in the ambient air domain and a fire induced pressure. The fire induced pressure is assumed to be small; thus, a perturbation analysis can be used to identify the effects of the fire on the ambient region. They also introduce a

radiative transport model to track the movement of energy induced by the fire. The derivation starts with the Navier Stokes equations for a compressible fluid in which ambient effects are taken into account. An interesting addition to the model is an oxygen transport equation, which accounts for the fact that fire requires oxygen to burn its fuel. They tie the burn rate to the local oxygen supply and the overall size of the fire, then use models for the heat flux terms to couple the convective energy transport equation and the radiation field. Similar to previous work, Lagrangian elements are used to account for fuel usage, and also as a way to visualize the smoke. And again, the computation cost of this type of work limits the complexity of the model they can use, not only for the radiation field, but also for means of solving the equations presented.

As mentioned before, the FDS model developed by NIST is one of the leading simulations at this time. A more recent version released is FDS Version 6 [47], and the background of the FDS model can be seen in previous release notes and manuals. The FDS model uses LES, which in essence assumes that viscosity damps vortices smaller than the size of the mesh being used. It is an extremely powerful method for solving the Navier-Stokes Equations. FDS is not specifically tailored to wildfires (as Wildland-urban interface Fire Dynamics Simulator (WFDS) [49] is), but the techniques used are worth consideration.

FDS uses governing equations derived from the Navier-Stokes equations. In particular, conservation of mass, mass fraction of species, momentum, and energy are used in conjunction with the equation of state to constitute this model. In addition to this system of equations, a constraint on pressure is used by taking the divergence of the conservation of momentum equation. In any type of fire, the geometry of the surfaces being modeled needs to be considered. FDS uses two different methods to accurately capture the features of complex geometry. One method is used for objects which are resolved by the grid, called immersed boundary method (IBM). IBM involves rewriting the momentum equations and using directional cosines to transform the Cartesian coordinate system to a streamline coordinate system. To model objects that are unresolved by the mesh, a second method of Lagrangian particles is used. Embedded meshes are also used to increase the accuracy of the solution in

areas where complex interactions occur. A separate application, Smokeview, is used to visualize the results from the model.

A modification of FDS was made to adapt the model to wildfires. The result is a model called Wildland-urban interface Fire Dynamics Simulator (WFDS) [49], which is a theoretical or physics based model (see Section 1.3) that accounts for fire/atmosphere and fire/fuel interactions. WFDS is a multi-phase model that accounts for the solid and gaseous fuel, while additionally modeling the thermal radiation of heat. A convective and radiative heat flux is a result of the fire/atmosphere interaction, which is computed by the conservation laws. The assumption that the combustion in the vegetation layer is mainly on the surface of the fuel bed allows the use of two computational grids, which reduces the computation cost. The equations derived are numerically solved in the same manner as those in the FDS model. The atmosphere is coupled to the fuel layer such that the vegetation is viewed as a source of drag on flow supplying the fire as well as a method of preheating the oxygen supplied to the fire. Additionally, moisture content of fuel, radiation of heat from the fire, and chemical equations for the process of pyrolysis are used to make the model more accurate and physical.

1.2.3 Techniques Involving Reactive Plumes

While all other solution techniques stem from the Navier-Stokes equations and are mostly concerned with the macroscopic effects, reactive plume models are concerned with both macroscopic and microscopic effects, including chemical reactions of molecules. Reactive plume models track concentrations of chemicals in the system, similar to the approach taken by Lagrangian particles. The chemical processes involved in fire itself are taken into account, allowing for the inclusion of fuel consumption and entrainment into and out of the plume. The reactive plume model is commonly used when there is interest in the number of pollutants present in the atmosphere. Specifically Georgopoulos & Seinfeld [26] present an application to plumes rising from a smokestack, or any other concentrated point source. The model accounts for both the macroscopic and microscopic effects of the plume, including the actual chemical reactions of the molecules present in the source and the

plume. For the scope of this thesis, macroscopic effects will be considered, making this type of approach impractical.

1.2.4 Conclusions

The focus of the derivation of this model will be closer to the models discussed in Section 1.2.1. It should be noted here that the large majority of models reviewed fall under the category of computational fluid dynamic (CFD) codes. CFD codes have many different titles and involve physical solution methods to capture the small scale physical features of the problem. Two broad categories of these CFD codes and physical solution methods are large eddy simulation (LES) and direct numerical simulation (DNS).

These types of models, especially the models developed by the government agencies listed above, do well at predicting the behavior of both indoor and outdoor fires. The simulations are accurate, and are presented in a way that appears realistic. In fact, models such as FDS have been widely accepted in applications pertaining to the development of standards on sprinkler systems in large industrial building and adoption by the fire service. The fire service uses FDS to recreate situations in which fallen firefighters have found themselves, not only to recreate the situations, but also to teach others what situations to avoid.

The largest drawback of these types of models (CFD, LES, DNS, etc.) is the computation time. To resolve the small scales of the problems, a large number of computation nodes need to be used, drastically increasing the computation times of the model. In fact, the computation times of these models has been known to approach the order of weeks for a single simulation. Due to this, there is no real-time capabilities and specifically, the model cannot be used in the field. By the time results are obtained, the calculations are no longer valid due to the fact that fire behavior can change much faster than results can be obtained.

The purpose of this model is not to say one approach is better than another. In fact, a combination and mutual understanding of both models would allow the community to benefit the most, which is the motivation for this type of work. In the model developed in this thesis, simplifying assumptions are used to narrow the

focus of the model to the key driving dynamics of the fire and fire plume. Due to this the computation time of the model is on the order of minutes. It is understood that the simplifying assumptions do sacrifice physical attributes of the problem, but as seen in the results, Chapters 4, 6, and 7, the key driving dynamics are captured accurately and there are many conclusions that can be made from the simulations. A long-term goal of the model presented in this work is to gain predictive capabilities, such that the model can be used in the field, either by incident command in charge of dispersing the resources or by smoke jumpers in the thick of the action. Either use will allow more well informed decisions to be made, addressing many of the issues discussed previously.

1.3 Previous Works–Wildfire Spread

While many of the papers reviewed in the previous section do deal with modeling of fire as well as the propagation of the plume, the papers reviewed in this section are concerned mainly with modeling the phenomenon of fire spread. Indeed, some of the models, such as WFDS, will be mentioned again in this section.

Fire spread models have been well known to span three separate categories, empirical, semi-empirical, and physical. The differences between these types of models is the approach in which the models are derived. The categories span from empirical models, which use algebraic laws in conjunction with experimental data and statistical methods to evaluate parameters, to physical models, which use numerical solutions of conservation laws to model the fire. Of the papers considered here, most are physical approaches derived from conservation equations and governing equations for motion of a flow, as will be the model presented later in this work. But a few approaches are derived from reaction diffusion equations. Some of the other approaches can be seen in such papers by Karafyllidis [31], Encinas [23], and Vaz [72]. The paper by Pastor et al. [59] reviews major works from 1940 to 2003 and Mell et al. [51] describe needs of models and the research conducted at NIST.

The problem of modeling wildfire has been outlined by Viegas [73]. There are seven stages of fire development, although not all seven occur in all fires. These stages are: preheating and pyrolysis, ignition, initial growth, secondary growth,

flame decay, extinction, and cooling. Additionally, fire propagation has been characterized into three different categories: ground fire, surface fire, and crown fire. Ground fires are those which occur underneath or within fuel beds. These types of fires are incredibly hard to detect and extinguish. Many times it seems as though the fire is surfacing at many different places. Surface fires are those which people might be most familiar with, and are characterized by a typical fuel bed lying on the ground. Crown fires are characterized as the situation where the tree-tops are burning. It is easy to see that each of these fires can lead to any other kind, and in a typical lifespan of a fire, all three categories can be observed. Viegas' review and subsequent laboratory tests are optimized for surface fires only. As was mentioned earlier, there are many factors that influence the propagation of fires. Here, three main influences are considered: topography, vegetation, and meteorology. Again it is seen that upslope regions have a large influence on the spread speed. The higher the angle of the slope, the faster the propagation. Interestingly, downslope regions have little effect on the propagation speed. The vegetation layer is composed of three regions, coincidentally the same names as the fire propagation. The largest effect the vegetation has on the fire is the moisture content of the fuel. If there is any moisture content, it acts as a heat sink. The fuel absorbs the heat to evaporate the moisture so the fuel can pyrolyze. Viegas has found that the weather effects the propagation of the fire the most. There are many factors in the weather that can either aid or hinder the propagation. A few examples are air temperature, humidity, precipitation, solar radiation, atmospheric stability, and especially wind [73]. In one way or another all of these issues need to be addressed in any fire model.

1.3.1 Wind and Slope Driven Models

The papers presented here are models for fire propagation applied to wildfires. There are many approaches and assumptions made to reduce the complex equations. Models such as Albini [2], Balbi et al. [8, 9, 10], and Morandini et al. [54] have been specifically tailored to wind and slope driven fires and focus largely on the flame-structure interaction with the fuel bed.

Albini derives a physical model based on governing equations for the flow.

This includes a mass flow and energy equation for the flame itself, while the flow is described by momentum equations and the flow of oxygen to the fire. A constant wind-speed is added to the system further reducing the equations. Focus is turned to the flame and its interaction with the fuel. Albini concluded that combustion takes place in the lower half of the flame structure, and in the wind driven situation, the flame angle is independent of the flame height [2].

Balbi's approach to the wind driven situation is much different. The first paper [10], is an improvement on a previous model [8]. The first improvement involves the tilt angle of the fire. The approach to the flame structure is geometrical; the flame is assumed to be of triangular structure. From this, the angle of the flame can be calculated from the quasi-analytical model for both high and low intensity winds. It should be noted that this model also accounts for topography, and the wind considered is taken to be flow induced up the slope. The second improvement deals with the backward rate of spread. The influx of fresh air by the induced flow up the slope slows the progress of the backward rate of spread [10]. The second paper [9] is much the same as the first. The model is based on key assumptions, mainly dealing with the flame structure, radiative effects, and velocity of flow driving the fire up the slope. It is additionally assumed that all gases in the model are perfect gases and the reactive gases are completely oxidized in the reaction. Again, the geometry of the problem is used in conjunction with the assumptions to derive the governing equations of the problem. This model simplifies the governing laws to a single equation that give the rate of spread as a function of wind slope and vegetation.

Morandini's approach is much like Balbi's. Many assumptions are made about the fire, including that the fuel bed is thermally thin, isotropic, and the fuel is homogeneous. The heat transferred from the fire is assumed to be through radiation, convection, and conduction, which is accounted for in fires in still air through a single diffusive term. Once fuel is on fire, the mass of fuel simply decreases at an exponential rate depending on the temperature, not through a specific mass conservation. The heat generated by the combustion reaction is taken to be constant for each unit of fuel. In the case of fire on a slope or under wind conditions, the radiative heat transfer is a decreasing function of distance using the inverse square

law. The equations for rays, representing the emitted heat, are written taking into account the loss due to distance. A simple trigonometric argument is used to calculate the flame angle based on the free stream velocity and the induced velocity by the fire up the slope. It was found that at low angles and slow speeds, radiation is the driving force for spreading the fire, but at an angle or under wind condition, convection starts to become more important due to flow attachment [54].

1.3.2 Multi-Phase Models

A multi-phase model is an approach that takes into account the different phases of matter influencing the physics of the problem. In the case of the wildfire, this commonly means modeling the solid fuel and the surrounding flow. Some models take this one step further and model the interaction between fuel and flow on several different scales, as seen in Sero [66] and Margerit [44]. It is customary to see the gaseous phase of the model described by the Navier-Stokes equations [44, 49, 56, 57, 61, 66], whereas the solid phase is modeled by conservation laws based on a simple chemical reaction. In some of the models, the fuel is taken to be either inhomogeneous [61] or on a microscopic level composed of oxygen, water, and fuel [44, 66]

Morvan [56, 57] used this approach in the two papers reviewed here. In the gaseous phase, the conservation (Navier-Stokes) laws are averaged over a control volume, where terms to allow for the transition of matter through different phases, the addition or loss of heat due to the reaction and radiation, and the drag forces due to vegetation. The model uses a $k-\epsilon$ turbulence model to describe the mixing region in the problem, radiation in the problem is governed by integrating the radiative transfer equation, and effects of soot generation and transport are accounted for. In the solid phase, the reaction dynamics are modeled using the law of mass action in conjunction with an Arrhenius law. Results show and validate that in the absence of wind conditions, wildfire propagation is driven by radiative heat transfer.

Sero et al. [66] and Margerit et al. [44] consider several scales in their models, including the macro-, meso-, and micro- scopic formulations of the problem. In the mesoscopic region, water vaporization and pyrolysis are considered in the vegetation

region, and in the fuel region, the chemical reactions of combustion and oxidation is accounted for. The fuel and vegetation regions are modeled by conservation laws that allow the exchange of fuel from each of the states, where in the vegetation layer, a conservation law for char allows the tracking of each of the species that occur in the chemical equation. Several assumptions are made to reduce the equations and boundary conditions between the two regions. To move to the macroscopic region, an averaging procedure is used to model the large scale effects of the problem. One will note that the equations are still conservation equations and appear similar to the mesoscopic equations. Much work was done to close the system and account for radiation to describe the flow in the air above the forest using the Navier-Stokes equations [66]. Several simplifications of the equations are considered including the reduction to two dimensions [44]. To do this, the height of the vegetation layer is assumed to be small as to induce an asymptotic expansion of the equations in the ratio of the vegetation height to the characteristic height of the forest fuel. The method of multiple scales is introduced to simplify the equations to two dimensions, while leaving the ability to keep more terms in the expansion.

Even though an overview of WFDS was given in the previous section, in this section, the modeling assumptions for WFDS are considered. Mell et al. [49] set out to derive a fully physical model, as a modification of the FDS model. The model uses separate but coupled models for the solid fuel and the gas fuel under combustion. In addition to this, a transient heat flux, which allows for both convective and radiative heat transfer, is used. This results from the numerical solutions of conservation laws of momentum, mass, energy, and major species. WFDS directly solves the governing equations for the fire/fuel and fire/atmosphere interactions without using simplifying assumptions to include the physical processes [50]. When considering the actual equations and derivation of the equations, the gas phase is modeled using the Navier-Stokes equations, where the influence of the grass fuel bed on the ambient wind flow is approximated by a drag term. Multiple computation grids are used to reduce computation time, where the LES model is used to approximate physical processes that occur on scales finer than the ones considered. Equations for conservation of species, conservation of energy, thermal radiation, and an equation

of state are written. The thermal radiation equation tracks the energy transfer, where the spectral frequency needs to be considered due to soot generation. Thus, a soot model is used as well. In the solid fuel, standard conservation equations are written, again with source terms to allow such additions and losses due to the processes of pyrolysis, radiation, and oxidation [50].

1.3.3 Reaction-Diffusion Models

Another approach to modeling the wildfire problem is to assume a reaction-diffusion type model. These models make assumptions about the physical processes, which allow for the use of the reaction diffusion model. The models rely heavily on a simple PDE for energy, which can appear as a heat equation [19, 74], or can appear much more complicated due to additional terms [6, 11, 52, 53, 67]. These additional terms allow for cooling, through Newton's law of cooling, radiative heat transfer, and heat sources. Due to the nature of these models, simplified numerical approaches can be employed, such as finite differencing [11, 52, 53, 67, 74] and finite element techniques [6, 11, 53] may be employed.

Montenegro [53] writes the standard reaction diffusion energy equation allowing for convection, diffusion, cooling and heating due to the fire. A simple two stage chemical reaction is used to describe the exothermic reaction. From this reaction, the law of mass action is used in conjunction with an Arrhenius law to approximate the reaction rate, while allowing for the derivation of the heat source due to the fire. The reaction is simplified to a single stage reaction to allow for simpler equations. A weak form of Laplace's equation is solved using a least squares and an optimization formulation for velocity, and both an implicit finite difference scheme and an adaptive finite element method is used to solve the non-dimensional system.

Balbi [11] proposes an elemental cellular approach to this model of a laboratory fire in the absence of wind and slope, with homogeneous fuel. Again, the standard reaction diffusion equation is written allowing for cooling and the addition of a heat source by assuming the fuel layer is thin. The diffusion term takes the place of the convective, radiative, and conductive transfer of heat. The model uses data from experiments to calculate the unknown parameters of the problem. By looking

for standing wave solutions, the problem can be reduced to an eigenvalue problem, where several cases of the solution need to be considered to fully solve the problem. Again, both finite difference and finite element schemes are used to numerically describe the problem.

Asensio & Ferrahut [6] use much of the same approach as the other papers reviewed in this section. A simplified chemical reaction is used with the Arrhenius law to approximate the reaction rate. Fuel degradation is assumed to be exponential in nature. Radiative heat transfer by optical path, cooling, convection, a heat source due to the exothermic reaction, and a phase change function to allow the change between exothermic and endothermic reactions are all considered in writing the reaction diffusion equation and mass equation. The system is put into weak form, existence and uniqueness are proved, and is numerically solved using a mixed finite element method.

Mercer & Weber [52] use the standard reaction diffusion equation, allowing for all modes of heat exchange as the others in this section. Here the radiative heat transfer is derived from Chandrasekhar's integro-differential equation. Weber provides initial conditions such that traveling wave solutions are present (due to the reduction of the system), and the system is numerically solved using finite differences. It was found that the speed of the combustion wave depends of the square root of the radiation heat transfer length.

Chetehouna [19] considers a multiphase approach that includes the drying of the fuel, pyrolysis, heat convection, heat conduction, and radiative heat transfer. Again the reaction diffusion equation is reduced to an eigenvalue problem by assuming a traveling wave solution, where an asymptotic expansion is taken in terms of the eigenvalue to obtain several order problems. Just as Chetehouna reduced a multi-phase formulation, Simeoni [67] does the same. Here it is assumed that the fuel is a bed of pine needles, modeled by cylinders randomly distributed across the fuel bed. The flow only in the horizontal direction is considered, and the model was verified by experiments in a wind tunnel. Weber [74] uses a reaction diffusion equation to derive a comprehensive model which accounts for advection, radiation, and the heat due to the reaction. The model is considered in both the gas and solid

phases. The equation is transformed to a moving reference frame, where a traveling wave solution can be used to reduce the PDE to an ODE for temperature. With this the solution suggests that fires propagate creating a series of grown ellipses that move in time, which agrees with field observations.

1.3.4 Geometric and Radiation Driven Models

The two approaches considered in this section are noticeably different from those mentioned in the previous sections. In Albini's paper [4], the notion that radiation is the driving spreading force of a fire in the absence of wind and slope is used and investigated. Thus, it is assumed that heat is only transported through radiation, the flame itself extends above a uniform fuel layer, and fuel particles are black bodies (only absorb energy and do not scatter). The radiation field that results is a PDE for the intensity of energy radiated throughout the region. The divergence of the net radiant flux is written as the integral over the solid angle of the intensity of the energy. The temperature of a particle depends on its stage in the combustion process. Thus, as a particle is heated, the water first evaporates and then the fuel particle ignites. After non-dimensionalization, the problem reduces to an eigenvalue problem that is solved both analytically and using an iterative solution. The model is able to predict the fire front shape and the intensity of the energy radiated into the fuel layer.

Dold & Zinoviev [20] have approached the problem of calculating the behavior of an unsteady fire line differently. The resulting approach is simpler and more geometrically approached. The authors introduce notation for fire line intensity through Byram's formula, which relates fire line intensity to spread rate, energy of combustion, and fuel load. Technically, Byram's formula is only valid for the case of a steady fire spread. In the steady case, geometry can be used to derive all necessary pieces of information, where Byram's formula is verified. Considering an unsteady fire spread is not so simple. The fire front is parametrized to allow the shape of the fire front to change and to track the movement into the fresh fuel. To describe the shape of the fire front over time, a total derivative is taken and set equal to the effects of arc length and the spread of fire into the fuel. The intensity of the fire is

written as an integral of the heat released, the pyrolysis speed, and the fire spread speed over the arc length. Simplifications of the model are taken using either a small fuel bed and a fast spread rate or fast pyrolysis and a spread rate slower than the burning speed. The dependence of the spread rate on intensity is examined for several different situations and assumptions. The intensity of the fire feeds energy back into the fresh vegetation ahead of the fire, which ultimately determines the spread rate of the fire.

Dold et al. [21] use much of the same formulation as the previous paper by Dold & Zineoveiv. Again, the fire line intensity is written as an integral over the fire region. Reductions are taken for large spread rates over fire burning rate, which simplifies the integral of intensity. The spread rate is assumed not to vary rapidly in time, which allows for a perturbation to be taken. Again, the relationship between spread rate and intensity is investigated, but this time it is a non-linear relationship, which allows for the investigation of stable fire spread and eruptive fire spread.

1.3.5 Conclusions

The fire model presented in this thesis will use aspects from each of the sections of previous works. The derivation of equations will closely follow the derivation from Section 1.3.2, where the different phases of matter will be considered across multiple models. The plume model will investigate the interaction between the plume and ambient atmosphere, whereas the fire model will investigate the interaction between the fire and the fuel layer. When coupled, these two models will resemble a multi-phase approach.

1.4 Formulation

As was mentioned, the model of wildfire in this thesis will be decomposed into models that examine fundamental interactions. This section will outline which chapters are concerned with which fundamental models, initial assumptions and geometry.

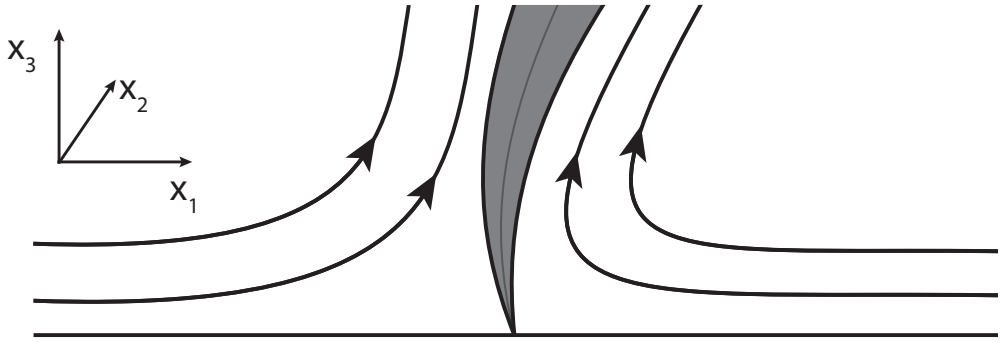

Figure 1.1: Plume Surrounded By Ambient Air in Cartesian Coordinate System in Upper Half-Plane

1.4.1 Plume Model

Chapter 2 through Chapter 4 describes the approach for deriving the plume model. The plume model focuses on the interaction between the plume and the surrounding ambient air. Before I present the equations of motion that describe the flow of the fluid, I need to make some initial assumptions about the geometry of the problem. Consider a Cartesian coordinate system in the upper half plane (see Figure 1.1), and assume that the fire lies along a line in the x_2 direction. I will also be making the simplification that the ambient air (outside the plume) is independent of the plume itself, except for entrainment effects. Thus, resulting in two disjoint dynamical systems (save entrainment): the ambient air system and the plume system. I assume the plume is narrow, and using the disjointedness of the two systems, the plume represents a jump discontinuity from the perspective of the ambient air system. The jump discontinuity allows the addition of ideas from fluid dynamics, which permit the plume to react more accurately to atmospheric conditions. I will use ideas from the theory of fluid-structure interactions [1] in analogy to the equations of motion that describe the flapping of a flag in the wind.

I use the Navier Stokes Equations to describe the motion of the fluid in the two-dimensional Cartesian geometry. The flow in the ambient air is driven by the thermally driven plume. As the hot gases rise from the fire, the gas in the plume rises and entrains the ambient air, thus inducing a flow throughout the entire domain. The rate of entrainment is determined by the relative velocity between the

plume and the ambient air system. This means the faster the plume rises relative to the ambient air, the faster the plume entrains air into the plume. Several more simplifying assumptions are made to reduce the system of equations. Due to the nature of the two systems, I formulate the problem as a boundary layer problem with corresponding inner and outer solutions. The inner solution corresponds to the plume, while the outer solution corresponds to the ambient air. Physical atmospheric effects are included in the system, which allows the stratification of density, hydrostatic pressure, and temperature. I implement the analytic set of equations in MATLAB to obtain numerical solutions. In the initial efforts, I use first order solution methods to describe interesting dynamical effects with rapid and efficient computation solution techniques. In future work, higher order solution techniques may be investigated to see if the effects of higher order accuracy outweigh computational costs.

The equations are solved using a time iterative method, where the plume properties are updated, followed by an update of the ambient air motion. Finally, the new position of the plume is calculated, and the results are plotted. In the graphical output, the plume is shaded by the density of the gases. The red, hot, colors indicate low density, and the blue, cool, colors indicate a higher density.

Energies are tracked though the plume to determine if the energies are emphasized at certain frequencies. Specifically, the kinetic energy and enstrophy are calculated due to their essential nature in physical processes.

1.4.2 Fire Model

The plume model accounts for a fire by using a stationary point source fire. The fire model described in Chapters 5 and 6 allows the description of the fire to be more than just a point source. It is assumed that a thin fuel layer lies on the ground underneath the fire plume, see Figure 1.2. Ideally, there are four regions that need to be considered: the unburned fuel region, the pyrolyzing fuel region, the fire region, and the smoldering fuel region. Physically, the fire radiates heat that converts solid fuel to gas fuel, and the gas fuel eventually burns. For means of a first approach to modeling the fire, this paradigm will be simplified even further, where

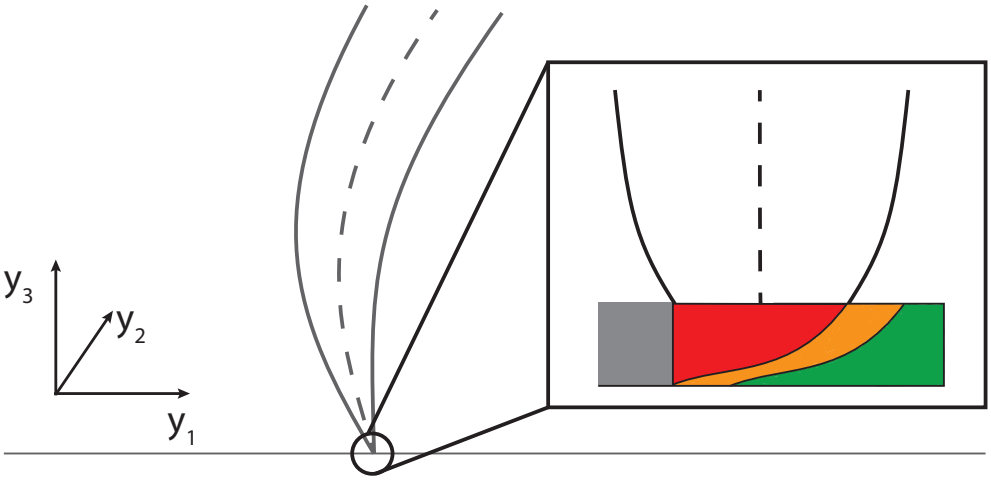

Figure 1.2: Fuel Layer With Distinct Regions for Fire Model

only a homogeneous fire region will be considered.

A control volume derivation is used to write conservation laws for total density, fuel density, oxygen density, and energy in the fire region. A quasi steady-state assumption is made to reduce the system to algebraic expressions for key pieces of data needed in making the model more physical and accurate. Once solved numerically and implemented in MATLAB, the fire model and plume models are coupled. In doing so, the information from the fire model is injected into the plume model through the point source fire and the ambient air flow influences the propagation of the fire. A feedback loop is created, allowing the fire to influence the propagation of the plume and the ambient air flow, which in turn influences the propagation of the fire.

Numerically the two models are coupled in a novel way. The situation of a crosswind flow in the plume model is used with a change of reference frame to describe the case of a propagating fire. Thus, instead of air moving past a stationary fire, a fire will be moving past stationary air. The same energies are tracked through the propagation of the plume to investigate the nature of the fire dynamics.

1.4.3 Extensions

There are many possible extensions that can be made to the plume and fire models. Some of these extensions are outlined in Chapter 8. One extension that was considered after the case of a propagating fire is the extension to fire propagation on a slope and is presented in Chapter 7. This extension involves a simple change in the implementation of the equations from the plume model.

The results from all chapters will be summarized and submitted for publication.

CHAPTER 2
Equations of Motion for Plume Model

In this chapter, the equations of motion and conservation equations will be derived for the plume model, describing both the plume and ambient air systems. The equations are derived from first principles, where simplifying assumptions and asymptotics are used to narrow the focus of the model down to the key driving dynamics of the fire plume. This is done in such a way that during future work, more terms in the asymptotic expansions can be used, making the assumptions more accurate and physical.

The situation under consideration in this model is a fire line oriented along the x_2 axis, as seen in Figure 2.1. The fire line is assumed to be nearly straight, and its width is taken to be small compared to the length scale in the x_1 direction–chosen relative to the distance the fire is expected to travel in a reasonable amount of time, as seen if Figure 2.1. From the well-defined fire line rises a sheet plume, which will bend and react to the wind conditions present in the ambient atmosphere. To reduce this three-dimensional situation to reflect the two-dimensional formulation from Section 1.4, a slice through the sheet plume, perpendicular to the fire line, is taken. With this, the situation reduces to the one shown in Figure 1.1.

Another important aspect of the model that will be exploited in this chapter is how the two systems (plume and ambient air) are connected; specifically, the two systems only interact through the entrainment of air. The plume is assumed to be narrow compared to the length scale of the ambient air region. With this, the assumption is that the plume represents a jump discontinuity from the perspective of the ambient air system, see Figure 2.2. This will be key in the derivation of the equations, not only in the ambient air system, but also in the plume system.

2.1 General Equations of Motion

The atmosphere is a complex fluid flowing on scales that reflect the importance of buoyancy, density and temperature stratification, and small scale mixing. To de-

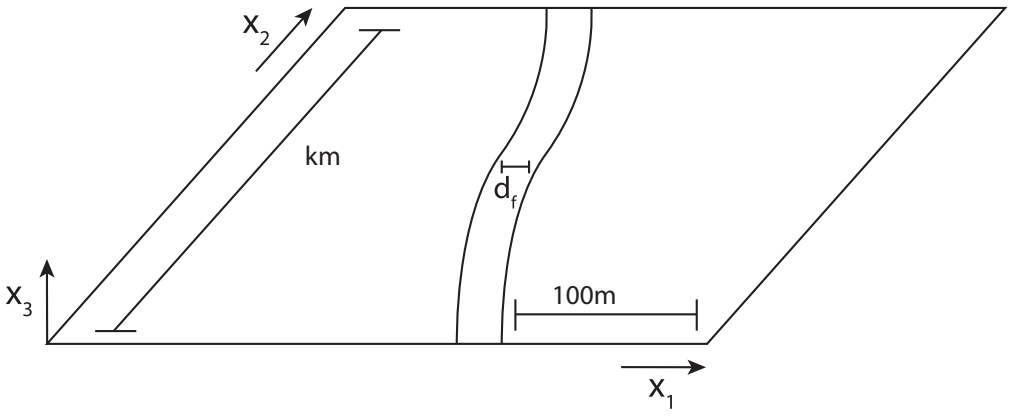

Figure 2.1: Cartesian Coordinate System in Upper Half-Plane

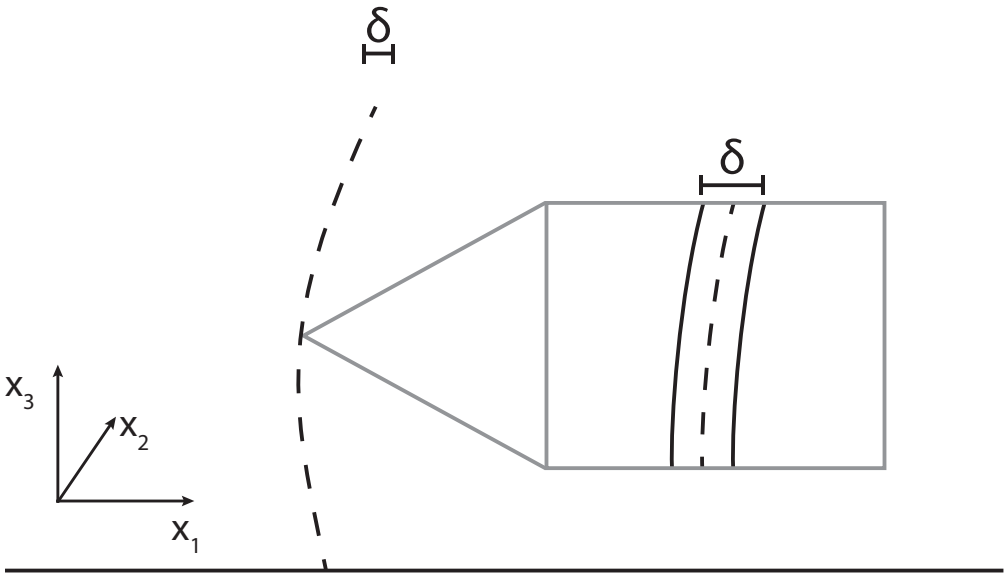

Figure 2.2: Perspective From Ambient Air

scribe the flow of this fluid, the unsteady Reynolds-averaged Navier-Stokes (uRaNS) equations for inviscid flow are written in three dimensions, along with conservation equations and an equation of state:

$$\rho_t + (\rho u_i)_{x_i} = 0 \tag{2.1.1a}$$

$$\rho\left[(u_i)_t + u_k(u_i)_{x_k}\right] + p_{x_i} - \rho g e_{g\,i} = T^{Re}_{ij\,x_j} \tag{2.1.1b}$$

$$\rho C_p\left[T_t + u_i T_{x_i}\right] - \left[p_t + u_i p_{x_i}\right] = Q + q^{Re}_{i\,x_i} \tag{2.1.1c}$$

$$p = \rho \bar{R} T. \tag{2.1.1d}$$

Here, $\mathbf{x} = (x_1, x_2, x_3)$ are cartesian coordinates (see Figure 2.1), t is time, ρ is density, T is temperature, $\mathbf{u}$ is velocity, p is pressure, Q is a heat source, $\mathbf{T}^{Re}$ is the Reynolds stress, $\mathbf{q}^{Re}$ is the Reynolds heat flux, g is gravity in direction $\mathbf{e}_g$, $\bar{R}$ is the ideal gas constant, and C_p is the specific heat at constant pressure.

The system (2.1.1) is non-dimensionalized by making the changes of variables:

$$\begin{aligned}
\tau &= \frac{t}{t_0} & y_i &= \frac{x_i}{l_i} & \rho &= \rho_0 \tilde{R}(y_i, \tau) \\
u_i &= U_0 v_i(y_i, \tau) & T &= T_0 \tilde{\theta}(y_i, \tau) & p &= p_0 P(y_i, \tau) \\
Q &= \frac{E_0}{t_0} \tilde{Q} & T^{Re} &= \eta_0 \tilde{T}^{Re}(y_i, \tau) & q^{Re} &= \xi_0 \tilde{q}^{Re}(y_i, \tau),
\end{aligned}$$

where t_0, l_i, ρ_0, U_0, T_0, p_0, E_0, η_0, and ξ_0 are the scaling constants for time, space, density, velocity, temperature, pressure, the heat source, the Reynolds stress, and the Reynolds heat flux respectively.

The flow induced by a line heat source representing a fire is of interest; thus, it is also assumed that the temperature, density and velocity have the form:

$$\star = \star_0 \begin{cases} \star_o(y_i, \tau) & \text{for } |y_1 - y_{1p}| \geq \frac{b}{2} \qquad (2.1.2a) \\ \star(y_i, \tau) & \text{for } |y_1 - y_{1p}| \leq \frac{b}{2}, \qquad (2.1.2b) \end{cases}$$

where $\star_o(y_i, \tau)$ represents scaled $\star$ outside the plume, and $\star(y_i, \tau)$ represents scaled $\star$ inside the plume. Also, define $y_{1p}(y_3, \tau)$ as the centerline of the plume and $b(y_3, \tau)$ is the width of the plume. In this section for the purposes of scaling, it will be assumed that the general form of these variables is $\star = \star_0 \cdot \tilde{\star}(y_i, \tau)$.

The changes of variables are substituted into (2.1.1) and simplified to obtain the non-dimensional system:

$$\tilde{R}_\tau + \frac{U_0 t_0}{l_3} \frac{l_3}{l_i} \left(\tilde{R} \tilde{v}_i \right)_{y_i} = 0 \tag{2.1.3a}$$

$$\tilde{R} \left[(\tilde{v}_i)_\tau + \frac{U_0 t_0}{l_3} \frac{l_3}{l_k} \left(\tilde{v}_k (\tilde{v}_i)_{y_k} \right) \right] + \frac{p_0 t_0}{\rho_0 U_0 l_3} \frac{l_3}{l_i} P_{y_i} - \frac{\tilde{R} t_0 g e_{g\,i}}{U_0} = \frac{\eta_0 t_0}{\rho_0 U_0 l_3} \frac{l_3}{l_j} \tilde{T}^{Re}_{ij\,y_j} \tag{2.1.3b}$$

$$\tilde{R}\left[\tilde{\theta}_\tau + \frac{U_0 t_0}{l_3}\frac{l_3}{l_i}\tilde{v}_i\tilde{\theta}_{y_i}\right] - \left[\frac{p_0}{\rho_0 C_p T_0}P_\tau + \frac{U_0 t_0 p_0}{\rho_0 C_p T_0 l_3}\frac{l_3}{l_i}\tilde{v}_i P_{y_i}\right] = \frac{E_0}{\rho_0 C_p T_0}\tilde{Q} + \frac{\xi_0 t_0}{\rho_0 C_p T_0 l_3}\frac{l_3}{l_i}\tilde{q}^{Re}_{i\,y_i} \quad (2.1.3c)$$

$$p_0 P = \rho_0 \tilde{R}\bar{R}T_0\tilde{\theta}. \quad (2.1.3d)$$

The thermal effects are separated from dynamical effects in the pressure. To do this, the dependent variables are scaled in a perturbation series [63] as follows:

$$\begin{aligned} P &= P^{(H)} + \beta P^{(H1)} + \sigma P^{(1)} & \tilde{v}_i &= \frac{l_3}{U_0 t_0}\tilde{v}_i^{(0)} \\ \tilde{R} &= \tilde{R}^{(0)} & \tilde{T}^{Re}_{ij} &= \tilde{T}^{(0)}_{ij} \\ \tilde{q}^{Re}_i &= \tilde{q}^{(0)} & \tilde{\theta} &= \tilde{\theta}^{(0)}, \end{aligned} \quad (2.1.4)$$

where here, $P^{(H)}(y_i,\tau)$ is the leading order hydrostatic pressure, $P^{(H1)}(y_i,\tau)$ is the order β correction to the hydrostatic pressure, and $P^{(1)}(y_i,\tau)$ is the dynamic pressure. It is assumed that the separation parameters, β and σ, are chosen such that a well ordered expansion in pressure is obtained (verification to follow).

Upon substituting these expansions into (2.1.3), the system reduces to:

$$\tilde{R}^{(0)}_\tau + \frac{l_3}{l_i}\left(\tilde{R}^{(0)}\tilde{v}_i^{(0)}\right)_{y_i} = 0 \quad (2.1.5a)$$

$$\frac{\rho_0 l_3^2}{p_0 t_0^2}\tilde{R}^{(0)}\left[(\tilde{v}_i^{(0)})_\tau + \frac{l_3}{l_k}\left(\tilde{v}_k^{(0)}(\tilde{v}_i^{(0)})_{y_k}\right)\right] + \frac{l_3}{l_i}\left(P^{(H)}_{y_i} + \beta P^{(H1)}_{y_i} + \sigma P^{(1)}_{y_i}\right) = \frac{\rho_0 l_3 g e_{g\,i}}{p_0}\tilde{R}^{(0)} + \frac{\eta_0}{p_0}\frac{l_3}{l_j}\tilde{T}^{(0)}_{ij\,y_j} \quad (2.1.5b)$$

$$\tilde{R}^{(0)}\left[\tilde{\theta}^{(0)}_\tau + \frac{l_3}{l_i}\tilde{v}_i^{(0)}\tilde{\theta}^{(0)}_{y_i}\right] - \left[\frac{p_0}{\rho_0 C_p T_0}\left(P^{(H)}_\tau + \beta P^{(H1)}_\tau + \sigma P^{(1)}_\tau\right) + \frac{p_0}{\rho_0 C_p T_0}\frac{l_3}{l_i}\tilde{v}_i^{(0)}\left(P^{(H)}_{y_i} + \beta P^{(H1)}_{y_i} + \sigma P^{(1)}_{y_i}\right)\right] = \frac{E_0}{\rho_0 C_p T_0}\tilde{Q} + \frac{\xi_0 t_0}{\rho_0 C_p T_0 l_3}\frac{l_3}{l_i}\tilde{q}^{(0)}_{i\,y_i} \quad (2.1.5c)$$

$$p_0\left(P^{(H)} + \beta P^{(H1)} + \sigma P^{(1)}\right) = \rho_0 \tilde{R}^{(0)}\bar{R}T_0\tilde{\theta}^{(0)}. \quad (2.1.5d)$$

2.1.1 Assumptions

The paradigm of interest is a plume of hot gases rising through, and disturbing, an ambient body of air. As discussed in Section 1.4, the rising gases in the plume entrain the ambient air, causing a flow that interacts with the plume and the fire. Scalings that are consistent with this scenario will be discussed. There are several assumptions, which are presented and discussed here, that ensure the balances and scalings are correct.

The driving force in the equations, specifically the momentum equation (2.1.5b), is the buoyancy force in the plume. Consequently, the leading pressure term needs to balance the gravity term. By the same token, in the temperature equation, (2.1.5c), the temperature terms need to balance the heat source term. Thus, the following definitions are taken:

$$\sigma = \frac{l_3^2}{\bar{R}T_0 t_0^2} \tag{2.1.6}$$

$$\bar{R} = \frac{p_0}{\rho_0 T_0} \Rightarrow p_0 = \bar{R}\rho_0 T_0 \tag{2.1.7}$$

$$\frac{\bar{R}}{C_p} = \frac{\gamma - 1}{\gamma}, \tag{2.1.8}$$

where $\gamma \equiv$ specific heat ratio. In addition, a scaled plume velocity is defined by:

$$V_p \propto \frac{E_0}{T_0 \rho_0 C_p}. \tag{2.1.9}$$

The balance (2.1.7) is obtained from the equation of state, (2.1.5d), and is used to relate pressure, temperature and density scales. Equation (2.1.8) is a classic relation from thermodynamics, and the definition (2.1.9) was made to simplify and scale expressions later in the plume system.

A perturbation analysis for σ and β small is made. It is verified in this section that this assumption of σ and β small is consistent with atmospheric flow on the scale of a wildfire. Note that if a length scale of 100m and a time scale of 4sec are taken:

$$\sigma = \frac{l_3^2}{\bar{R}T_0 t_0^2} \approx \frac{(100\text{m})^2}{\left(286.9\frac{\text{m}^2}{\text{sec}^2\text{K}}\right)(292.3669\text{K})(4\text{sec})^2} = 0.00745,$$

where the temperature scale used is $T_0 = \frac{p_0}{\bar{R}\rho_0} \approx \frac{101000\frac{\text{kg}}{\text{msec}^2}}{\left(286.9\frac{\text{m}^2}{\text{sec}^2\text{K}}\right)\left(1.2041\frac{\text{kg}}{\text{m}^3}\right)} = 292.3669\text{K}$. Also, it is taken that $\bar{R}$ is the gas constant for dry air. From this, it is verified that σ is a small parameter. The choice of σ in (2.1.6) was made to ensure that the $P^{(1)}$ term balances with the velocity terms in the momentum equation (2.1.5b). It must also be noted that physically σ represents the square of the Mach number. This can be seen by rewriting σ such that:

$$\sigma = \frac{\frac{l_3^2}{t_0^2}}{\bar{R}T_0} = \frac{\frac{l_3^2}{t_0^2}}{\text{c}^2} = \text{Ma}^2,$$

where the numerator can be thought of as the square of a velocity scale, and the denominator is c^2, the square of the sound speed.

It can be seen that $\bar{R}T_0$ is the sound speed by considering the original Navier-Stokes equations:

$$\rho_t + \nabla \cdot (\rho \mathbf{u}) = 0$$
$$\rho \left[\mathbf{u}_t + \mathbf{u} \cdot \nabla \mathbf{u}\right] = -\nabla p.$$

Take $p = p(\rho)$ and expanding the velocity and density in a perturbation expansion, one has $\mathbf{u} = \epsilon \mathbf{u}_1$, $\rho = \rho_0 + \epsilon \rho_1$. Keeping only the $O(\epsilon)$ terms:

$$\rho_{1\,t} + \rho_0 \nabla \cdot (\mathbf{u}_1) = 0$$
$$\rho_0 \mathbf{u}_{1\,t} = -\frac{\partial p}{\partial \rho}(\rho_0) \nabla \rho_1,$$

since ρ_0 is a constant. Upon taking the time derivative of the first, the divergence of the second, and combining, one obtains:

$$\frac{\partial \rho_1^2}{\partial t^2} = \frac{\partial p}{\partial \rho}(\rho_0) \nabla^2 \rho_1,$$

where it is recognized that $\frac{\partial p}{\partial \rho}(\rho_0) = c^2$. Additionally using the equation of state,

$p = \rho RT$, and taking the derivative with respect to density, one obtains:

$$\left.\frac{\partial p}{\partial \rho}\right|_{T=\text{const}} = RT,$$

with this, one has that $\bar{R}T_0 = c^2$ and represents the isothermal sound speed.

Thus, $\sigma = \text{Ma}^2$, where Ma is the Mach number and $\sigma \ll 1$ corresponds to a small Mach number for this flow, so that the characteristic velocities are small compared to the sound speed.

For later reference the size of some of the parameters will be provided to verify the perturbation analysis assumption:

$$\frac{l_3}{t_0^2 g} \approx \frac{100\text{m}}{\left(9.8\frac{\text{m}}{\text{sec}^2}\right)(4\text{sec})^2} = 0.6378$$

$$\beta = \frac{g l_3}{\bar{R}T_0} \approx \frac{\left(9.8\frac{\text{m}}{\text{sec}^2}\right)(100\text{m})}{(286.9\frac{\text{m}^2}{\text{sec}^2\text{K}})(292.3669\text{K})} = 0.011683,$$

where β represents a buoyancy parameter. Again, the physical meaning of β is investigated by rewriting the expression as:

$$\beta = \frac{g l_3}{\text{v}^2}\frac{\text{v}^2}{\bar{R}T_0} = \text{RiMa}^2,$$

where $\text{v}^2 = \frac{l_3^2}{t_0^2}$, and Ri is the Richardson number. Physically, this parameter represents the ratio of the rise velocity to the sound speed of the system. Thus, saying β is small corresponds to an $o(\text{Ma}^{-2})$ Richardson number for this flow.

The assumption about pressure, (2.1.4), could be thought of as the first three terms in an asymptotic expansion. There are various order problems that result from the single expansion. At this point, additional terms in the expansions are not considered. Later, first approximation systems will be discussed. These systems have been taken to be analogous to the $O(1)$ expansion of an asymptotic expansion problem [29], by letting the small parameters (β and σ) go to zero. From this, the first approximation system of the asymptotic expansion problem is obtained.

With these balances, the assumptions, (2.1.6)-(2.1.8), are substituted into the

non-dimensional system (2.1.5) to get the simplified system that will be used for the rest of this chapter:

$$\tilde{R}^{(0)}_{\tau} + \frac{l_3}{l_i}\left(\tilde{R}^{(0)}\tilde{v}^{(0)}_i\right)_{y_i} = 0 \tag{2.1.10a}$$

$$\frac{l_3^2}{\bar{R}T_0t_0^2}\tilde{R}^{(0)}\left[(\tilde{v}^{(0)}_i)_{\tau} + \frac{l_3}{l_k}\left(\tilde{v}^{(0)}_k(\tilde{v}^{(0)}_i)_{y_k}\right)\right] + \frac{l_3}{l_i}\left(P^{(H)}_{y_i} + \frac{gl_3}{\bar{R}T_0}P^{(H1)}_{y_i} + \frac{l_3^2}{\bar{R}T_0t_0^2}P^{(1)}_{y_i}\right) = \frac{gl_3e_{g\,i}}{\bar{R}T_0}\tilde{R}^{(0)} + \frac{\eta_0}{\bar{R}\rho_0T_0}\frac{l_3}{l_j}\tilde{T}^{(0)}_{ij\,y_j} \tag{2.1.10b}$$

$$\tilde{R}^{(0)}\left[\tilde{\theta}^{(0)}_{\tau} + \frac{l_3}{l_i}\tilde{v}^{(0)}_i\tilde{\theta}^{(0)}_{y_i}\right] - \frac{\gamma-1}{\gamma}\left[\left(P^{(H)}_{\tau} + \frac{gl_3}{\bar{R}T_0}P^{(H1)}_{\tau} + \frac{l_3^2}{\bar{R}T_0t_0^2}P^{(1)}_{\tau}\right) + \frac{l_3}{l_i}\tilde{v}^{(0)}_i\left(P^{(H)}_{y_i} + \frac{gl_3}{\bar{R}T_0}P^{(H1)}_{y_i} + \frac{l_3^2}{\bar{R}T_0t_0^2}P^{(1)}_{y_i}\right)\right] = V_p\tilde{Q} + \frac{\xi_0t_0}{\rho_0C_pT_0l_3}\frac{l_3}{l_i}\tilde{q}^{(0)}_{i\,y_i} \tag{2.1.10c}$$

$$P^{(H)} + \frac{gl_3}{\bar{R}T_0}P^{(H1)} + \frac{l_3^2}{\bar{R}T_0t_0^2}P^{(1)} = \tilde{R}^{(0)}\tilde{\theta}^{(0)}. \tag{2.1.10d}$$

The additional assumptions that $l_3, l_1 \ll l_2$ and $l_1 \propto l_3$ are made, and to set the coordinate system, choose:

$$\mathbf{e}_g = \begin{pmatrix} 0 \\ 0 \\ -1 \end{pmatrix}.$$

Due to the geometry of the problem, the solution method will be reminiscent of the solution to a boundary layer problem. With this, the solution of the system (2.1.10) represents the general solution to the boundary layer problem being examined. An additional set of assumptions will differentiate the inner and outer solutions, which will be discussed in Section 2.2 and Section 2.3.

2.2 Outer Solution

The ambient air system describes the flow of the fluid outside the plume, which includes the transportation of vorticity throughout the system. Mathematically, the dynamics of this system are viewed as the outer solution of a boundary layer problem. The two names (ambient air system and outer solution) will be interchanged as they

mean the same thing. The system (2.1.10) from above is used and it is additionally chosen that $\tilde{Q} = 0$, $\tilde{v} = v_o$, $\frac{\xi_0 t_0}{\rho_0 C_p T_0 l_3} \ll 1$, $\frac{\eta_0}{\bar{R}\rho_0 T_0} \ll 1$, $\sigma = \mathrm{Ma}^2$, and $\beta = \mathrm{RiMa}^2$. In the ambient air system only, following the expansion of pressure, let $\tilde{R} = R_o^{(H)} + \beta R_o^{(H1)} + \sigma R_o^{(1)}$, $\tilde{\theta} = \theta_o^{(H)} + \beta\theta_o^{(H1)} + \sigma\theta_o^{(1)}$.

Substituting these above assumptions and the limiting case assumptions (2.1.6), (2.1.7), (2.1.8) into (2.1.10), dropping the unneeded expansion notation and expanding results in the system:

$$\left(R_o^{(H)} + \beta R_o^{(H1)} + \sigma R_o^{(1)}\right)_\tau + \left[\left(R_o^{(H)} + \beta R_o^{(H1)} + \sigma R_o^{(1)}\right) v_{o1}\right]_{y_1} + \left[\left(R_o^{(H)} + \beta R_o^{(H1)} + \sigma R_o^{(1)}\right) v_{o3}\right]_{y_3} = 0 \tag{2.2.1a}$$

$$\sigma\left(R_o^{(H)} + \beta R_o^{(H1)} + \sigma R_o^{(1)}\right)\left[(v_{o1})_\tau + (v_{o1}(v_{o1})_{y_1}) + (v_{o3}(v_{o1})_{y_3})\right] + P_{y_1}^{(H)} + \beta P_{y_1}^{(H1)} + \sigma P_{y_1}^{(1)} = 0 \tag{2.2.1b}$$

$$\sigma\left(R_o^{(H)} + \beta R_o^{(H1)} + \sigma R_o^{(1)}\right)\left[(v_{o3})_\tau + (v_{o1}(v_{o3})_{y_1}) + (v_{o3}(v_{o3})_{y_3})\right] + P_{y_3}^{(H)} + \beta P_{y_3}^{(H1)} + \sigma P_{y_3}^{(1)} = -\beta\left(R_o^{(H)} + \beta R_o^{(H1)} + \sigma R_o^{(1)}\right) \tag{2.2.1c}$$

$$\left(R_o^{(H)} + \beta R_o^{(H1)} + \sigma R_o^{(1)}\right)\Big[\left(\theta_o^{(H)} + \beta\theta_o^{(H1)} + \sigma\theta_o^{(1)}\right)_\tau + v_{o1}\left(\theta_o^{(H)} + \beta\theta_o^{(H1)} + \sigma\theta_o^{(1)}\right)_{y_1} + v_{o3}\left(\theta_o^{(H)} + \beta\theta_o^{(H1)} + \sigma\theta_o^{(1)}\right)_{y_3}\Big] - \frac{\gamma-1}{\gamma}\left[P_\tau^{(H)} + \beta P_\tau^{(H1)} + \sigma P_\tau^{(1)} + v_{o1}\left(P_{y_1}^{(H)} + \beta P_{y_1}^{(H1)} + \sigma P_{y_1}^{(1)}\right) + v_{o3}\left(P_{y_3}^{(H)} + \beta P_{y_3}^{(H1)} + \sigma P_{y_3}^{(1)}\right)\right] = 0 \tag{2.2.1d}$$

$$\left(R_o^{(H)} + \beta R_o^{(H1)} + \sigma R_o^{(1)}\right)\left(\theta_o^{(H)} + \beta\theta_o^{(H1)} + \sigma\theta_o^{(1)}\right) = P^{(H)} + \beta P^{(H1)} + \sigma P^{(1)}. \tag{2.2.1e}$$

2.2.1 $O(1)$ Ambient Air System

A first approximation is made, using the fact that $\mathrm{Ma}^2 \ll 1$ ($\sigma \ll 1$) and $\beta \ll 1$ to get the first approximation system:

$$R_{o\tau}^{(H)} + \left(R_o^{(H)} v_{o1}\right)_{y_1} + \left(R_o^{(H)} v_{o3}\right)_{y_3} = 0 \tag{2.2.2a}$$

$$P_{y_1}^{(H)} = 0 \tag{2.2.2b}$$

$$P_{y_3}^{(H)} = 0 \tag{2.2.2c}$$

$$R_o^{(H)}\left[(\theta_o^{(H)})_\tau + v_{o1}(\theta_o^{(H)})_{y_1} + v_{o3}(\theta_o^{(H)})_{y_3}\right]$$
$$-\frac{\gamma-1}{\gamma}\left[P_\tau^{(H)} + v_{o1}P_{y_1}^{(H)} + v_{o3}P_{y_3}^{(H)}\right] = 0 \tag{2.2.2d}$$
$$P^{(H)} = R_o^{(H)}\theta_o^{(H)}. \tag{2.2.2e}$$

Use of the momentum equations, the energy equation, the boundary conditions, and the equation of state easily gives $\theta_o^{(H)} = 1$, $R_o^{(H)} = 1$, and $P^{(H)} = 1$.

2.2.2 $O(\beta)$ Ambient Air System

Continuing to separate orders, the next order system is the $O(\beta)$ system:

$$R_{o\tau}^{(H1)} + \left(R_o^{(H1)}v_{o1}\right)_{y_1} + \left(R_o^{(H1)}v_{o3}\right)_{y_3} = 0 \tag{2.2.3a}$$
$$P_{y_1}^{(H1)} = 0 \tag{2.2.3b}$$
$$P_{y_3}^{(H1)} = -R_o^{(H)} \tag{2.2.3c}$$
$$R_o^{(H)}\left[(\theta_o^{(H1)})_\tau + v_{o1}(\theta_o^{(H1)})_{y_1} + v_{o3}(\theta_o^{(H1)})_{y_3}\right]$$
$$-\frac{\gamma-1}{\gamma}\left[P_\tau^{(H1)} + v_{o1}P_{y_1}^{(H1)} + v_{o3}P_{y_3}^{(H1)}\right] = 0 \tag{2.2.3d}$$
$$P^{(H1)} = R_o^{(H1)} + \theta_o^{(H1)}. \tag{2.2.3e}$$

The expressions for the $O(\beta)$ corrections to density, temperature, and hydrostatic pressure can be found. Noting that the energy equation, (2.2.3d), can be written in terms of material derivatives yields:

$$\frac{D\theta_o^{(H1)}}{D\tau} = \frac{\gamma-1}{\gamma}\frac{DP^{(H1)}}{D\tau}.$$

Thus,

$$\frac{D\theta_o^{(H1)}}{D\tau} = (\gamma-1)\frac{DR_o^{(H1)}}{D\tau},$$

and integrating gives:

$$\theta_o^{(H1)} = (\gamma-1)R_o^{(H1)} + c_1.$$

Using the equation of state, one obtains:

$$P^{(H1)} = R_o^{(H1)} + (\gamma - 1)R_o^{(H1)} + c_1$$
$$P^{(H1)} = \gamma R_o^{(H1)} + c_1,$$

from which one obtains:

$$P_{y_3}^{(H1)} = \gamma R_{o\,y_3}^{(H1)}.$$

Using the momentum equation in the y_3 direction, one obtains the differential relation:

$$\gamma R_{o\,y_3}^{(H1)} = -R_o^{(H)} = -1$$
$$R_{o\,y_3}^{(H1)} = -\frac{1}{\gamma}.$$

Thus:

$$R_o^{(H1)} = -\frac{1}{\gamma}y_3 + c_2.$$

Using the boundary condition at the ground, $c_2 = 0$, and:

$$R_o^{(H1)} = -\frac{1}{\gamma}y_3.$$

Thus,

$$R_o^{(H1)} = -\frac{1}{\gamma}y_3$$
$$\theta_o^{(H1)} = \left(\frac{1}{\gamma} - 1\right)y_3 + c_1$$
$$P^{(H1)} = -y_3 + c_1.$$

Again using the boundary condition at the ground, $c_1 = 0$. This also ensures all three full expansions go to zero as $y_3 \to \infty$. After using the boundary conditions,

one obtains:

$$R_o^{(H1)} = -\frac{1}{\gamma} y_3 \tag{2.2.4}$$

$$\theta_o^{(H1)} = \left(\frac{1}{\gamma} - 1\right) y_3 \tag{2.2.5}$$

$$P^{(H1)} = -y_3. \tag{2.2.6}$$

With this, the full asymptotic expansions can be written as:

$$P = 1 - \beta y_3 + \sigma P^{(1)} \tag{2.2.7}$$

$$\theta = 1 - \beta \left(1 - \frac{1}{\gamma}\right) y_3 + \sigma \theta_o^{(1)} \tag{2.2.8}$$

$$R = 1 - \beta \frac{1}{\gamma} y_3 + \sigma R_o^{(1)}. \tag{2.2.9}$$

One can easily see that a first term approximation physically corresponds to an unstratified atmosphere. Keeping the $O(\beta)$ correction in the expansions allows each of the quantities to decrease as height increases. Physically, the two term approximation corresponds to a physically accurate stratified atmosphere. From here on, approximations of the asymptotic expansions are taken, such that only the first non-zero terms are included. Thus, the ambient air system is seen to be incompressible under this first term approximation. One will note that the $O(\beta)$ correction to the pressure will be used in the plume system where pressure gradient terms are needed.

2.2.3 $O(\sigma)$ Ambient Air System

Finally, the $O(\sigma)$ system is written as:

$$R_{o\,\tau}^{(1)} + \left(R_o^{(1)} v_{o1}\right)_{y_1} + \left(R_o^{(1)} v_{o3}\right)_{y_3} = 0 \tag{2.2.10a}$$

$$R_o^{(H)} \left[(v_{o1})_\tau + (v_{o1}(v_{o1})_{y_1}) + (v_{o3}(v_{o1})_{y_3})\right] + P_{y_1}^{(1)} = 0 \tag{2.2.10b}$$

$$R_o^{(H)} \left[(v_{o3})_\tau + (v_{o1}(v_{o3})_{y_1}) + (v_{o3}(v_{o3})_{y_3})\right] + P_{y_3}^{(1)} = 0 \tag{2.2.10c}$$

$$R_o^{(H)} \left[(\theta_o^{(1)})_\tau + v_{o1}(\theta_o^{(1)})_{y_1} + v_{o3}(\theta_o^{(1)})_{y_3}\right] - \frac{\gamma - 1}{\gamma} \left[P_\tau^{(1)} + v_{o1} P_{y_1}^{(1)} + v_{o3} P_{y_3}^{(1)}\right] = 0 \tag{2.2.10d}$$

$$P^{(1)} = R_o^{(1)} + \theta_o^{(1)}. \tag{2.2.10e}$$

For the purpose of this work, the $O(\sigma)$ system is used for the calculation of the velocity and vorticity. It is easily seen that expressions for the $O(\sigma)$ contributions of temperature and density can be written using a similar process to (2.2.3). In addition, Bernoulli's equation can also be used for a derivation of the pressure in this system, see Section 2.2.7.

2.2.4 Vorticity Transport Equation

The vorticity equation can be found from the $O(\sigma)$ equations, (2.2.10). The curl of the momentum equations is taken to derive the vorticity equation:

$$\omega_\tau + v_{o\,1}\omega_{y_1} + v_{o\,3}\omega_{y_3} = -\left(\nabla \cdot \hat{\mathbf{v}}\right)\omega,$$

where $\hat{\mathbf{v}} = (v_{o\,1}, v_{o\,3})^T$. Equation (2.2.1a) is used to find an expression for $(\nabla \cdot \hat{\mathbf{v}})$. This simplification results in:

$$\frac{D\omega}{D\tau} = \frac{\omega}{R_o}\frac{DR_o}{D\tau}. \tag{2.2.11}$$

Using the full three term expansion of density, (2.2.9), in (2.2.11) and following the expansion of the other ambient air variables, $\omega = \omega_0 + \beta\omega_1 + \sigma\omega_2$. Upon separating orders:

$$\frac{D\omega_0}{D\tau} = 0 \tag{2.2.12}$$

$$\frac{D\omega_1}{D\tau} = \frac{1}{\gamma}v_{o\,3}\omega_0 \tag{2.2.13}$$

$$\frac{D\omega_2}{D\tau} = -\omega_0\left(R_{o\,\tau}^{(1)} + R_{o\,y_1}^{(1)}v_1 + R_{o\,y_3}^{(1)}v_3\right). \tag{2.2.14}$$

Assuming constant density (a first non-zero approximation of the asymptotic expansion) means the $O(1)$ vorticity equation is solved and integration yields:

$$\frac{D\omega_0}{D\tau} = 0 \implies \omega_0 = \text{constant}. \tag{2.2.15}$$

Thus, the vorticity is constant along streamlines in the ambient air domain (up to a first order approximation). If it is assumed that all streamlines terminate at $\pm\infty$, and that there is no vorticity far from the plume, the result is:

$$\omega_0 = 0. \tag{2.2.16}$$

For the scope of this work, only the lowest order approximation to vorticity is used. It is easily seen that more terms in the approximation can be considered and would involve solving the corresponding order vorticity equation. Thus, the flow in the ambient air is irrotational, up to a first term approximation. With this and the asymptotic expansion of density, the ambient air flow is incompressible and irrotational, up to a first non-zero approximation.

2.2.5 Velocity in the Ambient Air

The flow in the ambient air is assumed to be induced by the point source fire and entrainment of air into the plume. In calculating the velocity in the ambient air, several features are used to simplify the calculation. From the perspective of the ambient air system, the plume represents a discontinuity. It is assumed that the net entrainment is into the plume. Thus, the entrainment can be represented by a line sink/vortex combination along the discontinuity that represents the plume. Once the system is discretized to be solved numerically, the line sink/vortex is represented by point sink/vortices at each computation node, see Section 3.1 for details on the discretization.

Since the flow is two-dimensional, irrotational, and incompressible, a potential flow solution to calculate the velocity is appropriate for computational points far from the discontinuity. Additionally, the velocity induced by the line sink/vortex combination on the discontinuity that represents the plume can be expressed as a Biot-Savart integral. The potential flow solution is used for all points away from singularities, and the Biot-Savart integral is used at points where singularities occur following Alben and Shelley [1]. From this, the velocity, potential, and stream functions can be written.

Following Marshall [45], the Helmholtz Representation Theorem is used to

write the velocity, $\bar{\mathbf{v}} = (\bar{u}, \bar{v})$, as:

$$\bar{\mathbf{v}} = \nabla\alpha + \nabla \times \boldsymbol{\beta}. \tag{2.2.17}$$

Here α is the scalar potential, $\boldsymbol{\beta}$ is the vector potential, and:

$$\alpha = \int_V G(\mathbf{y} - \mathbf{y}')\Delta(\mathbf{y}', t)\mathrm{d}v' \tag{2.2.18}$$

$$\boldsymbol{\beta} = -\int_V G(\mathbf{y} - \mathbf{y}')\boldsymbol{\omega}(\mathbf{y}', t)\mathrm{d}v', \tag{2.2.19}$$

where,

$$\nabla^2\alpha = \Delta = \nabla \cdot \bar{\mathbf{v}} \tag{2.2.20a}$$

$$\nabla^2\boldsymbol{\beta} = -\boldsymbol{\omega} = -\nabla \times \bar{\mathbf{v}}. \tag{2.2.20b}$$

For a two dimensional flow, $\boldsymbol{\beta} = \beta\mathbf{e}_{y_2}$, $\boldsymbol{\omega} = \omega\mathbf{e}_{y_2}$, and $G(\mathbf{y} - \mathbf{y}')$ represents the Green's function. In two dimensions $G(\mathbf{y} - \mathbf{y}')$ takes the form: $G(\mathbf{y} - \mathbf{y}') = \frac{1}{2\pi}\ln|\mathbf{y} - \mathbf{y}'|$, $\mathbf{y} = (y_1, 0, y_3)^T$. Thus,

$$\alpha = \int_A \frac{1}{2\pi}\ln|\mathbf{y} - \mathbf{y}'|\Delta(\mathbf{y}', t)\mathrm{d}a' \tag{2.2.21}$$

$$\beta = -\int_A \frac{1}{2\pi}\ln|\mathbf{y} - \mathbf{y}'|\omega(\mathbf{y}', t)\mathrm{d}a'. \tag{2.2.22}$$

2.2.5.1 Point Source/Sink or Vortex

The interest is to write the velocity induced by a single point source/vortex, away from any singularities. This can be done by using a pure potential flow solution.

It is well known that for a point source/sink, one has $\Delta(y_1 - y_1', y_3 - y_3') = m\delta(y_1 - y_1', y_3 - y_3')$, where m represents the source/sink strength. The expression for α can be obtained by substituting into (2.2.21):

$$\alpha = \frac{m}{2\pi}\ln\left((y_1 - y_1')^2 + (y_3 - y_3')^2\right)^{\frac{1}{2}}. \tag{2.2.23}$$

Similarly for a vortex, $\omega(y_1 - y_1', y_3 - y_3') = \Omega\delta(y_1 - y_1', y_3 - y_3')$, where Ω represents the point vortex strength. Upon substituting into (2.2.22), the expression

for β can be found:

$$\beta = -\frac{\Omega}{2\pi} \ln\left((y_1 - y_1')^2 + (y_3 - y_3')^2\right)^{\frac{1}{2}}. \tag{2.2.24}$$

Using the law of superposition and (2.2.17), an expression for the velocity, $\bar{\mathbf{v}}$, can be written as:

$$\bar{\mathbf{v}} = \nabla\alpha + \nabla \times \boldsymbol{\beta} = \begin{pmatrix} \frac{m(y_1 - y_1')}{2\pi\left[(y_1 - y_1')^2 + (y_3 - y_3')^2\right]} - \frac{\Omega(y_3 - y_3')}{2\pi\left[(y_1 - y_1')^2 + (y_3 - y_3')^2\right]} \\ \frac{m(y_3 - y_3')}{2\pi\left[(y_1 - y_1')^2 + (y_3 - y_3')^2\right]} + \frac{\Omega(y_1 - y_1')}{2\pi\left[(y_1 - y_1')^2 + (y_3 - y_3')^2\right]} \end{pmatrix}, \tag{2.2.25}$$

where it needs to be remembered that the source strength, $m = -S_v$, since the plume will entrain air, making it a sink. The method of images is used to ensure the ground is impenetrable or, $\bar{v} = 0$ when $y_3 = 0$. This leads to the expressions for $\bar{u}$ and $\bar{v}$:

$$\begin{aligned} \bar{u}(y_1, y_3) = &\frac{-S_v(y_1 - y_1')}{2\pi\left[(y_1 - y_1')^2 + (y_3 - y_3')^2\right]} + \frac{-S_v(y_1 - y_1')}{2\pi\left[(y_1 - y_1')^2 + (y_3 + y_3')^2\right]} \\ &- \frac{\Omega(y_3 - y_3')}{2\pi\left[(y_1 - y_1')^2 + (y_3 - y_3')^2\right]} + \frac{\Omega(y_3 + y_3')}{2\pi\left[(y_1 - y_1')^2 + (y_3 + y_3')^2\right]} \end{aligned} \tag{2.2.26a}$$

$$\begin{aligned} \bar{v}(y_1, y_3) = &\frac{-S_v(y_3 - y_3')}{2\pi\left[(y_1 - y_1')^2 + (y_3 - y_3')^2\right]} + \frac{-S_v(y_3 + y_3')}{2\pi\left[(y_1 - y_1')^2 + (y_3 + y_3')^2\right]} \\ &+ \frac{\Omega(y_1 - y_1')}{2\pi\left[(y_1 - y_1')^2 + (y_3 - y_3')^2\right]} - \frac{\Omega(y_1 - y_1')}{2\pi\left[(y_1 - y_1')^2 + (y_3 + y_3')^2\right]}. \end{aligned} \tag{2.2.26b}$$

From here, the Cauchy-Riemann equations,

$$\bar{u} = \frac{\partial\bar{\phi}}{\partial y_1} = \frac{\partial\bar{\psi}}{\partial y_3} \tag{2.2.27a}$$

$$\bar{v} = \frac{\partial\bar{\phi}}{\partial y_3} = -\frac{\partial\bar{\psi}}{\partial y_1}, \tag{2.2.27b}$$

are used to find:

$$\begin{aligned} \bar{\phi}(y_1, y_3) &= \int \bar{v}\, \mathrm{d}y_3 \\ &= \frac{-S_v}{4\pi}\left[\ln\left((y_1 - y_1')^2 + (y_3 - y_3')^2\right) + \ln\left((y_1 - y_1')^2 + (y_3 + y_3')^2\right)\right] \end{aligned}$$

$$+\frac{\Omega}{2\pi}\left[\arctan\left(\frac{y_3-y_3'}{y_1-y_1'}\right)-\arctan\left(\frac{y_3+y_3'}{y_1-y_1'}\right)\right] \tag{2.2.28}$$

$$\begin{aligned}\bar{\psi}(y_1,y_3) &= -\int \bar{v}\,\mathrm{d}y_1 \\ &= \frac{-S_v}{2\pi}\left[\arctan\left(\frac{y_3-y_3'}{y_1-y_1'}\right)+\arctan\left(\frac{y_3+y_3'}{y_1-y_1'}\right)\right] \\ &\quad \frac{\Omega}{4\pi}\left[\ln\left((y_1-y_1')^2+(y_3-y_3')^2\right)-\ln\left((y_1-y_1')^2+(y_3+y_3')^2\right)\right],\end{aligned} \tag{2.2.29}$$

where $\bar{\phi}$ is the velocity potential and $\bar{\psi}$ is the stream function. From this, (2.2.27) can be used as a check that all of expressions are correct.

2.2.5.2 Line Sink Vortex Combination

As mentioned above, the expressions for $(\bar{u},\bar{v})$, (2.2.26); $\bar{\phi}$, (2.2.28); and $\bar{\psi}$, (2.2.29), describe the flow induced by a single sink/vortex combination. Following the discretization in Section 3.1, the law of superposition needs to be used again to sum up the effects of the line sink/vortex combination. This simply involves integrating these expressions along the discontinuity, which represents the plume, and letting S_v and Ω vary with respect to s and τ.

For the velocity, $\hat{\mathbf{v}}(y_1,y_3,\tau)$, away from the discontinuity which represents the plume there are no singularities that need to be considered. Due to this, the expression for $\hat{\mathbf{v}}(y_1,y_3,\tau)$ is simply the integral over the plume of (2.2.26):

$$\begin{aligned}\hat{u}(y_1,y_3,\tau) = &\int_C \frac{-S_v(s',\tau)(y_1-y_1(s'))}{2\pi\left[(y_1-y_1(s'))^2+(y_3-y_3(s'))^2\right]}\,\mathrm{d}s' \\ &-\int_C \frac{S_v(s',\tau)(y_1-y_1(s'))}{2\pi\left[(y_1-y_1(s'))^2+(y_3+y_3(s'))^2\right]}\,\mathrm{d}s' \\ &-\int_C \frac{\Omega(s',\tau)(y_3-y_3(s'))}{2\pi\left[(y_1-y_1(s'))^2+(y_3-y_3(s'))^2\right]}\,\mathrm{d}s' \\ &+\int_C \frac{\Omega(s',\tau)(y_3+y_3(s'))}{2\pi\left[(y_1-y_1(s'))^2+(y_3+y_3(s'))^2\right]}\,\mathrm{d}s'\end{aligned} \tag{2.2.30a}$$

$$\begin{aligned}\hat{v}(y_1,y_3,\tau) = &\int_C \frac{-S_v(s',\tau)(y_3-y_3(s'))}{2\pi\left[(y_1-y_1(s'))^2+(y_3-y_3(s'))^2\right]}\,\mathrm{d}s' \\ &-\int_C \frac{S_v(s',\tau)(y_3+y_3(s'))}{2\pi\left[(y_1-y_1(s'))^2+(y_3+y_3(s'))^2\right]}\,\mathrm{d}s'\end{aligned}$$

$$+\int_C \frac{\Omega(s',\tau)(y_1-y_1(s'))}{2\pi\left[(y_1-y_1(s'))^2+(y_3-y_3(s'))^2\right]}\,\mathrm{d}s'$$
$$-\int_C \frac{\Omega(s',\tau)(y_1-y_1(s'))}{2\pi\left[(y_1-y_1(s'))^2+(y_3+y_3(s'))^2\right]}\,\mathrm{d}s', \tag{2.2.30b}$$

where $\hat{\mathbf{v}} = (\hat{u},\hat{v})$. Thus, the velocity away from the plume can be written as, $\hat{\mathbf{v}}(y_1,y_3,\tau) = (\hat{u},\hat{v})^T = (v_{o1},v_{o3})^T$. Similarly, using the Cauchy-Riemann equations, the expressions for the velocity potential and stream function, $\hat{\phi}$ and $\hat{\psi}$, can be written as:

$$\begin{aligned}\hat{\phi}(y_1,y_3,\tau) = &\int_C \frac{-S_v(s',\tau)}{4\pi}\ln\left((y_1-y_1(s'))^2+(y_3-y_3(s'))^2\right)\,\mathrm{d}s'\\ &+\int_C \frac{-S_v(s',\tau)}{4\pi}\ln\left((y_1-y_1(s'))^2+(y_3+y_3(s'))^2\right)\,\mathrm{d}s'\\ &+\int_C \frac{\Omega(s',\tau)}{2\pi}\left[\arctan\left(\frac{y_3-y_3(s')}{y_1-y_1(s')}\right)-\arctan\left(\frac{y_3+y_3(s')}{y_1-y_1(s')}\right)\right]\,\mathrm{d}s'\end{aligned} \tag{2.2.31}$$

$$\begin{aligned}\hat{\psi}(y_1,y_3,\tau) = &\int_C \frac{-S_v(s',\tau)}{2\pi}\left[\arctan\left(\frac{y_3-y_3(s')}{y_1-y_1(s')}\right)+\arctan\left(\frac{y_3+y_3(s')}{y_1-y_1(s')}\right)\right]\,\mathrm{d}s'\\ &-\int_C \frac{\Omega(s',\tau)}{4\pi}\ln\left((y_1-y_1(s'))^2+(y_3-y_3(s'))^2\right)\,\mathrm{d}s'\\ &+\int_C \frac{\Omega(s',\tau)}{4\pi}\ln\left((y_1-y_1(s'))^2+(y_3+y_3(s'))^2\right)\,\mathrm{d}s'.\end{aligned} \tag{2.2.32}$$

It needs to be remembered that in the above integrals, all plume points are integrated over to find the induced velocity at any ambient air grid point. The fact that the Cartesian grid and the plume discretization can be at different heights is not an issue.

Switching focus to the velocity just off the plume, more needs to be considered. Here, the velocities will be parameterized with respect to arc length. Let the position of the plume be $y_1 = y_1(s)$ and $y_3 = y_3(s)$. Substituting this in (2.2.30) above, gives a piece of velocity of interest. It also needs to be noted that when $s = s'$, a singularity occurs, so that the equations above for $\hat{\mathbf{v}}$ are not valid. This means that beyond the equations (2.2.30) above, the effect of the singularity at s on the induced velocity needs to be considered. Thus, the induced velocity can be written

as $\mathbf{v} = \hat{\mathbf{v}} +$ effect of singularity.

With these expressions, (2.2.30)-(2.2.32), the flow in the ambient air system far from the discontinuity can be described, up to a first order approximation and for strict potential flow. The equations derived in this section can be easily implemented in MATLAB with the discussion in Section 3.3. Additionally, the flow between the plume and ambient air systems can be coupled, as seen in Section 2.4. Contributions from the singularities will be discussed in the following subsection.

2.2.5.3 Decomposition of Velocity

While the expressions derived above describe the flow in the ambient air system, for means of implementation it is necessary to obtain expressions for the normal and tangential velocities of the ambient air at the outside edges of the plume (just off the plume). With discretized points, this is easily done by calculating the normal and tangential vectors, $\mathbf{n}(s,\tau) = (n_1, n_2)^T$ and $\mathbf{T}(s,\tau) = (T_1, T_2)^T$ respectively, at each discretized point.

This is done by the equations:

$$\mathbf{T}(s,\tau) = \frac{\dot{\mathbf{r}}(s,\tau)}{|\dot{\mathbf{r}}(s,\tau)|} \tag{2.2.33}$$

$$\mathbf{n}(s,\tau) = (T_2, -T_1)^T, \tag{2.2.34}$$

where $\mathbf{r}(s,\tau) = (y_{1\,p}, y_{3\,p})^T$ is the position vector of the centerline of the plume, and the dot, $\dot{\star}$, indicates a derivative with respect to arc length. Since the plume has two sides and noting the geometry in Figure 2.3, the normals on the $+$ and $-$ sides of the plume are opposite in sign. Thus,

$$\mathbf{n}_-(s,\tau) = -\mathbf{n}_+(s,\tau), \tag{2.2.35}$$

where the subscript denotes the side of the plume.

Notationally, let the normal velocity be denoted by $V_{n\,\pm}$ and the tangential velocity by $V_{t\,\pm}$, where the $\pm$ denotes the side of the plume. One would expect that to find the normal and tangential velocities one could simply compute the dot product of the velocity and the desired unit vector. Although, more needs to be

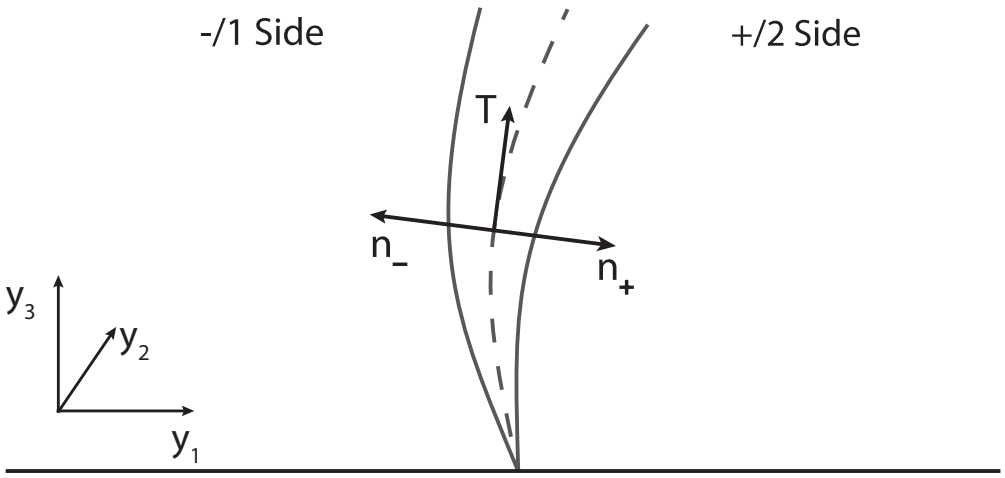

Figure 2.3: Geometry and Notation of Moving Dyad in Upper Half-Plane

considered.

The velocity on the discontinuity is calculated on a coordinate system fixed to the plume, as mentioned above by the parametrization with respect to arc length. The effects from a sink will effect the normal velocity, $V_{n\pm}(s,\tau)$, and the vortex will effect the tangential velocity, $V_{t\pm}(s,\tau)$, as seen in Figure 2.5. In the coordinate system fixed to the plume, a velocity pointing at the plume is taken to be negative, regardless of the side, and a velocity moving away from the plume is taken to be positive. Meaning, a velocity in the direction of the normal vector is positive, and a velocity opposite the direction of the normal vector is negative, see Figure 2.4 for clarification. This was done to set all velocities going into the plume as negative. Due to this and the coordinate system fixed to the plume, the velocity calculated on the discontinuity does not need to be decomposed by the use of unit vectors. With this and the information presented above, the normal and tangential velocities can be expressed as:

$$V_{n\pm}(s,\tau) = \hat{u}(s,\tau) + \text{effect of sink at } s \tag{2.2.36}$$

$$V_{t\pm}(s,\tau) = \hat{v}(s,\tau) + \text{effect of vortex at } s. \tag{2.2.37}$$

In order to describe the missing singularity contribution, it is necessary to

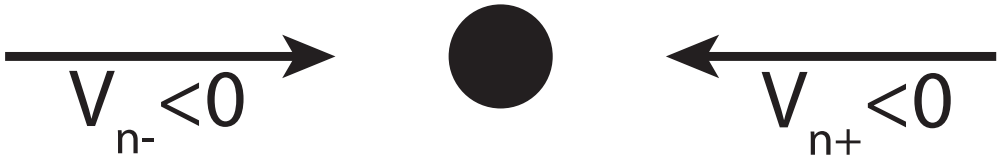

Figure 2.4: Decomposed Velocity Sign Convention

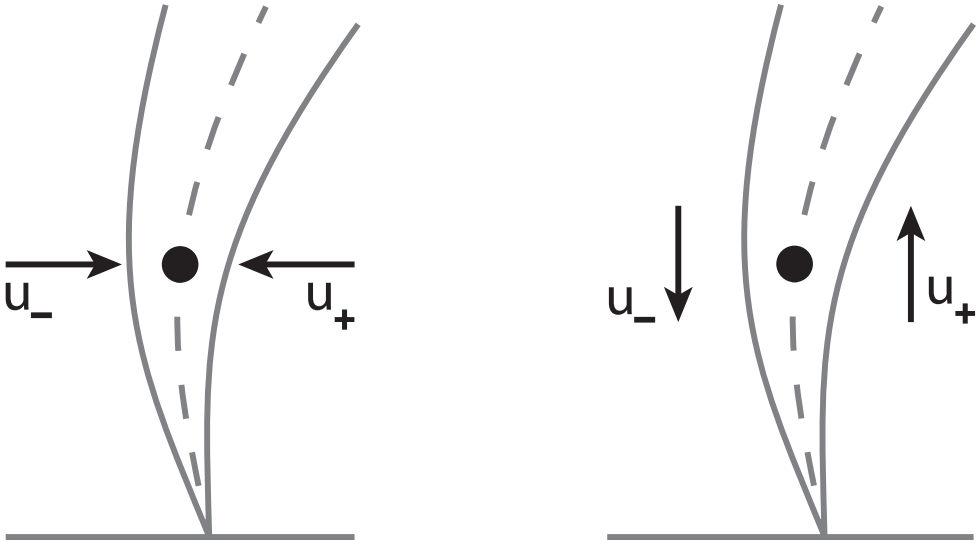

Figure 2.5: Velocity Induced by Sink and Vortex Respectively

discuss the theory behind the calculation of the velocity, and the effects from the flow induced by the plume.

In the calculation of the velocity just off the plume, the integrals (2.2.30) are taken in the principal value sense, due to the singularity that occurs when $s = s'$. That is, the effect of the sink or vortex at a point s is not taken into account in the calculation of the velocities at the spatial point $(y_1(s,\tau), y_3(s,\tau))$. The inclusion of these effects will give the missing piece, and create the difference in velocities on either side of the plume. This is induced by the sink/vortex combination, which is represented by the contribution of the singularity itself. The effect of the sink/vortex at the singularity is computed as follows.

Without loss, consider a perfectly vertical plume such that $y_{1\,p}(s,\tau) = 0$ and $y_{3\,p}(s,\tau) = s$ for $0 \leq s \leq 100$. The interest is in the value of u and v in the limit as

a point P goes to $(0, s')$, where the singularity occurs, to find the velocity induced by the sink/vortex at the singularity at the point s'.

The velocities are considered this time without any image terms:

$$\hat{u}(y_1, y_3, \tau) = \int_C \frac{-S_v(s', \tau) y_1}{2\pi \left[y_1^2 + (y_3 - y_3(s'))^2\right]} \, \mathrm{d}s' - \int_C \frac{\Omega(s', \tau)(y_3 - y_3(s'))}{2\pi \left[y_1^2 + (y_3 - y_3(s'))^2\right]} \, \mathrm{d}s'$$
$$\hat{v}(y_1, y_3, \tau) = \int_C \frac{-S_v(s', \tau)(y_3 - y_3(s'))}{2\pi \left[y_1^2 + (y_3 - y_3(s'))^2\right]} \, \mathrm{d}s' + \int_C \frac{\Omega(s', \tau) y_1}{2\pi \left[y_1^2 + (y_3 - y_3(s'))^2\right]} \, \mathrm{d}s'.$$

In the case of a vertical plume, $V_{n\pm} = \hat{u}$ and $V_{t\pm} = \hat{v}$. Considering the effects on the normal velocity first, one has:

$$\begin{aligned}
\hat{u}(y_1, y_3, \tau) &= \int_C \frac{-S_v(s', \tau) y_1}{2\pi \left[y_1^2 + (y_3 - y_3(s'))^2\right]} \, \mathrm{d}s' - \int_C \frac{\Omega(s', \tau)(y_3 - y_3(s'))}{2\pi \left[y_1^2 + (y_3 - y_3(s'))^2\right]} \, \mathrm{d}s' \\
&= \frac{-S_v(s', \tau)}{2\pi} \arctan\left(\frac{s' - y_3}{y_1}\right)\Bigg|_C + \frac{\Omega(s', \tau)}{4\pi} \ln\left(y_1^2 + (y_3 - s')^2\right)\Bigg|_C \\
&= \frac{-S_v(s, \tau)}{2\pi} \left(\arctan\left(\frac{\hat{y}_3 - y_3}{y_1}\right) + \arctan\left(\frac{y_3 - \tilde{y}_3}{y_1}\right)\right) \\
&\quad + \frac{\Omega(s, \tau)}{4\pi} \left(\ln\left(y_1^2 + (y_3 - \hat{y}_3)^2\right) - \ln\left(y_1^2 + (y_3 - \tilde{y}_3)^2\right)\right),
\end{aligned}$$

where $\hat{y}_3$ and $\tilde{y}_3$ are the endpoints of the plume and C is the simplified straight plume. Now, taking the limit as $y_1 \to 0^+$ from the right side of the plume:

$$\begin{aligned}
\lim_{y_1 \to 0^+} \hat{u} &= \frac{-S_v(s, \tau)}{2\pi} \left(\frac{\pi}{2} + \frac{\pi}{2}\right) + \frac{\Omega(s, \tau)}{2\pi} \ln\left(\frac{y_3 - \hat{y}_3}{y_3 - \tilde{y}_3}\right) \\
&= \frac{-S_v(s, \tau)}{2} + \frac{\Omega(s, \tau)}{2\pi} \ln\left(\frac{y_3 - \hat{y}_3}{y_3 - \tilde{y}_3}\right).
\end{aligned}$$

To obtain the induced velocity at the singularity, the limit as $\hat{y}_3, \tilde{y}_3 \to s$ is taken, resulting in:

$$\begin{aligned}
\lim_{\substack{y_1 \to 0^+ \\ \hat{y}_3, \tilde{y}_3 \to s}} \hat{u} &= \frac{-S_v(s, \tau)}{2} + \frac{\Omega(s, \tau)}{2\pi} \ln\left(\frac{y_3 - s}{y_3 - s}\right) \\
&= \frac{-S_v(s, \tau)}{2}. \qquad (2.2.38)
\end{aligned}$$

Similarly, if the limit is instead taken as $y_1 \to 0^-$, the effect of the singularity

on the normal velocity on the left side of the plume is:

$$\lim_{\substack{y_1\to 0^- \\ \hat{y}_3,\tilde{y}_3\to s}} \hat{u} = \frac{S_v(s,\tau)}{2}. \tag{2.2.39}$$

The same process is used to calculate the effects on the tangential velocity. This time one has:

$$\begin{aligned}
\hat{v}(y_1,y_3,\tau) &= \int_C \frac{-S_v(s',\tau)(y_3-y_3(s'))}{2\pi\left[y_1^2+(y_3-y_3(s'))^2\right]}\,\mathrm{d}s' - \int_C \frac{\Omega(s',\tau)y_1}{2\pi\left[y_1^2+(y_3-y_3(s'))^2\right]}\,\mathrm{d}s' \\
&= \frac{S_v(s',\tau)}{4\pi}\ln\left(y_1^2+(y_3-s')^2\right)\Big|_C + \frac{\Omega(s',\tau)}{2\pi}\arctan\left(\frac{s'-y_3}{y_1}\right)\Big|_C \\
&= \frac{S_v(s,\tau)}{4\pi}\left(\ln\left(y_1^2+(y_3-\hat{y}_3)^2\right)-\ln\left(y_1^2+(y_3-\tilde{y}_3)^2\right)\right) \\
&\quad + \frac{\Omega(s,\tau)}{2\pi}\left(\arctan\left(\frac{\hat{y}_3-y_3}{y_1}\right)+\arctan\left(\frac{y_3-\tilde{y}_3}{y_1}\right)\right).
\end{aligned}$$

Again, the limit as $y_1 \to 0^+$, from the right side of the plume, is taken:

$$\begin{aligned}
\lim_{y_1\to 0^+}\hat{v} &= \frac{S_v(s,\tau)}{2\pi}\ln\left(\frac{y_3-\hat{y}_3}{y_3-\tilde{y}_3}\right)+\frac{\Omega(s,\tau)}{2\pi}\left(\frac{\pi}{2}+\frac{\pi}{2}\right) \\
&= \frac{S_v(s,\tau)}{2\pi}\ln\left(\frac{y_3-\hat{y}_3}{y_3-\tilde{y}_3}\right)+\frac{\Omega(s,\tau)}{2}.
\end{aligned}$$

To obtain the induced velocity at the singularity, the limit as $\hat{y}_3, \tilde{y}_3 \to s$ is taken, resulting in:

$$\begin{aligned}
\lim_{\substack{y_1\to 0^+ \\ \hat{y}_3,\tilde{y}_3\to s}}\hat{v} &= \frac{S_v(s,\tau)}{2\pi}\ln\left(\frac{y_3-s}{y_3-s}\right)+\frac{\Omega(s,\tau)}{2} \\
&= \frac{\Omega(s,\tau)}{2}.
\end{aligned} \tag{2.2.40}$$

Similarly, if the limit is instead taken as $y_1 \to 0^-$, the effect of the singularity on the tangential velocity on the left side of the plume is:

$$\lim_{\substack{y_1\to 0^- \\ \hat{y}_3,\tilde{y}_3\to s}}\hat{u} = \frac{-\Omega(s,\tau)}{2}. \tag{2.2.41}$$

With this contribution from the singularity and adjusting the sign in each

case to match the normal vectors on each side of the plume, the full normal and tangential velocities, $V_{n\pm}$ and $V_{t\pm}$, can be written in the notation used above as:

$$V_{n-}(s,\tau) = \hat{u}(s,\tau) - \frac{S_v(s,\tau)}{2} \tag{2.2.42}$$

$$V_{n+}(s,\tau) = \hat{u}(s,\tau) - \frac{S_v(s,\tau)}{2} \tag{2.2.43}$$

$$V_{t-}(s,\tau) = \hat{v}(s,\tau) - \frac{\Omega(s,\tau)}{2} \tag{2.2.44}$$

$$V_{t+}(s,\tau) = \hat{v}(s,\tau) + \frac{\Omega(s,\tau)}{2}. \tag{2.2.45}$$

Here, $\hat{\mathbf{v}} = (\hat{u}, \hat{v})$ from Section 2.2.5.2 taken in the principal value sense, and the signs have been chosen to add or subtract the effects depending on the side of the plume and the corresponding unit vector.

One will note that the final decompositions, (2.2.42)-(2.2.45), with the inclusion of the effects of the singularity, are actually the decompositions of the full velocity, $\mathbf{v}$, and can be thought of as:

$$V_{n-}(s,\tau) = u(s,\tau) \tag{2.2.46}$$

$$V_{n+}(s,\tau) = u(s,\tau) \tag{2.2.47}$$

$$V_{t-}(s,\tau) = v(s,\tau) \tag{2.2.48}$$

$$V_{t+}(s,\tau) = v(s,\tau). \tag{2.2.49}$$

2.2.6 Addition of Crosswind Flow to Ambient Air

The velocity calculations, (2.2.42), do not account for the possibility of crosswind conditions in the ambient atmosphere. Here, let $\mathbf{cw} = \begin{pmatrix} cw, & 0 \end{pmatrix}^T$, where cw is the horizontal component of the crosswind flow.

For velocities calculated far from the discontinuity, the addition of the crosswind is trivial:

$$\hat{u} = \hat{u} + cw, \tag{2.2.50}$$

where $\hat{u}$ is calculated by (2.2.30).

Additional contributions to velocities calculated on the discontinuity need to

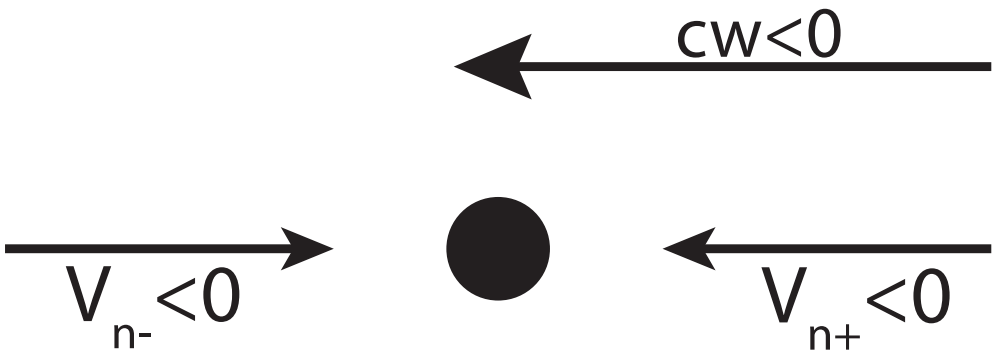

Figure 2.6: Effect of Crosswind on Normal Velocities

be decomposed due to the plume fixed coordinate system. Thus,

$$V_{n-}(s,\tau) = \hat{u}(s,\tau) - \frac{S_v(s,\tau)}{2} + \mathbf{cw}\cdot\mathbf{n}_-(s,\tau) \tag{2.2.51}$$

$$V_{n+}(s,\tau) = \hat{u}(s,\tau) - \frac{S_v(s,\tau)}{2} + \mathbf{cw}\cdot\mathbf{n}_+(s,\tau) \tag{2.2.52}$$

$$V_{t-}(s,\tau) = \hat{v}(s,\tau) - \frac{\Omega(s,\tau)}{2} + \mathbf{cw}\cdot\mathbf{T}(s,\tau) \tag{2.2.53}$$

$$V_{t+}(s,\tau) = \hat{v}(s,\tau) + \frac{\Omega(s,\tau)}{2} + \mathbf{cw}\cdot\mathbf{T}(s,\tau), \tag{2.2.54}$$

where this time $\hat{\mathbf{v}}$ is taken in the principal value sense as in Section 2.2.5.3. It is noted that using the sign convention outlined above, a negative crosswind will subtract from V_{n+} but add to V_{n-}. See Figure 2.6 for clarification.

2.2.7 System Pressure Calculation

Since the ambient air system has a two-dimensional, incompressible, irrotational flow, a potential flow solution for velocity is appropriate. Thus:

$$v_1 = \phi_{y_1} \qquad\qquad v_3 = \phi_{y_3}. \tag{2.2.55}$$

As a check, we can substitute this into the definition of vorticity to obtain:

$$\begin{aligned}\omega &= \frac{\partial}{\partial y_3}v_1 - \frac{\partial}{\partial y_1}v_3 \\ &= \phi_{y_1y_3} - \phi_{y_3y_1} = 0,\end{aligned}$$

and as one would expect, substituting the potential flow notation into the definition of incompressibility gives:

$$\begin{aligned}\nabla \cdot \mathbf{v} &= \frac{\partial}{\partial y_1} v_1 - \frac{\partial}{\partial y_3} v_3 \\ &= \phi_{y_1 y_1} + \phi_{y_3 y_3} = 0,\end{aligned}$$

Laplace's equation for the velocity potential.

To calculate the dynamic pressure, $P^{(1)}$, (2.2.55) is substituted into the $O(\sigma)$ momentum equations, (2.2.10). Using the momentum equation in the y_1 direction first results in:

$$\begin{aligned}[\phi_{y_1\tau} + \phi_{y_1}\phi_{y_1 y_1} + \phi_{y_3}\phi_{y_1 y_3}] + P^{(1)}_{y_1} &= 0 \\ \frac{\partial}{\partial y_1}\left[\phi_{y_1\tau} + \frac{1}{2}(\phi_{y_1})^2 + \frac{1}{2}(\phi_{y_3})^2 + P^{(1)}\right] &= 0 \\ \phi_{y_1\tau} + \frac{1}{2}(\phi_{y_1})^2 + \frac{1}{2}(\phi_{y_3})^2 + P^{(1)} &= c_1(y_3).\end{aligned}$$

From here, the constant can be found by differentiating with respect to y_3 and comparing to the momentum equation in the y_3 direction. Thus:

$$\frac{\partial}{\partial y_3}\left[\phi_{y_1\tau} + \frac{1}{2}(\phi_{y_1})^2 + \frac{1}{2}(\phi_{y_3})^2 + P^{(1)}\right] = \frac{\partial}{\partial y_3} c_1(y_3).$$

Comparing gives the result that $c_{1y_3} = 0$. Thus, $c_1 = \text{const}$ and using the boundary conditions far away from the plume, this constant is zero. Then the expression for the dynamic pressure can be written as:

$$P^{(1)} = -\left[\phi_\tau + \frac{1}{2}(\phi^2)_{y_1} + \frac{1}{2}(\phi^2)_{y_3}\right] \tag{2.2.56}$$

$$P^{(1)} = -\left[\phi_\tau + \frac{1}{2}\nabla(\phi^2)\right]. \tag{2.2.57}$$

Since the two systems (ambient air and plume) are disjoint except for entrainment effects, the analysis in this section completely describes the motion of the flow outside the plume up to a first order perturbation analysis. Although not considered here, more terms can easily be added to the expansion to gain added effects from

vorticity and stratification. Focus now shifts to the inner solution of the boundary layer problem.

2.3 Inner Solution

The plume system describes how the flow inside the plume evolves over time. In this section, the equations to describe this flow are derived, including the effects of entrainment from the ambient air system. The governing equations for the plume system can be derived in two different ways, one of which will be presented here, and the other is presented in Appendix A.

The equations (2.1.10) can be rescaled, noting that the majority of the velocity is in the vertical direction. The same procedure as in the ambient air system is used to derive an $O(1)$ system, which is put into conservation form and integrated across the plume. This is coupled with the assumption that each of the plume variables have a top-hat profile in order to evaluate integrals resulting from averaging the equations across the plume. This process results in the final form conservation laws of interest.

The plume system is thought of as the inner solution of a boundary layer problem. The system (2.1.10) from before is used, dropping the unnecessary expansion notation and taking $\tilde{v} = v$, $\tilde{R} = R$, and $\tilde{\theta} = \Theta$. Since the focus is on the plume system, the variables y_1, v_1, and v_3 need to be rescaled–noting that the main part of the velocity is in the y_3 direction, see Figure 2.7. This is done by letting:

$$y_1 = y_{1p} + \delta Y_1 \qquad \frac{\partial}{\partial y_1} = \frac{1}{\delta}\frac{\partial}{\partial Y_1}$$
$$v_1 = \delta V_p V_1 \qquad v_3 = V_p V_3,$$

where $y_1 = y_{1\,p}(y_3, \tau)$ is the centerline of the plume, and $\delta = \frac{d_f}{l_1}$, the ratio of the fire length scale and the length scale in the y_1 direction. Additionally, let $\frac{\xi_0 t_0}{\rho_0 C_p T_0 l_3} = V_p$ and similarly $\frac{\eta_0 t_0^2}{l_3^2 \rho_0} = V_p^2$.

Substituting these above assumptions and the limiting case assumptions (2.1.6),

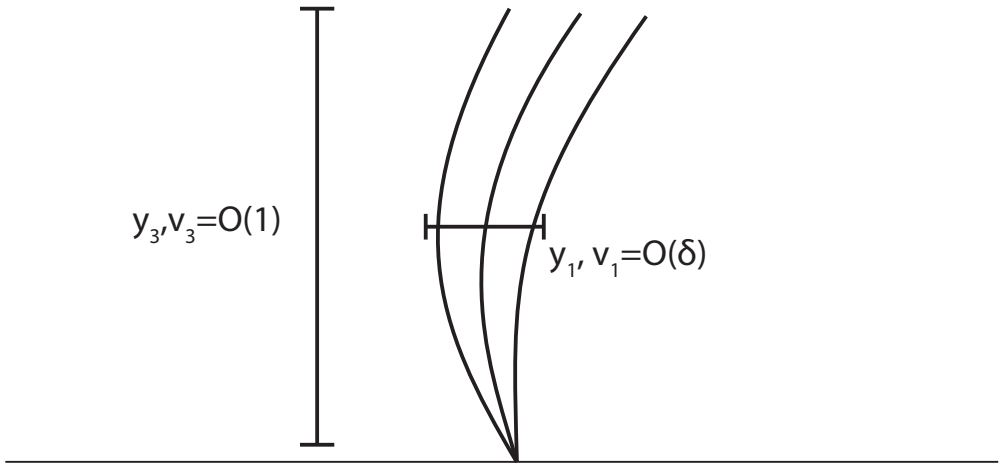

Figure 2.7: Velocity Rescaling for Inner Solution

(2.1.7), and (2.1.9) into (2.1.10) and expanding:

$$R_\tau + \left(RV_pV_1\right)_{Y_1} + \left(RV_pV_3\right)_{y_3} = 0 \tag{2.3.1a}$$

$$R\left[\delta V_p(V_1)_\tau + \delta V_p^2\left(V_1(V_1)_{Y_1}\right) + \delta V_p^2\left(V_3(V_1)_{y_3}\right)\right] + \frac{1}{\delta}\frac{\bar{R}T_0t_0^2}{l_3^2}\left(P^{(H)}_{Y_1} + \beta P^{(H1)}_{Y_1} + \sigma P^{(1)}_{Y_1}\right) = V_p^2\left(\frac{1}{\delta}\tilde{T}_{11Y_1} + \tilde{T}_{13y_3}\right) \tag{2.3.1b}$$

$$R\left[V_p(V_3)_\tau + V_p^2\left(V_1(V_3)_{Y_1}\right) + V_p^2\left(V_3(V_3)_{y_3}\right)\right] + \frac{\bar{R}T_0t_0^2}{l_3^2}\left(P^{(H)}_{y_3} + \beta P^{(H1)}_{y_3} + \sigma P^{(1)}_{y_3}\right) = -\frac{t_0^2 g}{l_3}R + V_p^2\left(\frac{1}{\delta}\tilde{T}_{31Y_1} + \tilde{T}_{33y_3}\right) \tag{2.3.1c}$$

$$R\left[\Theta_\tau + V_pV_1\Theta_{Y_1} + V_pV_3\Theta_{y_3}\right] - \frac{\gamma-1}{\gamma}\left[P^{(H)}_\tau + \beta P^{(H1)}_\tau + \sigma P^{(1)}_\tau + V_pV_1\left(P^{(H)}_{Y_1} + \beta P^{(H1)}_{Y_1} + \sigma P^{(1)}_{Y_1}\right) + V_pV_3\left(P^{(H)}_{y_3} + \sigma P^{(1)}_{y_3}\right)\right] = V_p\tilde{Q} + V_p\left(\frac{1}{\delta}\tilde{q}_{1Y_1} + \tilde{q}_{3y_3}\right) \tag{2.3.1d}$$

$$P^{(H)} + \beta P^{(H1)} + \sigma P^{(1)} = R\Theta. \tag{2.3.1e}$$

Time is rescaled such that $\tilde{\tau} = V_p\tau$, which means that $\frac{\partial}{\partial\tilde{\tau}} = \frac{1}{V_p}\frac{\partial}{\partial\tau}$. The Reynolds stresses and heat flux terms need to be scaled just as the velocity inside the plume was, noting the majority of the entrainment is in the Y_1 direction:

$$\tilde{T}_{11} = \hat{T}_{11} \qquad \tilde{T}_{13} = \hat{T}_{13} \qquad \tilde{T}_{31} = \delta\hat{T}_{31}$$
$$\tilde{T}_{33} = \delta\hat{T}_{33} \qquad \tilde{q}_1 = \delta\hat{q}_1 \qquad \tilde{q}_3 = \delta\hat{q}_3.$$

Substituting these new scalings into (2.3.1a) results in the reduction:

$$R_{\tilde{\tau}} + (RV_1)_{Y_1} + (RV_3)_{y_3} = 0.$$

Next, (2.3.1b) reduces to:

$$RV_p^2\delta\left[(V_1)_{\tilde{\tau}} + (V_1(V_1)_{Y_1}) + (V_3(V_1)_{y_3})\right] + \frac{1}{\delta}\frac{\bar{R}T_0t_0^2}{l_3^2}\left(P_{Y_1}^{(H)} + \beta P_{Y_1}^{(H1)} + \sigma P_{Y_1}^{(1)}\right) = V_p^2\left(\frac{1}{\delta}\hat{T}_{11Y_1} + \hat{T}_{13y_3}\right).$$

Similarly for V_3, (2.3.1c), reduces to:

$$RV_p^2\left[(V_3)_{\tilde{\tau}} + (V_1(V_3)_{Y_1}) + (V_3(V_3)_{y_3})\right] + \frac{\bar{R}T_0t_0^2}{l_3^2}\left(P_{y_3}^{(H)} + \beta P_{y_3}^{(H1)} + \sigma P_{y_3}^{(1)}\right) = -\frac{t_0^2g}{l_3}R + V_p^2\left(\hat{T}_{31Y_1} + \delta\hat{T}_{33y_3}\right),$$

and (2.3.1d) reduces to:

$$RV_p\left[\Theta_{\tilde{\tau}} + V_1\Theta_{Y_1} + V_3\Theta_{y_3}\right] - V_p\frac{\gamma-1}{\gamma}\left[P_{\tilde{\tau}}^{(H)} + \beta P_{\tau}^{(H1)} + \sigma P_{\tilde{\tau}}^{(1)} + V_1\left(P_{Y_1}^{(H)} + \beta P_{Y_1}^{(H1)} + \sigma P_{Y_1}^{(1)}\right) + V_3\left(P_{y_3}^{(H)} + \beta P_{y_3}^{(H1)} + \sigma P_{y_3}^{(1)}\right)\right] = V_p\tilde{Q} + V_p\left(\hat{q}_{1Y_1} + \delta\hat{q}_{3y_3}\right).$$

Finally, (2.3.1e) becomes:

$$P^{(H)} + \beta P^{(H1)} + \sigma P^{(1)} = R\Theta.$$

Thus, the plume system becomes:

$$R_{\tilde{\tau}} + (RV_1)_{Y_1} + (RV_3)_{y_3} = 0 \tag{2.3.2a}$$

$$RV_p^2\delta\left[(V_1)_{\tilde{\tau}} + (V_1(V_1)_{Y_1}) + (V_3(V_1)_{y_3})\right] + \frac{1}{\delta}\frac{\bar{R}T_0t_0^2}{l_3^2}\left(P_{Y_1}^{(H)} + \beta P_{Y_1}^{(H1)} + \sigma P_{Y_1}^{(1)}\right) = V_p^2\left(\frac{1}{\delta}\hat{T}_{11Y_1} + \hat{T}_{13y_3}\right) \tag{2.3.2b}$$

$$RV_p^2\left[(V_3)_{\tilde{\tau}} + (V_1(V_3)_{Y_1}) + (V_3(V_3)_{y_3})\right] + \frac{\bar{R}T_0t_0^2}{l_3^2}\left(P_{y_3}^{(H)} + \beta P_{y_3}^{(H1)} + \sigma P_{y_3}^{(1)}\right) = -\frac{t_0^2 g}{l_3}R + V_p^2\left(\hat{T}_{31Y_1} + \delta\hat{T}_{33y_3}\right) \tag{2.3.2c}$$

$$RV_p\left[\Theta_{\tilde{\tau}} + V_1\Theta_{Y_1} + V_3\Theta_{y_3}\right] - V_p\frac{\gamma-1}{\gamma}\Big[P_{\tilde{\tau}}^{(H)} + \beta P_{\tilde{\tau}}^{(H1)} + \sigma P_{\tilde{\tau}}^{(1)} + V_1\left(P_{Y_1}^{(H)} + \beta P_{Y_1}^{(H1)} + \sigma P_{Y_1}^{(1)}\right) + V_3\left(P_{y_3}^{(H)} + \beta P_{y_3}^{(H1)} + \sigma P_{y_3}^{(1)}\right)\Big] = V_p\tilde{Q} + V_p\left(\hat{q}_{1Y_1} + \delta\hat{q}_{3y_3}\right) \tag{2.3.2d}$$

$$P^{(H)} + \beta P^{(H1)} + \sigma P^{(1)} = R\Theta. \tag{2.3.2e}$$

Now let $\delta \to 0$ and use (2.2.7) to get $P_{y_3} = -\beta + \sigma P_{y_3}^{(1)}$ and $P_{Y_1} = \sigma P_{Y_1}^{(1)}$. The approximations $\mathrm{RiMa}^2 \ll 1$ ($\beta \ll 1$) and $\sigma \ll 1$ are used, which is similar to taking a first approximation (keep $O(1)$ terms). Upon substituting and rearranging, the system reduces to:

$$R_{\tilde{\tau}} + (RV_1)_{Y_1} + (RV_3)_{y_3} = 0 \tag{2.3.3a}$$

$$P_{Y_1}^{(1)} = V_p^2\hat{T}_{11\,Y_1} \tag{2.3.3b}$$

$$RV_p^2\left[(V_3)_{\tilde{\tau}} + (V_1(V_3)_{Y_1}) + (V_3(V_3)_{y_3})\right] - \frac{\bar{R}T_0t_0^2}{l_3^2}\beta = -\frac{t_0^2 g}{l_3}R + V_p^2\hat{T}_{31Y_1} \tag{2.3.3c}$$

$$RV_p\left[\Theta_{\tilde{\tau}} + V_1\Theta_{Y_1} + V_3\Theta_{y_3}\right] = V_p\tilde{Q} + V_p\hat{q}_{1Y_1} \tag{2.3.3d}$$

$$P^{(H)} = R\Theta. \tag{2.3.3e}$$

For the balances in the limiting case, choose $V_p^2 = \frac{gt_0^2}{l_3}$, and additionally using the definition of β and substituting into (2.3.3), the system becomes:

$$R_{\tilde{\tau}} + (RV_1)_{Y_1} + (RV_3)_{y_3} = 0 \tag{2.3.4a}$$

$$P^{(1)}_{Y_1} = \frac{gt_0^2}{l_3}\hat{T}_{11\,Y_1} \tag{2.3.4b}$$

$$R\left[(V_3)_{\tilde{\tau}} + (V_1(V_3)_{Y_1}) + (V_3(V_3)_{y_3})\right] - 1 = -R + \hat{T}_{31Y_1} \tag{2.3.4c}$$

$$R\left[\Theta_{\tilde{\tau}} + V_1\Theta_{Y_1} + V_3\Theta_{y_3}\right] = \tilde{Q} + \hat{q}_{1Y_1} \tag{2.3.4d}$$

$$P^{(H)} = R\Theta. \tag{2.3.4e}$$

2.3.1 Conservation Laws

Equations (2.3.4c) and (2.3.4d) can be written in conservation form, using (2.3.4a) to simplify. Thus, the system becomes:

$$R_{\tilde{\tau}} + (RV_1)_{Y_1} + (RV_3)_{y_3} = 0 \tag{2.3.5a}$$

$$P^{(1)}_{Y_1} = \frac{gt_0^2}{l_3}\hat{T}_{11\,Y_1} \tag{2.3.5b}$$

$$(RV_3)_{\tilde{\tau}} + (RV_1V_3)_{Y_1} + (RV_3^2)_{y_3} - 1 = -R + \hat{T}_{31Y_1} \tag{2.3.5c}$$

$$(R\Theta)_{\tilde{\tau}} + (RV_1\Theta)_{Y_1} + (RV_3\Theta)_{y_3} = \tilde{Q} + \hat{q}_{1Y_1} \tag{2.3.5d}$$

$$P^{(H)} = R\Theta. \tag{2.3.5e}$$

A top-hat profile is assumed for R, Θ, and V_3. A top-hat profile makes the assumption that a variable, $\star$, has approximately a constant distribution across some space. Here this space is taken as the plume. So in this case, a top-hat profile for R assumes that R is constant across the plume (constant in Y_1) for a given height y_3. See Figure 2.8 for the shape of the distribution. The top-hat assumption has a rich history in fluid dynamics and was made well known in the application to buoyant plumes by Morton et al. [55]. Although it seems to be a simple assumption, in the case of a narrow plume, the assumption is valid and close to what happens physically.

An alternate derivation of the conservation laws using a flux argument parameterized for a curvilinear coordinate system is presented in Appendix A and will be

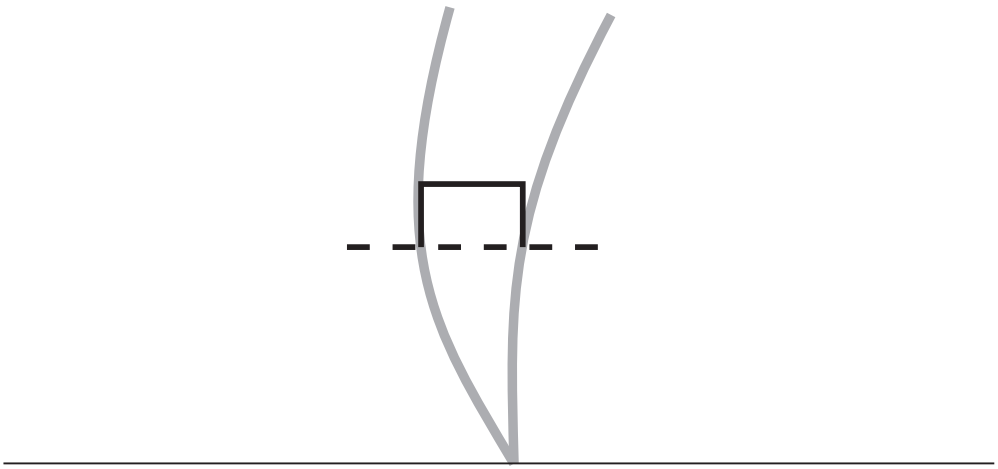

Figure 2.8: Top-Hat Profile

used in the implementation in Chapter 3.

The equations are integrated in terms of Y_1, where it is noted that:

$$\int_{y_{1p}-\frac{b}{2}}^{y_{1p}+\frac{b}{2}} \bullet \, \mathrm{d}y_1 = \frac{1}{\delta} \int_{-\frac{b}{2\delta}}^{\frac{b}{2\delta}} \bullet \, \mathrm{d}Y_1 \cong \frac{1}{\delta} \int_{-\infty}^{\infty} \bullet \, \mathrm{d}Y_1,$$

where b is the width of the plume. Upon integrating, (2.3.5a) can be written as:

$$\int_{y_{1p}-\frac{b}{2}}^{y_{1p}+\frac{b}{2}} R_{\tilde{\tau}} + (RV_1)_{Y_1} + (RV_3)_{y_3} \, \mathrm{d}Y_1 = 0.$$

The derivatives are moved outside the integrals resulting in:

$$\begin{aligned} \frac{\partial}{\partial \tilde{\tau}} \int_{y_{1p}-\frac{b}{2}}^{y_{1p}+\frac{b}{2}} R \, \mathrm{d}Y_1 - R\Big|_{y_{1\,p}+\frac{b}{2}} \left(y_{1\,p\,\tilde{\tau}} + \frac{b_{\tilde{\tau}}}{2} \right) + R\Big|_{y_{1\,p}-\frac{b}{2}} \left(y_{1\,p\,\tilde{\tau}} - \frac{b_{\tilde{\tau}}}{2} \right) \\ + \int_{y_{1p}-\frac{b}{2}}^{y_{1p}+\frac{b}{2}} (RV_1)_{Y_1} \, \mathrm{d}Y_1 + \frac{\partial}{\partial y_3} \int_{y_{1p}-\frac{b}{2}}^{y_{1p}+\frac{b}{2}} RV_3 \, \mathrm{d}Y_1 - RV_3\Big|_{y_{1\,p}+\frac{b}{2}} \left(y_{1\,p\,y_3} + \frac{b_{y_3}}{2} \right) \\ + RV_3\Big|_{y_{1\,p}-\frac{b}{2}} \left(y_{1\,p\,y_3} - \frac{b_{y_3}}{2} \right) = 0, \end{aligned}$$

and finally simplifying one obtains:

$$\begin{aligned}(Rb)_{\tilde{\tau}} + (RV_3 b)_{y_3} = &-(RV_1)\Big|_{y_{1p}-\frac{b}{2}}^{y_{1p}+\frac{b}{2}} + R\Big|_{y_{1\,p}+\frac{b}{2}}\left(y_{1\,p\,\tilde{\tau}} + \frac{b_{\tilde{\tau}}}{2}\right) \\ &- R\Big|_{y_{1\,p}-\frac{b}{2}}\left(y_{1\,p\,\tilde{\tau}} - \frac{b_{\tilde{\tau}}}{2}\right) + RV_3\Big|_{y_{1\,p}+\frac{b}{2}}\left(y_{1\,p\,y_3} + \frac{b_{y_3}}{2}\right) \\ &- RV_3\Big|_{y_{1\,p}-\frac{b}{2}}\left(y_{1\,p\,y_3} - \frac{b_{y_3}}{2}\right).\end{aligned}$$

Thus,

$$(Rb)_{\tilde{\tau}} + (bRV_3)_{y_3} = S_m, \tag{2.3.6}$$

where:

$$\begin{aligned}S_m = &-(RV_1)\Big|_{y_{1p}-\frac{b}{2}}^{y_{1p}+\frac{b}{2}} + R\Big|_{y_{1\,p}+\frac{b}{2}}\left(y_{1\,p\,\tilde{\tau}} + \frac{b_{\tilde{\tau}}}{2}\right) - R\Big|_{y_{1\,p}-\frac{b}{2}}\left(y_{1\,p\,\tilde{\tau}} - \frac{b_{\tilde{\tau}}}{2}\right) \\ &+ RV_3\Big|_{y_{1\,p}+\frac{b}{2}}\left(y_{1\,p\,y_3} + \frac{b_{y_3}}{2}\right) - RV_3\Big|_{y_{1\,p}-\frac{b}{2}}\left(y_{1\,p\,y_3} - \frac{b_{y_3}}{2}\right).\end{aligned}$$

One will notice that the source term, S_m, is comprised of several terms. The first term, $-(RV_1)\Big|_{y_{1p}-\frac{b}{2}}^{y_{1p}+\frac{b}{2}}$, represents the flux of mass inside the plume moving towards or away from the centerline, $y_{1\,p}$, depending on the sign. The remaining terms, when combined, are recognized as density of the gas times the material derivatives of $y_{1\,p} \pm \frac{b}{2}$, the velocity of the control volume. With this, S_m can be written as:

$$R\left(-V_1 + \frac{D}{Dt}\left(y_{1p} + \frac{b}{2}\right)\right)\Big|_{y_{1p}+\frac{b}{2}} + R\left(V_1 - \frac{D}{Dt}\left(y_{1p} - \frac{b}{2}\right)\right)\Big|_{y_{1p}-\frac{b}{2}}.$$

This is the net mass flux into the plume, and with this (2.3.6) is equivalent to (A.2.2).

When (2.3.5c) is integrated and simplified, one obtains:

$$\begin{aligned}(RV_3 b)_{\tilde{\tau}} + \left(RV_3^2 b\right)_{y_3} = &-(RV_1V_3)\Big|_{y_{1p}-\frac{b}{2}}^{y_{1p}+\frac{b}{2}} + b - Rb + \hat{T}_{31}\Big|_{y_{1p}-\frac{b}{2}}^{y_{1p}+\frac{b}{2}} \\ &+ RV_3\Big|_{y_{1\,p}+\frac{b}{2}}\left(y_{1\,p\,\tilde{\tau}} + \frac{b_{\tilde{\tau}}}{2}\right) - RV_3\Big|_{y_{1\,p}-\frac{b}{2}}\left(y_{1\,p\,\tilde{\tau}} - \frac{b_{\tilde{\tau}}}{2}\right)\end{aligned}$$

$$+ RV_3^2\Big|_{y_{1\,p}+\frac{b}{2}}\left(y_{1\,p\,y_3}+\frac{b_{y_3}}{2}\right) - RV_3^2\Big|_{y_{1\,p}-\frac{b}{2}}\left(y_{1\,p\,y_3}-\frac{b_{y_3}}{2}\right).$$

Thus,

$$(RV_3 b)_{\tilde{\tau}} + (RV_3^2 b)_{y_3} = bf + S_M, \tag{2.3.7}$$

where:

$$\begin{aligned} f &= 1 - R \\ S_M &= \hat{T}_{31}\Big|_{y_{1p}-\frac{b}{2}}^{y_{1p}+\frac{b}{2}} - (RV_1V_3)\Big|_{y_{1p}-\frac{b}{2}}^{y_{1p}+\frac{b}{2}} + RV_3\Big|_{y_{1\,p}+\frac{b}{2}}\left(y_{1\,p\,\tilde{\tau}}+\frac{b_{\tilde{\tau}}}{2}\right) \\ &\quad - RV_3\Big|_{y_{1\,p}-\frac{b}{2}}\left(y_{1\,p\,\tilde{\tau}}-\frac{b_{\tilde{\tau}}}{2}\right) + RV_3^2\Big|_{y_{1\,p}+\frac{b}{2}}\left(y_{1\,p\,y_3}+\frac{b_{y_3}}{2}\right) \\ &\quad - RV_3^2\Big|_{y_{1\,p}-\frac{b}{2}}\left(y_{1\,p\,y_3}-\frac{b_{y_3}}{2}\right). \end{aligned}$$

Again, one will notice that the source term, S_M, is made up of several terms. The first term is the momentum added to the plume through turbulent mixing. The remainder of the terms combine as before to give the net momentum flux into the plume. As it is written above, the remainder of the terms are seen as the control volume velocity, and again, (2.3.7) is equivalent to (A.3.6).

Finally, (2.3.5d) is integrated and simplified, so that one obtains:

$$\begin{aligned} (R\Theta b)_{\tilde{\tau}} + (RV_3\Theta b)_{y_3} &= -(RV_1\Theta)\Big|_{y_{1p}-\frac{b}{2}}^{y_{1p}+\frac{b}{2}} + b\tilde{Q} + \hat{q}_1\Big|_{y_{1p}-\frac{b}{2}}^{y_{1p}+\frac{b}{2}} \\ &\quad + R\Theta\Big|_{y_{1\,p}+\frac{b}{2}}\left(y_{1\,p\,\tilde{\tau}}+\frac{b_{\tilde{\tau}}}{2}\right) - R\Theta\Big|_{y_{1\,p}-\frac{b}{2}}\left(y_{1\,p\,\tilde{\tau}}-\frac{b_{\tilde{\tau}}}{2}\right) \\ &\quad + RV_3\Theta\Big|_{y_{1\,p}+\frac{b}{2}}\left(y_{1\,p\,y_3}+\frac{b_{y_3}}{2}\right) - RV_3\Theta\Big|_{y_{1\,p}-\frac{b}{2}}\left(y_{1\,p\,y_3}-\frac{b_{y_3}}{2}\right). \end{aligned}$$

Thus,

$$(bR\Theta)_{\tilde{\tau}} + (bRV_3\Theta)_{y_3} = bH + S_T, \tag{2.3.8}$$

where:

$$
\begin{aligned}
H &= \tilde{Q} \\
S_T &= \hat{q}_1 \Big|_{y_{1p}-\frac{b}{2}}^{y_{1p}+\frac{b}{2}} - (RV_1\Theta)\Big|_{y_{1p}-\frac{b}{2}}^{y_{1p}+\frac{b}{2}} + R\Theta\Big|_{y_{1\,p}+\frac{b}{2}} \left(y_{1\,p\,\tilde{\tau}} + \frac{b_{\tilde{\tau}}}{2}\right) \\
&\quad - R\Theta\Big|_{y_{1\,p}-\frac{b}{2}} \left(y_{1\,p\,\tilde{\tau}} - \frac{b_{\tilde{\tau}}}{2}\right) + RV_3\Theta\Big|_{y_{1\,p}+\frac{b}{2}} \left(y_{1\,p\,y_3} + \frac{b_{y_3}}{2}\right) \\
&\quad - RV_3\Theta\Big|_{y_{1\,p}-\frac{b}{2}} \left(y_{1\,p\,y_3} - \frac{b_{y_3}}{2}\right).
\end{aligned}
$$

The first term of S_T, is the thermal energy added to the plume through turbulent mixing. The remaining terms combine to give the net thermal energy flux into the plume. And again, (2.3.8) is equivalent to (A.5.2).

Since the variables in (2.3.5e) are either top-hat variables or independent of Y_1, the equation does not change. Thus, the equations have been reduced to the system:

$$(Rb)_{\tilde{\tau}} + (bRV_3)_{y_3} = S_m \tag{2.3.9a}$$

$$P^{(1)}\Big|_{y_{1p}-\frac{b}{2}}^{y_{1p}+\frac{b}{2}} = \frac{gt_0^2}{l_3}\hat{T}_{11}\Big|_{y_{1p}-\frac{b}{2}}^{y_{1p}+\frac{b}{2}} \tag{2.3.9b}$$

$$(bRV_3)_{\tilde{\tau}} + (bRV_3^2)_{y_3} = bf + S_M \tag{2.3.9c}$$

$$(bR\Theta)_{\tilde{\tau}} + (bRV_3\Theta)_{y_3} = bH + S_T \tag{2.3.9d}$$

$$P^{(H)} = R\Theta. \tag{2.3.9e}$$

2.3.2 Vorticity Transport Equation

Employing the same scalings that were used to rescale variables to describe the plume, the expression for vorticity is rescaled into the plume as well. So,

$$\omega = v_{1\,y_3} - v_{3\,y_1},$$

in the plume becomes:

$$\begin{aligned}\omega_p &= V_p\left(\delta V_{1\,y_3} - \frac{1}{\delta}V_{3\,Y_1}\right)\\ &\approx \delta V_{1\,y_3} - \frac{1}{\delta}V_{3\,Y_1}\\ &\sim -\frac{1}{\delta}V_{3\,Y_1} = \frac{1}{\delta}\Omega,\end{aligned} \tag{2.3.10}$$

where the final approximation is used because $\delta \ll 1$. With this, only the momentum equation for V_3, (2.3.2c) is needed:

$$\begin{aligned}RV_p^2\left[V_{3\,\tilde{\tau}} + V_1V_{3\,Y_1} + V_3V_{3\,y_3}\right] + \frac{\bar{R}T_0t_0^2}{l_3^2}\left(P_{y_3}^{(H)} + \mathrm{RiMa}^2P_{y_3}^{(H1)} + \mathrm{Ma}^2P_{y_3}^{(1)}\right) =\\ -\frac{t_0^2g}{l_3}R + V_p^2\left(\hat{T}_{31\,Y_1} + \delta\hat{T}_{33\,y_3}\right).\end{aligned} \tag{2.3.11}$$

Then, taking the Y_1 derivative:

$$\begin{aligned}&R_{Y_1}V_p^2\left[V_{3\,\tilde{\tau}} + V_1V_{3\,Y_1} + V_3V_{3\,y_3}\right]\\ &\quad+RV_p^2\left[V_{3\,\tilde{\tau}Y_1} + V_{1\,Y_1}V_{3\,Y_1} + V_1V_{3\,Y_1Y_1} + V_{3\,Y_1}V_{3\,y_3} + V_3V_{3\,y_3Y_1}\right]\\ &\qquad+\frac{\bar{R}T_0t_0^2}{l_3^2}\left(P_{y_3\,Y_1}^{(H)} + \mathrm{RiMa}^2P_{y_3\,Y_1}^{(H1)} + \mathrm{Ma}^2P_{y_3\,Y_1}^{(1)}\right) = -\frac{t_0^2g}{l_3}R_{Y_1}\\ &\qquad\qquad+V_p^2\left(\hat{T}_{31\,Y_1Y_1} + \delta\hat{T}_{33\,y_3Y_1}\right).\end{aligned} \tag{2.3.12}$$

With this, to derive the vorticity equation, one takes $-\frac{1}{\delta}$ times (2.3.12) while using (2.3.10) and (2.3.11) to simplify. One obtains:

$$\begin{aligned}\frac{1}{\delta}RV_p^2\left[\Omega_{\tilde{\tau}} + \left(V_1\Omega\right)_{Y_1} + \left(V_3\Omega\right)_{y_3}\right] = -\frac{1}{\delta}\frac{R_{Y_1}}{R}\frac{\bar{R}T_0t_0^2}{l_3^2}\left(P_{y_3}^{(H)} + \mathrm{RiMa}^2P_{y_3}^{(H1)} + \mathrm{Ma}^2P_{y_3}^{(1)}\right)\\ +\frac{1}{\delta}\frac{R_{Y_1}}{R}V_p^2\left(\hat{T}_{31\,Y_1} + \delta\hat{T}_{33\,y_3}\right) + \frac{1}{\delta}\frac{\bar{R}T_0t_0^2}{l_3^2}\left(P_{y_3\,Y_1}^{(H)} + \mathrm{RiMa}^2P_{y_3\,Y_1}^{(H1)}\right.\\ \left.+\mathrm{Ma}^2P_{y_3\,Y_1}^{(1)}\right) - \frac{V_p^2}{\delta}\left(\hat{T}_{31\,Y_1Y_1} + \delta\hat{T}_{33\,y_3Y_1}\right).\end{aligned}$$

With $V_p^2 = \frac{gt_0^2}{l_3}$, $P_{Y_1} = \sigma P_{Y_1}^{(1)}$, $P_{y_3}^{(H1)} = -\beta + \sigma P_{y_3}^{(1)}$, $\mathrm{RiMa}^2 = \frac{gl_3}{\bar{R}T_0}$, and $\mathrm{Ma}^2 =$

$\frac{l_3^2}{RT_0t_0^2}$ one obtains:

$$\frac{1}{\delta}R\left[\Omega_{\tilde{\tau}}+\left(V_1\Omega\right)_{Y_1}+\left(V_3\Omega\right)_{y_3}\right]=\frac{1}{\delta}\frac{R_{Y_1}}{R}-\frac{1}{\delta}\frac{l_3}{gt_0^2}\frac{R_{Y_1}}{R}P^{(1)}_{y_3}$$
$$+\frac{1}{\delta}\frac{R_{Y_1}}{R}\left(\hat{T}_{31\,Y_1}+\delta\hat{T}_{33\,y_3}\right)+\frac{1}{\delta}\frac{l_3}{gt_0^2}P^{(1)}_{y_3Y_1}-\frac{1}{\delta}\left(\hat{T}_{31\,Y_1Y_1}+\delta\hat{T}_{33\,y_3Y_1}\right),$$

and for $\delta \ll 1$ one obtains the following ordered equations:

$$O\left(\frac{1}{\delta}\right):\qquad R\left[\Omega_{\tilde{\tau}}+\left(V_1\Omega\right)_{Y_1}+\left(V_3\Omega\right)_{y_3}\right]=\frac{R_{Y_1}}{R}-\frac{l_3}{gt_0^2}\frac{R_{Y_1}}{R}P^{(1)}_{y_3}+\frac{R_{Y_1}}{R}\hat{T}_{31\,Y_1}$$
$$+\frac{l_3}{gt_0^2}P^{(1)}_{y_3Y_1}-\hat{T}_{31\,Y_1Y_1}\qquad(2.3.13)$$

$$O(1):\qquad 0=\frac{R_{Y_1}}{R}\hat{T}_{33\,y_3}-\hat{T}_{33\,y_3Y_1}.\qquad(2.3.14)$$

Only the largest contribution to the vorticity in the plume system will be considered. The $O\left(\frac{1}{\delta}\right)$ equation can be rewritten in conservative form, *viz.*:

$$\left(R\Omega\right)_{\tilde{\tau}}+\left(R\Omega V_1\right)_{Y_1}+\left(R\Omega V_3\right)_{y_3}=-\Omega RV_{1\,Y_1}-\Omega RV_{3\,y_3}+\frac{R_{Y_1}}{R}$$
$$-\frac{l_3}{gt_0^2}\frac{R_{Y_1}}{R}P^{(1)}_{y_3}+\frac{R_{Y_1}}{R}\hat{T}_{31\,Y_1}+\frac{l_3}{gt_0^2}P^{(1)}_{y_3Y_1}-\hat{T}_{31\,Y_1Y_1}.\qquad(2.3.15)$$

Following the same procedure as for the other conservation laws, (2.3.15) is integrated across the plume (with respect to Y_1). Thus,

$$\int_{y_{1p}-\frac{b}{2}}^{y_{1p}+\frac{b}{2}}\left(R\Omega\right)_{\tilde{\tau}}+\left(R\Omega V_1\right)_{Y_1}+\left(R\Omega V_3\right)_{y_3}\,\mathrm{d}Y_1=$$
$$\int_{y_{1p}-\frac{b}{2}}^{y_{1p}+\frac{b}{2}}-\Omega RV_{1\,Y_1}-\Omega RV_{3\,y_3}+\frac{R_{Y_1}}{R}-\frac{l_3}{gt_0^2}\frac{R_{Y_1}}{R}P^{(1)}_{y_3}+\frac{R_{Y_1}}{R}\hat{T}_{31\,Y_1}\,\mathrm{d}Y_1$$
$$+\int_{y_{1p}-\frac{b}{2}}^{y_{1p}+\frac{b}{2}}\frac{l_3}{gt_0^2}P^{(1)}_{y_3Y_1}-\hat{T}_{31\,Y_1Y_1}\,\mathrm{d}Y_1.$$

Upon moving the derivatives outside the integrals and simplifying yields:

$$\left(Rb\Omega\right)_{\tilde{\tau}}+\left(Rb\Omega V_3\right)_{y_3}=R\Omega\Big|_{y_{1\,p}+\frac{b}{2}}\left(y_{1\,p\,\tilde{\tau}}+\frac{b_{\tilde{\tau}}}{2}\right)-R\Omega\Big|_{y_{1\,p}-\frac{b}{2}}\left(y_{1\,p\,\tilde{\tau}}-\frac{b_{\tilde{\tau}}}{2}\right)$$

$$
\begin{aligned}
&+ R\Omega V_3\Big|_{y_{1\,p}+\frac{b}{2}}\left(y_{1\,p\,y_3}+\frac{b_{y_3}}{2}\right) - R\Omega V_3\Big|_{y_{1\,p}-\frac{b}{2}}\left(y_{1\,p\,y_3}-\frac{b_{y_3}}{2}\right)\\
&- R\Omega\left[-V_3\Big|_{y_{1\,p}+\frac{b}{2}}\left(y_{1\,p\,y_3}+\frac{b_{y_3}}{2}\right)+V_3\Big|_{y_{1\,p}-\frac{b}{2}}\left(y_{1\,p\,y_3}-\frac{b_{y_3}}{2}\right)\right]\\
&\quad - 2Rb\Omega V_1 - R\Omega(bV_3)_{y_3} + \frac{l_3}{gt_0^2}P^{(1)}_{y_3}\Big|_{y_{1p}-\frac{b}{2}}^{y_{1p}+\frac{b}{2}} - \hat{T}_{31\,Y_1}\Big|_{y_{1p}-\frac{b}{2}}^{y_{1p}+\frac{b}{2}}.
\end{aligned}
$$

Thus,

$$(Rb\Omega)_{\tilde{\tau}} + (Rb\Omega V_3)_{y_3} = G + S_G, \tag{2.3.16}$$

where:

$$
\begin{aligned}
G &= -2Rb\Omega V_1 - R\Omega(bV_3)_{y_3}\\
&\quad - R\Omega\left[-V_3\Big|_{y_{1\,p}+\frac{b}{2}}\left(y_{1\,p\,y_3}+\frac{b_{y_3}}{2}\right)+V_3\Big|_{y_{1\,p}-\frac{b}{2}}\left(y_{1\,p\,y_3}-\frac{b_{y_3}}{2}\right)\right]\\
S_G &= R\Omega\Big|_{y_{1\,p}+\frac{b}{2}}\left(y_{1\,p\,\tilde{\tau}}+\frac{b_{\tilde{\tau}}}{2}\right) - R\Omega\Big|_{y_{1\,p}-\frac{b}{2}}\left(y_{1\,p\,\tilde{\tau}}-\frac{b_{\tilde{\tau}}}{2}\right)\\
&\quad + R\Omega V_3\Big|_{y_{1\,p}+\frac{b}{2}}\left(y_{1\,p\,y_3}+\frac{b_{y_3}}{2}\right) - R\Omega V_3\Big|_{y_{1\,p}-\frac{b}{2}}\left(y_{1\,p\,y_3}-\frac{b_{y_3}}{2}\right)\\
&\quad + \frac{l_3}{gt_0^2}P^{(1)}_{y_3}\Big|_{y_{1p}-\frac{b}{2}}^{y_{1p}+\frac{b}{2}} - \hat{T}_{31\,Y_1}\Big|_{y_{1p}-\frac{b}{2}}^{y_{1p}+\frac{b}{2}}.
\end{aligned}
$$

The last two terms of S_G represent the vorticity added to the plume through system pressure gradients and entrainment. The remaining terms combine to give the net vorticity flux into the plume. And again, (2.3.16) is equivalent to (A.6.11).

Thus, the system of equations that will be used to describe the plume system becomes:

$$(Rb)_{\tilde{\tau}} + (bRV_3)_{y_3} = S_m \tag{2.3.17a}$$

$$P^{(1)}\Big|_{y_{1p}-\frac{b}{2}}^{y_{1p}+\frac{b}{2}} = \frac{gt_0^2}{l_3}\hat{T}_{11}\Big|_{y_{1p}-\frac{b}{2}}^{y_{1p}+\frac{b}{2}} \tag{2.3.17b}$$

$$(bRV_3)_{\tilde{\tau}} + (bRV_3^2)_{y_3} = bf + S_M \tag{2.3.17c}$$

$$(bR\Theta)_{\tilde{\tau}} + (bRV_3\Theta)_{y_3} = bH + S_T \tag{2.3.17d}$$

$$(Rb\Omega)_{\tilde{\tau}} + (Rb\Omega V_3)_{y3} = G + S_G \tag{2.3.17e}$$

$$P^{(H)} = R\Theta. \tag{2.3.17f}$$

Equation (2.3.17a) can be solved for Rb, resulting in $Rb = M$, which can be solved for $R \Rightarrow R = \frac{M}{b}$. Similarly, equation (2.3.17d) can be solved for $Rb\Theta$. Thus, $Rb\Theta = E$, which can be solved for $\Theta \Rightarrow \Theta = \frac{E}{M}$. Then using (2.3.17f) to get $P^{(H)} = \frac{E}{b}$, which can be solved for $b \Rightarrow b = \frac{E}{P^{(H)}}$. In the same manner, equations (2.3.17c) and (2.3.17e) can be solved for RbV_3 and $Rb\Omega$, resulting in expressions for V_3 and Ω respectively.

2.4 Entrainment Model

As mentioned earlier, the assumption is made that the faster the plume moves relative to the ambient air, the faster the plume entrains air. This is done by simply letting $v^{\pm}_{in/out}(s,\tau)$ represent the velocity at which air is entrained into the plume, where:

$$v^{\pm}_{in/out}(s,\tau) = A_{in/out} \cdot |V(s,\tau) - V_{t\pm}(s,\tau)|. \tag{2.4.1}$$

Here, $\pm$ represents the plus or minus side of the plume, noting the geometry and notation in Figure 2.9, and in/out denotes whether the rate represents the air mixing into (or out of) the plume. Also, $A_{in/out}$ is a constant representing the strength of mixing following [55]; $V(s,\tau)$ is the velocity inside the plume, along the centerline of the plume; and $V_{t\pm}(s,\tau)$ is the tangential velocity outside the plume (just off the plume). The expression (2.4.1) is substituted into the right-hand side of the conservation laws from Appendix A and is used with the numerical scheme to solve the system of equations from above, simplifying the complexity of the source terms.

Clearly, one can see that this simple model for the entrainment rate does exactly what the paradigm states: the faster the plume moves relative to the ambient air (or visa versa), the faster the plume will entrain the air.

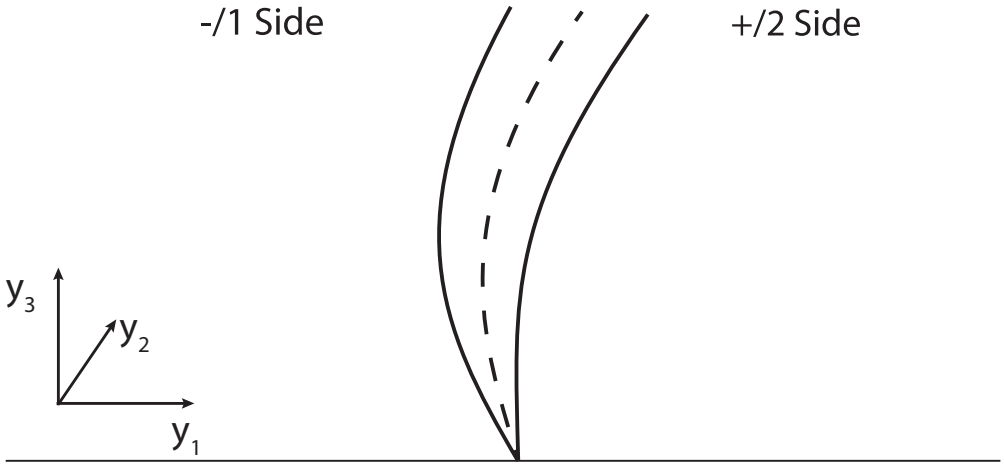

Figure 2.9: Notation and Geometry of the Plume

2.5 Conclusions

As derived in the previous sections, several simplifying assumptions have been made to reduce the problem of describing the flow inside and outside the fire plume. It is apparent that the two systems are disjoint, except for coupling due to entrainment as claimed before. Also, the size of the expansion parameters have been verified, which allows the perturbation analysis whose one term expansion has led to the simpler system that can be solved to determine the motion of the flow. As discussed, more terms can be added to account for effects due to vorticity, stratification of the atmosphere, etc. However, as more terms are added, the complexity of the problem is greatly increased. Effects such as these may be examined in future work.

Asymptotic expansions of the properties in the ambient air were used to determine that the flow in the ambient air system is two-dimensional, irrotational, and incompressible, allowing for a potential flow solution of velocity at points far away from the discontinuity that represents the plume. In addition to this, using the disjointedness of the two systems, the flow in the ambient air on the discontinuity was derived using a Biot-Savart integral.

The conservation laws in the plume system were derived in two different ways, and both approaches have been shown to be equivalent. In Cartesian coordinates,

an asymptotic approximation for small δ was used in conjunction with the assumption of a top-hat profile for all plume variables to evaluate the integrals that result from averaging the equations across the plume. In curvilinear coordinates, the conservation laws were derived using a control volume derivation outlined in Appendix A. Consistent with the paradigm, the source terms for entrainment were replaced with simple models based on the relative speed of the plume and ambient air, which greatly reduces the complexity of solving the plume system. The next step will be to implement these equations and solve them numerically to obtain solutions for different scenarios.

CHAPTER 3
Implementation of Equations for Plume Model

The equations from Chapter 2 can be implemented in MATLAB, or any other computer language, in a time evolving iteration. Information presented in this chapter includes the discretization of the domains, the numerical scheme needed to solve the conservation laws for the plume system, the implementation of velocity in the ambient air, boundary conditions, and the method of updating the position of the plume. The ideas behind the algorithms are presented here, while the MATLAB code is available upon request.

It first needs to be noted that the plume need not be vertical. In fact, a perfectly vertical plume is of little interest; it is much more interesting to see the plume react to its surroundings. When the plume starts to bend and respond to the ambient wind, a parameterization with respect to the height, y_3, is not most effective. Due to this, from here on, it will be assumed that all plume calculations are parametrized with respect to the arc length, s, unless stated otherwise. This requires a simple change of variables, and the derivation is described in Appendix A.

3.1 Discretization

To implement the equations in MATLAB, the domain needs to be discretized, creating computational nodes on the plume and in the ambient air system. The centerline of the plume is taken as $(y_{1\,p}(s,\tau), y_{3\,p}(s,\tau))$ and following Figure 3.1, nodes are placed along this curve at equally spaced increments of arc length, Δs. At each of these nodes, the properties of the plume (density, temperature, velocity, width, etc.) are assumed to be functions of (s,τ). In addition, this discretization is also used for the calculation of the velocity off the plume induced by the plume, which was discussed above. This is because the normal or tangential velocity just off the plume is computed on the coordinate system fixed to the plume at point s, or in terms of the discretization, at a set of specific arc length points associated with

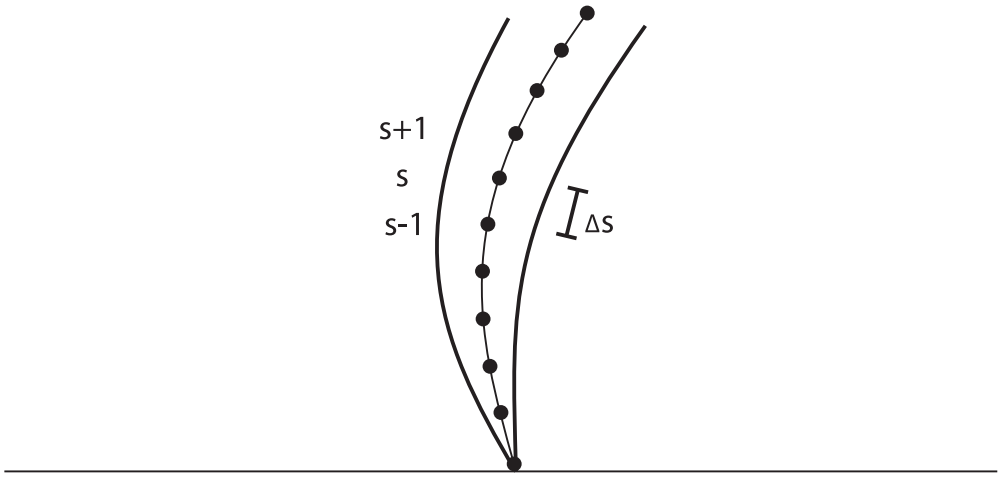

Figure 3.1: Discretization of Plume

the plume.

To create a discretized domain in the ambient air system, a simple Cartesian grid is employed. The nodes are equally spaced in the computational domain, where each of the properties (density, temperature, velocity, pressure, etc.) of the ambient air system are taken to be functions of (y_1, y_3, τ). For example, the velocity in the ambient air system, far from the plume is taken to be $\hat{\mathbf{v}}(y_1, y_3, \tau)$. This grid is used for the purpose of plotting arrows to indicate the motion of flow, and will allow for stratification of density, temperature, and pressure.

3.2 Implementation of Conservation Laws Inside the Plume

While the ideas of the conservation laws from Section 2.3.2 are used in the implementation, these conservation laws, (2.3.17), were derived for a nearly vertical plume. As mentioned above, this is not the case of interest. However, the conservation laws from Appendix A generalize the derivation, allowing a nearly arbitrary plume position in a curvilinear coordinate system fixed to the plume. These equations are discretized to calculate five key properties; these properties are the width of the plume, density, velocity, temperature, and vorticity inside the plume. The calculation of these properties depends on what is happening throughout the entire domain, including the ambient air system through entrainment, as mentioned in

Section 2.4. With all of these properties together, the flow inside the plume can be completely described.

To calculate the key properties, difference equations are used to approximate the derivatives in the conservation equations. Special care needs to be taken when numerically solving these conservation laws. Since after implementation the velocity inside the plume is allowed to change signs, a simple upwind (or downwind) scheme would not accurately solve the problem at hand. This is due to the direction of the propagation of information and the CFL condition for methods solving partial differential equations [70]. A simple diffusive scheme is adopted, keeping in mind the desire to minimize computation cost. The decision process and justification is outlined in Appendix B. Additionally, in order to keep the model simple, the source terms of entrainment are replaced with a simplified model, consistent with the paradigm, as shown in Section 2.4.

3.2.1 Implementation of Diffusive Scheme

Upon examining the choices of solution method in Appendix B, it was decided that the conservation laws from Appendix A should be solved as a coupled system. To achieve the system in terms of elementary variables, as discussed in Appendix B, the conservation of mass equation is used to simplify the other conservation laws. With this, the system of equations of interest is:

$$(Rb)_\tau + (RbV)_s = S_m \tag{3.2.1a}$$

$$V_\tau + \left(\frac{1}{2}V^2\right)_s = \frac{1}{Rb}\left(S_M + (1-R)\tilde{g}b\frac{\partial y_3}{\partial s} - VS_m\right) \tag{3.2.1b}$$

$$\Theta_\tau + (\Theta V)_s = \frac{1}{RbC_p}\left(S_T + b\tilde{Q} - \Theta C_p S_m\right) + V_s\Theta \tag{3.2.1c}$$

$$\Omega_\tau + (V\Omega)_s = \frac{1}{b}S_G. \tag{3.2.1d}$$

One notes that with advection type equations, the flux dictates which simple schemes (upwind or downwind) can be used. In the case at hand, a flux in either direction can be expected due to implementation techniques. Although, a positive flux moving up the plume is used the majority of the time. Thus, a simple first

order scheme will be used with conditions on whether an upwind or downwind is needed. As written, it appears as though the velocity equation is solved separate from the remaining three conservation equations. This is not the case. All equations are solved simultaneously as a fully coupled set of equations. The description below was written in this way because the velocity equation requires additional techniques for solution and it is easier to explain.

To implement the diffusive scheme on the PDE system (3.2.1), following Boudin [15], a second order diffusive term is added to (3.2.1b), giving:

$$V_\tau + (\frac{1}{2}V^2)_s = \epsilon\frac{1}{Rb}V_{ss} + f_v(s,\tau), \tag{3.2.2}$$

where ϵ is a small parameter, here taken to be $\epsilon = 0.005$, and $f_v(s,\tau)$ is the right-hand side of (3.2.1b). In this system of equations, (3.2.1), which is different than the applications of Boudin [15], the added diffusive term has been found to damp oscillations that result from the ill-behaved system. A sufficiently large ϵ is chosen to damp the oscillations from growing, but the choice needs to be small enough as to not damp the solution. Again, justification of the choice to add the diffusive term can be seen in Appendix B. Since a simple first order scheme is desired in this work, upwinding as well as downwinding in the spatial domain will be used when the flux deems appropriate. A simple forward differencing will be used in time to obtain the general scheme for (3.2.1b):

$$\begin{aligned} V_s^{\tau+1} = V_s^\tau &- \frac{\Delta t}{\Delta s}\left[F_v(V_s^\tau, V_{s+1}^\tau) - F_v(V_{s-1}^\tau, V_s^\tau)\right] \\ &+ \epsilon\frac{\Delta t}{\Delta s^2}\frac{1}{R_s^\tau b_s^\tau}\left(V_{s-1}^\tau - 2V_s^\tau + V_{s+1}^\tau\right) + f_{v\,s}^\tau, \end{aligned} \tag{3.2.3}$$

where,

$$F_v(u_l,u_r) = \begin{cases} \frac{1}{2}u_l^2 & V_{s+1}^\tau + V_s^\tau \geq 0 \\ \frac{1}{2}u_r^2 & V_{s+1}^\tau + V_s^\tau < 0, \end{cases}$$

u_l, u_r is the argument of F_v, $V(s,\tau) \approx V_s^\tau$, $f_v(s,\tau) = f_{v\,s}^\tau$, $R(s,\tau) \approx R_s^\tau$, and $b(s,\tau) \approx b_s^\tau$. It is seen that the scheme (3.2.3) is explicit, which allows for an expression for $V_s^{\tau+1}$ to be found.

The remaining equations, (3.2.1a), (3.2.1c), and (3.2.1d), each can be easily written in general as the PDE:

$$\frac{\partial \zeta}{\partial \tau} + \frac{\partial g(\zeta)}{\partial s} = f(s, \tau), \tag{3.2.4}$$

where it is seen that $\zeta = Rb$, Θ, and Ω; $g(\zeta) = \zeta V$; and $f(s, \tau)$ is the right-hand side of (3.2.1a), (3.2.1c), and (3.2.1d), respectively for the conservation of mass and temperature, and vorticity equations. The equation (3.2.4) will be solved by using upwind or downwind, depending on the sign of the flux. This will be done again using the simple condition such that:

$$Z_s^{\tau+1} = Z_s^\tau - \frac{\Delta t}{\Delta x}(F_\zeta(Z_s^\tau, Z_{s+1}^\tau) - F_\zeta(Z_{s-1}^\tau, Z_s^\tau)) + f_s^\tau, \tag{3.2.5}$$

where,

$$F_\zeta(u_l, u_r) = \begin{cases} u_l V_l^\tau & V_{s+1}^\tau + V_s^\tau \geq 0 \\ u_r V_r^\tau & V_{s+1}^\tau + V_s^\tau < 0, \end{cases}$$

u_l, u_r is the argument of F_ζ, $\zeta(s, \tau) \approx Z_s^\tau$, and $f(s, \tau) = f_s^\tau$ is the right-hand side of (3.2.1a), (3.2.1c), and (3.2.1d) respectively. This time a diffusive term is not needed because all difficulties and oscillations that occur in this system stem from the velocity equation. Thus, adding a diffusive term here would only damp the solutions.

From here, the schemes can be easily implemented to solve the system of equations. Note, although it is not written in a coupled form, the system of equations (3.2.1) will be solved as a fully coupled system using the schemes (3.2.3) and (3.2.5).

3.2.2 Initial and Boundary Conditions

As of yet, nothing has been said about the initial and boundary conditions to properly close the systems of equations (3.2.1). For now, the choice of the conditions will provide fire behavior to the system in the absence of a model for fire dynamics.

The initial conditions for the plume properties are:

$$R(s,0) = \begin{cases} \Xi & s = 0 \\ 1 & s > 0 \end{cases} \qquad \theta(s,0) = \begin{cases} \frac{1}{\Xi} & s = 0 \\ 1 & s > 0 \end{cases}$$

$$V(s,0) = \begin{cases} 1 & s = 0 \\ 0 & s > 0 \end{cases} \qquad \Omega(s,0) = \begin{cases} \tilde{\Xi} & s = 0 \\ 0 & s > 0, \end{cases}$$

where $0 \leq \Xi \leq 1$ is a constant and $|\tilde{\Xi}| \ll 1$ is a random small value. These initial conditions physically state that inside the point source fire at the ground, the air is hot and less dense than the air outside the fire.

The computational boundary condition at the top of the computational domain allows the air in the plume moving up to escape out of the top of the plume, which is achieved automatically by the upwind scheme. If the air is moving down at the top of the computational domain, the flux, F, is specified such that ambient air is pulled in. The majority of the time, the boundary condition at the top of the domain is not needed. When the plume reaches the height of the computation domain, the former condition is used.

At the fire point at the bottom of the plume, the boundary condition used is:

$$R(0,\tau) = \Xi \qquad \theta(0,\tau) = \frac{1}{\Xi}$$

$$V(0,\tau) = 1 + \bar{\Xi}(\tau) \qquad \Omega(0,\tau) = \tilde{\Xi}(\tau),$$

where again, $0 \leq \Xi \leq 1$ is a constant, $|\tilde{\Xi}| \ll 1$ is a random small value, and $|\bar{\Xi}| < 1$ is a random value. These random values are normally distributed and are chosen at random time increments. The prescribed values of velocity and vorticity are used to mimic the behavior of how fire "dances" with puffing and curling effects due to the absence of fire dynamics in the calculations.

Numerically, when the above scheme is implemented, the solution inside the plume is only computed up to the top of the plume, which explains why a positive flux is expected and the boundary condition at the top of the computation domain is rarely used. Anything above the top of the plume is assumed to be well mixed

ambient air. The top of the plume is calculated by tracking the position of a particle released into the fire. This is computed at each time step by solving the simple ODE:

$$\frac{\partial s_{top}(\tau)}{\partial t} = V(s_{top}(\tau), \tau),$$

which can be easily solved using a difference equation giving, $s_{top}(\tau+1) = s_{top}(\tau) + V(s_{top}(\tau), \tau)\Delta t$. This basically tracks a particle in the plume and calculates the distance it travels in time. Since the velocity is calculated on the discretized grid, the velocity needs to be interpolated to find its value at s_{top}. The top of the plume is an integer value, so a tolerance is set and once the particle reaches the tolerance, the integer value of the plume top is incremented.

With this idea and the ideas above, the flow inside the plume can be completely described, although the flow depends on the flow in the ambient air, which will be discussed in the coming section. The equations can be easily implemented into MATLAB or any other computer language to create the computational model to describe this flow.

3.3 Implementation of Velocity in Ambient Air

The flow induced by the plume is implemented as a Riemann sum representing a vortex sheet/line sink combination. Once the plume is discretized, each node in the plume represents a point vortex/sink combination. When the effects of each computation node is summed, the result is an approximation to the vortex sheet/line sink combination as needed.

The implementation of the velocity in the ambient air simply consists of approximating the integrals from the derivations in Section 2.2.5 as sums and distinguishing between the velocity far from the plume and the velocity near the plume.

Upon considering the velocity far from the plume first, one obtains the following sums:

$$\hat{u}(y_1, y_3, \tau) = \sum_{s'=1}^{N} \frac{-S_v(s', \tau)(y_1 - y_{1\,p}(s'))}{2\pi\left[(y_1 - y_{1\,p}(s'))^2 + (y_3 - y_{3\,p}(s'))^2\right]}\Delta s$$

$$
\begin{aligned}
&- \sum_{s'=1}^{N} \frac{S_v(s',\tau)(y_1 - y_{1\,p}(s'))}{2\pi\left[(y_1 - y_{1\,p}(s'))^2 + (y_3 + y_{3\,p}(s'))^2\right]}\Delta s \\
&- \sum_{s'=1}^{N} \frac{\Omega(s',\tau)(y_3 - y_{3\,p}(s'))}{2\pi\left[(y_1 - y_{1\,p}(s'))^2 + (y_3 - y_{3\,p}(s'))^2\right]}\Delta s \\
&+ \sum_{s'=1}^{N} \frac{\Omega(s',\tau)(y_3 + y_{3\,p}(s'))}{2\pi\left[(y_1 - y_{1\,p}(s'))^2 + (y_3 + y_{3\,p}(s'))^2\right]}\Delta s
\end{aligned}
$$

$$
\begin{aligned}
\hat{v}(y_1, y_3, \tau) = &\sum_{s'=1}^{N} \frac{-S_v(s',\tau)(y_3 - y_{3\,p}(s'))}{2\pi\left[(y_1 - y_{1\,p}(s'))^2 + (y_3 - y_{3\,p}(s'))^2\right]}\Delta s \\
&- \sum_{s'=1}^{N} \frac{S_v(s',\tau)(y_3 + y_{3\,p}(s'))}{2\pi\left[(y_1 - y_{1\,p}(s'))^2 + (y_3 + y_{3\,p}(s'))^2\right]}\Delta s \\
&+ \sum_{s'=1}^{N} \frac{\Omega(s',\tau)(y_1 - y_{1\,p}(s'))}{2\pi\left[(y_1 - y_{1\,p}(s'))^2 + (y_3 - y_{3\,p}(s'))^2\right]}\Delta s \\
&- \sum_{s'=1}^{N} \frac{\Omega(s',\tau)(y_1 - y_{1\,p}(s'))}{2\pi\left[(y_1 - y_{1\,p}(s'))^2 + (y_3 + y_{3\,p}(s'))^2\right]}\Delta s,
\end{aligned}
$$

using a simple one-sided Riemann approximation of the integrals (2.2.30), where N is the number of computational nodes used in the plume discretization. One will note that since all plume properties are only calculated up to the top of the plume, the contribution to the induced velocity for points $s' >$ plume top is zero.

More care needs to be used when considering the velocity just off the plume. This time, the integrals in the expressions for $\hat{u}$ and $\hat{v}$ are taken in the principal value sense, meaning the singularity is skipped. Thus, the discrete approximation for the full velocity just off the plume, up to the height of the plume, becomes:

$$
\begin{aligned}
V_{n\pm}(s,\tau) = &\sum_{\substack{s'=1 \\ s'\neq s}}^{N} \frac{-S_v(s',\tau)(y_{1\,p}(s) - y_{1\,p}(s'))}{2\pi\left[(y_{1\,p}(s) - y_{1\,p}(s'))^2 + (y_{3\,p}(s) - y_{3\,p}(s'))^2\right]}\Delta s \\
&- \sum_{\substack{s'=1 \\ s'\neq s}}^{N} \frac{S_v(s',\tau)(y_{1\,p}(s) - y_{1\,p}(s'))}{2\pi\left[(y_{1\,p}(s) - y_{1\,p}(s'))^2 + (y_{3\,p}(s) + y_{3\,p}(s'))^2\right]}\Delta s
\end{aligned}
$$

$$
\begin{aligned}
&- \sum_{\substack{s'=1 \\ s' \neq s}}^{N} \frac{\Omega(s',\tau)(y_{3\,p}(s) - y_{3\,p}(s'))}{2\pi\left[(y_{1\,p}(s) - y_{1\,p}(s'))^2 + (y_{3\,p}(s) - y_{3\,p}(s'))^2\right]} \Delta s \\
&+ \sum_{\substack{s'=1 \\ s' \neq s}}^{N} \frac{\Omega(s',\tau)(y_{3\,p}(s) + y_{3\,p}(s'))}{2\pi\left[(y_{1\,p}(s) - y_{1\,p}(s'))^2 + (y_{3\,p}(s) + y_{3\,p}(s'))^2\right]} \Delta s - \frac{S_v(s,\tau)}{2}
\end{aligned}
$$

$$
\begin{aligned}
V_{t\pm} s,\tau) = &\sum_{\substack{s'=1 \\ s' \neq s}}^{N} \frac{-S_v(s',\tau)(y_{3\,p}(s) - y_{3\,p}(s'))}{2\pi\left[(y_{1\,p}(s) - y_{1\,p}(s'))^2 + (y_{3\,p}(s) - y_{3\,p}(s'))^2\right]} \Delta s \\
&- \sum_{\substack{s'=1 \\ s' \neq s}}^{N} \frac{S_v(s',\tau)(y_{3\,p}(s) + y_{3\,p}(s'))}{2\pi\left[(y_{1\,p}(s) - y_{1\,p}(s'))^2 + (y_{3\,p}(s) + y_{3\,p}(s'))^2\right]} \Delta s \\
&+ \sum_{\substack{s'=1 \\ s' \neq s}}^{N} \frac{\Omega(s',\tau)(y_{1\,p}(s) - y_{1\,p}(s'))}{2\pi\left[(y_{1\,p}(s) - y_{1\,p}(s'))^2 + (y_{3\,p}(s) - y_{3\,p}(s'))^2\right]} \Delta s \\
&- \sum_{\substack{s'=1 \\ s' \neq s}}^{N} \frac{\Omega(s',\tau)(y_{1\,p}(s) - y_{1\,p}(s'))}{2\pi\left[(y_{1\,p}(s) - y_{1\,p}(s'))^2 + (y_{3\,p}(s) + y_{3\,p}(s'))^2\right]} \Delta s \pm \frac{\Omega(s,\tau)}{2},
\end{aligned}
$$

for $0 \leq s \leq$ plume top. For points above the plume top, a mollifier is used, following Krasny [34] and Alben & Shelley [1], to smooth the effect of the singularity in the free sheet. This results in:

$$
\begin{aligned}
V_{n\pm}(s,\tau) = &\sum_{s'=1}^{N} \frac{-S_v(s',\tau)(y_{1\,p}(s) - y_{1\,p}(s'))}{2\pi\left[(y_{1\,p}(s) - y_{1\,p}(s'))^2 + (y_{3\,p}(s) - y_{3\,p}(s'))^2 + \tilde{\delta}^2\right]} \Delta s \\
&- \sum_{s'=1}^{N} \frac{S_v(s',\tau)(y_{1\,p}(s) - y_{1\,p}(s'))}{2\pi\left[(y_{1\,p}(s) - y_{1\,p}(s'))^2 + (y_{3\,p}(s) + y_{3\,p}(s'))^2\right]} \Delta s \\
&- \sum_{s'=1}^{N} \frac{\Omega(s',\tau)(y_{3\,p}(s) - y_{3\,p}(s'))}{2\pi\left[(y_{1\,p}(s) - y_{1\,p}(s'))^2 + (y_{3\,p}(s) - y_{3\,p}(s'))^2 + \tilde{\delta}^2\right]} \Delta s \\
&+ \sum_{s'=1}^{N} \frac{\Omega(s',\tau)(y_{3\,p}(s) + y_{3\,p}(s'))}{2\pi\left[(y_{1\,p}(s) - y_{1\,p}(s'))^2 + (y_{3\,p}(s) + y_{3\,p}(s'))^2\right]} \Delta s - \frac{S_v(s,\tau)}{2}
\end{aligned}
$$

$$V_{t\pm}(s,\tau) = \sum_{s'=1}^{N} \frac{-S_v(s',\tau)(y_{3\,p}(s) - y_{3\,p}(s'))}{2\pi\left[(y_{1\,p}(s) - y_{1\,p}(s'))^2 + (y_{3\,p}(s) - y_{3\,p}(s'))^2 + \tilde{\delta}^2\right]}\Delta s$$
$$- \sum_{s'=1}^{N} \frac{S_v(s',\tau)(y_{3\,p}(s) + y_{3\,p}(s'))}{2\pi\left[(y_{1\,p}(s) - y_{1\,p}(s'))^2 + (y_{3\,p}(s) + y_{3\,p}(s'))^2\right]}\Delta s$$
$$+ \sum_{s'=1}^{N} \frac{\Omega(s',\tau)(y_{1\,p}(s) - y_{1\,p}(s'))}{2\pi\left[(y_{1\,p}(s) - y_{1\,p}(s'))^2 + (y_{3\,p}(s) - y_{3\,p}(s'))^2 + \tilde{\delta}^2\right]}\Delta s$$
$$- \sum_{s'=1}^{N} \frac{\Omega(s',\tau)(y_{1\,p}(s) - y_{1\,p}(s'))}{2\pi\left[(y_{1\,p}(s) - y_{1\,p}(s'))^2 + (y_{3\,p}(s) + y_{3\,p}(s'))^2\right]}\Delta s \pm \frac{\Omega(s,\tau)}{2},$$

where here $s_{top} < s \leq N$ and $\tilde{\delta} = 0.02$.

With this, the velocity both away from the discontinuity and on the discontinuity can be calculated. As it has been seen, the velocity on the discontinuity is computed using the discretization of the plume (the coordinate system fixed to the plume). This is because the normal and tangential components are needed at those specific heights, whereas the velocity away from the discontinuity can be calculated on the discretized Cartesian grid.

3.3.0.1 Addition of Crosswind Flow to Implementation of Ambient Air Velocity

As stated in the derivation of the velocity in the ambient air in Section 2.2.6, the case of a crosswind flow will be of interest for this work. After approximating the integrals in the expressions for the calculation of the velocity, both far from the plume and on the discontinuity, the effect of the crosswind can be simply added in the appropriate expressions following the derivations in Section 2.2.6.

For the velocity far from the plume, the calculation becomes:

$$\hat{u}(y_1, y_3, \tau) = \sum_{s'=1}^{N} \frac{-S_v(s',\tau)(y_1 - y_{1\,p}(s'))}{2\pi\left[(y_1 - y_{1\,p}(s'))^2 + (y_3 - y_{3\,p}(s'))^2\right]}\Delta s$$
$$- \sum_{s'=1}^{N} \frac{S_v(s',\tau)(y_1 - y_{1\,p}(s'))}{2\pi\left[(y_1 - y_{1\,p}(s'))^2 + (y_3 + y_{3\,p}(s'))^2\right]}\Delta s$$
$$- \sum_{s'=1}^{N} \frac{\Omega(s',\tau)(y_3 - y_{3\,p}(s'))}{2\pi\left[(y_1 - y_{1\,p}(s'))^2 + (y_3 - y_{3\,p}(s'))^2\right]}\Delta s$$

$$+\sum_{s'=1}^{N}\frac{\Omega(s',\tau)(y_3+y_{3\,p}(s'))}{2\pi\left[(y_1-y_{1\,p}(s'))^2+(y_3+y_{3\,p}(s'))^2\right]}\Delta s+cw$$

$$\begin{aligned}\hat{v}(y_1,y_3,\tau)=&\sum_{s'=1}^{N}\frac{-S_v(s',\tau)(y_3-y_{3\,p}(s'))}{2\pi\left[(y_1-y_{1\,p}(s'))^2+(y_3-y_{3\,p}(s'))^2\right]}\Delta s\\&-\sum_{s'=1}^{N}\frac{S_v(s',\tau)(y_3+y_{3\,p}(s'))}{2\pi\left[(y_1-y_{1\,p}(s'))^2+(y_3+y_{3\,p}(s'))^2\right]}\Delta s\\&+\sum_{s'=1}^{N}\frac{\Omega(s',\tau)(y_1-y_{1\,p}(s'))}{2\pi\left[(y_1-y_{1\,p}(s'))^2+(y_3-y_{3\,p}(s'))^2\right]}\Delta s\\&-\sum_{s'=1}^{N}\frac{\Omega(s',\tau)(y_1-y_{1\,p}(s'))}{2\pi\left[(y_1-y_{1\,p}(s'))^2+(y_3+y_{3\,p}(s'))^2\right]}\Delta s.\end{aligned}$$

When calculating the velocity on the discontinuity, the calculation becomes:

$$\begin{aligned}V_{n\pm}(s,\tau)=&\sum_{\substack{s'=1\\s'\neq s}}^{N}\frac{-S_v(s',\tau)(y_{1\,p}(s)-y_{1\,p}(s'))}{2\pi\left[(y_{1\,p}(s)-y_{1\,p}(s'))^2+(y_{3\,p}(s)-y_{3\,p}(s'))^2\right]}\Delta s\\&-\sum_{\substack{s'=1\\s'\neq s}}^{N}\frac{S_v(s',\tau)(y_{1\,p}(s)-y_{1\,p}(s'))}{2\pi\left[(y_{1\,p}(s)-y_{1\,p}(s'))^2+(y_{3\,p}(s)+y_{3\,p}(s'))^2\right]}\Delta s\\&-\sum_{\substack{s'=1\\s'\neq s}}^{N}\frac{\Omega(s',\tau)(y_{3\,p}(s)-y_{3\,p}(s'))}{2\pi\left[(y_{1\,p}(s)-y_{1\,p}(s'))^2+(y_{3\,p}(s)-y_{3\,p}(s'))^2\right]}\Delta s\\&+\sum_{\substack{s'=1\\s'\neq s}}^{N}\frac{\Omega(s',\tau)(y_{3\,p}(s)+y_{3\,p}(s'))}{2\pi\left[(y_{1\,p}(s)-y_{1\,p}(s'))^2+(y_{3\,p}(s)+y_{3\,p}(s'))^2\right]}\Delta s\\&-\frac{S_v(s,\tau)}{2}+\mathbf{cw}\cdot\mathbf{n}_{\pm}(s,\tau)\end{aligned}$$

$$\begin{aligned}V_{t\pm}(s,\tau)=&\sum_{\substack{s'=1\\s'\neq s}}^{N}\frac{-S_v(s',\tau)(y_{3\,p}(s)-y_{3\,p}(s'))}{2\pi\left[(y_{1\,p}(s)-y_{1\,p}(s'))^2+(y_{3\,p}(s)-y_{3\,p}(s'))^2\right]}\Delta s\\&-\sum_{\substack{s'=1\\s'\neq s}}^{N}\frac{S_v(s',\tau)(y_{3\,p}(s)+y_{3\,p}(s'))}{2\pi\left[(y_{1\,p}(s)-y_{1\,p}(s'))^2+(y_{3\,p}(s)+y_{3\,p}(s'))^2\right]}\Delta s\end{aligned}$$

$$+\sum_{\substack{s'=1\\s'\neq s}}^{N}\frac{\Omega(s',\tau)(y_{1\,p}(s)-y_{1\,p}(s'))}{2\pi\left[(y_{1\,p}(s)-y_{1\,p}(s'))^2+(y_{3\,p}(s)-y_{3\,p}(s'))^2\right]}\Delta s$$
$$-\sum_{\substack{s'=1\\s'\neq s}}^{N}\frac{\Omega(s',\tau)(y_{1\,p}(s)-y_{1\,p}(s'))}{2\pi\left[(y_{1\,p}(s)-y_{1\,p}(s'))^2+(y_{3\,p}(s)+y_{3\,p}(s'))^2\right]}\Delta s$$
$$\pm\frac{\Omega(s,\tau)}{2}+\mathbf{cw}\cdot\mathbf{T}(s,\tau),$$

for $0 \leq s \leq$ plume top. For points above the plume top:

$$V_{n\pm}(s,\tau)=\sum_{s'=1}^{N}\frac{-S_v(s',\tau)(y_{1\,p}(s)-y_{1\,p}(s'))}{2\pi\left[(y_{1\,p}(s)-y_{1\,p}(s'))^2+(y_{3\,p}(s)-y_{3\,p}(s'))^2+\tilde{\delta}^2\right]}\Delta s$$
$$-\sum_{s'=1}^{N}\frac{S_v(s',\tau)(y_{1\,p}(s)-y_{1\,p}(s'))}{2\pi\left[(y_{1\,p}(s)-y_{1\,p}(s'))^2+(y_{3\,p}(s)+y_{3\,p}(s'))^2\right]}\Delta s$$
$$-\sum_{s'=1}^{N}\frac{\Omega(s',\tau)(y_{3\,p}(s)-y_{3\,p}(s'))}{2\pi\left[(y_{1\,p}(s)-y_{1\,p}(s'))^2+(y_{3\,p}(s)-y_{3\,p}(s'))^2+\tilde{\delta}^2\right]}\Delta s$$
$$+\sum_{s'=1}^{N}\frac{\Omega(s',\tau)(y_{3\,p}(s)+y_{3\,p}(s'))}{2\pi\left[(y_{1\,p}(s)-y_{1\,p}(s'))^2+(y_{3\,p}(s)+y_{3\,p}(s'))^2\right]}\Delta s$$
$$-\frac{S_v(s,\tau)}{2}+\mathbf{cw}\cdot\mathbf{n}_{\pm}(s,\tau)$$

$$V_{t\pm}(s,\tau)=\sum_{s'=1}^{N}\frac{-S_v(s',\tau)(y_{3\,p}(s)-y_{3\,p}(s'))}{2\pi\left[(y_{1\,p}(s)-y_{1\,p}(s'))^2+(y_{3\,p}(s)-y_{3\,p}(s'))^2+\tilde{\delta}^2\right]}\Delta s$$
$$-\sum_{s'=1}^{N}\frac{S_v(s',\tau)(y_{3\,p}(s)+y_{3\,p}(s'))}{2\pi\left[(y_{1\,p}(s)-y_{1\,p}(s'))^2+(y_{3\,p}(s)+y_{3\,p}(s'))^2\right]}\Delta s$$
$$+\sum_{s'=1}^{N}\frac{\Omega(s',\tau)(y_{1\,p}(s)-y_{1\,p}(s'))}{2\pi\left[(y_{1\,p}(s)-y_{1\,p}(s'))^2+(y_{3\,p}(s)-y_{3\,p}(s'))^2+\tilde{\delta}^2\right]}\Delta s$$
$$-\sum_{s'=1}^{N}\frac{\Omega(s',\tau)(y_{1\,p}(s)-y_{1\,p}(s'))}{2\pi\left[(y_{1\,p}(s)-y_{1\,p}(s'))^2+(y_{3\,p}(s)+y_{3\,p}(s'))^2\right]}\Delta s$$
$$\pm\frac{\Omega(s,\tau)}{2}+\mathbf{cw}\cdot\mathbf{T}(s,\tau),$$

for $s_{top} < s \leq N$ and $\tilde{\delta} = 0.02$.

3.4 Plume Position Update

The final piece of information necessary for implementation is a method for updating the position of the plume. With the inclusion of the flag flapping ideas [1], the plume has the ability to react to the flow induced by itself and react to any atmospheric effects. An example of these atmospheric phenomenon is cross flow of any kind. In such instances, one would expect the plume to move from its initial vertical position. To implement the plume motion, the plume and its discrete points are thought of as a chain, with distinct links. Each link has the ability to rotate, using the computation nodes as pivot points. In the update of the position of the plume, the transverse momentum from Appendix A will be used to calculate the distance each node is "pushed" to one side or the other by such crosswind situations.

It is assumed that the first node in the plume (the point source fire) at $(y_1, y_3) = (0, 0)$ is fixed and not allowed to move. One can easily see that if w, the transverse velocity calculated from (A.4.7), is positive, the plume will move toward the + side of the domain (in the $\mathbf{n}_+$ direction) and if the transverse velocity is negative, the plume will move in the opposite direction (in the $\mathbf{n}_-$ direction). Then following Figure 3.2, the angle at which a given link is "pushed" is calculated by a simple geometric argument under the assumption that the angle of rotation is small. Since a rotation is arc length preserving, the assumption that the angle is small allows the arc swept by the rotation to be approximated by a simple line, allowing for this geometric argument.

The process for calculating the new position of a node is accomplished by using a rotation matrix. Care needs to be taken when using the rotation matrix because the pivot needs to be translated to the origin. The calculation proceeds by numerically translating the pivot back to the origin, rotating the link in the chain, translating the pivot back to its original position, and then moving the pivot to the previously rotated node. See Figure 3.3 for clarification. This process is done by

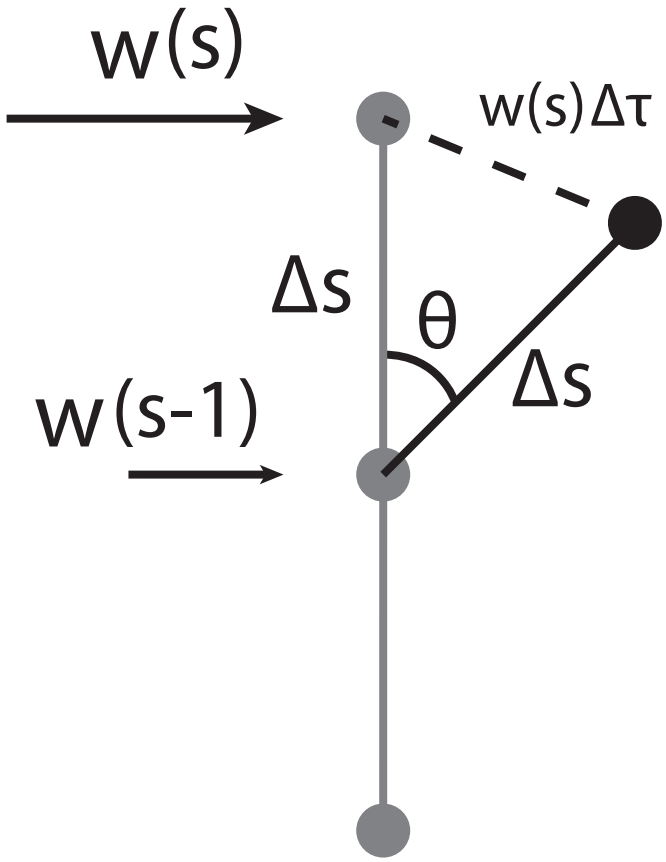

Figure 3.2: Angle Link Rotates

using an affine transformation matrix which takes the form:

$$\mathbf{A} =$$

$$\begin{bmatrix} 1 & 0 & \Delta x_{s-1} \\ 0 & 1 & \Delta y_{s-1} \\ 0 & 0 & 1 \end{bmatrix} \begin{bmatrix} 1 & 0 & y_{1\,p}(s-1,\tau) \\ 0 & 1 & y_{3\,p}(s-1,\tau) \\ 0 & 0 & 1 \end{bmatrix} \begin{bmatrix} \cos\theta & \sin\theta & 0 \\ -\sin\theta & \cos\theta & 0 \\ 0 & 0 & 1 \end{bmatrix} \begin{bmatrix} 1 & 0 & -y_{1\,p}(s-1,\tau) \\ 0 & 1 & -y_{3\,p}(s-1,\tau) \\ 0 & 0 & 1 \end{bmatrix}$$

$$= \begin{bmatrix} \cos\theta & \sin\theta & x_{s-1} + \Delta x_{s-1} - x_{s-1}\cos\theta - y_{s-1}\sin\theta \\ -\sin\theta & \cos\theta & y_{s-1} + \Delta y_{s-1} + x_{s-1}\sin\theta - y_{s-1}\cos\theta \\ 0 & 0 & 1 \end{bmatrix}, \tag{3.4.1}$$

where $(y_{1\,p}(s-1,\tau), y_{3\,p}(s-1,\tau)) = (x_{s-1}, y_{s-1})$ is the pivot point, and $(\Delta x_{s-1}, \Delta y_{s-1})$ is the change in pivot point due to previous link rotating and changing position.

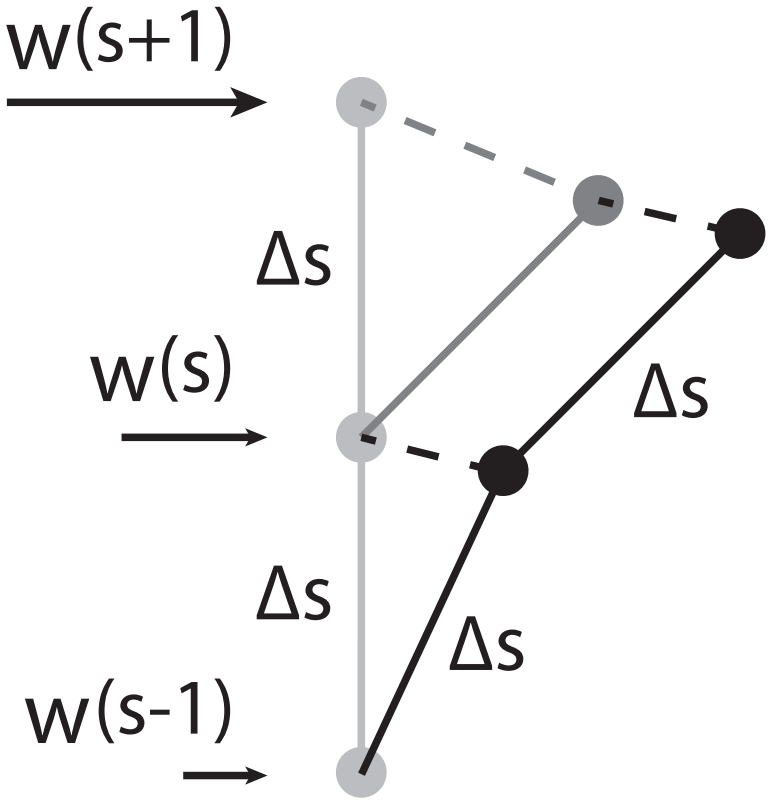

Figure 3.3: Calculation of New Position Procedure

The matrices in (3.4.1) represent the manipulations in reverse order. This means the first matrix is the translation to the previously rotated point, the next matrix is the translation from the origin back to the original position of the point, etc. The angle θ is simply calculated by equation:

$$\theta = \tan^{-1}\left(\frac{(w(s,\tau) - w(s-1,\tau))\,\Delta\tau}{\Delta s}\right), \tag{3.4.2}$$

and the rotation matrix is multiplied by the position at the previous time to get the new position:

$$\begin{bmatrix} y_{1\,p}(s,\tau+1) \\ y_{3\,p}(s,\tau+1) \\ 1 \end{bmatrix} = \mathbf{A} \begin{bmatrix} y_{1\,p}(s,\tau) \\ y_{3\,p}(s,\tau) \\ 1 \end{bmatrix}. \tag{3.4.3}$$

3.5 Summary

In this chapter the ideas needed to implement the equations derived in Chapter 2 in MATLAB were presented. Both systems were discretized into numerical domains: the plume with an arc length nodal chain, and the ambient air with a simple Cartesian grid. The discretization allows all of the equations to be implemented. A diffusive scheme was presented and applied to the conservation laws in the plume. Due to the implementation of the equations inside the plume and only calculating the plume variables up to the plume top, a positive flux (air moving toward the top of the plume) is always expected. The added functionality of a flux condition was implemented noting that the flux in each instance could be positive or negative, rendering a simple upwind or downwind scheme inapplicable. Boundary and initial conditions were chosen such that fire behavior was induced into the system. The integrals which represent the velocity in the ambient air are approximated by Riemann sums and implemented as such. Finally, the method for calculating the new position of the plume was derived using a transformation matrix.

With each of these pieces of information, the equations which describe the overall system flow can be implemented into MATLAB in a time iterating fashion to create a simple plume model using a stationary point source fire. Results from this model can be seen in Chapter 4.

CHAPTER 4
Plume Model Results

Using the methods described in Chapter 3 to numerically solve the equations derived in Chapter 2, results are obtained for an unforced plume, which represents a plume with no ambient air forcing, and a plume under the influence a constant crosswind in the ambient air. In both situations, hot air rises from a stationary point source fire and forms into a plume.

The shading of the plume is an indication of the density of the air, so the red represents a low density air, while the blue indicates air closer to the density of the ambient air system. The arrows present in the ambient air system are an indication of the flow in that region. As explained in Section 3.2.2, for now, random values are used at the stationary fire point to induce behavior seen in real fires. These random values induce a "puffing" and "curling" effect that propagates up from the fire point. When looking at the results, one will see both of these effects are prominent in the rising of the plume. As time progresses, it can be seen that some of the puffs pass through the top of the plume. It has been assumed that anything above the cutoff at the top of the plume is essentially well mixed air that has dissipated enough to be labeled ambient air.

The model is also used to track the energies present in the plume over time. The energy is visualized in the frequency domain to determine if the energy propagates at particular frequencies. The kinetic energy and enstrophy will be used, along with a frequency analysis to explore the power spectral density of the plume.

4.1 Unforced Plume

The simulation of an unforced plume shows a plume at different points in time, rising through ambient air, without the presence of ambient air forcing factors (i. e. wind). The simulation allows this unforced situation to be understood, and represents pure plume propagation. The flow in the ambient air system shows stagnation point behavior; the air is pulled in horizontally (most strongly around the

```
Error
                Velocity        Density         Temperature     Vorticity
del_s=2.000000  3.000464e+00    2.056374e+00    1.286080e+01    5.608752e-02

del_s=1.000000  1.454448e+00    4.956177e-01    8.398549e-01    2.530569e-02

del_s=0.500000  6.254961e-01    1.905474e-01    2.508221e-01    7.437515e-03

del_s=0.250000  2.880904e-01    7.626067e-02    8.940437e-02    5.262943e-03

Convergence
1.044714        2.052803        3.936696        1.148218
1.217399        1.379077        1.743475        1.766569
1.118479        1.321139        1.488248        0.498951
>>
```

Figure 4.1: Convergence Analysis of Numerical Scheme for Full Problem

fire point) and is then mixed into the plume as it rises. Due to the random values in the boundary conditions, each simulation is subtly different, but the overall behavior can be generalized by a single simulation as the random values only influence small variations.

A convergence analysis was conducted to determine the accuracy of the numerical scheme. Figure 4.1 verifies that the numerical scheme is convergent at first order speeds. All errors calculated in this convergence analysis are calculated in the L_2 norm. This convergence analysis indicates that if $\Delta s = 0.5$, the results are different from the "exact" solution by 0.2. This analysis was conducted for this simulation, and is assumed to be valid for all results presented in this thesis.

Figure 4.2 depicts a plume with a presence of puffs as seen in the solution at $t = 375$. As was stated above, the puffs rise and eventually pass through the top of the plume. Interestingly enough, it has been observed that the puffs move at different speeds and interact with one another. If a fast moving puff meets a slower moving puff, they interact by combining and moving at a new speed. The effect of the bending and puffing is random, so each time the simulation is run, the results look slightly different. Additionally, the time presented here on the title of the figures is scaled time.

As time progresses throughout the snapshots in Figure 4.2, one can see that the plume slightly bends back and forth due to the vorticity in the plume, and the interaction of the vorticity generated by the entrainment of air. This behavior is very similar to what was seen in the behavior of flags flapping in the wind [1].

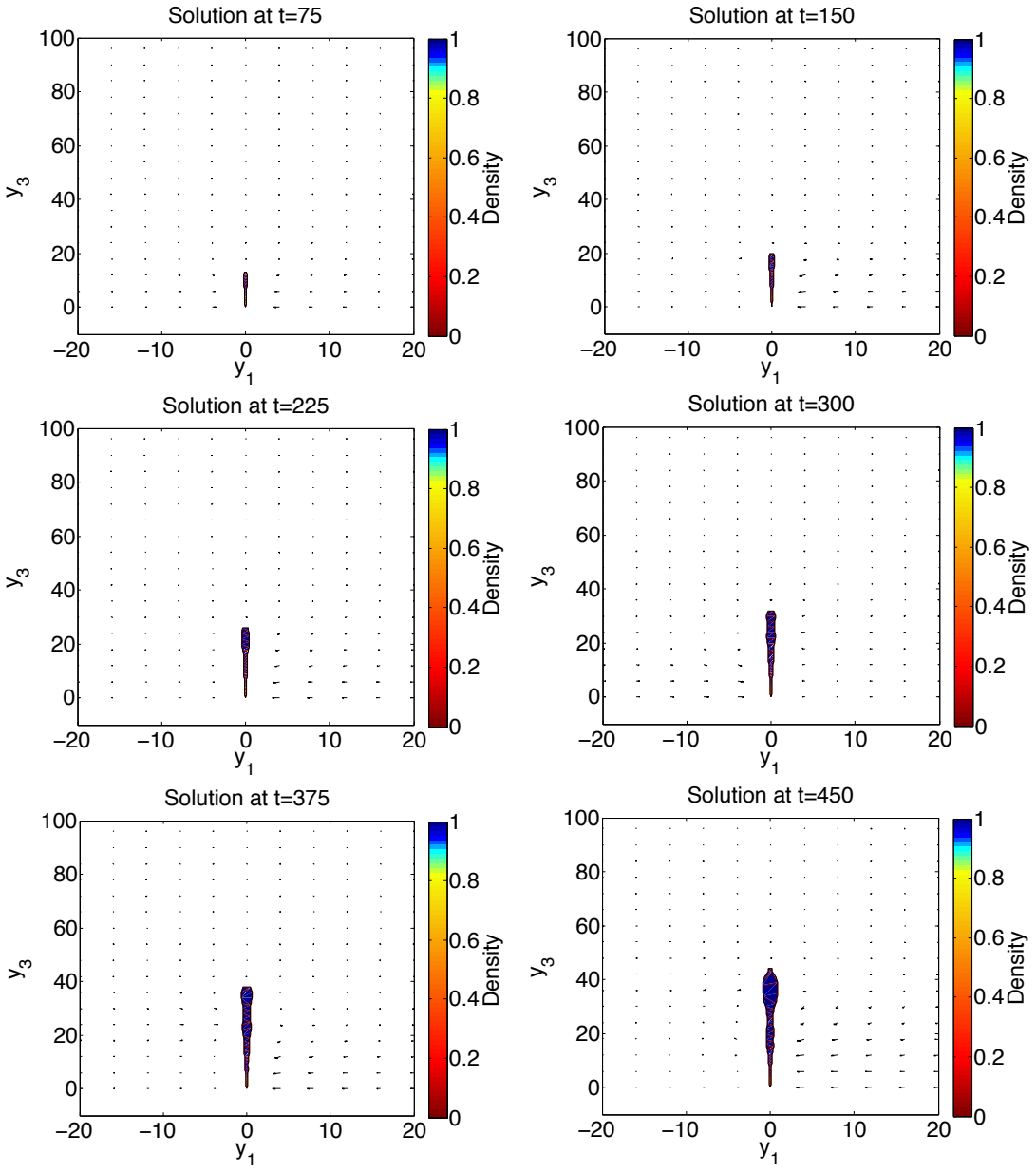

Figure 4.2: Numerical Solution for Unforced Plume

Since computation time is an interest of this work, the time it takes for the simulation to be generated has been tracked. It should be understood that computation times will vary greatly depending on the hardware of the computer used. Here, computation times averaged five minutes, where the time lapse from the beginning of the simulation to the end of the simulation was 450. Note, this number is scaled time. In true units of time, this represents 30 minutes of simulation time. As

previously stated, the computation time has been reduced to the order of minutes. More importantly, results can be obtained in sub-real-time.

4.2 Crosswind Influenced Plume

This section presents simulations depicting a plume that is subject to a constant crosswind. The case of a crosswind is considered in anticipation of a fire model that accounts for fire/plume interaction. The results in this section describe an air flow moving past and influencing the propagation of the fire plume created by a stationary fire. A simple change of reference can be used to turn this situation into a fire moving past stationary air, and thus allowing the fire to propagate. More information about this change of reference idea can be found in Chapter 6.

Figure 4.3 presents a simulation at different points in time. Again, the time in the title of the figures is a scaled quantity. The effects from the random values of velocity and vorticity prescribed at the point source fire are masked by the dominant crosswind that is identical in every simulation. The effects of puffing and bending can still be noticed, although this time the crosswind exerts significant influence on the behavior of the plume. For early times, the plume rises as it did in the unforced ambient air, but this time, as the the plume rises and develops, it gets caught in the crosswind and pulled with the ambient air flow. Buoyancy does play a significant role in the bending at the bottom of the plume near the fire. The hot air pulls the plume back to vertical. This force largely depends on the density of the air and the velocity at which the air rises. With random values of velocity and vorticity supplied at the fire, the plume also bends back and forth.

It is interesting to examine the flow in the ambient air as time progresses. The velocity induced by the point source fire and entrainment has a significant effect on what started as a crosswind flow. One can observe in Figure 4.3 at $t = 450$ that the arrows representing the flow in the ambient air system at the higher heights start to angle down towards the plume, indicating a strong entraining flow into the plume.

Again, the computation time of this simulation has been calculated. The time it takes to compute the crosswind flow models averages approximately five minutes. This time, the time lapse from the beginning of the simulation to the end

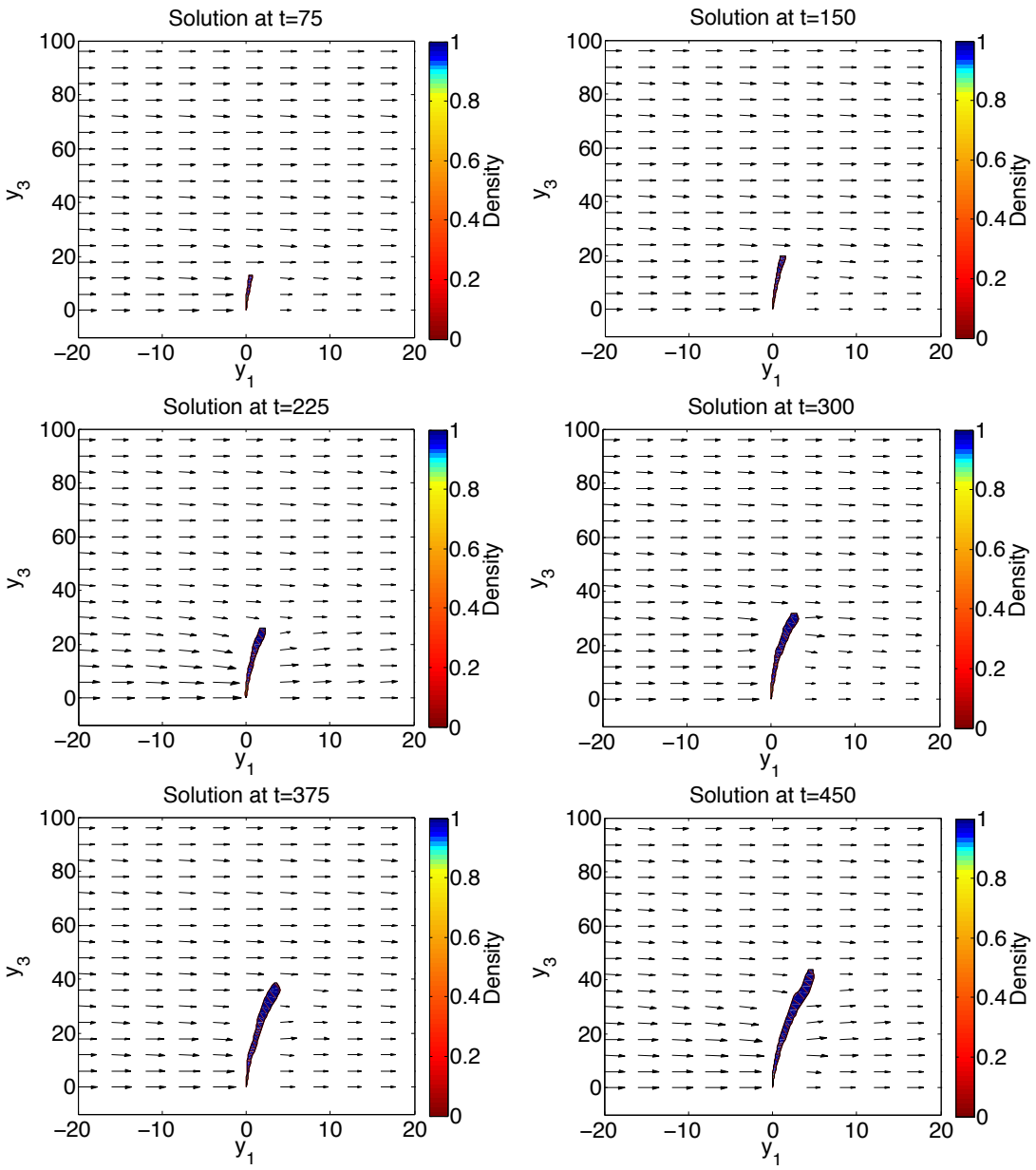

Figure 4.3: Numerical Solution for Crosswind Influenced Plume

of the simulation was 450 scaled units of time. In true units of time, this represents 30 minutes of simulation time. Again as previously stated, the computation time has been reduced to the order of minutes and the computation is still sub-real-time.

4.3 Frequency Analysis

The model from Chapters 2 and 3 shows that the "puffs" and "curls" in the plume appear to behave as waves as they propagate up through the plume. Following Alben and Shelley [1], a frequency analysis is performed to explore the energy spectrum of the system.

The frequency analysis is performed on two different energies present in the plume model: the kinetic energy due to the "puffing" nature of the fire, and the enstrophy due to the "curling" behavior. The fluctuations resulting in both of these features are due to induced fluctuations in velocity and vorticity at the point source fire. Since all values at the point source fire are prescribed, for now the effects of two different inputs are studied; the first is random behavior prescribed at the point source fire to simulate a real fire, while the second prescribes periodic forcing. Examination of the randomly forced system helps to understand the ability of the dynamics to respond to all frequencies, while study of periodic forcing can determine if harmonics are generated by non-linear interactions in the system.

The frequency analysis is performed at this point to determine how the energies propagate through the system under prescribed boundary conditions. In Chapter 6, the same frequency analysis will be performed. However, in Chapter 6 fire dynamics will be calculated making this analysis more interesting and revealing about the way in which energy propagates from a fire.

4.3.1 Kinetic Energy

A standard definition of kinetic energy will be used for this application. The kinetic energy density is defined as:

$$KE(s,\tau) = \frac{1}{2}R(s,\tau)b(s,\tau)|V(s,\tau)|^2. \tag{4.3.1}$$

One will note that as written above, the kinetic energy is a function of both time and space. To obtain the total kinetic energy contained within the plume,

(4.3.1) is integrated over the plume at a specific time:

$$KE(\tau) = \int_0^{\text{plume top}} \frac{1}{2} R(s,\tau) b(s,\tau) |V(s,\tau)|^2 \, \mathrm{d}s, \tag{4.3.2}$$

which is now understood to be only a function of time.

4.3.2 Enstrophy

Similar to the kinetic energy, the enstrophy density is defined as:

$$\varepsilon(s,\tau) = \frac{1}{2} R(s,\tau) b(s,\tau) |\Omega(s,\tau)|^2. \tag{4.3.3}$$

Again to obtain the total enstrophy contained within the plume, (4.3.3) is integrated over the plume:

$$\varepsilon(\tau) = \int_0^{\text{plume top}} \frac{1}{2} R(s,\tau) b(s,\tau) |\Omega(s,\tau)|^2 \, \mathrm{d}s, \tag{4.3.4}$$

which is now understood to be only a function of time.

4.3.3 The Fourier Transform

From these definitions, the Fourier transform can be used to examine the frequency make-up of the kinetic energy and enstrophy in frequency space. Although it seems trivial, the definition of the Fourier transform that will be used in this analysis should be specified since there are many definitions. The following definition is used:

$$\mathcal{F}(\omega) = \int_{-\infty}^{\infty} f(\tau) e^{-2\pi i \tau \omega} \, \mathrm{d}\tau. \tag{4.3.5}$$

Numerically, there are several options that are available for performing this transform and multiple approximations were considered. MATLAB has a built in fast Fourier transform function, a discrete fast Fourier transform could be used, or a simple approximation of (4.3.5) can be used. Here, the latter will be used, such that:

$$\mathcal{F}(\omega) = \int_0^{T_\mathrm{f}} f(\tau) e^{-2\pi i \tau \omega} \, \mathrm{d}\tau$$

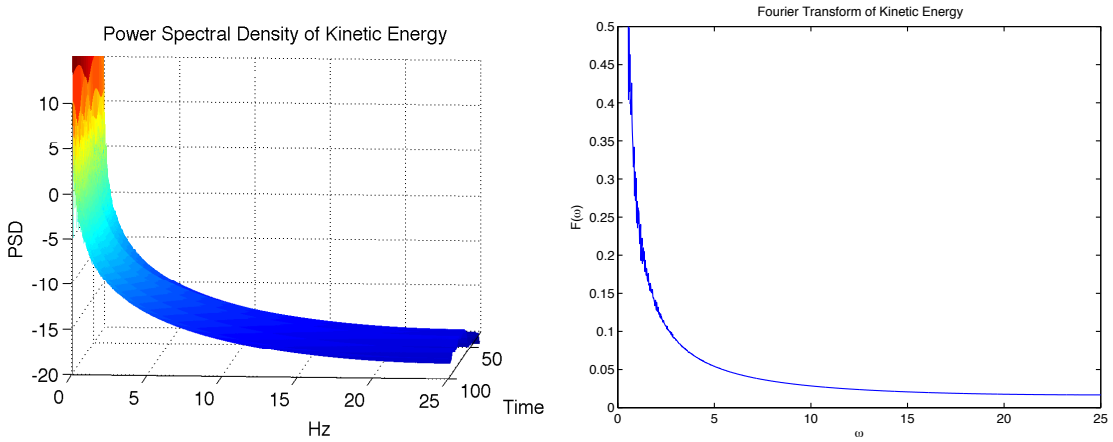

(a) Spectrogram **(b) Fourier Transform at t_f**

Figure 4.4: Fourier Transform of Kinetic Energy for Random Values

$$\begin{aligned}\mathcal{F}(\omega_k) &\approx \sum_{j=1}^{T_\mathrm{f}} f(\tau_j) e^{-2\pi i \tau_j \omega_k}\, \Delta\tau \\ &= \sum_{j=1}^{T_\mathrm{f}} f(\tau_j) e^{-2\pi i (j-1) \omega_k}\, \Delta\tau, \end{aligned} \tag{4.3.6}$$

where the reduction of the bounds on the integral is due to the fact that for $\tau > T_\mathrm{f}$, $f(\tau) = 0$ and the solution is not defined for negative time.

MATLAB's short-time Fourier transform was used to verify the results obtained by the simple numerical approximation, (4.3.6). The two methods were shown to be equivalent, but this verification will not be presented here. Thus, the simple numerical approximation (4.3.6) will be used. Similar to MATLAB's built in function, the Fourier transform data will be turned into a spectrogram, displaying a three-dimensional surface representing the power spectral density of the kinetic energy and enstrophy.

4.3.4 Random Fire Values

As stated in Section 3.2.2, random values for the velocity and vorticity inside the plume are prescribed at the fire point to simulate the way in which a fire "curls" and "puffs," as seen in naturally occurring fires.

The power spectral density of the kinetic energy and enstrophy are shown in

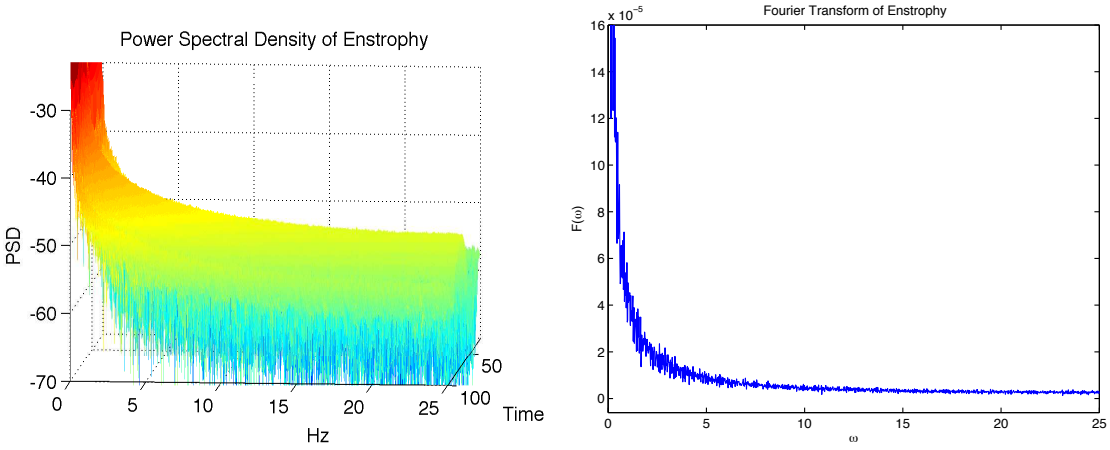

(a) Spectrogram **(b) Fourier Transform at t_f**

Figure 4.5: Fourier Transform of Enstrophy for Random Values

Figures 4.4 and 4.5 for random values of velocity and vorticity prescribed at the fire point. As one might expect, Figures 4.4 and 4.5 show that there is a frequency response on all frequencies, suggesting no clear frequency make-up of the random values in each of the energies. It should be noted that Figures 4.4a and 4.5a are the power spectral densities at various times and frequencies. Figure 4.4b and 4.5b are the Fourier transforms at the final time, and represents a (nearly) steady behavior. It can also be seen that the enstrophy responds more to the randomness than the kinetic energy does, which is also seen in Section 4.3.5.2.

It should be noted that the lack of random frequency dependence in kinetic energy at high frequencies is due to the small random fluctuations in the velocity. Had larger fluctuations been used in the velocity at the fire point, the same random behavior would be exhibited in the spectrogram and Fourier transform. Upon observation of the lower frequencies, the random response can be observed.

4.3.5 Harmonic Fire Values

The behavior of the model with periodic forcing is of interest to examine whether the frequency at which the periodic harmonic function oscillates is attenuated or amplified. This problem will be split into two separate cases, the first of which investigates a pure harmonic signal, and the second will add in the randomness of noise that was seen in section 4.3.4.

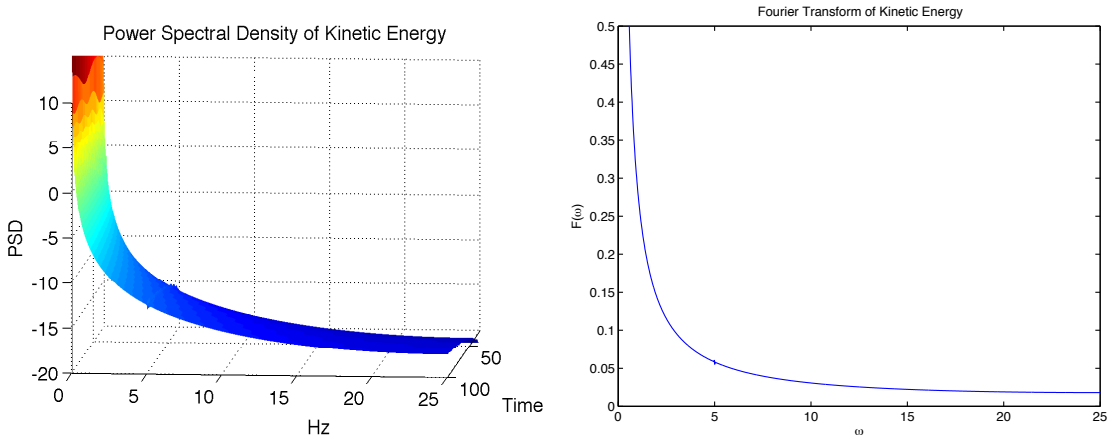

(a) Spectrogram **(b) Fourier Transform at t_f**

Figure 4.6: Fourier Transform of Kinetic Energy for Harmonic Forcing, $\chi = 5$ and $\bar{\chi} = 10$

4.3.5.1 Sinusoidal Forcing With No Noise

A simple sinusoidal forcing at a fixed frequency for both the velocity and vorticity is prescribed at the fire point in place of random values. This forcing is taken to be:

$$V(0,\tau) = 0.2 + \frac{1}{10}\sin(2\pi\chi\tau) = 0.2 + \frac{1}{10}\sin(2\pi\chi t\Delta\tau) \tag{4.3.7}$$

$$\Omega(0,\tau) = \frac{1}{4}\sin(2\pi\bar{\chi}\tau) = \frac{1}{4}\sin(2\pi\bar{\chi}t\Delta\tau), \tag{4.3.8}$$

where $0 \leq \chi \leq 20$, $0 \leq \bar{\chi} \leq 20$, and $\chi < \bar{\chi}$. Here, χ and $\bar{\chi}$ are the frequency of the harmonic functions for V and Ω respectively.

With a periodic harmonic function at a single frequency, one might expect the ability to recover the known frequency make-up after simulation and taking the Fourier transform. However, as seen in Figure 4.7, this is not the case. The single frequency prescribed to vorticity has been split into many harmonic frequencies and translated from the original input frequency in enstrophy. In contrast, it is easily seen that in Figure 4.6 the original input frequency of velocity is recovered.

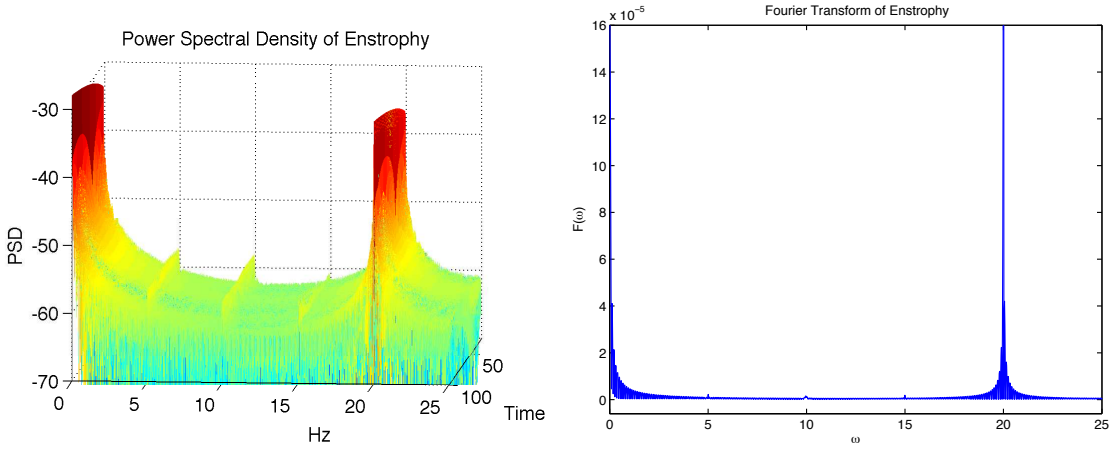

(a) Spectrogram **(b) Fourier Transform at t_f**

Figure 4.7: Fourier Transform of Enstrophy for Harmonic Forcing, $\chi = 5$ and $\bar{\chi} = 10$

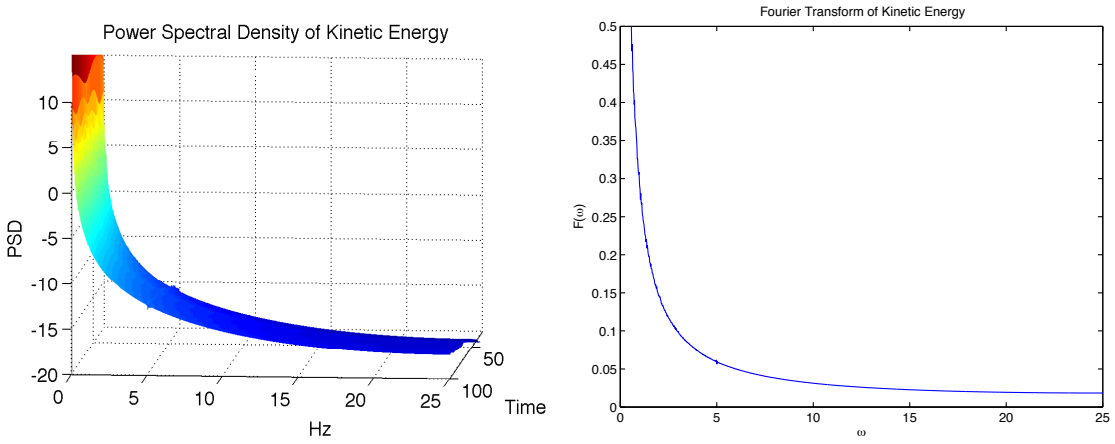

(a) Spectrogram **(b) Fourier Transform**

Figure 4.8: Fourier Transform of Kinetic Energy for Harmonic Forcing With Noise, $\chi = 5$ and $\bar{\chi} = 10$

4.3.5.2 Noise

To reintroduce the prescribed fire behavior, two different kinds of random noise are added to the above harmonic functions. The first is a constant small amplitude random noise that is added to the signal at every time step, whereas the second is the randomness that adds the "curling" and "puffing" effects of the fire and is similar to what is used in Section 4.3.4. The random values are normally distributed, chosen such that the velocity is always positive, and updated at random time intervals.

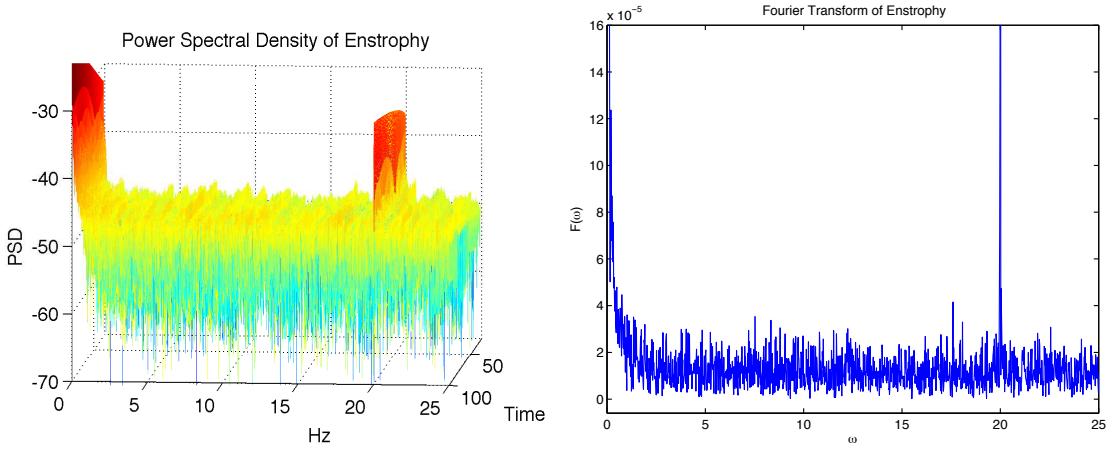

(a) Spectrogram **(b) Fourier Transform**

Figure 4.9: Fourier Transform of Enstrophy for Harmonic Forcing With Noise, $\chi = 5$ and $\bar{\chi} = 10$

Figures 4.8 and 4.9 show the results. As one might expect, the effects from Sections 4.3.4 and 4.3.5.1 appear to be superposed. As was mentioned earlier, the random values (noise) affects the enstrophy more prominently and this is clearly seen in Figure 4.9. The effect of the random forcing is less prominent in the kinetic energy, although it is still noticeable. One can see that some of the imposed frequency spikes are still prominent in both plots, showing that information regarding the signal can still be recovered.

4.4 Conclusions

Use of the simplified model developed in Chapters 2 and 3 results in realistic dynamics for the interaction of the plume with the ambient atmosphere, and is much faster and simpler than a CFD type code which uses DNS or LES to simulate the dynamics of a plume. The computation time needed to run this simplified model is on the order of minutes, while some of the larger more detailed CFD models run on the order of days and weeks. This shows that although the simplified model is not as detailed, the model captures behavior that may be useful in situations where predictive data is needed in real time.

Several structures and behaviors summarized in these chapters suggest that the ideas from a flag flapping in the wind can be adapted to the paradigm of a

plume rising in ambient air. The simulation of such behavior results in a physical structure of the plume rising. When the snapshots of any of the results are stitched together into a movie, the resulting simulation truly appears to be a plume rising from a point source fire, almost like watching smoke rise from a candle.

The wave-like behavior observed in both the flag waving and the puffing of the plume prompted a study of the frequency make-up of the kinetic energy and enstrophy, which was used to track both of these physical phenomena respectively. The situation studied here, specifically the interaction of the ambient air/plume systems does not result in the emergence of periodic dependency on propagation, damping, or amplification of the frequency from a harmonic function prescribed at the fire point. This analysis suggests that the wave-like behavior is chaotic in nature.

The random forcing of the velocity and enstrophy used to simulate the "curling" and "puffing" of the fire did not result in an amplification of any particular frequencies. Instead, the random values are propagated as noise, just as one would see in signal processing without a resonant frequency. Additionally, when a pure signal was used as the forcing for velocity and vorticity at the fire point, translations and splitting of the frequencies were observed and attributed to the effects of the non-linear system.

Also, as expected, when random values were superposed on the pure signal, the results from the random test and the pure signal test appear to be superposed and the random values were perceived as noise. It is noted that enstrophy was more susceptible to the random noise. This can be explained by the fact that the magnitude of the enstrophy is very small compared to that of the kinetic energy, or even the noise.

The basic framework and a working model for atmospheric scale fire/flow interaction have been provided here. A fire model has been developed, see Chapter 5, to couple to this plume model. Up to this point, fire properties are prescribed at a stationary point source. A fire model based on combustion equations will allow the fire to propagate through a homogeneous fuel bed. This fire model will allow the calculation of spread rates, and most importantly allow the coupling of the information from the fire model to the plume model. With this, the plume model

will have the added data from modeled fire dynamics, which will make the results more physical and accurate.

CHAPTER 5
Fire Model Derivation

Results up to this point have been obtained while prescribing boundary conditions to the point source fire to simulate fire behavior. In this chapter, a fire model is derived, not only to calculate fire dynamics to use at the point source fire in the plume model, but also to allow the fire to participate in the dynamical processes as more than a prescribed point source. This simple fire model allows the calculation of the fire propagation rate, the velocity of the rising air from the fire, the temperature and density of the fire, etc.

With the addition of the fire dynamics to the model, several more aspects of the problem can be investigated. A frequency analysis will again be performed and compared to the results already obtained to determine if there are any characteristic frequencies at which the disturbances propagate. The results will also determine if the fire behaves as prescribed random values at the fire point, or as the harmonic forcing.

The fire in this model is assumed to burn due of a thin layer of homogeneous fuel on the ground underneath the fire plume. As stated in Section 1.4 there are four regions that need to be considered in this model, see Figure 1.2. The green region is the unburned fuel region, the orange is the pyrolyzing region, the red is the fire region, and the gray is the smoldering region. Physically, the fire radiates heat that converts solid fuel to gaseous fuel, where eventually the gas fuel burns. In this work, the formulation of the problem is simplified even further and only a fire region will be considered. This can be seen in Figure 5.1, where the fire is represented as a control volume.

It will be noted that this simplified fire model will neglect the effects of heat transfer from the fire. The fire propagation speed will be relative to the amount of oxygen supplied to the fire. Here, an implicit assumption has been made that the more oxygen that supplies the fire, the faster the reaction rate of combustion, and the faster the fire consumes the fuel. Thus, the fire has to propagate faster through

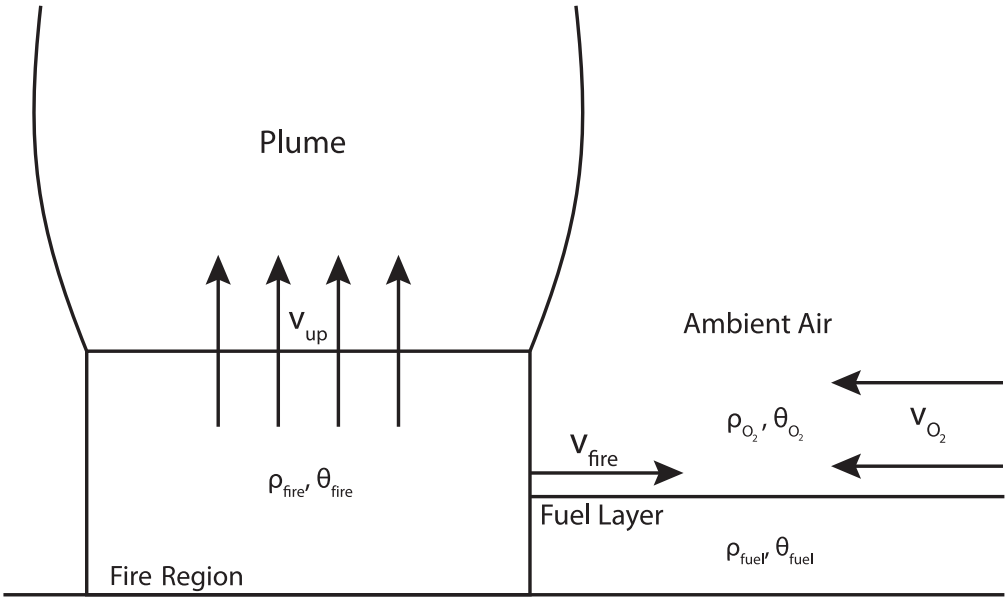

Figure 5.1: Control Volume for Fire Region

the fuel.

5.1 Conservation Laws

Since the fire is allowed to propagate, the control volume has a velocity in the y_1 direction, v_{fire}. The thin layer of fuel of constant height can be seen on the ground under a flow of oxygen, with velocity v_{O_2}, supplying the fire. As the fire burns, the buoyant air rises, with velocity v_{up}, and forms into the fire plume. The geometry from Figure 5.1 is used in conjunction with a simplified chemical equation:

$$\text{fuel} + O_2 \xrightarrow{\Re} \text{by-products} + \text{heat},$$

which describes the complex reactions that take place during combustion and a control volume derivation (similar to the approach from Appendix A) to obtain conservation laws for the fire system.

5.1.1 Total Density Equation

Let ρ_{fire} be the mass density in the fire, the width of the fire is b, and the height of the fire region is h. Just as in the plume model, Δy_2 is the x_2 direction, into the page. This mass density will include the fuel density, the density of the oxygen, and the density of the by-products. The mass in the control volume is easily written as:

$$\Delta y_2 \int_0^b \int_0^h \rho_{\text{fire}} \, \mathrm{d}y_3 \mathrm{d}y_1.$$

Thus, the rate of change of mass is equal to the density flux entering the control volume minus the density flux exiting the control volume:

$$\Delta y_2 \frac{\partial}{\partial \tau} \int_0^b \int_0^h \rho_{\text{fire}} \, \mathrm{d}y_3 \mathrm{d}y_1 = \Delta y_2 \int_0^h (v_{\text{fire}} \rho_{\text{fuel}}) \Big|_{y_1=b} + (v_{O_2} \rho_{O_2}) \Big|_{y_1=b} \mathrm{d}y_3 - \Delta y_2 \int_0^b (v_{\text{up}} \rho_{\text{fire}}) \Big|_{y_3=h} \mathrm{d}y_1. \quad (5.1.1)$$

It should be noted that v_{fire} represents the speed at which the fire propagates and is really composed of two separate terms, such that $v_{\text{fire}} = v_{\text{CV}} + \frac{\partial b}{\partial \tau}$. Here the first term represents the speed at which the control volume is moving, and the second represents the speed at which the control volume expands.

Dropping the common Δy_2 and additionally assuming all quantities on the boundary are constant across their respective edges, $\rho_{\text{fire}} = \rho_{\text{fire}}(\tau)$, and $h = h(\tau)$, (5.1.1) reduces to:

$$\frac{\partial}{\partial \tau} (\rho_{\text{fire}} b h) = (v_{\text{fire}} \rho_{\text{fuel}}) \Big|_{y_1=b} h + (v_{O_2} \rho_{O_2}) \Big|_{y_1=b} h - (v_{\text{up}} \rho_{\text{fire}}) \Big|_{y_3=h} b.$$

If it is additionally assumed $h =$ constant, the conservation law becomes:

$$\frac{\partial}{\partial \tau} (\rho_{\text{fire}} b) = \left(v_{\text{CV}} + \frac{\partial b}{\partial \tau} \right) \rho_{\text{fuel}} \Big|_{y_1=b} + (v_{O_2} \rho_{O_2}) \Big|_{y_1=b} - (v_{\text{up}} \rho_{\text{fire}}) \Big|_{y_3=h} \frac{b}{h}. \quad (5.1.2)$$

Physically, the right-hand side represents the amount of fuel added to the control volume do to the control volume moving and expanding, the influx of oxygen due to induced flow, and the loss of mass due to the rising hot air.

5.1.2 Fuel Density Equation

Let ρ_{fuel} be the fuel density. Following the same procedure as in Section 5.1.1, the fuel mass in the control volume is written as:

$$\Delta y_2 \int_0^b \int_0^h \rho_{\text{fuel}} \, \mathrm{d}y_3 \mathrm{d}y_1.$$

The conservation equation for the fuel density is easily written:

$$\Delta y_2 \frac{\partial}{\partial \tau} \int_0^b \int_0^h \rho_{\text{fuel}} \, \mathrm{d}y_3 \mathrm{d}y_1 = \Delta y_2 \int_0^h \left((v_{\text{fire}} \rho_{\text{fuel}}) \Big|_{y_1=b} - \int_0^b \Re \, \mathrm{d}y_1 \right) \mathrm{d}y_3, \tag{5.1.3}$$

where $\Re$ represents the reaction rate of combustion and will be defined later in this work. Again, dropping the common Δy_2 and noting all quantities on the boundary are constant across their respective edges, $\rho_{\text{fuel}} = \rho_{\text{fuel}}(\tau)$, $h = h(\tau)$, and the reaction rate is constant throughout the control volume, (5.1.3) reduces to:

$$\frac{\partial}{\partial \tau} \left(\rho_{\text{fuel}} b h \right) = (v_{\text{fire}} \rho_{\text{fuel}}) \Big|_{y_1=b} h - b h \Re.$$

When $h =$ constant is applied, the conservation law becomes:

$$\frac{\partial}{\partial \tau} \left(\rho_{\text{fuel}} b \right) = \left(v_{\text{CV}} + \frac{\partial b}{\partial \tau} \right) \rho_{\text{fuel}} \Big|_{y_1=b} - b \Re. \tag{5.1.4}$$

The right-hand side of this conservation equation physically states that fuel density is increased as the fire propagates and decreases due to the consumption of combustion.

5.1.3 Oxygen Density Equation

Let ρ_{O_2} be the oxygen density. Similarly, the oxygen mass in the control volume is written as:

$$\Delta y_2 \int_0^b \int_0^h \rho_{O_2} \, \mathrm{d}y_3 \mathrm{d}y_1,$$

and the conservation equation for the oxygen density is written:

$$\Delta y_2 \frac{\partial}{\partial \tau} \int_0^b \int_0^h \rho_{O_2} \, \mathrm{d}y_3 \mathrm{d}y_1 = \Delta y_2 \int_0^h \left((v_{O_2} \rho_{O_2}) \Big|_{y_1=b} - \int_0^b \Re \, \mathrm{d}y_1 \right) \mathrm{d}y_3. \tag{5.1.5}$$

Again, noting all quantities on the boundary are constant across their respective edges, $\rho_{O_2} = \rho_{O_2}(\tau)$, $h = h(\tau)$, and the reaction rate is constant throughout the control volume, (5.1.5) reduces to:

$$\frac{\partial}{\partial \tau}\left(\rho_{O_2} bh\right) = \left(v_{O_2}\rho_{O_2}\right)\Big|_{y_1=b} h - bh\Re.$$

If it is additionally taken that $h =$ constant, the conservation law becomes:

$$\frac{\partial}{\partial \tau}\left(\rho_{O_2} b\right) = \left(v_{O_2}\rho_{O_2}\right)\Big|_{y_1=b} - b\Re. \tag{5.1.6}$$

Just as in the fuel density equation, the right-hand side physically states that oxygen density increases as the flow of oxygen increases and the oxygen density decreases due to the consumption of combustion.

5.1.4 By-Product Density Equation

Let ρ_{by} represent the by-product density. The by-product mass in the control volume is written as:

$$\Delta y_2 \int_0^b \int_0^h \rho_{\text{by}}\, \mathrm{d}y_3 \mathrm{d}y_1,$$

and the conservation equation for the by-product density is written:

$$\Delta y_2 \frac{\partial}{\partial \tau} \int_0^b \int_0^h \rho_{\text{by}}\, \mathrm{d}y_3 \mathrm{d}y_1 = \Delta y_2 \int_0^b \left(- \left(v_{\text{up}}\rho_{\text{fire}}\right)\Big|_{y_1=h} + \int_0^h \Re\, \mathrm{d}y_3 \right) \mathrm{d}y_1.$$

Again, noting all quantities on the boundary are constant across their respective edges, $\rho_{\text{by}} = \rho_{\text{by}}(\tau)$, $h = h(\tau)$, and the reaction rate is constant throughout the control volume, this reduces to:

$$\frac{\partial}{\partial \tau}\left(\rho_{\text{by}} bh\right) = -\left(v_{\text{up}}\rho_{\text{fire}}\right)\Big|_{y_1=h} b + bh\Re.$$

Additionally, using $h =$ constant, the conservation law becomes:

$$\frac{\partial}{\partial \tau}\left(\rho_{\text{by}} b\right) = -\left(v_{\text{up}}\rho_{\text{fire}}\right)\Big|_{y_1=h} \frac{b}{h} + b\Re. \tag{5.1.7}$$

Here, the equation states that the density of by-products increases with the reaction rate of combustion, and decreases due to the buoyant air rising to form the fire plume.

5.1.5 Energy Density Equation

Let $\rho_{\text{fire}}\theta C_p$ be the total energy density in the fire, where θ is the temperature of the fire, and C_p is the specific heat at constant pressure. The energy is written as:

$$\Delta y_2 \int_0^b \int_0^h \rho_{\text{fire}}\theta C_p \, \mathrm{d}y_3 \mathrm{d}y_1.$$

Thus, the rate of change of energy is equal to the energy density flux entering the control volume minus the energy density flux exiting the control volume:

$$\begin{aligned}\Delta y_2 \frac{\partial}{\partial \tau} \int_0^b \int_0^h \rho_{\text{fire}}\theta C_p \, \mathrm{d}y_3 \mathrm{d}y_1 = \Delta y_2 \int_0^h (v_{\text{fire}}\rho_{\text{fuel}}\theta_{\text{fuel}}C_{p\,\text{fuel}}) \Big|_{y_1=b} \mathrm{d}y_3 \\ + \Delta y_2 \int_0^h \left((v_{O_2}\rho_{O_2}\theta_{O_2}C_{p\,O_2}) \Big|_{y_1=b} + \int_0^b \Re\Delta_h \, \mathrm{d}y_1 \right) \mathrm{d}y_3 \\ - \Delta y_2 \int_0^b (v_{\text{up}}\rho_{\text{fire}}\theta C_p) \Big|_{y_3=h} \mathrm{d}y_1.\end{aligned}$$

Additionally assuming all quantities on the boundary are constant across their respective edges, $\theta = \theta(\tau)$, $C_p = C_p(\tau)$, and $h = h(\tau)$, this reduces to:

$$\begin{aligned}\frac{\partial}{\partial \tau} (\rho_{\text{fire}}\theta C_p b h) = (v_{\text{fire}}\rho_{\text{fuel}}\theta_{\text{fuel}}C_{p\,\text{fuel}}) \Big|_{y_1=b} h + (v_{O_2}\rho_{O_2}\theta_{O_2}C_{p\,O_2}) \Big|_{y_1=b} h \\ - (v_{\text{up}}\rho_{\text{fire}}\theta C_p) \Big|_{y_3=h} b + bh\Re\Delta_h.\end{aligned}$$

Again, using the fact that $h = \text{constant}$, the conservation law becomes:

$$\begin{aligned}\frac{\partial}{\partial \tau} (\rho_{\text{fire}}\theta C_p b) = (v_{\text{fire}}\rho_{\text{fuel}}\theta_{\text{fuel}}C_{p\,\text{fuel}}) \Big|_{y_1=b} + (v_{O_2}\rho_{O_2}\theta_{O_2}C_{p\,O_2}) \Big|_{y_1=b} \\ - (v_{\text{up}}\rho_{\text{fire}}\theta C_p) \Big|_{y_3=h} \frac{b}{h} + b\Re\Delta_h\end{aligned}$$

$$\frac{\partial}{\partial \tau} (\rho_{\text{fire}}\theta C_p b) = \left(\left(v_{\text{CV}} + \frac{\partial b}{\partial \tau} \right) \rho_{\text{fuel}}\theta_{\text{fuel}}C_{p\,\text{fuel}} \right) \Big|_{y_1=b} + (v_{O_2}\rho_{O_2}\theta_{O_2}C_{p\,O_2}) \Big|_{y_1=b}$$

$$- \left(v_{\text{up}}\rho_{\text{fire}}\theta C_p\right)\Big|_{y_3=h}\frac{b}{h} + b\Re\Delta_h. \quad (5.1.8)$$

Physically this conservation of energy equation states that the energy density increases due to the addition of fuel, oxygen, and the exothermic combustion reaction, but decreases due to the hot buoyant air rising to form a fire plume.

Using the total density equation to simplify, this becomes:

$$\frac{\partial}{\partial\tau}\left(\theta C_p\right) = \frac{\left(v_{\text{CV}} + \frac{\partial b}{\partial\tau}\right)\rho_{\text{fuel}}}{\rho_{\text{fire}}b}\left(\theta_{\text{fuel}}C_{p\,\text{fuel}} - \theta C_p\right)\Big|_{y_1=b} + \frac{v_{O_2}\rho_{O_2}}{\rho_{\text{fire}}b}\left(\theta_{O_2}C_{p\,O_2} - \theta C_p\right)\Big|_{y_1=b} + \frac{\Re}{\rho_{\text{fire}}}\Delta_h. \quad (5.1.9)$$

5.1.6 Final Form Conservation Laws

With these derivations, the simplified chemical equation:

$$A(\text{fuel}) + B(O_2) \xrightarrow{k_1} C(\text{by-products}) + D(\text{heat}),$$

which now allows for the stoichiometric constants to be different, and $\Re = k_1(\theta)\rho^A_{\text{fuel}}\rho^B_{O_2}$, the system of conservation laws becomes:

$$\frac{\partial}{\partial\tau}\left(\rho_{\text{fire}}b\right) = \left(v_{\text{fire}}\rho_{\text{fuel}}\right)\Big|_{y_1=b} + \left(v_{O_2}\rho_{O_2}\right)\Big|_{y_1=b} - \left(v_{\text{up}}\rho_{\text{fire}}\right)\Big|_{y_3=h}\frac{b}{h} \quad (5.1.10)$$

$$\frac{\partial}{\partial\tau}\left(\rho_{\text{fuel}}b\right) = \left(v_{\text{fire}}\rho_{\text{fuel}}\right)\Big|_{y_1=b} - Abk_1(\theta)\rho^A_{\text{fuel}}\rho^B_{O_2} \quad (5.1.11)$$

$$\frac{\partial}{\partial\tau}\left(\rho_{O_2}b\right) = \left(v_{O_2}\rho_{O_2}\right)\Big|_{y_1=b} - Bbk_1(\theta)\rho^A_{\text{fuel}}\rho^B_{O_2} \quad (5.1.12)$$

$$\frac{\partial}{\partial\tau}\left(\theta C_p\right) = \frac{v_{\text{fire}}\rho_{\text{fuel}}}{\rho_{\text{fire}}b}\left(\theta_{\text{fuel}}C_{p\,\text{fuel}} - \theta C_p\right)\Big|_{y_1=b} + \frac{v_{O_2}\rho_{O_2}}{\rho_{\text{fire}}b}\left(\theta_{O_2}C_{p\,O_2} - \theta C_p\right)\Big|_{y_1=b} + D\frac{k_1(\theta)}{\rho_{\text{fire}}}\rho^A_{\text{fuel}}\rho^B_{O_2}\Delta_h. \quad (5.1.13)$$

The reaction rate $\Re$ was approximated using the simplified chemical equation and a law of mass action derivation. It will be noted that while $v_{\text{fire}} = v_{\text{CV}} + \frac{\partial b}{\partial\tau}$, the velocity of the fire will be written as v_{fire} from here on, with the understanding that the velocity is comprised of multiple parts.

5.2 Non-Dimensional Form

The conservation laws above are still in dimensional form. In order to couple the fire model to the plume model, the scalings of the variables must be the same. To do this, all variables are non-dimensionalized, just as they were in the plume model. Once in non-dimensional form, the equations can be solved and implemented.

Let $\tilde{\rho}_\star = \frac{\rho_\star}{\rho_0}$, $\tilde{\theta}_\star = \frac{\theta_\star}{\theta_0}$, $\tilde{b} = \frac{b}{l_1}$, $\tilde{v}_\star = \frac{v_\star}{v_0}$, $\tilde{h} = \frac{h}{l_3}$, $\tilde{\tau} = \tau\frac{v_0}{l_1}$, $\tilde{C}_{p\star} = \frac{C_{p\star}}{C_{p\,\mathrm{air}}}$, $\tilde{\Delta}_h = \frac{\Delta_h}{\theta_0 C_{p\,\mathrm{air}}}$, where it is understood that $\tilde{\star}$ denotes a dimensionless variable. Substituting these rescaling into the equations and dropping unnecessary dimensionless notation, one obtains the following equations:

$$\frac{\partial}{\partial\tau}\left(\rho_{\mathrm{fire}}b\right) = \left(v_{\mathrm{fire}}\rho_{\mathrm{fuel}}\right)\Big|_{y_1=b} + \left(v_{O_2}\rho_{O_2}\right)\Big|_{y_1=b} - \frac{l_1}{l_3}\left(v_{\mathrm{up}}\rho_{\mathrm{fire}}\right)\Big|_{y_3=h}\frac{b}{h} \tag{5.2.1}$$

$$\frac{\partial}{\partial\tau}\left(\rho_{\mathrm{fuel}}b\right) = \left(v_{\mathrm{fire}}\rho_{\mathrm{fuel}}\right)\Big|_{y_1=b} - \frac{l_1}{v_0}\rho_0^{A+B-1}Abk_1(\theta)\rho_{\mathrm{fuel}}^A\rho_{O_2}^B \tag{5.2.2}$$

$$\frac{\partial}{\partial\tau}\left(\rho_{O_2}b\right) = \left(v_{O_2}\rho_{O_2}\right)\Big|_{y_1=b} - \frac{l_1}{v_0}\rho_0^{A+B-1}Bbk_1(\theta)\rho_{\mathrm{fuel}}^A\rho_{O_2}^B \tag{5.2.3}$$

$$\begin{aligned}\frac{\partial}{\partial\tau}\left(\theta C_p\right) = {} & \frac{v_{\mathrm{fire}}\rho_{\mathrm{fuel}}}{\rho_{\mathrm{fire}}b}\left(\theta_{\mathrm{fuel}}C_{p\,\mathrm{fuel}} - \theta C_p\right)\Big|_{y_1=b} + \frac{v_{O_2}\rho_{O_2}}{\rho_{\mathrm{fire}}b}\left(\theta_{O_2}C_{p\,O_2} - \theta C_p\right)\Big|_{y_1=b} \\ & + \frac{l_1}{v_0}\rho_0^{A+B-1}D\frac{k_1(\theta)}{\rho_{\mathrm{fire}}}\rho_{\mathrm{fuel}}^A\rho_{O_2}^B\tilde{\Delta}_h.\end{aligned} \tag{5.2.4}$$

5.2.1 Quasi-Steady State Assumption

The three-dimensional paradigm in Chapter 2 states that the fire line is well defined and nearly straight. Such a situation could be though of as a steady state or equilibrium state and is achieved after the fire has become well developed while propagating through the homogeneous fuel bed. Thus, a quasi-steady state assumption is made for the conservation laws. A quasi-steady state assumption exploits the fact that the fire propagates for a long time, and once this equilibrium has been achieved, there are small variations of the dependent variables in time.

Using the quasi-steady state assumption of small variations for long times, the ODEs in time can be reduced to algebraic equations:

$$0 = \left(v_{\mathrm{fire}}\rho_{\mathrm{fuel}}\right)\Big|_{y_1=b} + \left(v_{O_2}\rho_{O_2}\right)\Big|_{y_1=b} - \frac{l_1}{l_3}\left(v_{\mathrm{up}}\rho_{\mathrm{fire}}\right)\Big|_{y_3=h}\frac{b}{h} \tag{5.2.5}$$

$$0 = (v_{\text{fire}}\rho_{\text{fuel}})\Big|_{y_1=b} - \frac{l_1}{v_0}\rho_0^{A+B-1}Abk_1(\theta)\rho_{\text{fuel}}^A\rho_{O_2}^B \tag{5.2.6}$$

$$0 = (v_{O_2}\rho_{O_2})\Big|_{y_1=b} - \frac{l_1}{v_0}\rho_0^{A+B-1}Bbk_1(\theta)\rho_{\text{fuel}}^A\rho_{O_2}^B \tag{5.2.7}$$

$$\begin{aligned} 0 = {} & \frac{v_{\text{fire}}\rho_{\text{fuel}}}{\rho_{\text{fire}}b}\left(\theta_{\text{fuel}}C_{p\,\text{fuel}} - \theta C_p\right)\Big|_{y_1=b} + \frac{v_{O_2}\rho_{O_2}}{\rho_{\text{fire}}b}\left(\theta_{O_2}C_{p\,O_2} - \theta C_p\right)\Big|_{y_1=b} \\ & + \frac{l_1}{v_0}\rho_0^{A+B-1}D\frac{k_1(\theta)}{\rho_{\text{fire}}}\rho_{\text{fuel}}^A\rho_{O_2}^B\tilde{\Delta}_h. \end{aligned} \tag{5.2.8}$$

Upon coupling the fire model to the plume model and the ambient air, the velocity of the atmospheric flow moving toward the fire will be known due to the calculations in the ambient air. Thus, velocity of the oxygen entering the fire can be written as:

$$v_{O_2} = v_{\text{fire}} + \chi, \tag{5.2.9}$$

where χ is the known velocity along the ground calculated by the plume model just ahead of the plume. With this, the above system of algebraic equations will be used to solve for expressions for the unknowns.

Equation (5.2.9) can be substituted into equations (5.2.6) and (5.2.7), where after manipulation, an expression for the velocity of the fire can be obtained:

$$v_{\text{fire}} = \frac{-\chi\rho_{O_2}\big|_{y_1=b} - (A-B)\frac{l_1}{v_0}\rho_0^{A+B-1}bk_1(\theta)\rho_{\text{fuel}}^A\rho_{O_2}^B}{\left(\rho_{O_2} - \rho_{\text{fuel}}\right)\big|_{y_1=b}}. \tag{5.2.10}$$

Since, $v_{O_2} = v_{\text{fire}} + \chi$:

$$\begin{aligned} v_{O_2} &= \frac{-\chi\rho_{O_2}\big|_{y_1=b} - (A-B)\frac{l_1}{v_0}\rho_0^{A+B-1}bk_1(\theta)\rho_{\text{fuel}}^A\rho_{O_2}^B}{\left(\rho_{O_2} - \rho_{\text{fuel}}\right)\big|_{y_1=b}} + \chi \\ v_{O_2} &= \frac{-(A-B)\frac{l_1}{v_0}\rho_0^{A+B-1}bk_1(\theta)\rho_{\text{fuel}}^A\rho_{O_2}^B - \chi\rho_{\text{fuel}}\big|_{y_1=b}}{\left(\rho_{O_2} - \rho_{\text{fuel}}\right)\big|_{y_1=b}}. \end{aligned} \tag{5.2.11}$$

With this, (5.2.10) is substituted into (5.2.6) to obtain an expression for b, the width if the fire:

$$b = \frac{\chi\rho_{O_2}\rho_{\text{fuel}}\big|_{y_1=b}}{\frac{l_1}{v_0}\rho_0^{A+B-1}k_1(\theta)\rho_{\text{fuel}}^A\rho_{O_2}^B\left(B\rho_{\text{fuel}}\big|_{y_1=b} - A\rho_{O_2}\big|_{y_1=b}\right)}. \tag{5.2.12}$$

The use of (5.2.12) in (5.2.10) results in the simplification of the expression for the fire velocity:

$$v_{\text{fire}} = \frac{A\chi\rho_{O_2}\big|_{y_1=b}}{\left(B\rho_{\text{fuel}}\big|_{y_1=b} - A\rho_{O_2}\big|_{y_1=b}\right)}, \tag{5.2.13}$$

and (5.2.11) can be written as:

$$v_{O_2} = \frac{B\chi\rho_{\text{fuel}}\big|_{y_1=b}}{\left(B\rho_{\text{fuel}}\big|_{y_1=b} - A\rho_{O_2}\big|_{y_1=b}\right)}. \tag{5.2.14}$$

Equation (5.2.5) can be simplified using expressions for the known quantities:

$$\begin{aligned}
\frac{l_1}{l_3}\left(\rho v_{\text{up}}\right)\Big|_{y_3=h}\frac{b}{h} &= \frac{A\chi\rho_{O_2}\big|_{y_1=b}}{\left(B\rho_{\text{fuel}}\big|_{y_1=b} - A\rho_{O_2}\big|_{y_1=b}\right)}\rho_{\text{fuel}} + \frac{B\chi\rho_{\text{fuel}}\big|_{y_1=b}}{\left(B\rho_{\text{fuel}}\big|_{y_1=b} - A\rho_{O_2}\big|_{y_1=b}\right)}\rho_{O_2} \\
\left(\rho v_{\text{up}}\right)\Big|_{y_3=h} &= \frac{l_3}{l_1}\left(\frac{h\frac{l_1}{v_0}\rho_0^{A+B-1}k_1(\theta)\rho_{\text{fuel}}^A\rho_{O_2}^B\left(B\rho_{\text{fuel}}\big|_{y_1=b} - A\rho_{O_2}\big|_{y_1=b}\right)}{\chi\rho_{O_2}\rho_{\text{fuel}}\big|_{y_1=b}}\right) \\
&\qquad\left(\frac{A\chi\rho_{O_2}\rho_{\text{fuel}}\big|_{y_1=b} + B\chi\rho_{\text{fuel}}\rho_{O_2}\big|_{y_1=b}}{\left(B\rho_{\text{fuel}}\big|_{y_1=b} - A\rho_{O_2}\big|_{y_1=b}\right)}\right) \\
\left(\rho v_{\text{up}}\right)\Big|_{y_3=h} &= \frac{l_3}{l_1}\frac{h\frac{l_1}{v_0}\rho_0^{A+B-1}k_1(\theta)\rho_{\text{fuel}}^A\rho_{O_2}^B}{\chi\rho_{O_2}\rho_{\text{fuel}}\big|_{y_1=b}}\left((A+B)\chi\rho_{O_2}\rho_{\text{fuel}}\big|_{y_1=b}\right) \\
\left(\rho v_{\text{up}}\right)\Big|_{y_3=h} &= (A+B)h\frac{l_3}{v_0}\rho_0^{A+B-1}k_1(\theta)\rho_{\text{fuel}}^A\rho_{O_2}^B,
\end{aligned} \tag{5.2.15}$$

and (5.2.8) can be rewritten as:

$$\theta C_p = \frac{1}{A+B}\left(B\theta_{O_2}C_{p\,O_2} + A\theta_{\text{fuel}}C_{p\,\text{fuel}} + D\tilde{\Delta}_h\right). \tag{5.2.16}$$

An equation of state is also used such that $p = \rho_{\text{fire}}\theta$, where p is pressure. Thus, ρ can be written as:

$$\rho_{\text{fire}} = \frac{pC_p}{\frac{1}{(A+B)}\left(B\theta_{O_2}C_{p\,O_2} + A\theta_{\text{fuel}}C_{p\,\text{fuel}} + D\tilde{\Delta}_h\right)}, \tag{5.2.17}$$

and (5.2.15) can be solved for v_{up}:

$$v_{\text{up}}\big|_{y_3=h} = \frac{\theta}{p}(A+B)h\frac{l_3}{v_0}\rho_0^{A+B-1}k_1(\theta)\rho_{\text{fuel}}^A\rho_{O_2}^B$$

$$v_{\text{up}}\big|_{y_3=h} = \frac{\left(B\theta_{O_2}C_{p\,O_2} + A\theta_{\text{fuel}}C_{p\,\text{fuel}} + D\tilde{\Delta}_h\right)}{pC_p}h\frac{l_3}{v_0}\rho_0^{A+B-1}k_1(\theta)\rho_{\text{fuel}}^A\rho_{O_2}^B. \quad (5.2.18)$$

It is assumed that all stoichiometric constants are equal, $A = B = C = D = 1$. With this, the expressions for all unknown quantities are reduced to the following expressions:

$$b = \frac{\chi\big|_{y_1=b}}{\frac{l_1}{v_0}\rho_0 k_1(\theta)\left(\rho_{\text{fuel}}\big|_{y_1=b} - \rho_{O_2}\big|_{y_1=b}\right)} \quad (5.2.19)$$

$$v_{\text{fire}} = \frac{\chi\rho_{O_2}\big|_{y_1=b}}{(\rho_{\text{fuel}} - \rho_{O_2})\big|_{y_1=b}} \quad (5.2.20)$$

$$v_{O_2} = \frac{\chi\rho_{\text{fuel}}\big|_{y_1=b}}{(\rho_{\text{fuel}} - \rho_{O_2})\big|_{y_1=b}} \quad (5.2.21)$$

$$\theta C_p = \frac{1}{2}\left(\theta_{O_2}C_{p\,O_2} + \theta_{\text{fuel}}C_{p\,\text{fuel}} + \tilde{\Delta}_h\right) \quad (5.2.22)$$

$$v_{\text{up}}\big|_{y_3=h} = \frac{\left(\theta_{O_2}C_{p\,O_2} + \theta_{\text{fuel}}C_{p\,\text{fuel}} + \tilde{\Delta}_h\right)}{pC_p}h\frac{l_3}{v_0}\rho_0 k_1(\theta)\rho_{\text{fuel}}\rho_{O_2} \quad (5.2.23)$$

$$\rho_{\text{fire}} = \frac{pC_p}{\frac{1}{2}\left(\theta_{O_2}C_{p\,O_2} + \theta_{\text{fuel}}C_{p\,\text{fuel}} + \tilde{\Delta}_h\right)}. \quad (5.2.24)$$

5.2.2 Bernoulli's Principle

The pressure in the equation of state will be calculated by solving Bernoulli's equation for the pressure just in front of the propagating fire. Bernoulli's equation states:

$$p = 1 - \frac{1}{2}\rho_{O_2}^2\chi^2, \quad (5.2.25)$$

where the constant was evaluated by using the boundary conditions far from the plume. With this, the expressions for the unknown quantities can be written as:

$$b = \frac{\chi\big|_{y_1=b}}{\frac{l_1}{v_0}\rho_0 k_1(\theta)\left(\rho_{\text{fuel}}\big|_{y_1=b} - \rho_{O_2}\big|_{y_1=b}\right)} \quad (5.2.26)$$

$$v_{\text{fire}} = \frac{\chi\rho_{O_2}\big|_{y_1=b}}{(\rho_{\text{fuel}} - \rho_{O_2})\big|_{y_1=b}} \tag{5.2.27}$$

$$v_{O_2} = \frac{\chi\rho_{\text{fuel}}\big|_{y_1=b}}{(\rho_{\text{fuel}} - \rho_{O_2})\big|_{y_1=b}} \tag{5.2.28}$$

$$\theta C_p = \frac{1}{2}\left(\theta_{O_2} C_{p\,O_2} + \theta_{\text{fuel}} C_{p\,\text{fuel}} + \tilde{\Delta}_h\right) \tag{5.2.29}$$

$$p = 1 - \frac{1}{2}\rho_{O_2}^2\chi^2 \tag{5.2.30}$$

$$v_{\text{up}}\big|_{y_3=h} = \frac{\left(\theta_{O_2} C_{p\,O_2} + \theta_{\text{fuel}} C_{p\,\text{fuel}} + \tilde{\Delta}_h\right)}{\left(1 - \frac{1}{2}\rho_{O_2}^2\chi^2\right) C_p} h\frac{l_3}{v_0}\rho_0 k_1(\theta)\rho_{\text{fuel}}\rho_{O_2} \tag{5.2.31}$$

$$\rho_{\text{fire}} = \frac{\left(1 - \frac{1}{2}\rho_{O_2}^2\chi^2\right) C_p}{\frac{1}{2}\left(\theta_{O_2} C_{p\,O_2} + \theta_{\text{fuel}} C_{p\,\text{fuel}} + \tilde{\Delta}_h\right)}. \tag{5.2.32}$$

5.3 Implementation

As was previously stated, the goal of deriving a fire model is to couple the information obtained from the fire model to the point source fire in the plume model. This will eliminate the need for guessed random values for boundary conditions at the fire. This coupling will be done in two different ways. The first occurs through the point source fire and is straight forward. The values calculated through the algebraic equations above will be used for the boundary condition at the fire point in the plume model. The second coupling is through the ambient air system, and was seen in the expression for the velocity of the oxygen, $v_{O_2} = v_{\text{fire}} + \chi$. This second coupling allows the flow in the ambient air system to influence the speed at which the fire propagates.

One can easily see that after the fire model is used to calculate the fire values, to use these values as boundary conditions in the plume model:

$$\rho_{\text{fire}} = R(0,\tau) \qquad \theta = \Theta(0,\tau) \qquad v_{\text{up}} = V(0,\tau).$$

These values from the fire model take the place of the random values that were used in Section 3.2.2. Although, values of vorticity at the fire point are still assumed to be random and are implemented exactly as stated in Section 3.2.2.

The plume model was implemented under the assumption that the point source

fire is stationary, but this fire model now allows the fire to propagate. The plume model code will be used in this implementation with a simple change of reference of the plume model results obtained with a crosswind present in the ambient air. The case of the crosswind in the plume model is thought of as air moving past a stationary fire. As was stated, this time the fire is allowed to propagate. So, a reference fixed to the fire is chosen, and the case of the crosswind is now thought of as a fire moving past stationary air. Meaning for implementation,

$$\mathbf{cw} = \begin{pmatrix} v_{\text{fire}} \\ 0 \end{pmatrix}, \tag{5.3.1}$$

assuming there are no other ambient air wind conditions.

Additionally, for visualization purposes only, the distance the fire travels over time can be computed using the simple equation:

$$\text{fire distance}\big|_{t=\tau} = \text{fire distance}\big|_{t=\tau-1} + v_{\text{fire}}(\tau)\Delta\tau. \tag{5.3.2}$$

All MATLAB code for the fire model is available upon request.

5.3.1 Parameter Values

For implementation, many parameter values need to be chosen such that the model can be evaluated after coupling to the plume model. These parameters are largely based on the composition of the fuel bed. It is assumed that the fire and fuel bed are of constant height $h = 1\text{m}$, and the fuel layer is homogeneously composed of evenly distributed pine needles.

With the choice of the fuel bed composition, the physical quantities can be determined. Values determined by papers referenced in this section served as a reference value. Some parameters needed to be adjusted due to the simplicity of the model. The density of oxygen is misleading in name. Here, due to the composition of air, reactants and oxidizers are present. Thus, ρ_{O_2} is chosen as $\rho_{O_2} = 1.2\frac{\text{kg}}{\text{m}^3}$, which represents the density of air at ambient temperature. If the fuel density is chosen for a packed fuel bed without voids, a value would be chosen following [25]. However,

this is not the case in normal wildfires. There are voids between fuel particles, and the crown of a tree and the ground, effectively lowering the fuel load density. This effective fuel load density is called the bulk density. Values were chosen from [58] for the bulk density of brush and litter and [69] for the bulk density of crown fuel. The values were averaged, such that $\rho_{\text{fuel}} = 6.8\frac{\text{kg}}{\text{m}^3}$. Additionally, it is taken that the temperature of the ambient air is $\theta_{\text{ambient}} = 292\text{K}$, matching the values taken in the plume model. With this, it is taken that all oxygen and fuel entering the control volume representing the fire is at the ambient temperature. This means that there is no preheating of the fuel. This is due to the assumption of no radiation, convection, or conduction influencing the propagation of fire, as seen in (5.2.20).

Here, the choices of specific heats are, $C_{p\,O_2} = 1.005\frac{\text{kJ}}{\text{kg K}}$ and $C_{p\,\text{fuel}} = 1.8\frac{\text{kJ}}{\text{kg K}}$, following [46]. The value of the heat of combustion is taken for live pine needles calculated in [65], $\Delta_h = 7000\frac{\text{kJ}}{\text{kg}}$, and modified to $\Delta_h = 3000\frac{\text{kJ}}{\text{kg}}$ for implementation. The specific heat capacity of air at 1100K, a typical temperature within a fire, is taken to be $C_p = 1.155\frac{\text{kJ}}{\text{kg K}}$.

To approximate the reaction rate, an Arrhenius Law is used such that $k_1(\theta) = A\theta^B e^{\frac{-E_a}{R\theta}}$, where A is a pre-reaction rate, E_a is the activation energy, and R is the ideal gas constant. The values of $A = 6.4 \times 10^9$, $B = 1$, and $E_a = 105\frac{\text{kJ}}{\text{kg}}$ were found in a table of rate constants [76] and were chosen for a reaction between nitrogen and oxygen. These values are used as reference values in the model. Adjustments need to be made due to the fact that many reactions take place during combustion. For implementation, it is chosen that $A = 6.4 \times 10^9$, $B = 1$, and $E_a = 41.5\frac{\text{kJ}}{\text{kg}}$. The value of R is taken to be $R = 286.9\frac{\text{m}^2}{\text{sec}^2\text{K}} = 286.9\frac{\text{J}}{\text{kgK}}$, which is consistent with the choice in the plume model.

The values of these quantities above are non-dimensionalized giving the quantities:

$$\tilde{\rho}_{\text{fuel}} = \frac{6.8\frac{\text{kg}}{\text{m}^3}}{1.2\frac{\text{kg}}{\text{m}^3}} = 5.667 \tag{5.3.3}$$

$$\tilde{\rho}_{O_2} = \frac{1.2\frac{\text{kg}}{\text{m}^3}}{1.2\frac{\text{kg}}{\text{m}^3}} = 1 \tag{5.3.4}$$

$$\tilde{\theta}_{\text{fuel}} = \frac{292K}{292K} = 1 \tag{5.3.5}$$

$$\tilde{\theta}_{O_2} = \frac{292K}{292K} = 1 \tag{5.3.6}$$

$$\tilde{h} = \frac{1\text{m}}{100\text{m}} = .01 \tag{5.3.7}$$

$$\tilde{b} = \frac{b}{100\text{m}} \tag{5.3.8}$$

$$\tilde{C}_{p\,\text{fuel}} = \frac{1.8\frac{\text{kJ}}{\text{kg K}}}{1.005\frac{\text{kJ}}{\text{kg K}}} = 1.79 \tag{5.3.9}$$

$$\tilde{C}_{p\,O_2} = \frac{1.005\frac{\text{kJ}}{\text{kg K}}}{1.005\frac{\text{kJ}}{\text{kg K}}} = 1 \tag{5.3.10}$$

$$\tilde{C}_{p\,\text{fire}} = \frac{1.155\frac{\text{kJ}}{\text{kg K}}}{1.005\frac{\text{kJ}}{\text{kg K}}} = 1.149 \tag{5.3.11}$$

$$\tilde{\Delta}_h = \frac{3000\frac{\text{kJ}}{\text{kg}}}{1.005\frac{\text{kJ}}{\text{kg K}} \cdot 292\text{K}} = 10.22. \tag{5.3.12}$$

It can be easily seen that scaling constants have been chosen such that, $\rho_0 = \rho_{\text{air}}$, $\theta_0 = 292\text{K}$, $l_3 = 100\text{m}$, and $l_1 = 100\text{m}$. Additionally chose $v_0 = \frac{l_3}{t_0} = \frac{100}{4}\frac{\text{m}}{\text{sec}} = 25\frac{\text{m}}{\text{sec}}$, which is consistent with the values chosen in the plume model, Section 2.1.1.

CHAPTER 6
Fire Model Results

The equations from Chapter 5 are implemented in MATLAB using the parameters and methods in Section 5.3, solved numerically, and coupled to the plume model to obtain the results shown in this chapter.

Again, the red shading of the plume indicates a low density air, a blue shading of the plume indicates air close to the density of the ambient air, and the arrows present in the ambient air system are an indication of the flow. This time, one will note the presence of red and black bars underneath the fire plume. The red bar is an indication of the width of the fire, and the back bar is an indication of the distance the fire has traveled during the simulation. The red bar is not always visible. This is due to the fact that the majority of the time the width of the fire is small and the scales used for plotting are relatively large.

One will notice that these results are consistent with the implementation techniques outlined in Chapter 5, with the fire appearing to propagate to the right side of the figures. This was achieved through the use of a reference frame fixed to the fire, where a crosswind was used to indicate the flow due to the fire moving. In each of the figures shown below, the fire plume reacts as one would expect.

An analogy was used to determine if the behavior of the plume was physically accurate. Consider a person walking at constant speed. At fixed intervals of time, say five seconds, the person releases a balloon. After a balloon is released, the effect of buoyancy causes it to rise over the position on the ground at which it was released. After all balloons are released, if an observer were to describe the profile of the balloons, due to constant speed, the balloons would create a straight line with negative slope. Variations in speed of the fire propagating, or in the analogy variations in the speed at which the person walks, only effect the slope of the profile of the balloons.

Just as in Chapter 4, the model was again used to track the various energies in the plume to determine if the addition of fire dynamics to the system effects the

frequency analysis. The results from the frequency analysis are again presented as a spectrogram and as plots in the frequency domain.

6.1 Fire Propagation

The implementation technique of using a change of reference has allowed the fire to propagate, representing the culmination of a fully functioning wildfire model. The results are presented in Figure 6.1. The results look much like the results presented in Chapter 4 for the crosswind case, as one would expect. It is interesting to see the effect of the values now prescribed by the fire model.

Figure 6.1 depicts a plume, interestingly, without the presence of puffs as seen in the solution at $t = 375$. As time progresses throughout the snapshots, one can see that the plume responds to not only the crosswind, but the buoyancy and vorticity as discussed in Chapter 4. Just as in the analogy of balloons, the smoke released at the beginning of the simulation is fixed above that point, as the fire continues to propagate. Again, the time in these figures is scaled time.

Here, computation times averaged around six minutes, where the time lapse from the beginning of the simulation to the end of the simulation was 600. Note, this number is scaled time. In true units of time, this represents 40 minutes of simulation time. Even with the added fire model, computation times have been kept sub-real-time. In this amount of time, the fire, on average, has propagated approximately 2.4 units of length, or 240m, which corresponds to an average approximate fire propagation speed of $6\frac{\text{m}}{\text{min}}$.

The fire propagation can be visualized by Figure 6.2 in a plot of traveled fire distance versus time. It can be seen that the fire propagates at a relatively constant speed, although there are some variations in this propagation speed. As will be mentioned in the coming frequency analysis, these variations are small due to the quasi-steady state assumption.

6.2 Frequency Analysis

The same frequency analysis from Chapter 4 was performed on the same energies in the plume, enstrophy and kinetic energy. Since the random values of vorticity

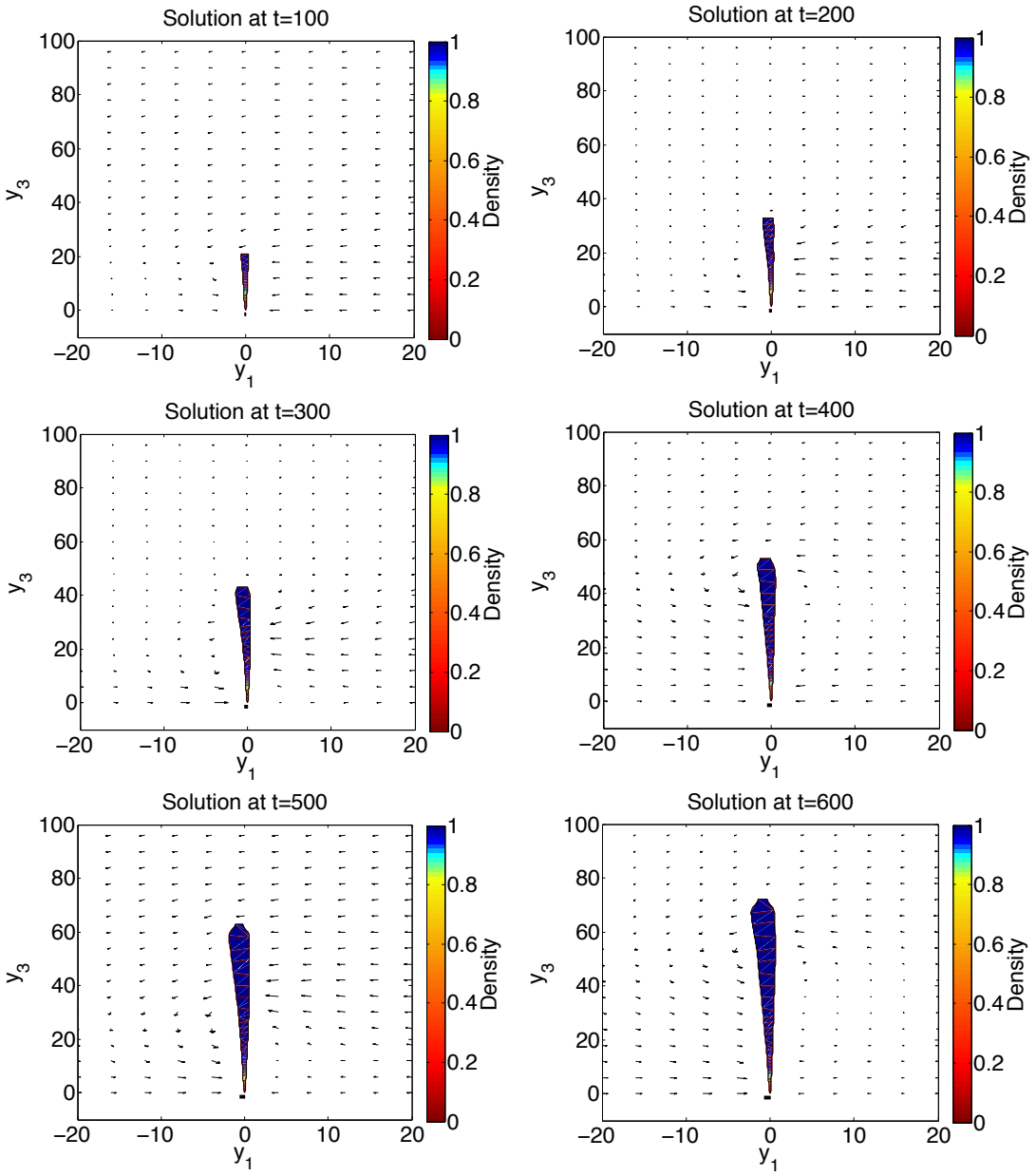

Figure 6.1: Numerical Solution for Fire Model

are still used at the fire point, from Section 3.2.2, the spectral results for vorticity closely mirror those seen in Chapter 4.

The power spectral density of the kinetic energy and enstrophy with values calculated by the fire model are shown in Figures 6.3 and 6.4. At first glance, it appears as though the spectral results shown in Figure 6.3 suggest there is no frequency dependence on the propagation of kinetic energy throughout the plume.

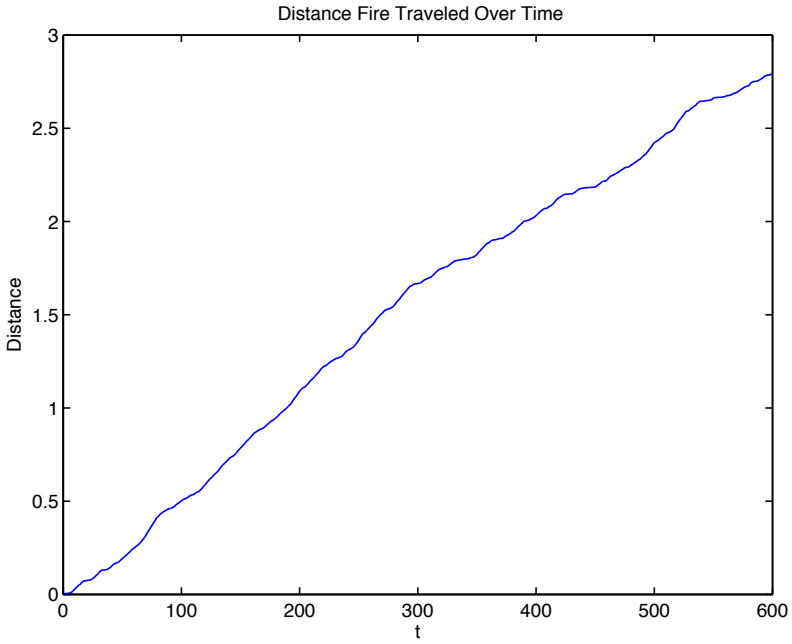

Figure 6.2: Progression of Fire Propagation

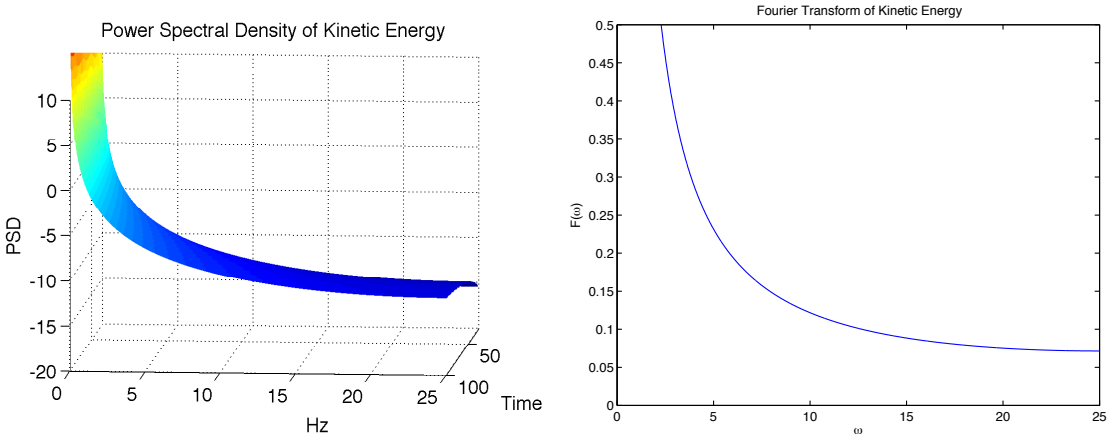

(a) Spectrogram **(b) Fourier Transform at t_f**

Figure 6.3: Fourier Transform of Kinetic Energy for Fire Model Inputs

Although, upon examining the extreme low frequencies of the kinetic energy in Figure 6.3b, it is easily seen that there are random frequency responses, as seen in Figure 6.5, which closely resembles the results from the random input in the plume model.

The results from Figure 6.5 surprisingly suggest the fire model behaves as the randomly forced plume model results from Chapter 4. The need to isolate the

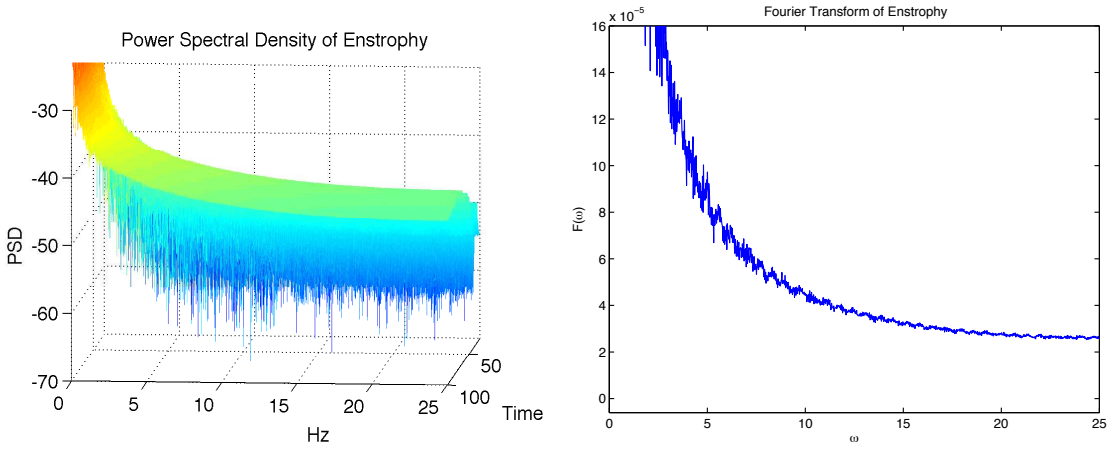

(a) Spectrogram **(b) Fourier Transform at t_f**

Figure 6.4: Fourier Transform of Enstrophy for Fire Model Inputs

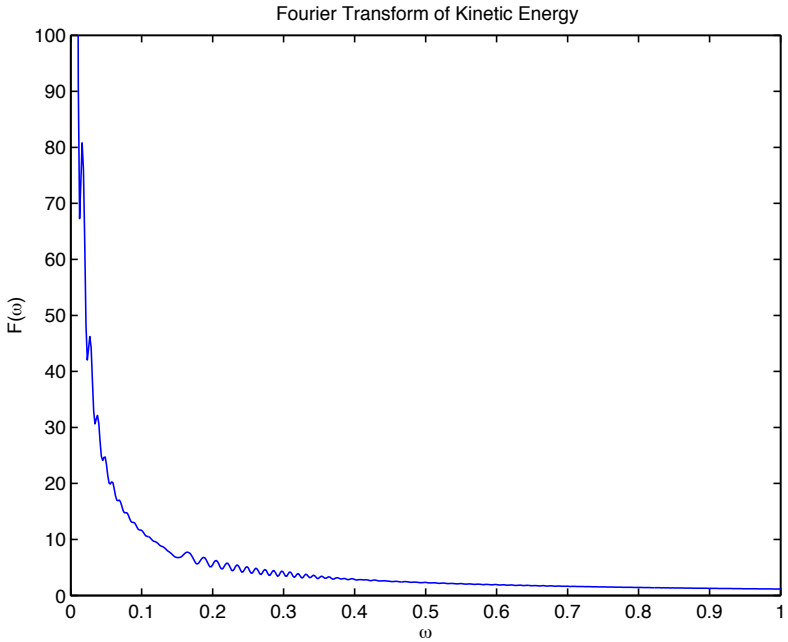

Figure 6.5: Magnified Fourier Transform of Kinetic Energy

low frequencies in the Fourier transform results is attributed to the effects of the quasi-steady state assumption. This assumption imposed small variations over long periods of time. The frequency dependence for the kinetic energy in the model is induced by the fluctuations in the velocity, but the quasi-steady state assumption assumed these variations are small. Thus, the frequency dependence is small as well.

Additionally, there are slight differences between the results for enstrophy from

these results and those shown in Chapter 4. The largest difference is the magnitude of the transformed values. The differences here can be a result of the other values needed for computing enstrophy, such as density and width of the plume. These values are still influenced by the fire model, resulting in the slight differences.

6.3 Conclusions

The extremely simplified model developed in Chapter 5 has resulted in a realistic addition to the plume model developed in Chapters 2 and 3. This additional model allows an interaction between the plume and ambient atmosphere with a fire to be investigated. The two models were coupled, creating a feedback loop allowing the flow in the ambient air system to influence the propagation of the fire, and vice versa. Closely following the results from the plume model, the results of the coupled models can be obtained in sub-real-time, which is a welcomed by-product of a simplified model. All below comments should be considered, noting that the fire model is extremely simplified, and as such, does a decent job describing the complex physical processes.

The fire model adds the rate of fire propagation to the predicted quantities. As seen in the figures, and more clearly in the video of the simulation, it appears as though the fire propagation speed varies drastically from one plot to another. This variation can be attributed to the frame rate of the simulation and plots, and also, due to the fact that the fire tends to propagate quickly for a short period of time, then slow down to consume the fresh fuel it has just moved into. Although, as seen from Figure 6.2, long-time trends suggest the fire does propagate at a nearly constant rate. It must be fully understood that the only connection between the plume system and the fire model, at this point, is the velocity of the flow supplying oxygen to the fire system.

The frequency analysis of the fire model has revealed the characterization of the behavior of the fire. While at first glance, the model appeared to have no frequency dependence in kinetic energy, but after closer examination of the lower frequencies, a random response was identified. As was mentioned before, the investigation was focused on the low frequencies due to the quasi-steady state assumption used to

derive this model. The quasi-steady state assumption also explains why the puffing behavior is absent in the results here. This puffing behavior could be attributed to several characteristics of the model. Most influential of these characteristics is the absence of the transfer of energy from the fire into the fuel layer and the homogeneity of the fuel layer. As a fire moves through different fuels, the energy gained through combustion will vary, affecting the buoyancy of the gas in the plume.

CHAPTER 7
Fire Propagation on a Slope

The models presented in the previous chapters represent a simplified wildfire model. They have been developed for a fire propagating across a homogeneous fuel bed on a constant topography. There are several possible extensions of the above wildfire model. One extension, which will be investigated here, is the possibility of changes in topography of the land. As was reported by many previous works cited in Chapter 1, a slope has a large effect on not only the propagation speed of the fire, but also the dynamics of the flow of the problem.

The situation of a fire propagating along a flat topography (Chapter 5) can be easily adapted to the case of a slope driven fire though the implementation of the equations derived in Chapter 2. In dealing with sloped coordinate systems, care needs to be taken in resolving forces, especially gravity, to account for contributions in directions normal and tangential to the slope. With this in mind, the equations from Chapter 2 are rederived for slope fires. In this derivation, not all equations are affected. Only the equations that change from the derivation in Chapter 2 are presented here. In addition, all implementation techniques are identical to those in Chapter 3 unless stated otherwise.

The differences in derivation occur in the momentum equations. Figure 7.1 shows the two coordinates systems used for these calculations. The unprimed coordinates are termed the calculational coordinate system, and the primed coordinates are the physical coordinates. As the name suggests, the calculational coordinate system is used for all computations, and after the results are obtained, they are mapped to the physical coordinates. All calculations conducted within the calculational coordinate system proceed as in Chapters 2 and 5 with a change in the direction of gravity.

The choice of a sloped topography induces a change in the effect of gravity. It is assumed that the ground is sloped at an angle of φ, measured from the positive y_1' axis, see Figure 7.1. In physical coordinates, gravity still points in the $\mathbf{e}_g' =$

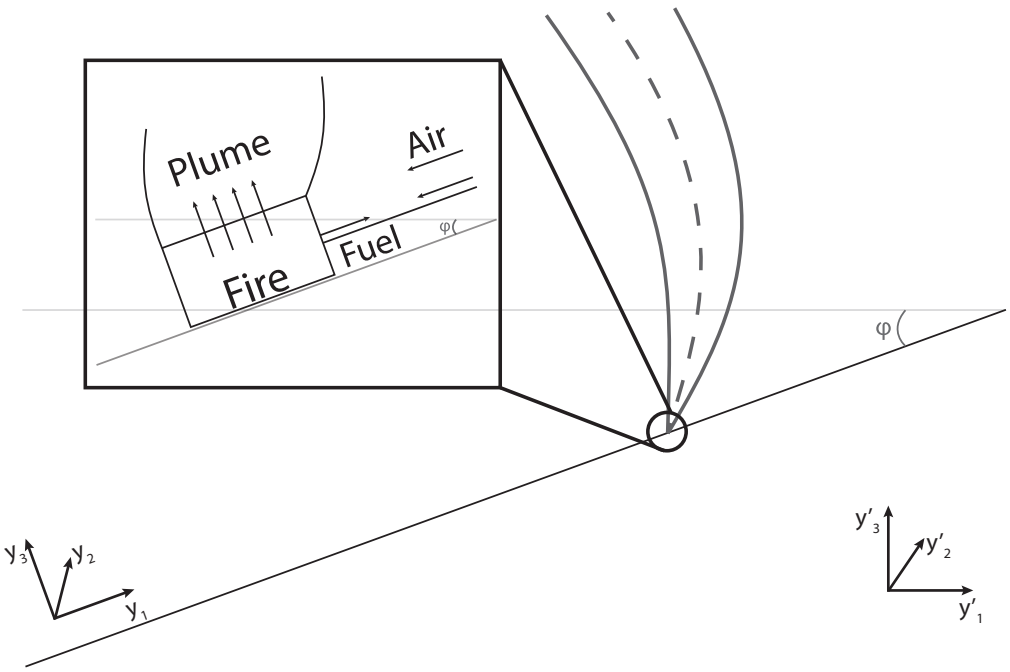

Figure 7.1: Geometry for Fires on Inclines

$\begin{pmatrix} 0, & 0, & -1 \end{pmatrix}^T$ direction, although its effects now need to be decomposed into its normal and tangential components or the calculational coordinates, again see Figure 7.1. Thus, the choice of the unit vector $\mathbf{e}_g$ needs to be rotated by the angle φ:

$$\mathbf{e}_g = \begin{pmatrix} \cos\varphi & 0 & -\sin\varphi \\ 0 & 1 & 0 \\ \sin\varphi & 0 & \cos\varphi \end{pmatrix} \begin{pmatrix} 0 \\ 0 \\ -1 \end{pmatrix} = \begin{pmatrix} \sin\varphi \\ 0 \\ -\cos\varphi \end{pmatrix}.$$

With this, the momentum equations of the general solution to the boundary layer problem can be written as:

$$\begin{aligned} &\frac{l_3^2}{\bar{R}T_0 t_0^2}\tilde{R}^{(0)}\left[(\tilde{v}_1^{(0)})_\tau + \left(\tilde{v}_1^{(0)}(\tilde{v}_1^{(0)})_{y_1}\right) + \left(\tilde{v}_3^{(0)}(\tilde{v}_1^{(0)})_{y_3}\right)\right] \\ &+ \left(P_{y_1}^{(H)} + \frac{gl_3}{\bar{R}T_0}P_{y_1}^{(H1)} + \frac{l_3^2}{\bar{R}T_0 t_0^2}P_{y_1}^{(1)}\right) = \frac{gl_3\sin\varphi}{\bar{R}T_0}\tilde{R}^{(0)} + \frac{\eta_0}{\bar{R}\rho_0 T_0}\left(\tilde{T}_{11\,y_1}^{(0)} + \tilde{T}_{13\,y_3}^{(0)}\right) \end{aligned} \tag{7.0.1}$$

$$\frac{l_3^2}{\bar{R}T_0 t_0^2}\tilde{R}^{(0)}\left[(\tilde{v}_3^{(0)})_\tau + \left(\tilde{v}_1^{(0)}(\tilde{v}_3^{(0)})_{y_1}\right) + \left(\tilde{v}_3^{(0)}(\tilde{v}_3^{(0)})_{y_3}\right)\right]$$

$$+\frac{l_3}{l_i}\left(P^{(H)}_{y_3}+\frac{gl_3}{\bar{R}T_0}P^{(H1)}_{y_3}+\frac{l_3^2}{\bar{R}T_0t_0^2}P^{(1)}_{y_3}\right)=\frac{-gl_3\cos\varphi}{\bar{R}T_0}\tilde{R}^{(0)}+\frac{\eta_0}{\bar{R}\rho_0T_0}\left(\tilde{T}^{(0)}_{31\,y_1}+\tilde{T}^{(0)}_{33\,y_3}\right), \tag{7.0.2}$$

where the equations are written for the horizontal and vertical directions respectively. These equations reduce to (2.1.10) for $\varphi = 0$.

The remainder of this chapter exactly follows the derivation in Chapter 2. All assumptions used in Chapter 2 are mirrored here, even if not explicitly stated. The equations are scaled to describe the plume system, where conservation laws for the system are derived, and ambient air system where separated $O(1)$, $O(\beta)$, and $O(\sigma)$ systems are obtained.

7.1 Outer Solution-Ambient Air System

In the ambient air system, the two momentum equations can be written as:

$$\begin{aligned}\sigma\left(R_o^{(H)}+\beta R_o^{(H1)}+\sigma R_o^{(1)}\right)&\left[(v_{o1})_\tau+(v_{o1}(v_{o1})_{y_1})+(v_{o3}(v_{o1})_{y_3})\right]\\&+P^{(H)}_{y_1}+\beta P^{(H1)}_{y_1}+\sigma P^{(1)}_{y_1}=\beta\sin\varphi\left(R_o^{(H)}+\beta R_o^{(H1)}+\sigma R_o^{(1)}\right)\end{aligned} \tag{7.1.1}$$

$$\begin{aligned}\sigma\left(R_o^{(H)}+\beta R_o^{(H1)}+\sigma R_o^{(1)}\right)&\left[(v_{o3})_\tau+(v_{o1}(v_{o3})_{y_1})+(v_{o3}(v_{o3})_{y_3})\right]\\&+P^{(H)}_{y_3}+\beta P^{(H1)}_{y_3}+\sigma P^{(1)}_{y_3}=-\beta\cos\varphi\left(R_o^{(H)}+\beta R_o^{(H1)}+\sigma R_o^{(1)}\right),\end{aligned} \tag{7.1.2}$$

where it is easily seen that the same asymptotic expansion, induced by the expansion in pressure, is used for density.

Again, the perturbation analysis is performed to separate the effects of the multiple scales in the above equations. It is clearly seen that the $O(1)$ system remains the same as in Chapter 2 due to the fact that the terms added for the slope contribute on the $O(\beta)$ scale. Thus, $P^{(H)} = 1$, $R_o^{(H)} = 1$, and $\theta_o^{(H)} = 1$. So, the focus shifts to the $O(\beta)$ system.

7.1.1 $O(\beta)$ System

This time, the full $O(\beta)$ system can be written as:

$$R^{(H1)}_{o\tau}+\left(R_o^{(H1)}v_{o1}\right)_{y_1}+\left(R_o^{(H1)}v_{o3}\right)_{y_3}=0 \tag{7.1.3a}$$

$$P_{y_1}^{(H1)} = \sin\varphi R_o^{(H)} \tag{7.1.3b}$$

$$P_{y_3}^{(H1)} = -\cos\varphi R_o^{(H)} \tag{7.1.3c}$$

$$\begin{aligned} R_o^{(H)} &\left[(\theta_o^{(H1)})_\tau + v_{o\,1}(\theta_o^{(H1)})_{y_1} + v_{o\,3}(\theta_o^{(H1)})_{y_3}\right] \\ &-\frac{\gamma-1}{\gamma}\left[P_\tau^{(H1)} + v_{o\,1}P_{y_1}^{(H1)} + v_{o\,3}P_{y_3}^{(H1)}\right] = 0 \end{aligned} \tag{7.1.3d}$$

$$P^{(H1)} = R_o^{(H1)} + \theta_o^{(H1)}. \tag{7.1.3e}$$

Following the same procedure as before, the energy equation, (7.1.3d), and the equation of state, (7.1.3e), can be used to derive a differential relation between pressure and density. This time, there are contributions in both the y_1 and y_3 directions due to the inclined topography. Using the momentum equations in both directions, (7.1.3b) and (7.1.3c), and the previous differential relations, one obtains the equations:

$$\gamma R_{o\,y_1}^{(H1)} = \sin\varphi R_o^{(H)} = \sin\varphi \tag{7.1.4}$$

$$\gamma R_{o\,y_3}^{(H1)} = -\cos\varphi R_o^{(H)} = -\cos\varphi, \tag{7.1.5}$$

which can be solved for the $O(\beta)$ correction of density. Thus, the $O(\beta)$ corrections can be calculated:

$$\begin{aligned} R_o^{(H1)} &= -\frac{1}{\gamma}\left(y_3\cos\varphi - y_1\sin\varphi\right) \\ \theta_o^{(H1)} &= -\left(1-\frac{1}{\gamma}\right)\left(y_3\cos\varphi - y_1\sin\varphi\right) \\ P^{(H1)} &= -\left(y_3\cos\varphi - y_1\sin\varphi\right), \end{aligned}$$

where again the boundary condition at the ground was used. With this, the full asymptotic expansions of the ambient air variables can be written as:

$$P = 1 - \beta\left(y_3\cos\varphi - y_1\sin\varphi\right) + \sigma P^{(1)} \tag{7.1.6}$$

$$\theta = 1 - \beta\left(1-\frac{1}{\gamma}\right)\left(y_3\cos\varphi - y_1\sin\varphi\right) + \sigma\theta_o^{(1)} \tag{7.1.7}$$

$$R = 1 - \beta\frac{1}{\gamma}\left(y_3\cos\varphi - y_1\sin\varphi\right) + \sigma R_o^{(1)}. \tag{7.1.8}$$

Again, if $\varphi = 0$ these expressions are exactly those from Chapter 2.

In continuing to separate orders one will notice that the $O(\sigma)$ system remains the same as the system derived in Chapter 2. Again, this is due to the fact that the terms added due to the new topography contribute on the $O(\beta)$ scale. The fact that the $O(\sigma)$ system remains unchanged means the vorticity equation is unchanged as well. Since at this point in this work, only the first non-zero term is used as approximations of the asymptotic expansions are used, for implementation, there are no changes to the ambient air variables that need to be made for the addition of the slope.

7.2 Inner Solution-Plume System

To describe the plume, which represents the inner layer of the problem, the variables must be rescaled. The rescalings are identical to those in Chapter 2, and are made noting that the majority of the velocity inside the plume is in the y_3 direction. Upon substituting the rescaled velocity, distance, and time into (7.0.1) and (7.0.2), the momentum equations can be written as:

$$\begin{aligned}
&RV_p^2\delta\left[(V_1)_{\tilde{\tau}} + (V_1(V_1)_{Y_1}) + (V_3(V_1)_{y_3})\right] \\
&\qquad + \frac{1}{\delta}\frac{\bar{R}T_0t_0^2}{l_3^2}\left(P_{Y_1}^{(H)} + \beta P_{Y_1}^{(H1)} + \sigma P_{Y_1}^{(1)}\right) = \frac{t_0^2 g}{l_3}R\sin\varphi + V_p^2\left(\frac{1}{\delta}\hat{T}_{11Y_1} + \hat{T}_{13y_3}\right) \\
&RV_p^2\left[(V_3)_{\tilde{\tau}} + (V_1(V_3)_{Y_1}) + (V_3(V_3)_{y_3})\right] \\
&\qquad + \frac{\bar{R}T_0t_0^2}{l_3^2}\left(P_{y_3}^{(H)} + \beta P_{y_3}^{(H1)} + \sigma P_{y_3}^{(1)}\right) = -\frac{t_0^2 g}{l_3}R\cos\varphi + V_p^2\left(\hat{T}_{31Y_1} + \delta\hat{T}_{33y_3}\right).
\end{aligned}$$

The derivatives of pressure are known from the newly derived expansions, (7.1.6), such that $P_{Y_1} = \delta\beta\sin\varphi + \sigma P_{Y_1}^{(1)}$ and $P_{y_3} = -\beta\cos\varphi + \sigma P_{y_3}^{(1)}$. It is seen that this time, the asymptotic expansion in pressure has been rescaled for the plume system. Meaning, inside the plume, in terms of Y_1,

$$P = 1 - \beta\left(y_3\cos\varphi - (y_{1\,p} + \delta Y_1)\sin\varphi\right) + \sigma P^{(1)}.$$

Substituting these expressions into the above equations results in the reduc-

tion:

$$RV_p^2\delta\left[(V_1)_{\tilde{\tau}}+(V_1(V_1)_{Y_1})+(V_3(V_1)_{y_3})\right]$$
$$+\frac{1}{\delta}\frac{\bar{R}T_0t_0^2}{l_3^2}\left(\delta\beta\sin\varphi+\sigma P_{Y_1}^{(1)}\right)=\frac{t_0^2g}{l_3}R\sin\varphi+V_p^2\left(\frac{1}{\delta}\hat{T}_{11Y_1}+\hat{T}_{13y_3}\right)$$
$$RV_p^2\left[(V_3)_{\tilde{\tau}}+(V_1(V_3)_{Y_1})+(V_3(V_3)_{y_3})\right]$$
$$+\frac{\bar{R}T_0t_0^2}{l_3^2}\left(-\beta\cos\varphi+\sigma P_{y_3}^{(1)}\right)=-\frac{t_0^2g}{l_3}R\cos\varphi+V_p^2\left(\hat{T}_{31Y_1}+\delta\hat{T}_{33y_3}\right).$$

Again following the derivation from Chapter 2, a first approximation in σ and β is made ($\sigma \ll 1$ and $\beta \ll 1$). Additionally, since the interest is in a narrow plume, the limit is taken as $\delta \to 0$, which results in the $O(1)$ momentum equations for the plume system:

$$P_{Y_1}^{(1)}=V_p^2\hat{T}_{11Y_1}$$
$$RV_p^2\left[(V_3)_{\tilde{\tau}}+(V_1(V_3)_{Y_1})+(V_3(V_3)_{y_3})\right]-\frac{\bar{R}T_0t_0^2}{l_3^2}\beta\cos\varphi=-\frac{t_0^2g}{l_3}R\cos\varphi+V_p^2\hat{T}_{31Y_1}.$$

It is again taken that $V_p^2=\frac{gt_0^2}{l_3}$ to ensure the fundamental balances between the buoyancy terms and the entrainment terms, and the definition of β is used to further reduce the momentum equations:

$$P_{Y_1}^{(1)}=\frac{gt_0^2}{l_3}\hat{T}_{11Y_1}$$
$$R\left[(V_3)_{\tilde{\tau}}+(V_1(V_3)_{Y_1})+(V_3(V_3)_{y_3})\right]-\cos\varphi=-R\cos\varphi+\hat{T}_{31Y_1}.$$

The equations can be written in conservation form:

$$P_{Y_1}^{(1)}=\frac{gt_0^2}{l_3}\hat{T}_{11Y_1} \tag{7.2.1}$$
$$(RV_3)_{\tilde{\tau}}+(RV_1V_3)_{Y_1}+\left(RV_3^2\right)_{y_3}-\cos\varphi=-R\cos\varphi+\hat{T}_{31Y_1}, \tag{7.2.2}$$

and the derivation continues as it did in Chapter 2 by integrating the system of across the plume.

One will note that again, the momentum equation in the horizontal direction

implies that there are pressure gradients across the plume, albeit they are small due to the scalings in the expansion of pressure. One will also notice that this pressure gradient is exactly the same as in Chapter 2, where the inclined slope has no effect on the pressure jump.

The derivation of the energy equation also contains derivatives of pressure, which as seen above has changed from the derivation in Chapter 2. Although, to leading order, the alterations due to the slope do not contribute or effect implementation. That is, from (2.3.2), the energy equation can be written as:

$$RV_p\left[\Theta_{\tilde{\tau}}+V_1\Theta_{Y_1}+V_3\Theta_{y_3}\right]-V_p\frac{\gamma-1}{\gamma}\Big[P^{(H)}_{\tilde{\tau}}+\beta P^{(H1)}_{\tilde{\tau}}+\sigma P^{(1)}_{\tilde{\tau}} + V_1\left(P^{(H)}_{Y_1}+\beta P^{(H1)}_{Y_1}+\sigma P^{(1)}_{Y_1}\right)+V_3\left(P^{(H)}_{y_3}+\beta P^{(H1)}_{y_3}+\sigma P^{(1)}_{y_3}\right)\Big] = V_p\tilde{Q}+V_p\left(\hat{q}_{1Y_1}+\delta\hat{q}_{3y_3}\right).$$

Upon substitution of the pressure expansion (7.1.6), the energy equation becomes:

$$RV_p\left[\Theta_{\tilde{\tau}}+V_1\Theta_{Y_1}+V_3\Theta_{y_3}\right]-V_p\frac{\gamma-1}{\gamma}\Big[\sigma P^{(1)}_{\tilde{\tau}}+V_1\left(\delta\beta\sin\varphi+\sigma P^{(1)}_{Y_1}\right) + V_3\left(-\beta\cos\varphi+\sigma P^{(1)}_{y_3}\right)\Big] = V_p\tilde{Q}+V_p\left(\hat{q}_{1Y_1}+\delta\hat{q}_{3y_3}\right).$$

Taking a first approximation in both β and σ and allowing $\delta\to 0$ results in the same energy equation as in Chapter 2:

$$R\left[\Theta_{\tilde{\tau}}+V_1\Theta_{Y_1}+V_3\Theta_{y_3}\right]=\tilde{Q}+\hat{q}_{1Y_1}.$$

In the averaging process, all conservation laws are integrated with respect to Y_1. Since all changes to the momentum equations induced by the inclined slope are constants with respect to Y_1, the final form integral conservation equations will be identical to the ones in Chapter 2, with the constant multiples reflected in the above equations. Thus, the final form conservation laws for the plume system as derived in Cartesian coordinates becomes:

$$(Rb)_{\tilde{\tau}}+(bRV_3)_{y_3}=S_m \tag{7.2.3a}$$

$$P^{(1)}\Big|_{y_{1p}-\frac{b}{2}}^{y_{1p}+\frac{b}{2}} = \frac{gt_0^2}{l_3}\hat{T}_{11}\Big|_{y_{1p}-\frac{b}{2}}^{y_{1p}+\frac{b}{2}} \tag{7.2.3b}$$

$$(bRV_3)_{\tilde{\tau}} + (bRV_3^2)_{y_3} = bf + S_M \tag{7.2.3c}$$

$$(bR\Theta)_{\tilde{\tau}} + (bRV_3\Theta)_{y_3} = bH + S_T \tag{7.2.3d}$$

$$(Rb\Omega)_{\tilde{\tau}} + (Rb\Omega V_3)_{y_3} = G + S_G \tag{7.2.3e}$$

$$P^{(H)} = R\Theta, \tag{7.2.3f}$$

where the only change is to f. Here, $f = \cos\varphi\,(1-R)$.

7.2.1 Control Volume Conservation Laws

As was stated in Chapter 2, Chapter 3, and Appendix A, the integral derivation of these conservation equations is only valid for a nearly vertical plume. The interest in this work is in an arbitrary plume position. Thus, the curvilinear complement of the conservation laws need to be derived. The only changes to the curvilinear equations, mirroring the Cartesian counterparts, is the change of the effect of gravity to account for a rotation in coordinate system. Again, the changes to the equations from Appendix A will only be reflected in the axial and transverse momentum equations. In the same manner as before, only the axial and transverse momentum equations will be rederived here. For the reference in the coming derivation, it must be noted that $\mathbf{T}\cdot\mathbf{e}_g = T_1\sin\varphi - T_2\cos\varphi = \frac{\partial y_1}{\partial s}\sin\varphi - \frac{\partial y_3}{\partial s}\cos\varphi$. Similarly, $\mathbf{n}\cdot\mathbf{e}_g = n_1\sin\varphi - n_2\cos\varphi = \frac{\partial y_1}{\partial \nu}\sin\varphi - \frac{\partial y_3}{\partial \nu}\cos\varphi$.

7.2.1.1 Conservation of Axial Momentum

Using the same derivation as in Appendix A, the scaled axial momentum equation can be written as:

$$(RbV)_\tau = -\left(RbV^2\right)_s + S_M - \frac{t_0^2\bar{R}T_0}{l_3^2}b\frac{\partial P}{\partial s} + Rb\tilde{g}\sin\varphi\frac{\partial y_1}{\partial s} - Rb\tilde{g}\frac{\partial y_3}{\partial s}\cos\varphi, \tag{7.2.4}$$

where this time, it is seen that the force of gravity must be decomposed to gain the correct contribution relative to the inclined slope. Writing the derivative of pressure

using the definition from (7.1.6) as:

$$\begin{aligned}\frac{\partial P}{\partial s} &= \frac{\partial y_1}{\partial s}\frac{\partial P}{\partial y_1} + \frac{\partial y_3}{\partial s}\frac{\partial P}{\partial y_3} \\ &= \beta \sin\varphi \frac{\partial y_1}{\partial s} - \beta \cos\varphi \frac{\partial y_3}{\partial s} \\ &= \frac{g l_3}{\bar{R} T_0} \sin\varphi \frac{\partial y_1}{\partial s} - \frac{g l_3}{\bar{R} T_0} \cos\varphi \frac{\partial y_3}{\partial s},\end{aligned}$$

allows the conservation law to be written as:

$$(RbV)_\tau = -\left(RbV^2\right)_s + S_M + (1-R)\,\tilde{g} b \frac{\partial y_3}{\partial s}\cos\varphi - (1-R)\,\tilde{g} b \frac{\partial y_1}{\partial s}\sin\varphi. \quad (7.2.5)$$

For implementation, the mass equation, (A.2.2), is used to simplify this expression to:

$$\begin{aligned}V_\tau + \left(\frac{1}{2}V^2\right)_s = \frac{1}{Rb}\Bigg(&S_M + (1-R)\,\tilde{g} b \frac{\partial y_3}{\partial s}\cos\varphi \\ &- (1-R)\,\tilde{g} b \frac{\partial y_1}{\partial s}\sin\varphi - V S_m\Bigg).\end{aligned} \quad (7.2.6)$$

7.2.1.2 Conservation of Transverse Momentum

The conservation of transverse momentum can be though of as the normal complement to the axial momentum equation. Just as in the derivation of the axial momentum equation, the derivation is identical to that shown in Appendix A with a rotation of coordinates. The transverse momentum equation can be written as:

$$\begin{aligned}(Rbw)_\tau = &-(RbwV)_s + R_o^+ V_{n+} v_{in}^+ + R_o^- V_{n-} v_{in}^- - R w v_{out}^+ - R w v_{out}^- - \frac{t_0^2 \bar{R} T_0}{l_3^2} b \frac{\partial P}{\partial \nu} \\ &+ R b \tilde{g} \frac{\partial y_1}{\partial \nu}\sin\varphi - R b \tilde{g} \frac{\partial y_3}{\partial \nu}\cos\varphi.\end{aligned} \quad (7.2.7)$$

Writing the derivative of pressure as:

$$\begin{aligned}\frac{\partial P}{\partial \nu} &= \frac{\partial y_1}{\partial \nu}\frac{\partial P}{\partial y_1} + \frac{\partial y_3}{\partial \nu}\frac{\partial P}{\partial y_3} \\ &= \beta \sin\varphi \frac{\partial y_1}{\partial \nu} - \beta \cos\varphi \frac{\partial y_3}{\partial \nu}\end{aligned}$$

$$= \frac{gl_3}{\bar{R}T_0}\sin\varphi\frac{\partial y_1}{\partial \nu} - \frac{gl_3}{\bar{R}T_0}\cos\varphi\frac{\partial y_3}{\partial \nu},$$

allows the conservation law to be written as:

$$\begin{aligned}(Rbw)_\tau = &-(RbwV)_s + R_o^+ V_{n+} v_{in}^+ + R_o^- V_{n-} v_{in}^- - Rwv_{out}^+ - Rwv_{out}^- \\ &+ (1-R)b\tilde{g}\frac{\partial y_3}{\partial \nu}\cos\varphi - (1-R)b\tilde{g}\frac{\partial y_1}{\partial \nu}\sin\varphi. \end{aligned} \tag{7.2.8}$$

For implementation, this can be easily solved for w the transverse velocity of the plume using the fact that $b \sim \delta$ and $\frac{\partial}{\partial \nu} \sim \frac{1}{\delta}$:

$$w = \frac{R_o^+ V_{n+} v_{in}^+ - R_o^- V_{n-} v_{in}^-}{R(v_{out}^+ + v_{out}^-)} + (1-R)\frac{b\tilde{g}\frac{\partial y_3}{\partial \nu}\cos\varphi}{R(v_{out}^+ + v_{out}^-)} - (1-R)\frac{b\tilde{g}\frac{\partial y_1}{\partial \nu}\sin\varphi}{R(v_{out}^+ + v_{out}^-)}.$$

All remaining conservation equations are unchanged in the rotation of coordinates, and are implemented as before in Chapter 3.

7.3 Implementation & Results

The equations this chapter are implemented in MATLAB using the same implementation as in Section 5.3 and Chapter 3 to be solved numerically. The MATLAB code is available upon request. For the results presented in this section, unless stated otherwise, $\varphi = 30$ degrees. The only difference between the code used in the fire model and the code used here is the direction of gravity. Due to this, the equations and solution method used are identical, save the changes noted in this chapter for the conservation laws. When results are obtained, one will note the results are relative to the calculational coordinate system, see Figure 7.1. To obtain the results in the physical coordinate system, relative to the incline, the results are simply rotated to reflect the inclined geometry. This rotation is clearly reflected in Figure 7.2. One will note that the angle between the plume and the horizontal ground in Figure 7.2a appears to be smaller than the angle between the plume and the inclined ground in Figure 7.2b. This is due to the aspect ratio of the figures, the angles are identical.

The presentation of the results mirror those in Chapters 4 and 6, such that

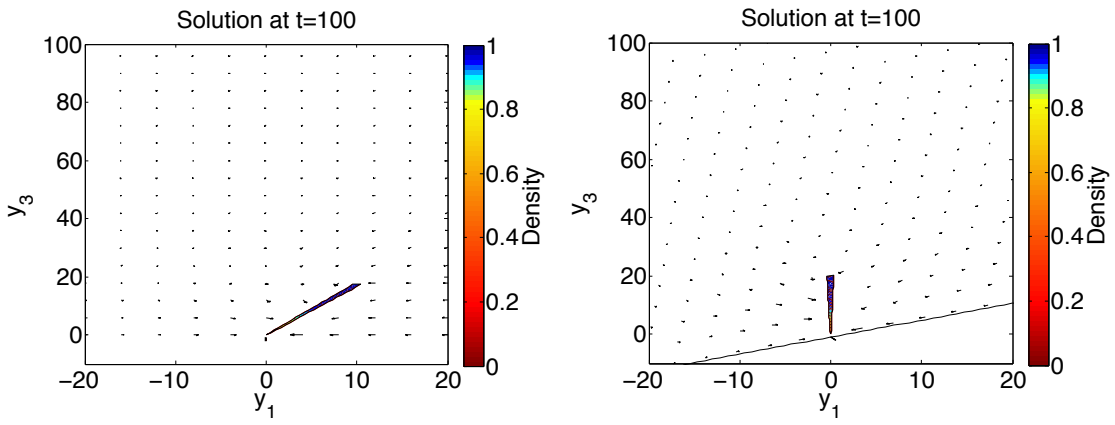

(a) Calculational Coordinates **(b) Physical Coordinates**

Figure 7.2: Results in Calculational and Physical Coordinate Systems

the shading of the plume is an indication of the density of the air, the arrows are an indication of the flow, and the black and red bars indicate the width of the fire and the distance the fire has traveled respectively. As with Chapter 6, the same change of reference was applied to the crosswind flow simulation from Chapter 4 to allow the fire to propagate.

The same frequency analysis that has been performed in each results section is again used to determine this time if the addition of an inclined slope to the system effects the frequency analysis. The results from the frequency analysis are again presented as a spectrogram and as plots in the frequency domain. Since the implementation of the equations has not changed from the fire model, the frequency dependence is identical to the results in Chapter 6.

7.3.1 Fire Propagation on an Inclined Slope

The same implementation of the equations from Chapter 5 is used for the fire propagating on a slope, with the small changes mentioned above. The results of the extension of the simple wildfire model are presented in Figure 7.3. The results do show a realistic behavior of fire propagating along the slope, while the plume reacts to the propagation of the fire.

Figure 7.3 depicts a plume, moving along the topography at various times throughout the simulation. Just as was found in Chapter 6, the plume does not

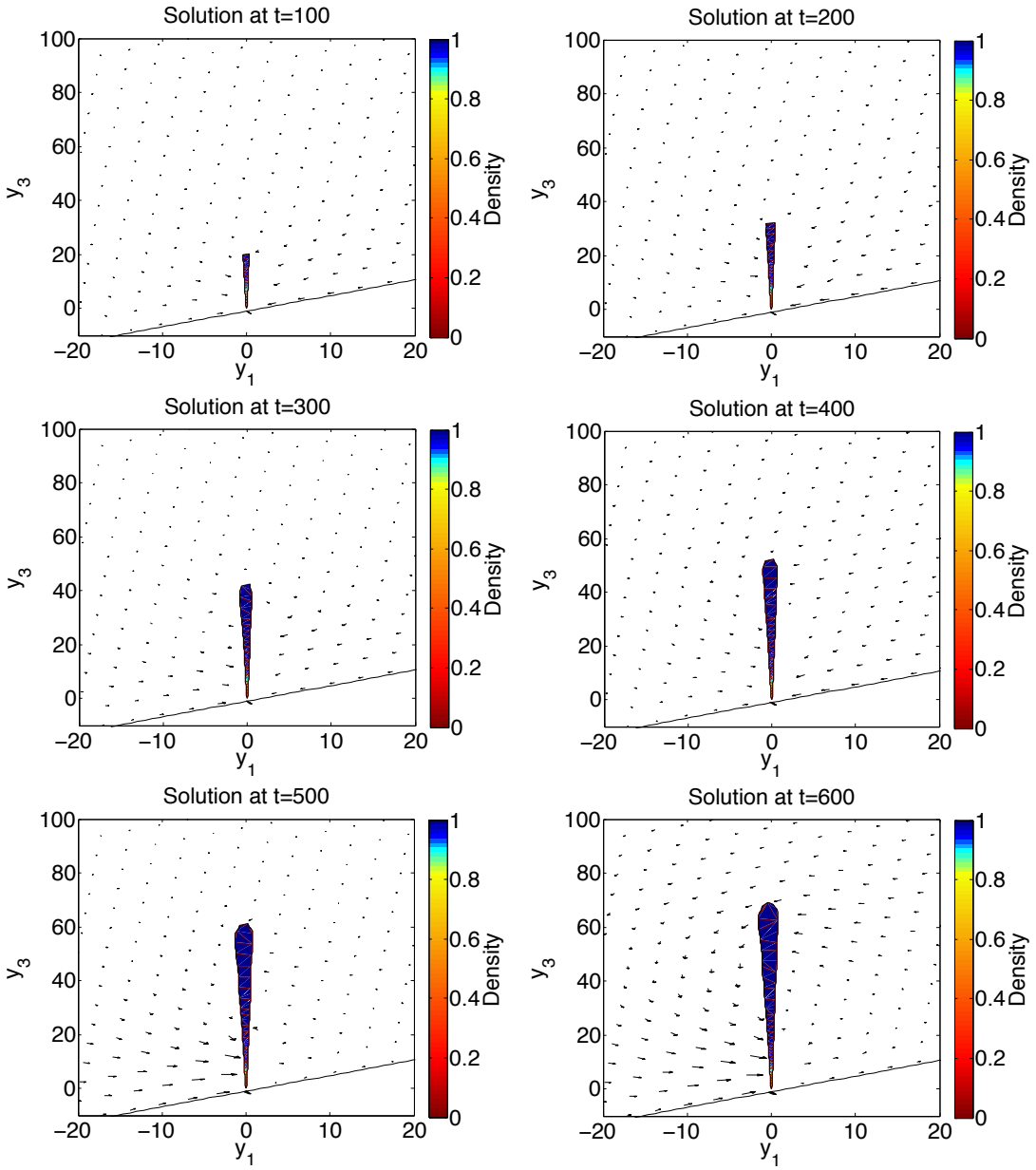

Figure 7.3: Numerical Solution for Slope Fire Model, $\varphi = 30$ Degrees

contain the puffing behavior that was expected. This can again be attributed to the simplified fire model. As before, the time in the title of these figures is scaled time.

One will note that the plume appears to remain nearly vertical throughout the duration of the simulation. This is an interesting result due to the fact that the results from the fire model indicate a significant curvature of the plume due to propagation. Additionally, as noted below, the propagation speed of the fire is

much slower than that of the fire model. All of this evidence points to the existence of an upslope flow that forces the plume to remain nearly vertical and slows the propagation speed of the fire.

As with the fire model, computation times averaged around six minutes, where the time lapse from the beginning of the simulation to the end of the simulation was 600. In true units of time, this represents 40 minutes of simulation time, which is well below real-time. In this amount of time, the fire, on average, has propagated about 1.3 units of length, or about 130m, for an approximate fire spread rate of $3.21 \frac{\text{m}}{\text{min}}$.

Again, the fire propagation can be visualized through the plot of fire propagation distance over time, as seen in Figure 7.4. The fire is again seen to propagate at a nearly constant rate, due to the quasi-steady state assumption. The fire propagation speed for various angles of the incline (and decline) were also investigated to determine if the model can capture the propagation accurately. Note here, that a negative angle corresponds to an incline, and a positive angle corresponds to a decline. As seen in Figure 7.5, one can see that the fire propagates faster on flat ground versus an incline. This result is counterintuitive, due to the fact that fires do propagate faster up inclines. This discrepancy is due to the absence of heat transfer in the fire model.

To investigate this further, consider why real fires propagate faster up inclines. On these inclines, there is a strong upslope flow that pushes the fire toward the unburned fuel. This is called flow attachment. After the flow is attached, the effects of radiation, conduction, and convection dominate, preheating the fuel so the fire can propagate faster up the slope.

In the simplified fire model presented here, the model does predict the presence of a strong upslope flow, but in the absence of the transfer of heat, the fire cannot propagate faster. Additionally, in this model, the strong upslope flow impedes the fire propagation due to the mechanics of fire propagation. A strong upslope flow means the downslope flow is small. In the case of an incline, the fire propagation speed is proportional to this downslope flow, hence, the fire propagates slower than on flat ground. This also explains why the fire propagates faster on the decline.

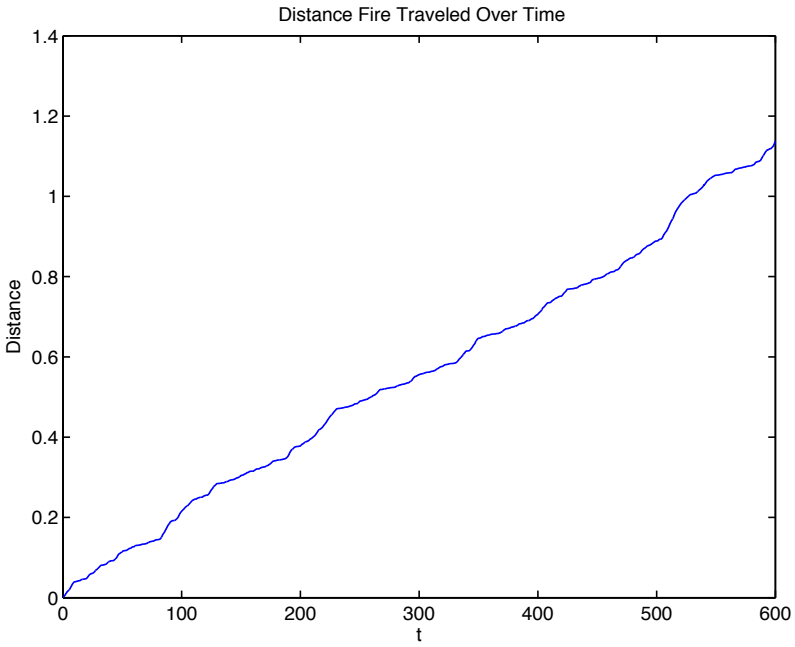

Figure 7.4: Progression of Fire Propagation

The strong upslope flow is then proportional to the fire propagation speed, which is large in this case.

This unphysical result can be addressed by allowing the effect of convection to preheat the fuel in a small region within the fuel layer. The hotter fuel will ignite faster, causing the fire to propagate more quickly as seen in nature.

7.3.2 Frequency Analysis

The same frequency analysis from Chapter 4 and 5 was performed on the same energies in the plume, enstrophy and kinetic energy. Since the implementation is identical to that of the fire model, the results of the frequency analysis are identical as well.

The power spectral density of the kinetic energy and enstrophy with values calculated by the fire model are shown in Figures 7.6 and 7.7. As before, upon closer examination of the kinetic energy, it is observed that there are random frequency responses, as seen if Figure 7.8. All conclusions drawn from the results in Chapter 6 can be applied here as well.

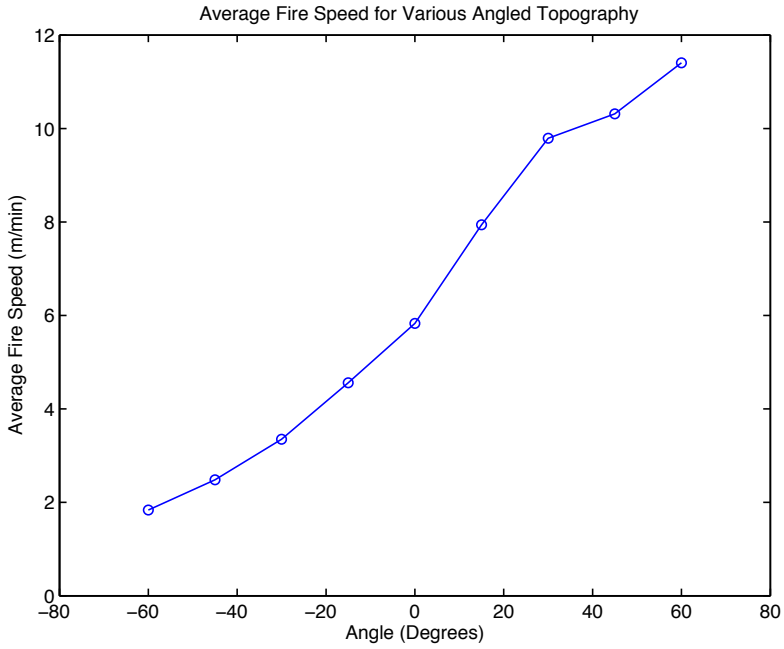

Figure 7.5: Fire Propagation Speed for Various Angled Topographies

7.4 Conclusions

The slope wildfire model developed in this Chapter is one possible extension of the simplified wildfire model developed in the previous chapters. The results in the previous section validate that the model can be successfully adapted to account for topography of land, which is one step toward a model that will be able to be implemented for field use.

The same conclusions can be drawn about the fire propagation characteristics as in the fire model. The fire tends to propagate quickly, then slows down while the fuel is consumed. It is an interesting result from the simulations used here, that the fire does propagate more slowly up the slope than on flat ground. The main reason fires do propagate faster up slopes is flow attachment, as seen in Chapter 1, which allows the fire to transfer energy more quickly to the fuel layer. This attachment is induced by an upslope flow that is stronger than the down slope flow, tilting the flame structure toward the fuel. In the absence of the transfer of energy, the slower propagation speed is due to the changes in air flow on the slope topography. In this model, the change in flow can result in the change in propagation speed.

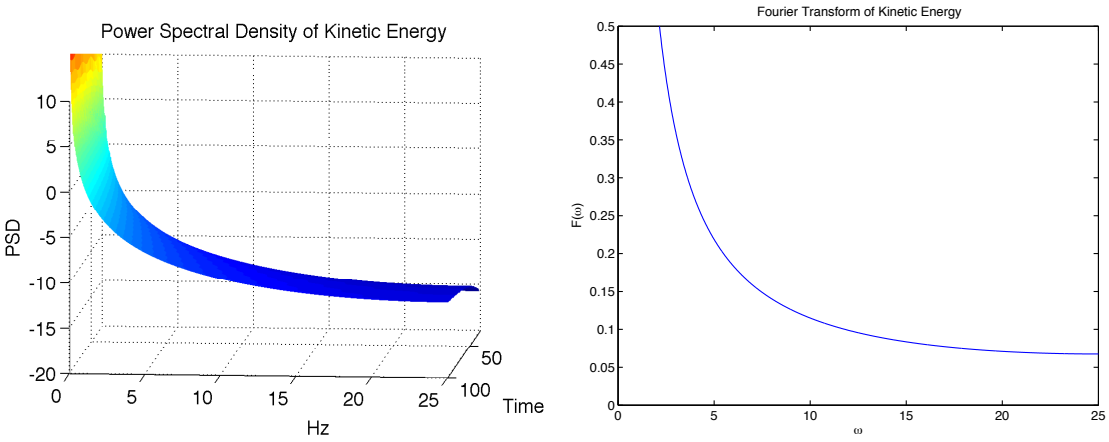

(a) Spectrogram (b) Fourier Transform at t_f

Figure 7.6: Fourier Transform of Kinetic Energy for Slope Fire Model Inputs

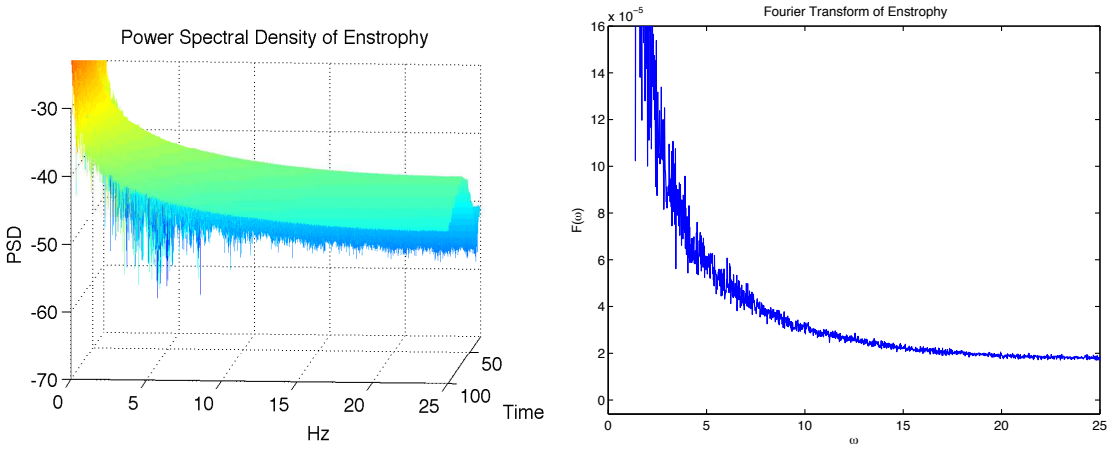

(a) Spectrogram (b) Fourier Transform at t_f

Figure 7.7: Fourier Transform of Enstrophy for Slope Fire Model Inputs

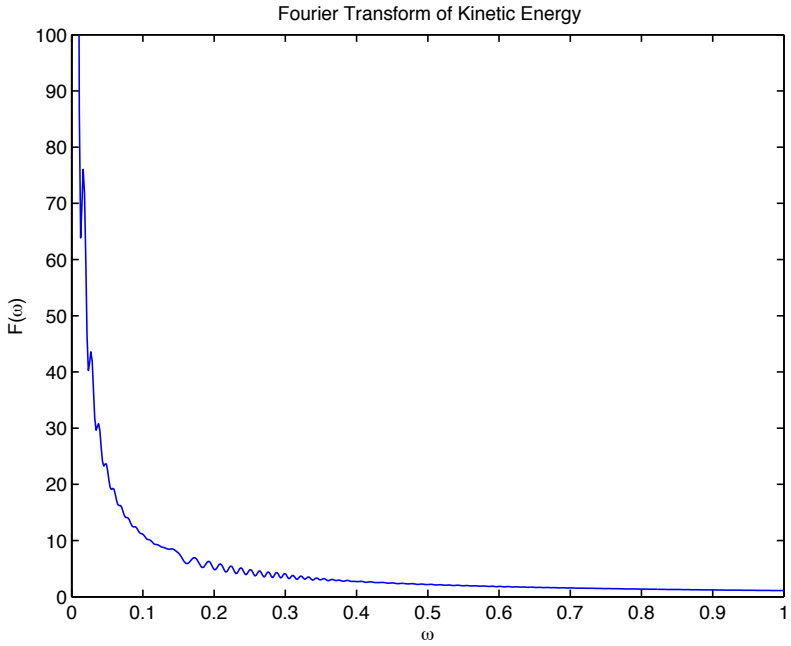

Figure 7.8: Magnified Fourier Transform of Kinetic Energy

CHAPTER 8
Future Work

There are several directions that can be investigated in moving this project forward. This model is still in its infancy, and there is still a large amount of work and verification to be done before the model can be integrated into a tool that can be used in the field. The basic framework and a working wildfire model, including models focused on the interaction between the plume, ambient air and the fire, has been provided in this thesis. The models were derived from first principles, effectively narrowing the focus of the models to the key driving dynamics of the systems. As was seen in all results chapters, the goal of reducing computation time has been achieved, where all results were obtained in faster than real-time computation speeds. The simplifying assumptions used to narrow the focus of the models sometimes sacrifices physical attributes of the problem. Future work in most cases will be focused on verifying and modifying the assumptions to match what physically occurs in nature, while asserting the fact that computation cost should be kept to a minimum.

8.1 Modification of Simplifying Assumptions

8.1.1 Plume Model

The plume model was derived by a method reminiscent of the solution to a boundary layer problem. In each solution (outer and inner) a perturbation expansion of the dependent variables was used to reduce the Navier-Stokes equations to a more manageable set of equations. Several first approximations were made by only using the first non-zero term from these asymptotic expansions.

In the ambient air system, these first non-zero approximations resulted in a linear profile of pressure, and constant density and temperature. This effectively restricts the validity of the model to low height plumes (of $O(\beta^{-1})$ in dimensional height). As the plume extends further into the atmosphere, the error in stratification will be more and more prominent. In future work, if more terms in the asymptotic

expansions of ambient air variables were used, (e. g., to an $O(\beta^2)$ approximation), the variation of pressure, density, and temperature with height would correct the effects of stratification to the ambient air system.

Inclusion of these terms in the ambient air system will extend the validity of this approach to much higher fire plumes. The more terms that are used from the expansions, the more accurate the expansion become. It must be noted that as more terms are retained in the expansions, the more complex the equations become. For example, the $O(\beta)$ vorticity equation for ω_1 depends on ω_0, and the density variation with height. Thus, the ambient air system is no longer incompressible at this order, so that a potential flow solution of the ambient air system is no longer valid.

In the plume system, only the first order contributions to the equations were considered. Additional orders and contributions can be considered to see if any additional dynamics contribute on other orders.

8.1.2 Fire Model

The fire model was derived using control volume balances under the assumption that only a fire region needs to be considered. Physically, there are four regions that are present: an unburned fuel region, a pyrolyzing fuel region, a fire region, and a smoldering fuel region, see Figure 1.2. The assumption that only a fire region needs to be considered induces an assumption of heat propagation. In this model, the fire propagates due to the supply stream of oxygen. The faster the supply oxygen moves, the faster the fire propagates. This assumes that the faster the supply stream brings oxygen to the fire, the faster the combustion reaction takes place and the faster the rate of consumption of fuel. This assumption does not allow for the transfer of heat from the fire to the fuel through radiation, convection, or conduction.

Future work would allow for a model in all four regions, tracking the exchange of mass and energy from each fuel state, and more importantly, the radiation of heat from the fire. Simple conservation laws can be used, derived through control volume arguments. This time the equations should allow for the energy contained within the bonds of the molecules, whereas the derivation of mass is similar to what has been

shown in this thesis. Radiation can be accounted by following a derivation due to Albini [4]. Fuel particles can be assumed to be black bodies, where the intensity of heat radiated from the fire is a decreasing function of both distance traveled through the fuel layer and the number of particles absorbing the energy as it passes. This could be achieved by calculating the distance of a fuel particle from the fire and integrating over the intensity of all fuel particles in the fire region within a line of sight. Allowing for this energy transfer would help the fire propagate by preheating the fuel, and is more physical than the assumption used here.

Allowing for multiple regions within the fire layer also induces other physical aspects of the problem. Consumed, or nearly consumed, fuel comprises the smoldering region. While cooling does occur within this region, say proportional to the ambient temperature (i.e., Newton's law of cooling), the consumed fuel is considerably hotter than the ambient temperature. Allowing for multiple regions would also mean allowing for non-constant ambient air properties such as a temperature jump across the plume. This would induce a pressure gradient across the plume, and a flow from high temperature to low temperature, facilitating the propagation of the fire. In addition to this, the existence of hotter matter in the system might locally increase the temperature of the ambient air, again inducing a flow in the region.

Although fire on slopes have been investigated in this thesis, the addition of the transport of heat to the fire model would drastically change the behavior of the fire. It is well known that when fires ascend slopes, they have the ability to attach to the slope, substantially increasing the speed at which the fire propagates. This attachment increases the heat transferred through radiation, convection, and conduction, heating the fuel faster and allowing the fire to propagate faster.

A simple improvement of the slope model presented in Chapter 7 could account for some heat transfer to allow the physical propagation of the fire. Specifically, the hot gas rising vertically from the fire has both a normal and tangential component when on a slope. The normal component represents the air rising into the fire plume, whereas the tangential component of this velocity will move hot air through the fuel layer. This hot air will preheat a small region of fuel, effectively accounting for the transfer of heat from the fire to the fuel through convection. Consequently, this

would provide the means necessary for the fire to propagate faster up inclines, and relatively equal propagation speeds for declines and flat ground.

Currently, the fire model only considers a homogeneous fuel bed. It is well known that in nature, the fuel load is rarely homogeneous. There are pockets of air between pine needles, and on a larger scale, there are empty spaces between trees and leaves. This influences the effective fuel load and the dynamics of the flow within the fuel layer. Allowing for a nonhomogeneous fuel bed would affect the propagation speed and behavior. Additionally, the vegetation layer is never smooth. Trees stick up at different heights and air can pass between all the air pockets between trees and leaves. The vegetation creates drag force on the ambient air as it is drawn into the fire. Not only is this a drag force, but as the air is drawn through the fuel layer, it becomes susceptible to heating due to the transfer of energy from the fire. These additional forces and heating will affect the amount and temperature of oxygen that is delivered to the fire, therefore affecting the behavior of the fire and its propagation speed.

Another exercise that could be used to test the capabilities of the model would be to combine several homogeneous fuel beds with different fuel compositions together to see the effects on the fire plume. Along the same lines, a topography could be pieced together in the same way, moving from flat ground to an incline and finally to a decline. Such simulations would determine if the model is capable of handling realistic topographies and fuel compositions such as those faced in the real world.

Combustion and pyrolyzation are complex sets of reactions that take place over varying time scales. There are many factors that influence the rates at which these reactions take place. Specifically, the moisture content of the fuel has a very large effect on the propagation speed of the fire. If the fuel first needs to be dried before pyrolyzation can occur, the fire will propagate much more slowly than it would if the fuel was already dried. The loss of moisture can be modeled as an evaporation process, where the water converts to vapor as it is heated. Using more complex and physical chemical reactions and the tracking of each of the species present in the reaction (i.e., oxygen, nitrogen, carbon, etc.) to model the transfer of species from fuel to by-products would allow the combustion process to be modeled much more

accurately.

This tracking of species could be complemented by a Lagrangian particle approach, where individual smoke and fuel particles are released at the fire. This would aid in the tracking of fuel consumed by the fire and additionally the visualization of the smoke. Particularly, the particles could give an indication to when the smoke has dissipated enough to return to the classification of ambient air.

While it is seen that there are many improvements that can be made to this simple wildfire model, it must be remembered that the goal of this work is to obtain a simplified model which can run at computation speeds faster than real-time. In order to keep this computation time reasonable for use in the field, physical attributes need to be balanced with computation times of implementation, meaning this model was never intended to be the most physically accurate model. Many models reviewed in Chapter 1 are extremely accurate due to the inclusion of detailed physical processes. However, these are the same models that require the use of CFD codes to solve the complex equations, greatly increasing the computation time.

8.2 Extensions of Wildfire Model

There are several extensions and different applications to which this simple model can be applied, and not all applications are specialized for fires. The plume model may be applied to any thermally buoyant sheet plume induced by a one-dimensional concentrated heat source, where the specialized two-dimensional geometry used this thesis may be applied. An example of this would be an extension to trench fires.

In examining extensions of the wildfire model as applied to wildfires, the most difficult of any future work will be to extend the models to a full three-dimensional geometry. This challenging task can be divided into two steps. First, as an intermediate step between the working model and a full three dimensional model, the perfectly straight fire line could be allowed the ability to curve. This curvature would be slowly varying, and include many different effects due to the propagation speed of different areas of the fire. For example, if the fire line was now assumed to have fixed length in the y_2 direction, one might see the ends travel slower than the

center of the fire line. This would effect the heating of fuel in front of the fire line, possibly speeding up the propagation of the ends of the fire line. This intermediate extension could be thought of physically as taking a section of a fire front, big enough to allow small variations, but not large enough that the variations in curvature are dominant. Additionally, with a third dimension, effects along the fire line need to be considered. Such effects might include flows along the fire line induced by gradients in temperature and pressure.

Finally, the full extension to a three-dimensional model can be made. This would involve rederiving and solving the governing equation in their three-dimensional form. The process of extension to a fully physical model can be though of as rederiving this work, without the simplifying assumptions used to narrow the focus of the model to the key driving dynamics of the fire plume and fire. The derivation and solution procedure would have to reflect the goal to keep computation time at a minimum.

At this point, the models presented above have been implemented in MATLAB, where all differential equations have been solved using first order accurate schemes in both time and space. To increase accuracy, at the expense of computation time, more accurate solution schemes could be developed to see the effect on the solution. Due to the time iterating solution method and the dependence of the solution on previous time steps chosen in this thesis, explicit methods in time should be used for ease of calculations. An additional computation time saving procedure that could be employed to save a small amount of time in the code would be the use of a Taylor series approximation of all trigonometric functions. It is known that trigonometric functions are computationally intensive to calculate, and using a few terms of the Taylor series could reduce some of this time. A majority of the code has been vectorized to decrease computation time, but some functions containing "for" loops are called a large number of times during the simulation. This has a large effect on the computation time by greatly increasing the number of computations needed to be performed.

It has been mentioned that a similar solution procedure could be achieved by implementation into any computer language. If field integration is an ultimate

goal, consideration of other computer languages might be a possible future project. MATLAB is an extremely high level computing language, and is well optimized for linear algebra computations. Fortran, C, or C++ may be a more suited option for development of a program which can be widely used by firefighters in the field. Additionally, integration for use in the field needs to account for actual topography of land, and more importantly real-time weather conditions. This would require the integration of the model with national weather and land topography databases, with constant real-time updates. This type of integration with real-time information would be critical to the accuracy of the model since it is well known that weather conditions and topography greatly effect the behavior of a fire.

As has been stated throughout this thesis, the model presented here was developed in the hope that a derivation using asymptotics and simplifying assumptions could accurately capture the behavior of a fire and fire plume. Inspiration from many sources, including the behavior of a flag flapping in the wind [1] and the behavior of indoor fires [63], have been used in the beginning derivation of this model, but ultimately as the derivation progressed, the approach became entirely novel. Results show that the model is a viable approach for predicting the behavior of these simplified wildfires. This model presents a simple approach to a complex problem, and in the hope that one day it will be used in the field, physical attributes need to be balanced with the computation time to allow well informed decisions to be made regarding firefighting efforts.

LITERATURE CITED

[1] S. Alben and M. Shelley, *Flapping states of a flag in an inviscid fluid: Bistability and the transition to chaos*, Phys. Rev. Lett., 100 (2008), pp. 074301–1–4.

[2] F. A. Albini, *A model for the wind-blown flame from a line fire*, Combust. Flame, 43 (1981), pp. 155–174.

[3] F. A. Albini, *Wildland fires: Predicting the behavior of wildland fires–among nature's most potent forces–can save lives, money, and natural resources*, Amer. Sci., 72 (1984), pp. 590–597.

[4] F. A. Albini, *A model for fire spread in wildland fuels by radiation*, Combust. Sci. Technol., 42 (1985), pp. 229–258.

[5] D. Artley, R. Mangan, P. Moy, P. Schaenman, P. Woodard, M. DeGrosky, M. Argabright, and B. O'Brien, *Large fire cost review for FY2009*, Guidance Group, Inc., Eatonville, WA, August 2010.

[6] M. I. Asensio and L. Ferragut, *On a wildland fire model with radiation*, Int. J. Numer. Methods Eng., 54 (2002), pp. 137–157.

[7] V. Babrauskas and R. D. Peacock, *Heat release rate: The single most important variable in fire hazard*, Fire Safety Journal, 18 (1992), pp. 255–272.

[8] J.H. Balbi, Jean Louis Rossi, Thierry Marcelli, and P.A. Santoni, *A 3D physical real-time model of surface fires*, Combust. Sci. Technol., 179 (2007), pp. 2511–2537.

[9] J. H. Balbi, F. Morandini, X. Silvani, J. B. Filippi, and F. Rinieri, *A physical model for wildland fires*, Combust. Flame, 156 (2009), pp. 2217–2230.

[10] J. H. Balbi, J. L. Rossi, T. Marcelli, and F. J. Chatelon, *Physical modeling of surface fire under nonparallel wind and slope conditions*, Combust. Sci. Technol., 182 (2010), pp. 922–939.

[11] J. H. Balbi, P. A. Santoni, and J. L. Dupuy, *Dynamic modelling of fire spread across a fuel bed*, Int. J. Wildland Fire, 9 (1999), pp. 275–284.

[12] E. Ballam, *Searching for answers: Researchers working toward reliable indoor tracking devices*, Firehouse, 36 (2011), pp. 80–81.

[13] H. R. Baum and K. B. McGrattan, *Simulation of large industrial outdoor fires*, in Fire Safety Science–Proceedings of the Sixth International Symposium, M. Curtat, ed., Int. Assoc. for Fire Safety Science, Poitiers, France, 2000, pp. 611–622.

[14] H. R. Baum, K. B. McGrattan, and R. G. Rehm, *Three dimensional simulations of fire plume dynamics*, in Fire Safety Science–Proceedings of the Fifth International Symposium, Y. Hasemi, ed., Int. Assoc. for Fire Safety Science, Melbourne, Australia, 1997, pp. 511–522.

[15] L. Boudin and J. Mathiaud, *A numerical scheme for the one-dimensional pressureless gases system*, Numer. Methods Part. D. E., (2011), pp. 1–18.

[16] N. Bryner, D. Madrzykowski, and D. W. Stroup, *Performance of thermal exposure sensors in personal alert safety system (PASS) devices*, National Institute of Standards and Technology, Gaithersburg, MD, 2005.

[17] M. Carmo, F. Moreira, P. Casimiro, and P. Vaz, *Land use and topography influences on wildfire occurrence in northern Portugal*, Landscape Urban Plan., 100 (2011), pp. 169–176.

[18] S. L. Caudle, I. A. Munn, M. V. Frank, and E. G. Niemi, *Fiscal year 2008 large-cost fire independent review*, ECONorthwest, Eugene, OR, 2009.

[19] K. Chetehouna, M. Er-Riani, and O. Séro-Guillaume, *On the rate of spread for some reaction-diffusion models of forest fire propagation*, Numer. Heat Transf., Part A, 46 (2004), pp. 765–784.

[20] J. W. Dold and A. Zinoviev, *Fire eruption through intensity and spread rate interaction mediated by flow attachment*, Combust. Theor. Model., 13 (2009), pp. 763–793.

[21] J. W. Dold, A. Zinoviev, and E. Leslie, *Intensity accumulation in unsteady firelines: A simple model for vegetation engagement*, Fire Safety Journal, 46 (2011), pp. 63–69.

[22] M. K. Donnelly, W. D. Davis, J. R. Lawson, and M. J. Selepak, *Thermal environment for electronic equipment used by first responders*, National Institute of Standards and Technology, Gaithersburg, MD, 2006.

[23] A. Hernández Encinas, L. Hernández Encinas, S. Hoya White, A. Martín del Rey, and G. Rodríguez Sánchez, *Simulation of forest fire fronts using cellular automata*, Adv. Eng. Software, 38 (2007), pp. 372–378.

[24] T. Fabian, J. L. Borgerson, S. I. Kerber, P. D. Gandhi, C. S. Baxter, C. S. Ross, J. E. Lockey, and J. M. Dalton, *Firefighter exposure to smoke particulates*, Underwriters Laboratories Inc., Northbrook, IL, 2010.

[25] W. L. Fons, *Analysis of fire spread in light forest fuels*, J. Agric. Res., 72 (1946), pp. 93–121.

[26] P. G. Georgopoulos and J. H. Seinfeld, *Mathematical modeling of turbulent reacting plumes–I. General theory and model formulation*, Atmos. Environ., 20 (1986), pp. 1791–1807.

[27] B. Harvey, *Thermal imaging in wildland firefighting*, Firehouse, 36 (2011), pp. 50–53.

[28] G. Heskestad, *Dynamics of the fire plume*, Philos. Trans. R. Soc. Lond. Ser. A Math. Phys. Eng. Sci., 356 (1998), pp. 2815–2833.

[29] M. H. Holmes, *Introduction to the Foundations of Applied Mathematics*, 1st ed., Springer, New York, NY, 2009.

[30] International Fire Service Training Association Committee, *Essentials of Fire Fighting*, 4th ed., Fire Protection Publications, Stillwater, OK, 1998.

[31] I. Karafyllidis, *Design of a dedicated parallel processor for the prediction of forest fire spreading using cellular automata and genetic algorithms*, Eng. Appl. Artif. Intell., 17 (2004), pp. 19–36.

[32] P. Kaval, *Perceived and actual wildfire danger: An economic and spatial analysis study in Colorado (USA).*, J. Environ. Management, 90 (2009), pp. 1862–7.

[33] S. Kerber, *Impact of ventilation on fire behavior in legacy and contemporary residential construction*, Underwriters Laboratories Inc., Northbrook, IL, 2010.

[34] R. Krasny, *Desingularization of periodic vortex sheet roll-up*, J. Comput. Phys., 65 (1986), pp. 292–313.

[35] J. R. Lawson, *Fire fighters' protective clothing and thermal environments of structural fire fighting*, National Institute of Standards and Technology, Gaithersburg, MD, 1996.

[36] J. R. Lawson and R. L. Vettori, *Thermal measurements for fire fighters' protective clothing*, ASTM Spec. Tech. Publ., 1427 (2003), pp. 163–177.

[37] J. R. Lawson, W. D. Walton, N. P. Bryner, and F. K. Amon, *Estimates of thermal properties for fire fighters' protective clothing materials*, National Institute of Standards and Technology, Gaithersburg, MD, 2005.

[38] R. J. LeVeque, *Numerical Methods for Conservation Laws*, 2nd ed., Birkhäuser Verlag, Boston, MA, 1992.

[39] R. R. Linn, J. L. Winterkamp, D. R. Weise, and C. Edminster, *A numerical study of slope and fuel structure effects on coupled wildfire behaviour*, Int. J. Wildland Fire, 19 (2010), pp. 179–201.

[40] T. Ma and J. G. Quintiere, *Numerical simulation of axi-symmetric fire plumes: Accuracy and limitations*, Fire Safety Journal, 38 (2003), pp. 467–492.

[41] D. Madrzykowski, *Fatal training fires: Fire analysis for the fire service*, in International Interflam Conference, 11th Proceedings, London, England, 2007, pp. 1169–1180.

[42] D. Madrzykowski and D. W. Stroup, *Flammability hazard of materials*, in Fire Protection Handbook, 20th ed., A. E. Cote, C. C. Grant, Jr. Hall, J. R., and R. E. Solomon, eds., National Fire Protection Assoc., Quincy, MA, 2008, pp. 31–48.

[43] L. Malangone, P. Russo, and S. Vaccaro, *Effects of wind and terrain slope on flames propagation in a vegetative fuel bed*, in XXXIV Meeting of the Italian Section of the Combustion Institute, Rome, Italy, 2011, pp. 1–6.

[44] J. Margerit and O. Séro-Guillaume, *Modelling forest fires. part II: Reduction to two-dimensional models and simulation of propagation*, Int. J. Heat Mass Transf., 45 (2002), pp. 1723–1737.

[45] J. S. Marshall, *Inviscid Incompressible Flow*, Wiley-Interscience, New York, NY, 2001.

[46] S. McAllister, I. Grenfell, A. Hadlow, W. M. Jolly, M. Finney, and J. Cohen, *Piloted ignition of live forest fuels*, Fire Safety Journal, 51 (2012), pp. 133–142.

[47] R. J. McDermott, G. P. Forney, K. B. McGrattan, and W. E. Mell, *Fire Dynamics Simulator Version 6: Complex geometry, embedded meshes, and quality assessment*, in V European Conference on Computational Fluid Dynamics ECCOMAS CFD, C. F. Pereira, A. Sequeira, and J. M. C. Pereira, eds., Lisbon, Portugal, 2010.

[48] T. McNeal, *Wildland urban interface: Ensuring the "defensibility" of defensible space*, Fire Eng., 164 (2011), pp. 81–84.

[49] W. E. Mell, M. A. Jenkins, J. Gould, and P. Cheney, *A physics-based approach to modelling grassland fires*, Int. J. Wildland Fire, 16 (2007), pp. 1–22.

[50] W. E. Mell, M. A. Jenkins, J. Gould, and P. Cheney, *A physics-based approach to modelling grassland fires*, Accessory Publication: Int. J. Wildland Fire, 16 (2007), pp. 1–22.

[51] W. E. Mell, S. L. Manzello, A. Maranghides, D. Butry, and R. G. Rehm, *The wildland–urban interface fire problem–current approaches and research needs*, Int. J. Wildland Fire, 19 (2010), pp. 238–251.

[52] G. N. Mercer and R. O. Weber, *Radiation enhanced combustion wave speeds*, Proc. R. Soc. Lond. Ser. A Math. Phys. Eng. Sci., 453 (1997), pp. 1543–1549.

[53] R. Montenegro, A. Plaza, L. Ferragut, and M. I. Asensio, *Application of a nonlinear evolution model to fire propagation*, Nonlinear Anal., 30 (1997), pp. 2873–2882.

[54] F. Morandini, P A. Santoni, and J. H. Balbi, *The contribution of radiant heat transfer to laboratory-scale fire spread under the influences of wind and slope*, Fire Safety Journal, 36 (2001), pp. 519–543.

[55] B. R. Morton, G. Taylor, and J. S. Turner, *Turbulent gravitational convection from maintained and instantaneous sources*, Proc. R. Soc. Lond. Ser. A Math. Phys. Eng. Sci., 234 (1956), pp. 1–23.

[56] D. Morvan and J. L. Dupuy, *Modeling of fire spread through a forest fuel bed using a multiphase formulation*, Combust. Flame, 127 (2001), pp. 1981–1994.

[57] D. Morvan, J. L. Dupuy, B. Porterie, and M. Larini, *Multiphase formulation applied to the modeling of fire spread through a forest fuel bed*, Proc. Combust. Inst., 28 (2000), pp. 2803–2809.

[58] R. Ottmar and A. Andreu, *Litter and duff bulk densities in the southern United States*, USDA Forest Service, Seattle, WA, 2007.

[59] E. Pastor, L. Zarate, J. Planas, and J. Arnaldos, *Mathematical models and calculation systems for the study of wildland fire behaviour*, Prog. Energy Combust. Sci., 29 (2003), pp. 139–153.

[60] J. J. Pauly, *The Great Chicago Fire as a national event*, Amer. Quart., 36 (1984), pp. 668–683.

[61] B. Porterie, D. Morvan, M. Larini, and J. C. Loraud, *Wildfire propagation: A two-dimensional multiphase approach*, Combust. Explo. Shock Waves, 34 (1998), pp. 26–38.

[62] S. Potter, *Retrospect: October 8, 1871: The Great Chicago Fire.*, Weatherwise, 63 (2010), pp. 10–13.

[63] R. G. Rehm and H. R. Baum, *The equations of motion for thermally driven, buoyant flows*, J. Res. National Bureau Standards, 83 (1978), pp. 297–308.

[64] D. N. Riahi, *Analysis and modeling for a turbulent convective plume*, Math. Comput. Modelling, 28 (1998), pp. 57–63.

[65] C.F. Schemel, A. Simeoni, H. Biteau, J.D. Rivera, and J.L. Torero, *A Calorimetric Study of Wildland Fuels*, Exp. Thermal Fluid Sci., 32 (2008), pp. 1381–1389.

[66] O. Séro-Guillaume and J. Margerit, *Modelling forest fires part I: A complete set of equations derived by extended irreversible thermodynamics*, Int. J. Heat Mass Transf., 45 (2002), pp. 1705–1722.

[67] A. Simeoni, P. A. Santoni, M. Larini, and J. H. Balbi, *Reduction of a multiphase formulation to include a simplified flow in a semi-physical model of fire spread across a fuel bed*, Int. J. Thermal Sci., 42 (2003), pp. 95–105.

[68] D. R. Steppan and M. J. Pabich, *Performance of special extinguishment agents for firefighter use*, Underwriters Laboratories Inc., Northbrook, IL, 2008.

[69] W. Tachajapong, J. Lozano, S. Mahalingam, X. Zhou, and D. R. Weise, *An investigation of crown fuel bulk density effects on the dynamics of crown fire initiation in shrublands*, Combust. Sci. Technol., 180 (2008), pp. 593–615.

[70] J. W. Thomas, *Numerical Partial Differential Equations: Finite Difference Methods*, Springer, New York, NY, 1995.

[71] United States Department of Agriculture Forest Service, *Fire and aviation management fiscal year 2010 accountability report*, United States Department of Agriculture Forest Service, Washington, DC, 2011.

[72] G. C. Vaz, J. C. S. Andre, and D. X. Viegas, *Fire spread model for a linear front in a horizontal solid porous fuel bed in still air*, Combust. Sci. Technol., 176 (2004), pp. 135–182.

[73] D. X. Viegas, *Forest fire propagation*, Philos. Trans. R. Soc. Lond. Ser. A Math. Phys. Eng. Sci., 356 (1998), pp. 2907–2928.

[74] R. O. Weber, *Toward a comprehensive wildlife spread model*, Int. J. Wildland Fire, 1 (1991), pp. 245–248.

[75] A. L. Westerling, A. Gershunov, T. J. Brown, D. R. Cayan, and M. D. Dettinger, *Climate and wildfire in the western United States*, Bull. Amer. Meteorological Soc., 84 (2003), pp. 595–604.

[76] F. Westley, *Table of recommended rate constants for chemical reactions occurring in combustion*, National Standard Reference Data System, 67 (1980), pp. 1–110.

[77] Y. B. Zel'Dovich, *Gravitational instability: An approximate theory for large density perturbations*, Astronom. Astrophys., 5 (1970), pp. 84–89.

APPENDIX A
Conservation Laws by Control Volume Argument

The derivation of the plume system in Chapter 2 is based on reducing the Navier-Stokes equations to the one-dimensional transport equations of mass, momentum, energy, and vorticity for flow in a narrow channel. However, this derivation is only valid for a nearly vertical plume. In this Appendix, I present a derivation of the same system from a conservation argument parametrized for a curvilinear coordinate system.

A.1 Formulation

The plume need not be vertical, in fact, it is much more interesting to see the plume react to its surroundings. Here, the plume is taken to be narrow and $(y_{1\,p}(s,\tau), y_{3\,p}(s,\tau))$ is the plume centerline, where s is arc-length.

Let $b(s,\tau)$ be the width of the plume, and let the plume variables be defined as follows: R is the density, V is velocity in the s direction (along the plume), w is transverse velocity, Θ is temperature, and Ω is vorticity. Here s is the spatial variable along the plume (i.e., tangent to the centerline), ν is the spatial variable normal to the plume, see figure A.1. The essence of the control volume argument is that all functions are parameterized with respect to arc-length, s. Specifically, while V could depend on s, ν, and τ, it is assumed that it is a function of only s and τ. Equations of mass, axial momentum, transverse momentum, energy, and vorticity are derived by examining the balance of mass, momentum, and energy for a control volume lying between an arbitrary location s along the plume and a "nearby" location $s + \Delta s$.

The transverse momentum equation used for this derivation gives the result:

$$\frac{\partial P}{\partial \nu} = O(\sigma), \tag{A.1.1}$$

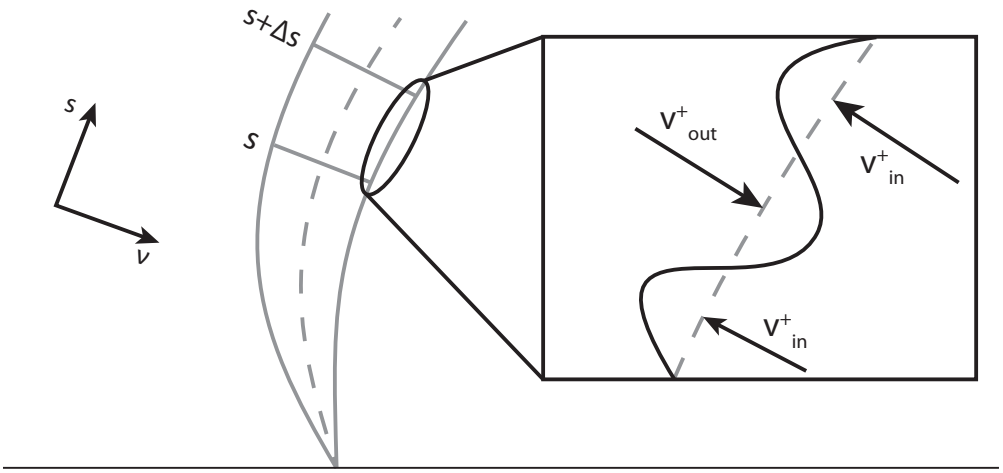

Figure A.1: Entrainment Model and Conservation Coordinates in Upper Half-Plane

which implies from the asymptotic expansion of pressure:

$$\frac{\partial P^{(H)}}{\partial \nu} = 0 \qquad \frac{\partial P^{(H1)}}{\partial \nu} = 0 \qquad \frac{\partial P^{(1)}}{\partial \nu} = O(1).$$

This result is used in several of the derivations and can be seen in Section A.4.

The $\star^{\pm}$ notation denotes whether the outer, or ambient air variable, is evaluated on the right or left side if the plume, respectively. Let $v^{\pm}_{in\backslash out}$ be the entrainment or mixing velocity into or out of the plume. This means that v^{+}_{out} is the velocity of the air on the right-hand side of the plume being mixed out of the plume. Similarly v^{+}_{in} represents the velocity of the air on the right-hand side of the plume being mixed into the plume, again see figure A.1.

A.2 Conservation of Mass

The rate of change of the mass in the control volume is equal to the net rate at which mass enters the control volume, which is equal to the inflow rate minus the outflow rate. Namely, the mass in the control volume is taken as $R(s,\tau)b(s,\tau)\Delta s\Delta y_2$, where Δy_2 is the depth of the control volume (into the page). Then:

$$\frac{\partial}{\partial \tau}(Rb\Delta s\Delta y_2) = \text{flux in} - \text{flux out}$$

$$
\begin{aligned}
&= RbV|_s \Delta y_2 - RbV|_{s+\Delta s} \Delta y_2 + R_o^+ v_{in}^+ \Delta s \Delta y_2 \\
&\quad + R_o^- v_{in}^- \Delta s \Delta y_2 - R v_{out}^+ \Delta s \Delta y_2 - R v_{out}^- \Delta s \Delta y_2 \\
\frac{\partial}{\partial \tau}(Rb) &= \frac{RbV|_s - RbV|_{s+\Delta s}}{\Delta s} + R_o^+ v_{in}^+ + R_o^- v_{in}^- - R v_{out}^+ - R v_{out}^-.
\end{aligned}
$$

Taking the limit as $\Delta s \to 0$ gives:

$$
\frac{\partial}{\partial \tau}(Rb) = -\frac{\partial}{\partial s}(RbV) + R_o^+ v_{in}^+ + R_o^- v_{in}^- - R v_{out}^+ - R v_{out}^-. \tag{A.2.1}
$$

Using the same scalings as in Chapter 2 and the fact that $l_3 \approx l_1$, the scaled mass equation can be written as:

$$
\frac{\partial}{\partial \tau}(Rb) = -\frac{\partial}{\partial s}(RbV) + R_o^+ v_{in}^+ + R_o^- v_{in}^- - R v_{out}^+ - R v_{out}^- = -\frac{\partial}{\partial s}(RbV) + S_m. \tag{A.2.2}
$$

A.3 Conservation of Axial Momentum

Again, the amount of momentum in the control volume is written as $R(s,\tau)b(s,\tau)V(s,\tau)\Delta s \Delta y_2$. Then, the balance of momentum is expressed as:

$$
\begin{aligned}
\frac{\partial}{\partial \tau}(RbV \Delta s \Delta y_2) &= \text{flux in} - \text{flux out} + \text{supply} \\
&= RbV^2\big|_s \Delta y_2 - RbV^2\big|_{s+\Delta s} \Delta y_2 + R_o^+ V_{t+} v_{in}^+ \Delta s \Delta y_2 \\
&\quad + R_o^- V_{t-} v_{in}^- \Delta s \Delta y_2 - RV v_{out}^+ \Delta s \Delta y_2 \\
&\quad - RV v_{out}^- \Delta s \Delta y_2 + Pb|_s \Delta y_2 - Pb|_{s+\Delta s} \Delta y_2 \\
&\quad + P\left(b|_{s+\Delta s} - b|_s\right) \Delta y_2 - Rbg_{||} \Delta s \Delta y_2.
\end{aligned} \tag{A.3.1}
$$

The second to last term expresses the difference in pressure force due to the variation of the width of the control volume. Also, $g_{||}$ is the component of gravity in the s direction, $g_{||} = g\frac{\partial y_3}{\partial s} = g\mathbf{e}_g \cdot \mathbf{T}$.

The expression for the pressure force due to the variation in the width of the plume in (A.3.1) can be derived as follows. Upon examining Figure A.2, one can see that:

$$
\frac{1}{2}b(s+\Delta s) - \frac{1}{2}b(s) \approx \frac{1}{2}b(s) + \frac{1}{2}\Delta s \frac{\partial b}{\partial s} + \ldots - \frac{1}{2}b(s)
$$

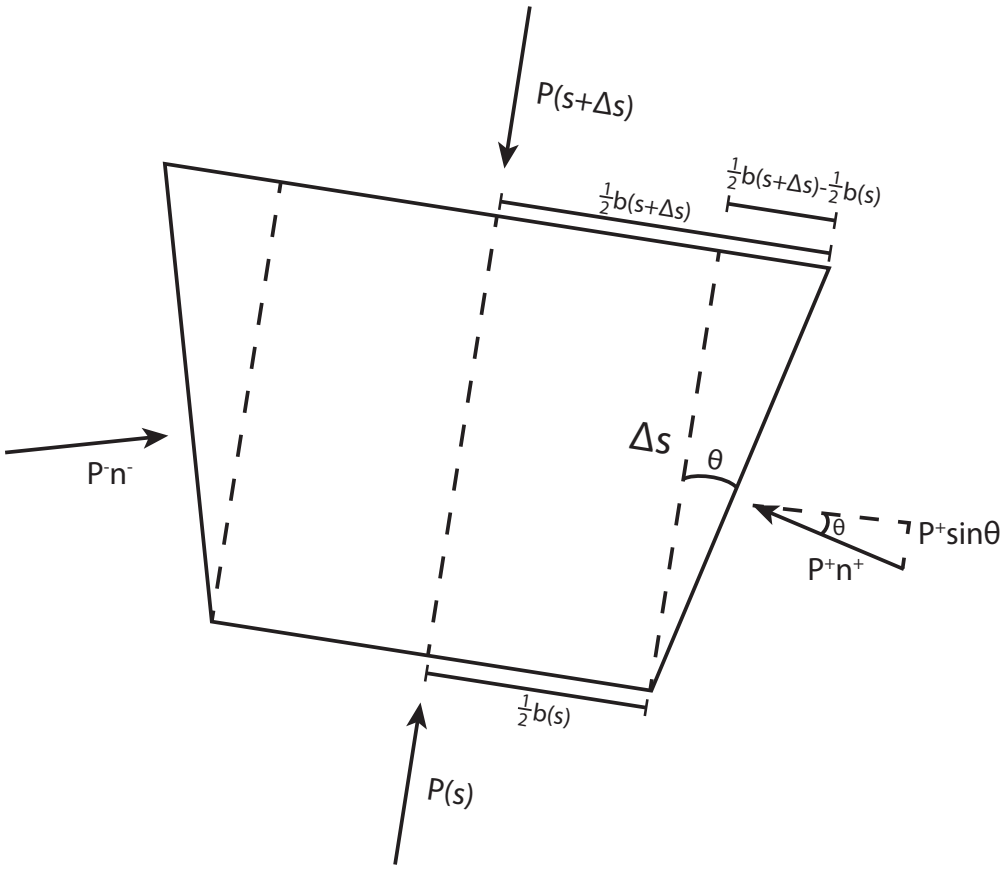

Figure A.2: Pressure on the Control Volume

$$= \frac{1}{2}\Delta s \frac{\partial b}{\partial s} + O(\Delta s^2).$$

The vector $P^+\mathbf{n}^+$ is resolved into its s and ν components as seen in Figure A.3. Additionally, one can see that if $\frac{\partial b}{\partial s}$ is small:

$$\begin{aligned}\sqrt{\Delta s^2 + \left(\frac{\Delta s}{2}\frac{\partial b}{\partial s}\right)^2} &= \Delta s\sqrt{1 + \left(\frac{1}{2}\frac{\partial b}{\partial s}\right)^2} \\ &\approx \Delta s + \Delta s\left(\frac{1}{2}\left(\frac{\partial b}{\partial s}\right)^2\right) + \dots \\ &\approx \Delta s,\end{aligned}$$

and the two triangles in Figure A.3 are similar. From this it is seen that $\sin\theta \approx \frac{1}{2}\frac{\partial b}{\partial s}$ and $P^+\sin\theta = P^+\mathbf{n}^+ \cdot \mathbf{e}_s \approx \frac{1}{2}P^+\frac{\partial b}{\partial s}$.

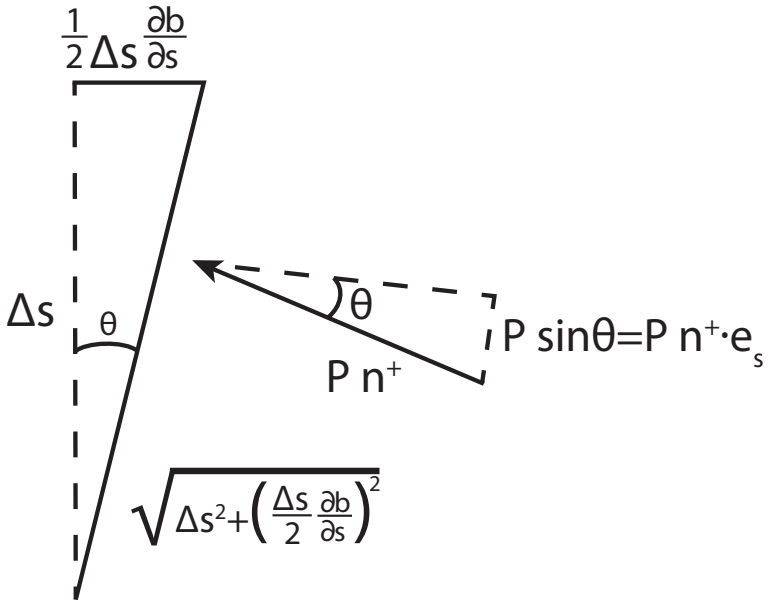

Figure A.3: Resolved Pressure Vector

A similar argument could be used to find the expression for P^-, but since equation (A.1.1) implies that the leading order pressures are equal on either side of the plume, the expression is not needed. Thus, the contribution of the pressure force due to the variations in the width of the plume in (A.3.1) is doubled.

After manipulation, (A.3.1) can be written as:

$$\begin{aligned}\frac{\partial}{\partial\tau}(RbV) = \frac{RbV^2|_s - RbV^2|_{s+\Delta s}}{\Delta s} + R_o^+ V_{t+} v_{in}^+ + R_o^- V_{t-} v_{in}^- - \\ RVv_{out}^+ - RVv_{out}^- + \frac{Pb|_s - Pb|_{s+\Delta s}}{\Delta s} \\ + P\left(\frac{b|_{s+\Delta s} - b|_s}{\Delta s}\right) - Rbg_{||}.\end{aligned}$$

Taking the limit as $\Delta s \to 0$ yields the final form of the conservation of momentum equation:

$$\begin{aligned}\frac{\partial}{\partial\tau}(RbV) = -\frac{\partial}{\partial s}(RbV^2) + R_o^+ V_{t+} v_{in}^+ + R_o^- V_{t-} v_{in}^- - RVv_{out}^+ - RVv_{out}^- \\ - b\frac{\partial P}{\partial s} - Rbg_{||}.\end{aligned} \tag{A.3.2}$$

Using the asymptotic expansions for pressure, (2.2.7), where scalings similar to what was used in the previous derivations are implied and the definition of β is used, it is easily seen that:

$$\frac{\partial P}{\partial s} = \frac{\partial y_3}{\partial s}\frac{\partial P}{\partial y_3} \tag{A.3.3}$$

$$= -g\frac{\partial y_3}{\partial s}. \tag{A.3.4}$$

Thus,

$$\frac{\partial}{\partial \tau}(RbV) = -\frac{\partial}{\partial s}(RbV^2) + R_o^+ V_{t+} v_{in}^+ + R_o^- V_{t-} v_{in}^- - RVv_{out}^+ - RVv_{out}^- + (1-R)gb\frac{\partial y_3}{\partial s}. \tag{A.3.5}$$

The scaled axial momentum equation can be written in the same way as:

$$\begin{aligned}
\frac{\partial}{\partial \tau}(RbV) &= -\frac{\partial}{\partial s}(RbV^2) + R_o^+ V_{t+} v_{in}^+ + R_o^- V_{t-} v_{in}^- - RVv_{out}^+ - RVv_{out}^- \\
&\quad + \frac{t_0^2}{l_3}(1-R)gb\frac{\partial y_3}{\partial s} \\
\frac{\partial}{\partial \tau}(RbV) &= -\frac{\partial}{\partial s}(RbV^2) + R_o^+ V_{t+} v_{in}^+ + R_o^- V_{t-} v_{in}^- - RVv_{out}^+ - RVv_{out}^- \\
&\quad + (1-R)\tilde{g}b\frac{\partial y_3}{\partial s} \\
\frac{\partial}{\partial \tau}(RbV) &= -\frac{\partial}{\partial s}(RbV^2) + S_M + (1-R)\tilde{g}b\frac{\partial y_3}{\partial s}.
\end{aligned} \tag{A.3.6}$$

A.4 Conservation of Transverse Momentum

The amount of transverse momentum in the control volume is written as $R(s,\tau)b(s,\tau)w(s,\tau)\Delta s\Delta y_2$. The balance of momentum is expressed as:

$$\begin{aligned}
\frac{\partial}{\partial \tau}(Rbw\Delta s\Delta y_2) &= \text{flux in} - \text{flux out} + \text{supply} \\
&= RwbV|_s\,\Delta y_2 - RwbV|_{s+\Delta s}\,\Delta y_2 + R_o^+ V_{n+} v_{in}^+ \Delta s\Delta y_2 \\
&\quad + R_o^- V_{n-} v_{in}^- \Delta s\Delta y_2 - Rwv_{out}^+ \Delta s\Delta y_2 - Rwv_{out}^- \Delta s\Delta y_2 \\
&\quad - P^+\Delta y_2\Delta s + P^-\Delta y_2\Delta s - Rbg\frac{\partial y_3}{\partial \nu}\Delta y_2\Delta s.
\end{aligned} \tag{A.4.1}$$

Thus:

$$\frac{\partial}{\partial \tau}(Rbw) = \frac{RbwV|_s - RbwV|_{s+\Delta s}}{\Delta s} + R_o^+ V_{n+} v_{in}^+ + R_o^- V_{n-} v_{in}^- - Rwv_{out}^+ - Rwv_{out}^- - P^+ + P^- - Rbg\frac{\partial y_3}{\partial \nu}.$$

Taking the limit as $\Delta s \to 0$ yields the conservation of transverse momentum equation:

$$\begin{aligned}\frac{\partial}{\partial \tau}(Rbw) &= -\frac{\partial}{\partial s}(RbwV) + R_o^+ V_{n+} v_{in}^+ + R_o^- V_{n-} v_{in}^- - Rwv_{out}^+ - Rwv_{out}^- - \Delta P \\ &\quad - Rbg\frac{\partial y_3}{\partial \nu} \\ &= -\frac{\partial}{\partial s}(RbwV) + R_o^+ V_{n+} v_{in}^+ + R_o^- V_{n-} v_{in}^- - Rwv_{out}^+ - Rwv_{out}^- \\ &\quad - \int_{y_{1\,p}-\frac{b}{2}}^{y_{1\,p}+\frac{b}{2}} \frac{\partial P}{\partial \nu}\,\mathrm{d}s - Rbg\frac{\partial y_3}{\partial \nu} \\ &= -\frac{\partial}{\partial s}(RbwV) + R_o^+ V_{n+} v_{in}^+ + R_o^- V_{n-} v_{in}^- - Rwv_{out}^+ - Rwv_{out}^- - b\frac{\partial P}{\partial \nu} \\ &\quad - Rbg\frac{\partial y_3}{\partial \nu}. \end{aligned} \tag{A.4.2}$$

The supply to the system represents the difference in pressure force due to the variation of the width of the box and can be written as $\Delta P \Delta y_2 \Delta s$. This was derived by using a similar argument as in Section A.3 and Figure A.2. Only this time, the ν component of $P \cdot \mathbf{n}^+$ was used. Additionally, the ν component of gravity is used, instead of the tangential component as in Section A.3.

Again, it is known that:

$$\frac{\partial P}{\partial \nu} = \frac{\partial y_3}{\partial \nu}\frac{\partial P}{\partial y_3} \tag{A.4.3}$$

$$= -g\frac{\partial y_3}{\partial \nu}. \tag{A.4.4}$$

Thus,

$$\frac{\partial}{\partial \tau}(Rbw) = -\frac{\partial}{\partial s}(RbwV) + R_o^+ V_{n+} v_{in}^+ + R_o^- V_{n-} v_{in}^- - Rwv_{out}^+ - Rwv_{out}^-$$

$$+ (1-R)bg\frac{\partial y_3}{\partial \nu}. \tag{A.4.5}$$

It is taken that $b \sim \delta$, where δ is small, and $\frac{\partial}{\partial \nu} \sim O(\frac{1}{\delta})$. In the limit as $\delta \to 0$, the convective and time derivative terms are small, whereas all other terms balance. Thus:

$$b\frac{\partial P}{\partial \nu} = R_o^+ V_{n+} v_{in}^+ + R_o^- V_{n-} v_{in}^- - Rwv_{out}^+ - Rwv_{out}^- - Rbg\frac{\partial y_3}{\partial \nu}, \tag{A.4.6}$$

which verifies (A.1.1) using (A.4.3). Using the asymptotic expansion of pressure, an expression for transverse velocity can be written as:

$$\begin{aligned} w\left(R(v_{out}^+ + v_{out}^-)\right) &= R_o^+ V_{n+} v_{in}^+ + R_o^- V_{n-} v_{in}^- + (1-R)bg\frac{\partial y_3}{\partial \nu} \\ w &= \frac{R_o^+ V_{n+} v_{in}^+ + R_o^- V_{n-} v_{in}^-}{R(v_{out}^+ + v_{out}^-)} + (1-R)\frac{bg\frac{\partial y_3}{\partial \nu}}{R(v_{out}^+ + v_{out}^-)}. \end{aligned}$$

After accounting for the sign convention of the normal velocities outlined in Section 2.2.5.3, the expression becomes:

$$w = \frac{R_o^+ V_{n+} v_{in}^+ - R_o^- V_{n-} v_{in}^-}{R(v_{out}^+ + v_{out}^-)} + (1-R)\frac{bg\frac{\partial y_3}{\partial \nu}}{R(v_{out}^+ + v_{out}^-)},$$

and the scaled version is written as:

$$\begin{aligned} w &= \frac{R_o^+ V_{n+} v_{in}^+ - R_o^- V_{n-} v_{in}^-}{R(v_{out}^+ + v_{out}^-)} + \frac{t_0^2}{l_3}(1-R)\frac{bg\frac{\partial y_3}{\partial \nu}}{R(v_{out}^+ + v_{out}^-)} \\ w &= \frac{R_o^+ V_{n+} v_{in}^+ - R_o^- V_{n-} v_{in}^-}{R(v_{out}^+ + v_{out}^-)} + (1-R)\frac{b\tilde{g}\frac{\partial y_3}{\partial \nu}}{R(v_{out}^+ + v_{out}^-)}. \end{aligned} \tag{A.4.7}$$

A.5 Conservation of Energy

The amount of energy in the control volume is written as $R(s,\tau)b(s,\tau)\Theta C_p(s,\tau)\Delta s \Delta y_2$, and the balance of energy is expressed as:

$$\begin{aligned} \frac{\partial}{\partial \tau}(Rb\Theta C_p \Delta s \Delta y_2) &= \text{flux in} - \text{flux out} + \text{supply} \\ &= RbV\Theta C_p|_s \, \Delta y_2 - RbV\Theta C_p|_{s+\Delta s} \, \Delta y_2 + R_o^+ \theta_o^+ C_{p\,\text{air}} v_{in}^+ \Delta s \Delta y_2 \end{aligned}$$

$$
\begin{aligned}
&+ R_o^- \theta_o^- C_{p\,\mathrm{air}} v_{in}^- \Delta s \Delta y_2 - R\Theta C_p v_{out}^+ \Delta s \Delta y_2 - R\Theta C_p v_{out}^- \Delta s \Delta y_2 \\
&+ \Delta s \Delta y_2 Qb \\
\frac{\partial}{\partial \tau}(Rb\Theta C_p) &= \frac{RbV\Theta C_p|_s - RbV\Theta C_p|_{s+\Delta s}}{\Delta s} + R_o^+ \theta_o^+ C_{p\,\mathrm{air}} v_{in}^+ + R_o^- \theta_o^- C_{p\,\mathrm{air}} v_{in}^- \\
&- R\Theta C_p v_{out}^+ - R\Theta C_p v_{out}^- + Qb,
\end{aligned}
$$

where Q is a heat source term due to the fire.

Taking the limit as $\Delta s \to 0$ results in:

$$
\begin{aligned}
\frac{\partial}{\partial \tau}(Rb\Theta C_p) = &-\frac{\partial}{\partial s}(RbV\Theta C_p) + R_o^+ \theta_o^+ C_{p\,\mathrm{air}} v_{in}^+ + R_o^- \theta_o^- C_{p\,\mathrm{air}} v_{in}^- - R\Theta C_p v_{out}^+ \\
&- R\Theta C_p v_{out}^- + Qb. \qquad \text{(A.5.1)}
\end{aligned}
$$

The scaled equation can be written as:

$$
\begin{aligned}
\frac{\partial}{\partial \tau}(Rb\Theta C_p) = &-\frac{\partial}{\partial s}(RbV\Theta C_p) + R_o^+ \theta_o^+ C_{p\,\mathrm{air}} v_{in}^+ + R_o^- \theta_o^- C_{p\,\mathrm{air}} v_{in}^- - R\Theta C_p v_{out}^+ \\
&- R\Theta C_p v_{out}^- + \tilde{Q} b \\
\frac{\partial}{\partial \tau}(Rb\Theta C_p) = &-\frac{\partial}{\partial s}(RbV\Theta C_p) + S_T + \tilde{Q} b, \qquad \text{(A.5.2)}
\end{aligned}
$$

where $\tilde{Q} = \frac{l_3}{\rho_0 v_0 T_0 C_{p\,\mathrm{air}}} Q$.

A.6 The Vorticity Equation

In order to derive the vorticity equation in curvilinear coordinates, the momentum equations are considered with the full two-dimensional influences. To do this, the mass equation and two momentum equations, (2.1.1a) and (2.1.1b), are written with their appropriate scalings as:

$$
\begin{aligned}
R_t + (Rv_1)_{y_1} + (Rv_3)_{y_3} &= 0 \\
R(v_{1\,t} + v_1 v_{1\,y_1} + v_3 v_{1\,y_3}) + P_{y_1} &= \tilde{T}_{11\,y_1} + \tilde{T}_{13\,y_3} \\
R(v_{3\,t} + v_1 v_{3\,y_1} + v_3 v_{3\,y_3}) + P_{y_3} + Rg &= \tilde{T}_{31\,y_1} + \tilde{T}_{33\,y_3}.
\end{aligned}
$$

Following the same procedure as before, the curl of the momentum equations

is taken to write the vorticity equation as:

$$\Omega_\tau + (v_1\Omega)_{y_1} + (v_3\Omega)_{y_3} = \frac{R_{y_3}}{R^2}P_{y_1} - \frac{R_{y_1}}{R^2}P_{y_3} + \frac{R_{y_1}}{R^2}\left[\tilde{T}_{31\,y_1} + \tilde{T}_{33\,y_3}\right] - \frac{R_{y_3}}{R^2}\left[\tilde{T}_{11\,y_1} + \tilde{T}_{13\,y_3}\right] + \frac{1}{R}\left[\tilde{T}_{11\,y_1y_3} + \tilde{T}_{13\,y_3y_3} - \left(\tilde{T}_{31\,y_1y_1} + \tilde{T}_{33\,y_3y_1}\right)\right]. \quad \text{(A.6.1)}$$

In the curvilinear coordinate system fixed to the plume, (A.6.1) is approximated by:

$$\Omega_\tau + (w\Omega)_\nu + (V\Omega)_s = \frac{R_s}{R^2}P_\nu - \frac{R_\nu}{R^2}P_s + \frac{R_\nu}{R^2}\left[\tilde{T}_{31\,\nu} + \tilde{T}_{33\,s}\right] - \frac{R_s}{R^2}\left[\tilde{T}_{11\,\nu} + \tilde{T}_{13\,s}\right] + \frac{1}{R}\left[\tilde{T}_{11\,\nu s} + \tilde{T}_{13\,ss} - \left[\tilde{T}_{31\,\nu\nu} + \tilde{T}_{33\,s\nu}\right]\right]. \quad \text{(A.6.2)}$$

The vorticity equation (A.6.2) is integrated over the control volume. Each term will generate a Δy_2, so the common term is simplified from each side. The equation becomes:

$$\int_{-\frac{b}{2}}^{\frac{b}{2}}\int_{s}^{s+\Delta s}\Omega_\tau \mathrm{d}s\mathrm{d}\nu + \int_{s}^{s+\Delta s}\int_{-\frac{b}{2}}^{\frac{b}{2}}(w\Omega)_\nu \mathrm{d}\nu\mathrm{d}s + \int_{-\frac{b}{2}}^{\frac{b}{2}}\int_{s}^{s+\Delta s}(V\Omega)_s \mathrm{d}s\mathrm{d}\nu = + \int_{-\frac{b}{2}}^{\frac{b}{2}}\int_{s}^{s+\Delta s}\frac{R_s}{R^2}P_\nu - \frac{R_\nu}{R^2}P_s \mathrm{d}s\mathrm{d}\nu + \varkappa,$$

where,

$$\varkappa = \int_{-\frac{b}{2}}^{\frac{b}{2}}\int_{s}^{s+\Delta s}\frac{R_\nu}{R^2}\left[\tilde{T}_{31\,\nu} + \tilde{T}_{33\,s}\right] - \frac{R_s}{R^2}\left[\tilde{T}_{11\,\nu} + \tilde{T}_{13\,s}\right] + \frac{1}{R}\left[\tilde{T}_{11\,\nu s} + \tilde{T}_{13\,ss} - \left[\tilde{T}_{31\,\nu\nu} + \tilde{T}_{33\,s\nu}\right]\right]\mathrm{d}s\mathrm{d}\nu. \quad \text{(A.6.3)}$$

Continuing to simplify by moving the derivatives through the integrals and evaluating, the equation can be simplified to:

$$\Delta s(\Omega b)_\tau - b_\tau\Omega\Delta s + \Delta s(w\Omega)\Big|_{-\frac{b}{2}}^{\frac{b}{2}} + (V\Omega)\Big|_{s}^{s+\Delta s} b = -P_\nu\frac{1}{R}\Big|_{s}^{s+\Delta s} b + P_s\frac{1}{R}\Big|_{-\frac{b}{2}}^{\frac{b}{2}} + \varkappa. \quad \text{(A.6.4)}$$

Here, on the boundary of the plume, R is the same on either side and the pressure gradient in the ν direction is small ($O(\beta)$). Thus, the final vorticity equation is

written as:

$$(\Omega b)_\tau - b_\tau \Omega + (V\Omega)_s b = \tilde{\varkappa}, \tag{A.6.5}$$

where $\tilde{\varkappa} = \frac{1}{\Delta s}\varkappa - (w\Omega)\Big|_{-\frac{b}{2}}^{\frac{b}{2}}$. This equation can be easily put into conservation form to mirror the form of the remaining conservation laws by multiplying (A.6.5) by R to obtain a conserved quantity. Also, let $\bar{\varkappa} = R\tilde{\varkappa}$:

$$R(\Omega b)_\tau - Rb_\tau \Omega + R(V\Omega)_s b = \bar{\varkappa} \tag{A.6.6}$$

$$(R\Omega b)_\tau - R_\tau \Omega b - Rb_\tau \Omega + (RbV\Omega)_s - (Rb)_s V\Omega = \bar{\varkappa} \tag{A.6.7}$$

$$(R\Omega b)_\tau - (Rb)_\tau \Omega + (RbV\Omega)_s - (Rb)_s V\Omega = \bar{\varkappa} \tag{A.6.8}$$

$$(R\Omega b)_\tau + (RbV\Omega)_s = \bar{\varkappa} + \Omega((Rb)_\tau + V(Rb)_s) \tag{A.6.9}$$

$$(R\Omega b)_\tau + (RbV\Omega)_s = \bar{\varkappa} + \Omega(S_m - V_s Rb). \tag{A.6.10}$$

The last step is achieved using the conservation of mass equation (A.2.2). The source term, $\varkappa$, is rewritten using the notation of the source terms of entrainment as:

$$\bar{\varkappa} = \frac{R}{b\Delta s}\int_{-\frac{b}{2}}^{\frac{b}{2}}\int_{s}^{s+\Delta s} \frac{R_\nu}{R^2}\left[\tilde{T}_{31\,\nu} + \tilde{T}_{33\,s}\right] - \frac{R_s}{R^2}\left[\tilde{T}_{11\,\nu} + \tilde{T}_{13\,s}\right] + \frac{1}{R}\left[\tilde{T}_{11\,\nu s} + \tilde{T}_{13\,ss} - \left[\tilde{T}_{31\,\nu\nu} + \tilde{T}_{33\,s\nu}\right]\right] \mathrm{d}s\mathrm{d}\nu - \frac{R}{b}(w\Omega)\Big|_{-\frac{b}{2}}^{\frac{b}{2}}.$$

For the purposes of this work, $\bar{\varkappa}$ will be written as $\bar{\varkappa} = \frac{R}{b}S_G$. The source terms for entrainment are obtained by Figure A.4, and can be written as $S_G = R_o V_{t+\frac{2}{b}} v_{in}^+ - R_o V_{t-\frac{2}{b}} v_{in}^- - R\Omega v_{out}^+ - R\Omega v_{out}^-$.

Thus, the scaled vorticity equation is written as:

$$(R\Omega b)_\tau + (RbV\Omega)_s = \frac{R}{b}S_G + \Omega(S_m - V_s Rb). \tag{A.6.11}$$

With this, the system of final form conservation laws and vorticity equation

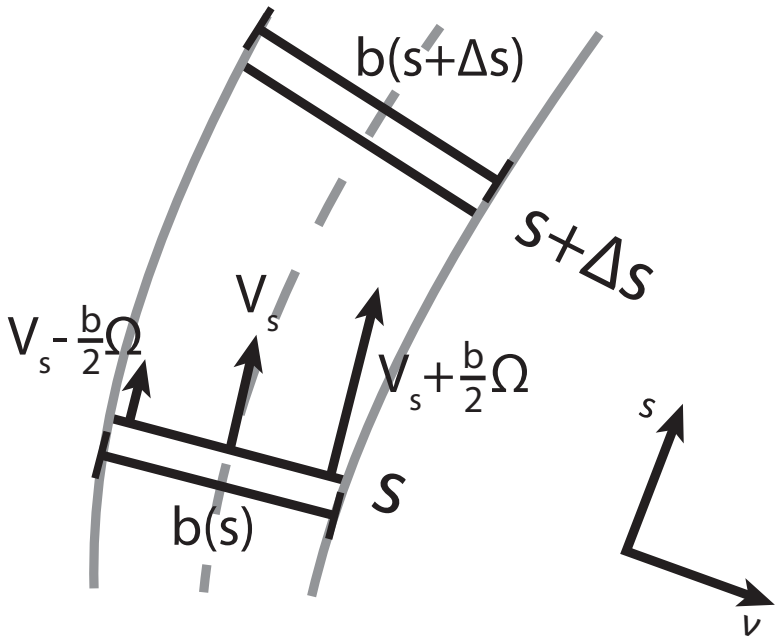

Figure A.4: Source of Entrainment of Vorticity

for the plume system in curvilinear coordinates fixed to the plume are obtained:

$$\frac{\partial}{\partial\tau}(Rb) = -\frac{\partial}{\partial s}(RbV) + S_m \tag{A.6.12a}$$

$$\frac{\partial}{\partial\tau}(RbV) = -\frac{\partial}{\partial s}(RbV^2) + S_M + (1-R)b\tilde{g}\frac{\partial y_3}{\partial s} \tag{A.6.12b}$$

$$w = \frac{R_o^+ V_{n+} v_{in}^+ - R_o^- V_{n-} v_{in}^-}{R(v_{out}^+ + v_{out}^-)} + (1-R)\frac{b\tilde{g}\frac{\partial y_3}{\partial \nu}}{R(v_{out}^+ + v_{out}^-)} \tag{A.6.12c}$$

$$\frac{\partial}{\partial\tau}(Rb\Theta C_p) = -\frac{\partial}{\partial s}(RbV\Theta C_p) + S_T - R\Theta C_p v_{out}^- + \tilde{Q}b. \tag{A.6.12d}$$

$$\frac{\partial}{\partial\tau}(Rb\Omega) = -\frac{\partial}{\partial s}(RbV\Omega) + \frac{R}{b}S_G + \Omega(S_m - V_s Rb), \tag{A.6.12e}$$

where the transverse velocity equation is only used in Section 3.4. The remaining equations are equivalent to (2.3.17a), (2.3.17c), (2.3.17d), and (2.3.17e), respectively in Chapter 2.

APPENDIX B
Justification of Diffusive Scheme to Numerically Solve System

In an exercise to determine which numerical scheme should be used to solve the conservation laws for the plume system (A.6.12),

$$\begin{aligned}
(Rb)_\tau + (RbV)_s &= S_m \\
(RbV)_\tau + (RbV^2)_s &= S_M + (1-R)bg_{||} \\
(Rb\Theta C_p)_\tau + (Rb\Theta C_p V)_s &= S_T + bQ\frac{1}{C_p} \\
(Rb\Omega)_\tau + (RbV\Omega)_s &= \frac{R}{b}S_G + \Omega(S_m - V_s Rb),
\end{aligned}$$

several simplifications are considered. It is known that as a system, these equations possess less-than-ideal properties. For instance, the system is defective, and thus is not a strict-hyperbolic system. This poses an issue since most, if not all, standard schemes were developed especially for the strict-hyperbolic case.

Following one of the exercises from LeVeque [38], several simplifications of the above system are considered. Namely, the simplification down to the pressureless gas equations will be closely examined here. To solve these simplified systems, a Godunov approach is used, along with a simple upwind and diffusive scheme following [15]. The results from the different schemes will be compared to determine which scheme will be used in the full problem.

B.1 Uncoupled Simple System

Here, a system for density and velocity is considered. Thus, conservation of mass and momentum are the only two equations remaining. This system can easily be recognized as the pressureless gas equations [77]. Letting ρ be the density and v

be the velocity, the system being considered is:

$$\rho_t + (\rho v)_x = 0 \tag{B.1.1}$$

$$v_t + (\frac{1}{2}v^2)_x = 0, \tag{B.1.2}$$

where the initial and boundary conditions are chosen to be:

$$\begin{aligned} \rho(0,t) &= \frac{1}{2} \\ \rho(x,0) &= 1; \quad x \neq 0 \\ v(0,t) &= 1 \\ v(x,0) &= 0; \quad x \neq 0, \end{aligned}$$

which can be obtained by simplifying the above conservation of momentum equation with the conservation of mass equation. Additionally, in this approach, one will notice that (B.1.2) is uncoupled from (B.1.1). This means that (B.1.2) can be solved first, and the newly calculated v can be used in (B.1.1).

B.1.1 Upwind

Considering (B.1.2) first, the upwind scheme is simply:

$$v_k^{n+1} = v_k^n - \frac{\Delta t}{\Delta x}\left[F_v(v_k^n, v_{k+1}^n) - F_v(v_{k-1}^n, v_k^n)\right],$$

where,

$$F_v(u_l, u_r) = \begin{cases} \frac{1}{2}u_l^2 & v_k^n + v_{k-1}^n \geq 0 \\ \frac{1}{2}u_r^2 & v_k^n + v_{k-1}^n < 0. \end{cases}$$

With the initial conditions considered, $v_k^n \geq 0$, thus the upwind scheme is always:

$$v_k^{n+1} = v_k^n - \frac{\Delta t}{2\Delta x}(v_k^{n\,2} - v_{k-1}^{n\,2}). \tag{B.1.3}$$

Then, (B.1.1) is solved in the same way. The scheme is simply:

$$\rho_k^{n+1} = \rho_k^n - \frac{\Delta t}{\Delta x}(F_\rho(\rho_k^n, \rho_{k+1}^n) - F_\rho(\rho_{k-1}^n, \rho_k^n)),$$

where,

$$F_\rho(u_l, u_r) = \begin{cases} u_l v_l^{n+1} & v_k^{n+1} + v_{k-1}^{n+1} \geq 0 \\ u_r v_r^{n+1} & v_k^{n+1} + v_{k-1}^{n+1} < 0, \end{cases}$$

Again, with the initial conditions considered, $v_k^n \geq 0$, thus the upwind scheme is always:

$$\rho_k^{n+1} = \rho_k^n - \frac{\Delta t}{\Delta x}(\rho_k^n v_k^{n+1} - \rho_{k-1}^n v_{k-1}^{n+1}). \tag{B.1.4}$$

B.1.2 Godunov

In this implementation, Godunov's method is almost identical to the above upwind scheme, although this time, the condition is slightly changed. For (B.1.2), it is taken that:

$$v_k^{n+1} = v_k^n - \frac{\Delta t}{\Delta x}\left[F_v(v_k^n, v_{k+1}^n) - F_v(v_{k-1}^n, v_k^n)\right], \tag{B.1.5}$$

where this time,

$$F_v(u_l, u_r) = \begin{cases} f_v(u_l) & \frac{f_v(u_r) - f_v(u_l)}{u_r - u_l} \geq 0 \\ f_v(u_r) & \frac{f_v(u_r) - f_v(u_l)}{u_r - u_l} < 0, \end{cases}$$

where $f_v(u_\star) = \frac{1}{2}u_\star^2$, and u_l, u_r is the argument of F_v.

For (B.1.1), the process is the same. Here,

$$\rho_k^{n+1} = \rho_k^n - \frac{\Delta t}{\Delta x}\left[F_\rho(\rho_k^n, \rho_{k+1}^n) - F_\rho(\rho_{k-1}^n, \rho_k^n)\right], \tag{B.1.6}$$

where this time,

$$F_\rho(u_l, u_r) = \begin{cases} f_\rho(u_l) & \frac{f_\rho(u_r) - f_\rho(u_l)}{u_r - u_l} \geq 0 \\ f_\rho(u_r) & \frac{f_\rho(u_r) - f_\rho(u_l)}{u_r - u_l} < 0, \end{cases}$$

where $f_\rho(u_\star) = u_\star v_\star^{n+1}$, and u_l, u_r is the argument of F_ρ.

B.1.3 Simplified Godunov

The simplified Godunov's method is used to ensure all possibilities of the sign of $f'(u)$ are considered, following LeVeque [38]. For (B.1.2), it is taken that:

$$v_k^{n+1} = v_k^n - \frac{\Delta t}{\Delta x}\left[F_v(v_k^n, v_{k+1}^n) - F_v(v_{k-1}^n, v_k^n)\right], \tag{B.1.7}$$

where this time,

$$F_v(u_l, u_r) = \begin{cases} \min_{u_l \le u \le u_r} f_v(u) & u_l \le u_r \\ \min_{u_r \le u \le u_l} f_v(u) & u_l > u_r, \end{cases}$$

where $f_v(u_\star) = \frac{1}{2}u_\star^2$, and u_l, u_r is the argument of F_v.

For (B.1.1), the process is the same. Thus,

$$\rho_k^{n+1} = \rho_k^n - \frac{\Delta t}{\Delta x}\left[F_\rho(\rho_k^n, \rho_{k+1}^n) - F_\rho(\rho_{k-1}^n, \rho_k^n)\right], \tag{B.1.8}$$

where,

$$F_\rho(u_l, u_r) = \begin{cases} \min_{u_l \le u \le u_r} f_\rho(u) & u_l \le u_r \\ \min_{u_r \le u \le u_l} f_\rho(u) & u_l > u_r, \end{cases}$$

$f_\rho(u_\star) = u_\star v_\star^{n+1}$, and u_l, u_r is the argument of F_ρ.

B.1.4 Diffusive Scheme

When considering (B.1.2), following [15], the scheme is simply an upwind scheme with an added second order derivative diffusive term. The second order derivative is approximated using a second order difference equation to give:

$$v_k^{n+1} = v_k^n - \frac{\Delta t}{\Delta x}\left[F_v(v_k^n, v_{k+1}^n) - F_v(v_{k-1}^n, v_k^n)\right] + \epsilon\frac{\Delta t}{\Delta x^2}\frac{1}{\rho_k^n}\left(v_{k-1}^n - 2v_k^n + v_{k+1}^n\right),$$

where,

$$F_v(u_l, u_r) = \begin{cases} \frac{1}{2}u_l^2 & v_k^n + v_{k-1}^n \ge 0 \\ \frac{1}{2}u_r^2 & v_k^n + v_{k-1}^n < 0. \end{cases}$$

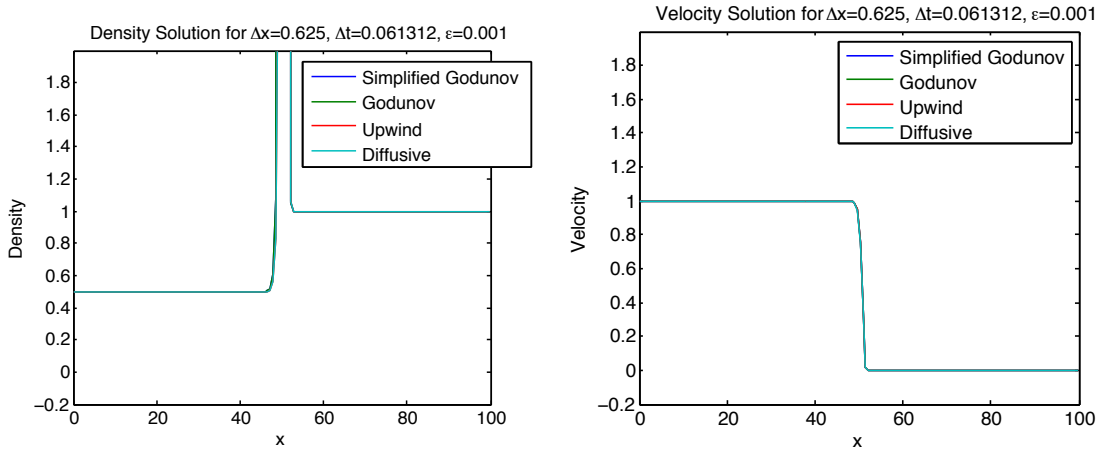

(a) Density Solution **(b) Velocity Solution**

Figure B.1: Solution to Uncoupled System

With the initial conditions considered, $v_k^n \geq 0$, thus the upwind scheme is always:

$$v_k^{n+1} = v_k^n - \frac{\Delta t}{2\Delta x}({v_k^n}^2 - {v_{k-1}^n}^2) + \epsilon \frac{\Delta t}{\Delta x^2}\frac{1}{\rho_k^n}\left(v_{k-1}^n - 2v_k^n + v_{k+1}^n\right), \tag{B.1.9}$$

where ϵ is a small parameter to be determined.

Then, (B.1.1) is solved following the upwind scheme in Section B.1.1:

$$\rho_k^{n+1} = \rho_k^n - \frac{\Delta t}{\Delta x}(\rho_k^n v_k^{n+1} - \rho_{k-1}^n v_{k-1}^{n+1}). \tag{B.1.10}$$

B.1.5 Numerical Results

The above schemes are implemented and the system is solved numerically. Figure B.1 shows that the numerical results from the above schemes in fact agree upon the same solution, and that solution is what one would expect the solution to look like. All solutions are present, however, due to the agreement some solutions are hidden underneath others.

It must be noted that the exact solution of the system in this section and all following sections has not been computed. This is due to the fact that the analytical solution of the pressureless gas is incredibly difficult to compute. The solution to this system is simple enough that intuitively, the behavior of the exact solution is known. It is understood that at this point, high level qualitative behavior can be

determined and compared. Section B.6 addresses the issue of convergence and error analysis.

It is also worth mentioning that the spike in the density is an expected feature of the solution. On one part of the domain the air is moving, but in the other it is not. Thus, there is a buildup of mass at the interface between the moving and stationary air, which, in the case of the plume, can physically be explained by a "puff" of air (an increase in the width of the plume).

B.2 Coupled Simple System

In this simplified system, again only density and velocity will be considered. Thus, conservation of mass and momentum will be the only two equations remaining, and again, this system can be recognized as the pressureless gas equations.

The system is clearly the same as in Section B.1, but this time, the equations will be solved simultaneously to see if there is change in behavior when exploiting the uncoupled velocity equation (see Section B.1). The system is written as:

$$\begin{aligned} \mathbf{y}_t + \mathbf{f}_x &= 0 \qquad \text{(B.2.1)} \\ \mathbf{y} &= (\rho, v)^T \\ \mathbf{f} &= (\rho v, \frac{1}{2}v^2)^T. \end{aligned}$$

B.2.1 Upwind

This time, both equations will be solved together, meaning (B.2.1) will be solved. Thus,

$$\mathbf{y}_k^{n+1} = \mathbf{y}_k^n - \frac{\Delta t}{\Delta x}\left[\mathbf{F}(\mathbf{y}_k^n, \mathbf{y}_{k+1}^n) - \mathbf{F}(\mathbf{y}_{k-1}^n, \mathbf{y}_k^n)\right],$$

where,

$$\mathbf{F}(\mathbf{u}_l, \mathbf{u}_r) = \begin{cases} \mathbf{f}(\mathbf{u}_l) & v_k^n + v_{k-1}^n \geq 0 \\ \mathbf{f}(\mathbf{u}_r) & v_k^n + v_{k-1}^n < 0, \end{cases}$$

and $\mathbf{f}(u_\star) = (\rho_\star v_\star, \frac{1}{2}v_\star^2)^T$. Again, with the initial conditions considered, $v_k^n \geq 0$, thus

the upwind scheme is always:

$$\mathbf{y}_k^{n+1} = \mathbf{y}_k^n - \frac{\Delta t}{\Delta x}\left[\mathbf{f}_k^n - \mathbf{f}_{k-1}^n\right]. \tag{B.2.2}$$

B.2.2 Godunov

The same simplified Godunov scheme from above will be used, just in vector form. The Godunov scheme will be rederived here as the definition of dividing by a vector is unclear. Since the simplified Godunov and Godunov schemes in vector notation are the same, only one is considered. As with all Godunov type schemes, a Riemann problem is solved on each mesh spacing. The Riemann problem considered is:

$$\begin{aligned} &\mathbf{y}_t + \mathbf{f}_x = 0 \\ &\mathbf{y}(x,0) = \begin{cases} \mathbf{y}_l & x < 0 \\ \mathbf{y}_r & x > 0, \end{cases} \end{aligned}$$

for $t > 0$ and $x \in \mathbb{R}$. In quasi-linear form, this becomes:

$$\begin{aligned} &\mathbf{y}_t + \mathbf{A}\mathbf{y}_x = 0 \\ &\mathbf{y}(x,0) = \begin{cases} \mathbf{y}_l & x < 0 \\ \mathbf{y}_r & x > 0, \end{cases} \end{aligned}$$

where $\mathbf{A} = \mathbf{f}'$ is the Jacobian matrix, and:

$$\mathbf{A} = \begin{bmatrix} v & \rho \\ 0 & v \end{bmatrix}.$$

It is clearly seen that the eigenvalues of this matrix are $\lambda_1 = v$ and $\lambda_2 = v$, with corresponding eigenvectors $\mathbf{r}_1 = (1,0)^T$, $\mathbf{r}_2 = (0,0)^T$. Thus, the system is defective and clearly not strict-hyperbolic. Following LeVeque [38] to determine the Hugoniot Locus, the Rankine-Hugoniot condition becomes:

$$\tilde{\rho}\tilde{v} - \hat{\rho}\hat{v} = s(\tilde{\rho} - \hat{\rho})$$

$$\frac{1}{2}(\tilde{v}^2 - \hat{v}^2) = s(\tilde{v} - \hat{v}),$$

where $\tilde{\mathbf{y}}, \hat{\mathbf{y}}$ are two connected states, and it is assumed that $\hat{\mathbf{y}}$ is known. Then, solving for s and $\tilde{v}$:

$$s = \hat{v} \tag{B.2.3}$$

$$\tilde{v} = \hat{v}. \tag{B.2.4}$$

With this, take:

$$\tilde{\rho}_p(\xi; \hat{\mathbf{y}}) = \hat{\rho}(1 + \xi), \tag{B.2.5}$$

for $p = 1, 2$, and here the $p = 1$ case is the same as the $p = 2$ case, except that $\mathbf{r}_1 \neq \mathbf{r}_2$. This is because $\lambda_1 = \lambda_2$, and normally $\tilde{\mathbf{y}}_1$ would correspond to λ_1, $\tilde{\mathbf{y}}_2$ would correspond to λ_2, etc. Then, $\tilde{v}(\xi; \hat{\mathbf{y}}) = \hat{v}$ and $\tilde{\mathbf{y}}_p(\xi; \hat{\mathbf{y}}) = \hat{\mathbf{y}}_p + \hat{\rho}\xi\mathbf{r}_1$, $p = 1, 2$. With this, it can be verified that $\frac{\partial}{\partial \xi}\tilde{\mathbf{y}}_p(0; \hat{\mathbf{y}}) = \hat{\rho}\mathbf{r}_1 \propto \mathbf{r}_1$ and $s_p(0; \hat{\mathbf{y}}) = \lambda_p$.

To explore the possibilities of shock waves and rarefactions, the theory behind the problem needs to be examined. In particular, it needs to be established whether or not the problem has a genuine non-linearity. To be genuinely non-linear, $\nabla\lambda_p(\mathbf{y}) \cdot \mathbf{r}_p(\mathbf{y}) \neq 0 \ \forall \mathbf{y}$. Is is easy to verify, that for this system, (B.2.1), $\nabla\lambda_p(\mathbf{y}) \cdot \mathbf{r}_p(\mathbf{y}) = 0$ $\forall \mathbf{y}$. Thus, the entire system (both fields) is called linearly degenerate and cannot contain shock waves or rarefactions, only contact discontinuities. This can be seen in Figure B.2.

Using this, a typical solution of the Riemann problem can be explained. Starting again with the Rankine-Hugoniot conditions between states $\mathbf{y}$ and $\hat{\mathbf{y}}$, one has:

$$\rho v - \hat{\rho}\hat{v} = s(\rho - \hat{\rho})$$
$$\frac{1}{2}(v^2 - \hat{v}^2) = s(v - \hat{v}),$$

and this time, it is taken that $s = v = \hat{v}$. With this, it is trivial to see that the

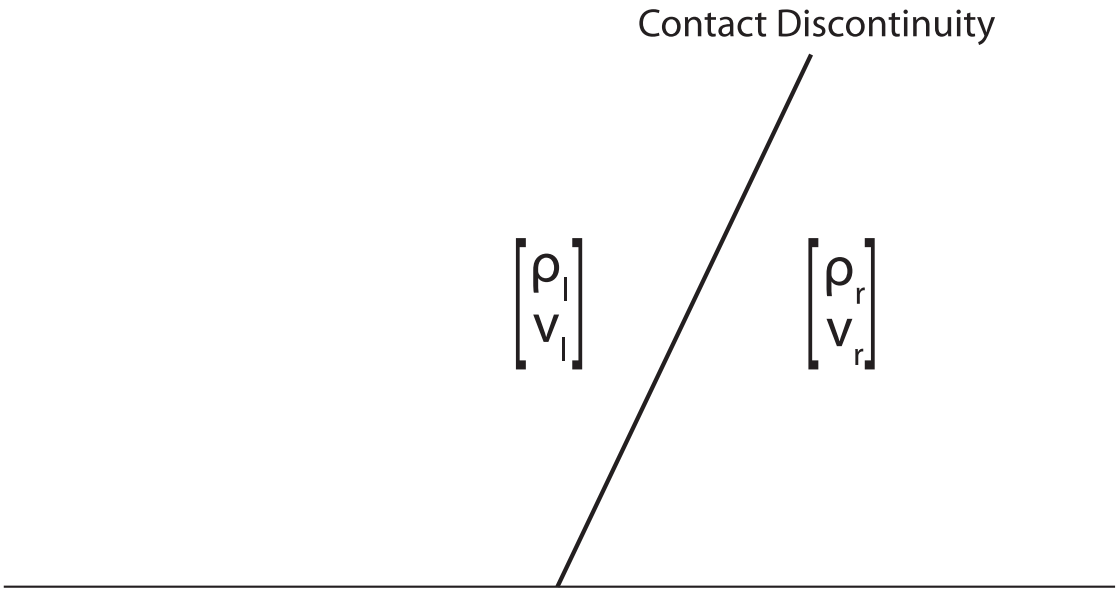

Figure B.2: Typical Solution to the Riemann Problem

Rankine-Hugoniot conditions are satisfied, and:

$$\begin{aligned}\mathbf{y} - \hat{\mathbf{y}} &= \begin{bmatrix} \rho - \hat{\rho} \\ v - \hat{v} \end{bmatrix} \\ &= (\rho - \hat{\rho}) \begin{bmatrix} 1 \\ 0 \end{bmatrix} \propto \mathbf{r}_1,\end{aligned}$$

using $s = v = \hat{v}$. Thus, the jump is in the direction $\mathbf{r}_1$, and by this exercise, it would seem that the velocity is constant across the contact discontinuity. But, as will be shown in Section B.4, given the nature of the plume and the characteristics of Burgers' equation, a discontinuous velocity will eventually form in this problem.

From this, the scheme becomes:

$$\mathbf{y}_k^{n+1} = \mathbf{y}_k^n - \frac{\Delta t}{\Delta x}\left[\mathbf{F}(\mathbf{y}_k^n, \mathbf{y}_{k+1}^n) - \mathbf{F}(\mathbf{y}_{k-1}^n, \mathbf{y}_k^n)\right], \tag{B.2.6}$$

where this time,

$$\mathbf{F}(\mathbf{u}_l, \mathbf{u}_r) = \begin{cases} \mathbf{f}(\mathbf{u}_l) & v_k^n < 0 \\ \mathbf{f}(\mathbf{u}_r) & v_k^n > 0, \end{cases}$$

where $\mathbf{f}(\mathbf{u}_\star) = (\rho_\star v_\star, \frac{1}{2}v_\star^2)^T$, and $\mathbf{u}_l, \mathbf{u}_r$ is the argument of $\mathbf{F}$.

B.2.3 Diffusive Scheme

When coupling the equations, the scheme becomes,

$$\mathbf{y}_k^{n+1} = \mathbf{y}_k^n - \frac{\Delta t}{\Delta x}\left[\mathbf{F}(\mathbf{y}_k^n, \mathbf{y}_{k+1}^n) - \mathbf{F}(\mathbf{y}_{k-1}^n, \mathbf{y}_k^n)\right] + \epsilon\frac{\Delta t}{\Delta x^2}\mathbf{\Psi},$$

where,

$$\mathbf{F}(\mathbf{u}_l, \mathbf{u}_r) = \begin{cases} \mathbf{f}(\mathbf{u}_l) & v_k^n + v_{k-1}^n \geq 0 \\ \mathbf{f}(\mathbf{u}_r) & v_k^n + v_{k-1}^n < 0, \end{cases}$$

where $\mathbf{f}(u_\star) = (\rho_\star v_\star, \frac{1}{2}v_\star^2)^T$ and $\mathbf{\Psi} = (0, \frac{1}{\rho_k^n}\left(v_{k-1}^n - 2v_k^n + v_{k+1}^n\right))^T$. Again, with the initial conditions considered, $v_k^n \geq 0$, thus the upwind scheme is always:

$$\mathbf{y}_k^{n+1} = \mathbf{y}_k^n - \frac{\Delta t}{\Delta x}\left[\mathbf{f}_k^n - \mathbf{f}_{k-1}^n\right] + \epsilon\frac{\Delta t}{\Delta x^2}\mathbf{\Psi}. \tag{B.2.7}$$

B.2.4 Numerical Results

Once again, the schemes were implemented to obtain the numerical results shown in Figure B.3. The numerical results from the above schemes do agree with each other and the results from the previous section. All solutions are present, however, due to the agreement some solutions are hidden underneath others. With the agreement between the coupled and uncoupled approaches, either method can be used to obtain the same results.

B.3 Physically Conserved System

As with the previous two approaches, only density and velocity will be considered. But, this time, the physically conserved quantities will be examined. Thus, the system being considered is:

$$\rho_t + (\rho v)_x = 0 \tag{B.3.1}$$

$$(\rho v)_t + (\rho v^2)_x = 0, \tag{B.3.2}$$

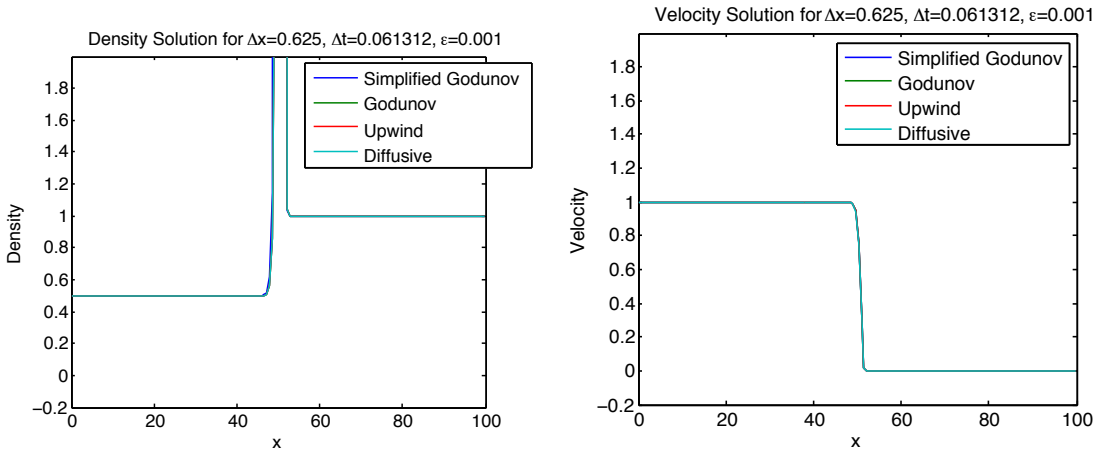

(a) Density Solution **(b) Velocity Solution**

Figure B.3: Solution to Coupled System

with initial and boundary conditions chosen to be:

$$\begin{aligned}
\rho(0,t) &= \frac{1}{2} \\
\rho(x,0) &= 1; \quad x \neq 0 \\
\rho v(0,t) &= \frac{1}{2} \\
\rho v(x,0) &= 0; \quad x \neq 0,
\end{aligned}$$

which can be obtained by setting the right-hand side of the unsimplified conservation of mass and momentum equations to zero. Again, the equations will be solved simultaneously, so the system is written as:

$$\begin{aligned}
\mathbf{y}_t + \mathbf{f}_x &= 0 \qquad\qquad (B.3.3) \\
\mathbf{y} &= (\rho, \rho v)^T = (u, \nu)^T \\
\mathbf{f} &= (\rho v, \rho v^2)^T = \left(\nu, \frac{\nu^2}{u}\right)^T.
\end{aligned}$$

Using the fact that $v = \frac{\nu}{u}$, one can solve for u and ν and then calculate v.

B.3.1 Upwind

As with Section B.2, both equations will be solved together, meaning (B.3.3) will be solved. Thus the upwind method is:

$$\mathbf{y}_k^{n+1} = \mathbf{y}_k^n - \frac{\Delta t}{\Delta x}\left[\mathbf{F}(\mathbf{y}_k^n, \mathbf{y}_{k+1}^n) - \mathbf{F}(\mathbf{y}_{k-1}^n, \mathbf{y}_k^n)\right],$$

where,

$$\mathbf{F}(\mathbf{u}_l, \mathbf{u}_r) = \begin{cases} \mathbf{f}(\mathbf{u}_l) & v_k^n + v_{k-1}^n \geq 0 \\ \mathbf{f}(\mathbf{u}_r) & v_k^n + v_{k-1}^n < 0. \end{cases}$$

It is taken that $\mathbf{f}(u_\star) = \left(\nu_\star, \frac{\nu_\star^2}{u_\star}\right)^T$, and it is noted that $v_k^n = \frac{\nu_k^n}{u_k^n}$. Again, with the initial conditions considered, $v_k^n \geq 0$, thus the upwind scheme is always:

$$\mathbf{y}_k^{n+1} = \mathbf{y}_k^n - \frac{\Delta t}{\Delta x}\left[\mathbf{f}_k^n - \mathbf{f}_{k-1}^n\right]. \tag{B.3.4}$$

B.3.2 Godunov

The derivation of the vector Godunov scheme for this system is identical to the previous section, and again, the Godunov scheme used is the vectorized form of the scheme presented above. Here, the Riemann problem considered will be:

$$\mathbf{y}_t + \mathbf{f}_x = 0$$
$$\mathbf{y}(x,0) = \begin{cases} \mathbf{y}_l & x < 0 \\ \mathbf{y}_r & x > 0, \end{cases}$$

for $t > 0$ and $x \in \mathbb{R}$. In quasi-linear form, this becomes:

$$\mathbf{y}_t + \mathbf{A}\mathbf{y}_x = 0$$
$$\mathbf{y}(x,0) = \begin{cases} \mathbf{y}_l & x < 0 \\ \mathbf{y}_r & x > 0, \end{cases}$$

where $\mathbf{A} = \mathbf{f}'$ is the Jacobian matrix, and:

$$\mathbf{A} = \begin{bmatrix} 0 & 1 \\ -\frac{\nu^2}{u} & 2\frac{\nu}{u} \end{bmatrix}.$$

It is clearly seen that the eigenvalues of this matrix is $\lambda_1 = \frac{\nu}{u}$, $\lambda_2 = \frac{\nu}{u}$, with corresponding eigenvectors $\mathbf{r}_1 = (\frac{u}{\nu}, 1)^T$, $\mathbf{r}_2 = (0, 0)^T$. Again, the system is defective and clearly not strict-hyperbolic. Following LeVeque [38] in the same process as before, by picking two connected states, expressions for s and $\tilde{\nu}$ can be found:

$$s = \frac{\hat{\nu}}{\hat{u}} \tag{B.3.5}$$

$$\tilde{v} = \frac{\hat{\nu}\tilde{u}}{\hat{u}}. \tag{B.3.6}$$

This time, with the choice of:

$$\tilde{u}_p(\xi; \hat{\mathbf{y}}) = \hat{u}(1 + \xi), \tag{B.3.7}$$

it can be verified that $\tilde{\mathbf{y}}_p(\xi; \hat{\mathbf{y}}) = \hat{\mathbf{y}}_p(1 + \xi)$ for $p = 1, 2$, $\frac{\partial}{\partial \xi}\tilde{\mathbf{y}}_p(0; \hat{\mathbf{y}}) = \hat{\nu}\mathbf{r}_1 \propto \mathbf{r}_1$, and $s_p(0; \hat{\mathbf{y}}) = \lambda_p$.

The definition of genuine non-linearity is again used to determine whether or not shock waves and rarefactions are present in this problem. It is easy to verify, that for this system, (B.3.3), $\nabla\lambda_p(\mathbf{y}) \cdot \mathbf{r}_p(\mathbf{y}) = 0 \ \forall \mathbf{y}$. Thus, the entire system (both fields) is called linearly degenerate and cannot contain shock waves or rarefactions, only contact discontinuities, as seen in Figure B.2.

Using this, a typical solution of the Riemann problem can be explained. Starting again with the Rankine-Hugoniot conditions between states $\mathbf{y}$ and $\hat{\mathbf{y}}$, one has:

$$\nu - \hat{\nu} = s(u - \hat{u})$$

$$\frac{\nu^2}{u} - \frac{\hat{\nu^2}}{u} = s(\nu - \hat{\nu}),$$

and this time, it is taken that $s = \frac{\nu}{u} = \frac{\hat{\nu}}{\hat{u}}$. With this, it is trivial to see that the

Rankine-Hugoniot conditions are satisfied using $\hat{\nu} = \frac{\nu\hat{u}}{u}$, and:

$$\begin{aligned}
\mathbf{y} - \hat{\mathbf{y}} &= \begin{bmatrix} u - \hat{u} \\ \nu - \hat{\nu} \end{bmatrix} \\
&= \begin{bmatrix} \rho - \hat{\rho} \\ \rho v - \hat{\rho}\hat{v} \end{bmatrix} \\
&= (\rho - \hat{\rho}) \begin{bmatrix} 1 \\ v \end{bmatrix} \\
&= (\rho - \hat{\rho}) v \begin{bmatrix} \frac{1}{v} \\ 1 \end{bmatrix} \propto \mathbf{r}_1,
\end{aligned}$$

using $s = \frac{\nu}{u} = \frac{\hat{\nu}}{\hat{u}}$, and $\frac{u}{\nu} = \frac{1}{v}$. Thus, the jump is in the direction $\mathbf{r}_1$, and by this exercise, it would seem that the velocity is constant across the contact discontinuity. But again, as it will be shown in Section B.4, given the nature of the plume and the characteristics of Burgers' equation, a discontinuous velocity will eventually form in this problem.

From this, the scheme becomes:

$$\mathbf{y}_k^{n+1} = \mathbf{y}_k^n - \frac{\Delta t}{\Delta x} \left[\mathbf{F}(\mathbf{y}_k^n, \mathbf{y}_{k+1}^n) - \mathbf{F}(\mathbf{y}_{k-1}^n, \mathbf{y}_k^n) \right], \tag{B.3.8}$$

where this time,

$$\mathbf{F}(\mathbf{u}_l, \mathbf{u}_r) = \begin{cases} \mathbf{f}(\mathbf{u}_l) & v_k^n < 0 \\ \mathbf{f}(\mathbf{u}_r) & v_k^n > 0, \end{cases}$$

where $\mathbf{f}(\mathbf{u}_\star) = (\rho_\star v_\star, \frac{1}{2} v_\star^2)^T$, and $\mathbf{u}_l, \mathbf{u}_r$ is the argument of $\mathbf{F}$.

B.3.3 Diffusive Scheme

Due to the nature of the way in which the diffusive scheme was derived, a system written in full conservation form cannot be solved. The mass equation needs to be used to simplify and decouple the momentum equation, as shown in the first two systems.

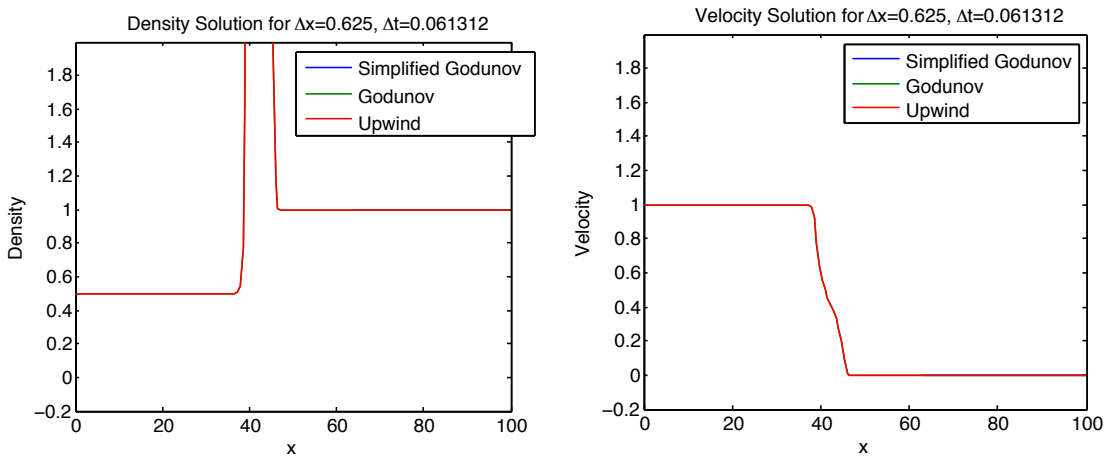

(a) Density Solution **(b) Velocity Solution**

Figure B.4: Solution to Physically Conserved System

B.3.4 Numerical Results

The numerical schemes were implemented and Figure B.4 shows that the numerical results from the above schemes are drastically different than the previous sections. The Godunov scheme has blown up, and is not even present on the plot.

Even though equation (B.3.3) uses physically conserved quantities, it is easy to see from the plots that this solution method doesn't give an accurate or consistent scheme for the problem. The discontinuity has been smeared by the numerical scheme(s) and the jump is not even propagating with the correct speed.

B.4 Continuous Initial Data

Each of the above sections were tested again, this time with continuous initial data for velocity. The continuous initial data was prescribed to only the velocity equation. This is due to the fact that the issues for the system originate in the velocity equation. Two different initial conditions were used, one which provided a continuous profile at $t = 0$, and a second which slowly increased the value at $x = 0$ to create a profile continuous in time. The schemes used were exactly those above, the new continuous data was applied to the systems in Sections B.1, B.2, and B.3.

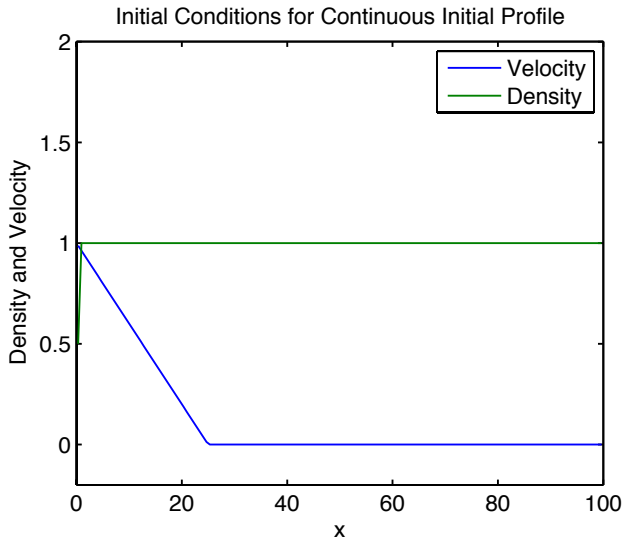

Figure B.5: Continuous Initial Data

B.4.1 Continuous Initial Data

The continuous initial data is given provided that the initial profile is continuous at $t = 0$, then time progresses. Namely, the data used in the simplified problems above, is:

$$\rho(x,0) = \begin{cases} \frac{1}{2} & x \leq 0 \\ 1 & x > 0, \end{cases} \tag{B.4.1}$$

and,

$$v(x,0) = \begin{cases} 1 & x \leq 0 \\ 1 - \frac{x}{25} & 0 < x < 25 \\ 0 & x > 25, \end{cases} \tag{B.4.2}$$

as shown in Figure B.5. This initial data is used in the simplified problems above to obtain the results below.

B.4.1.1 Uncoupled Simple System

The system from Section B.1 is rerun with the initial data, (B.4.1) and (B.4.2), and the results are shown in Figure B.6. As no exact solution has been derived, visually one can see that the four schemes used to solve this problem agree upon the solution. The agreement is so well, that as before, some solutions are hidden under others. Starting from the smooth initial condition, the value at $x = 0$ propagated to

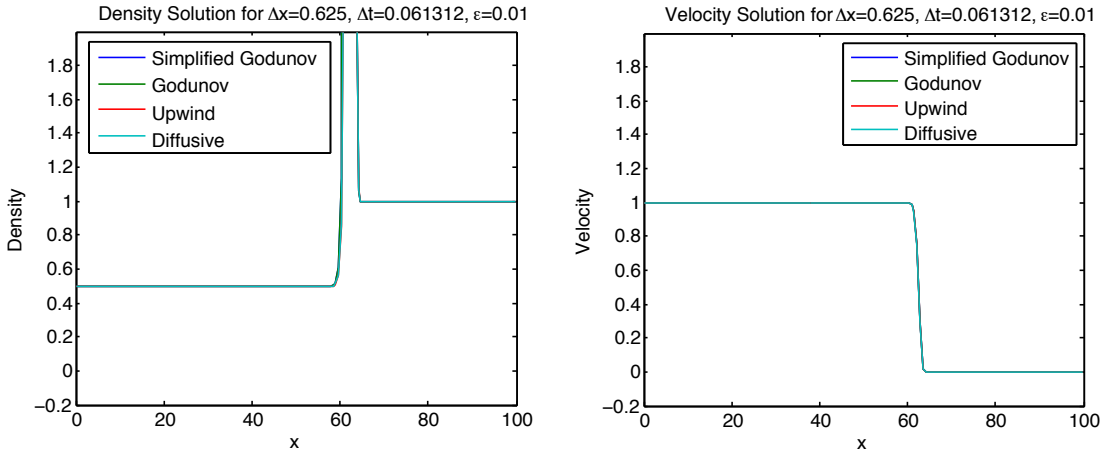

(a) Density Solution **(b) Velocity Solution**

Figure B.6: Solution to Uncoupled System With Continuous Initial Data

the right, until the solution forms a discontinuity. Once the shock appeared in the solution, the whole discontinuity propagated as before. Visually, it seems as though there was greater agreement between the various schemes, although this would be better proved if an exact solution was present.

B.4.1.2 Coupled Simple System

The numerical solution of the system from Section B.2 is rerun with the new initial data and the results are shown in Figure B.7. As it was seen when using the discontinuous initial conditions, the agreement between schemes in Sections B.1 and B.2 visually looks to be very good.

B.4.1.3 Physically Conserved System

The system from Section B.3 is rerun with the new initial data and the results are shown in Figure B.8. Just as what was seen in the results from Section B.3, the numerical results for this simulation is drastically different than what was seen in the above two solutions. The Godunov scheme blows up instantly, and most of the solution is not even represented on the plot. The upwind scheme smears the discontinuity that forms from the continuous initial data, and when compared to the solutions from the previous two solutions, the discontinuity in this simulation travels more slowly.

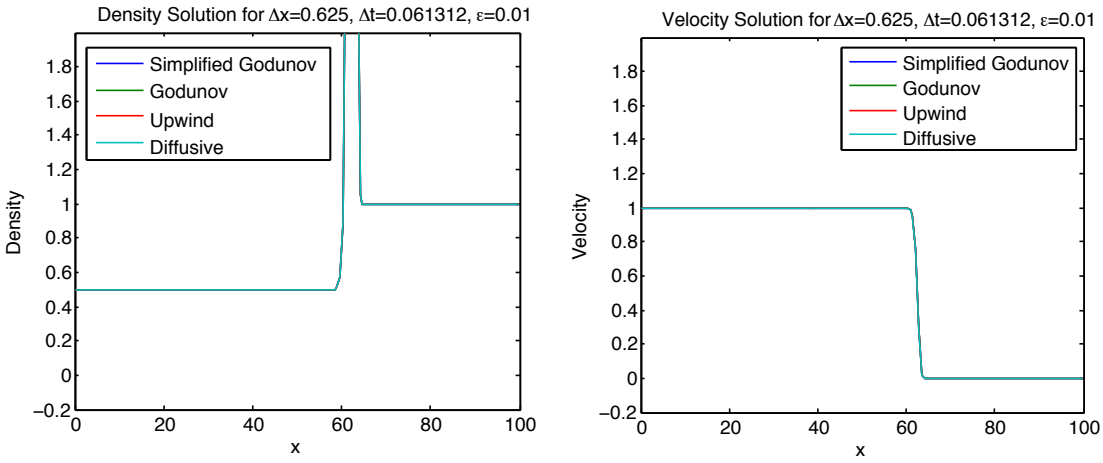

(a) Density Solution **(b) Velocity Solution**

Figure B.7: Solution to Coupled System With Continuous Initial Data

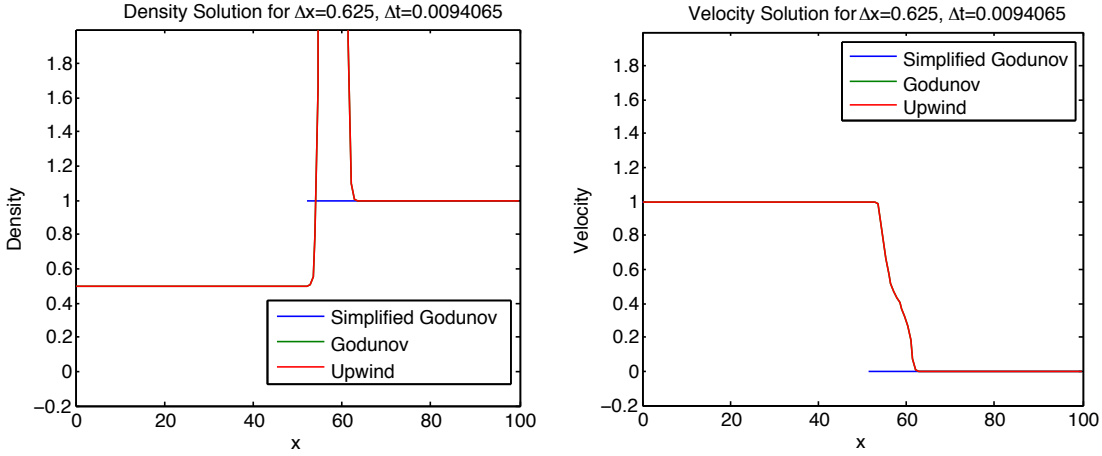

(a) Density Solution **(b) Velocity Solution**

Figure B.8: Solution to Physically Conserved System With Continuous Initial Data

B.4.2 Initial Data Continuous in Time

This time, in an attempt to create a continuous profile in time, the value of the velocity at $x = 0$ is slowly increased up to a value of 1. This slow increase eliminates the discontinuity in the initial data and the solution, until the problem creates one. Namely, the initial and boundary data used in this simplified problems

is:

$$\rho(x,0) = \begin{cases} \frac{1}{2} & x \leq 0 \\ 1 & x > 0, \end{cases} \tag{B.4.3}$$

and,

$$\begin{aligned} v(x,0) &= 0 \\ v(0,t) &= \frac{2t}{N} \quad \text{for } v(0,t) < 1. \end{aligned} \tag{B.4.4}$$

Again, this initial and boundary data is used in the simplified problems from Sections B.1-B.3 to obtain the following results.

B.4.2.1 Uncoupled Simple System

The system from Section B.1 is rerun with the initial and boundary data, (B.4.3) and (B.4.4). The numerical results are shown at different times throughout the simulation including the final time, $T_{\text{final}} = 100$. Figure B.9 displays the numerical results at three different times, so each row of figures represents the solution of density and velocity, respectively, at different times. In the first row, $t = 25$, it can be seen that the profile in v is growing from $x = 0$, but the solution has not yet formed a discontinuity. At $t = 50$, the second row of figures in Figure B.9, the value of v at $x = 0$ has reached its highest value. From this moment in time on, the value from $x = 0$ will propagate to the right, causing the solution to form a discontinuity. Once the discontinuity is formed, the familiar profile is formed at the final time, which can be seen in the third row of figures in Figure B.9.

B.4.2.2 Coupled Simple System

The system from Section B.2 is rerun with the new initial and boundary data and the results are shown at various times in Figure B.10. The plots show the solution at $t = 25$, 50, and 100 in each row respectively. As with all previous sections involving the coupled system, the results are very similar to the results obtained by the uncoupled system. Visually, the solutions are identical, which attests to the fact that using the uncoupled velocity equation makes little difference to the overall solution.

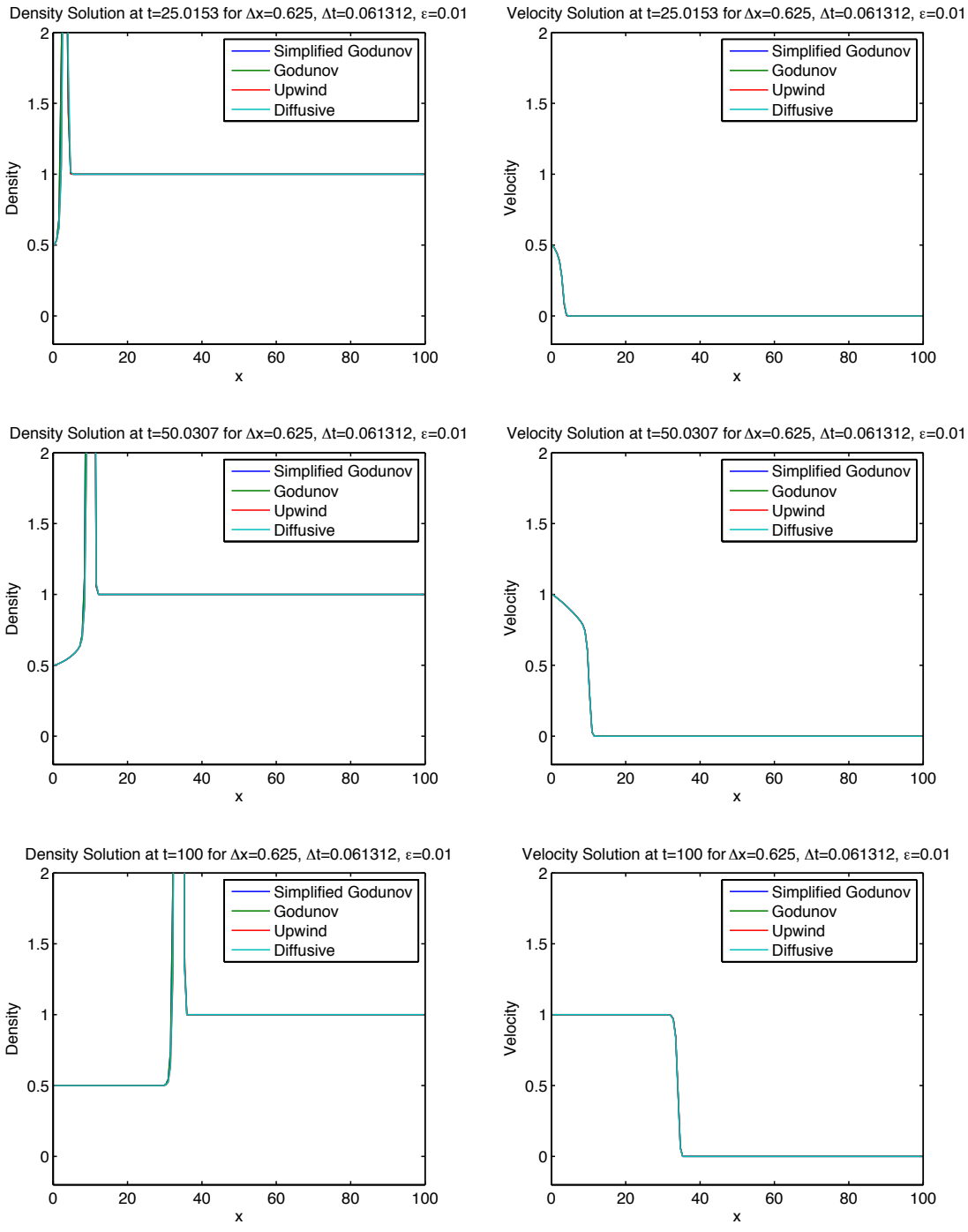

Figure B.9: Solution to Uncoupled System With Continuous in Time Data

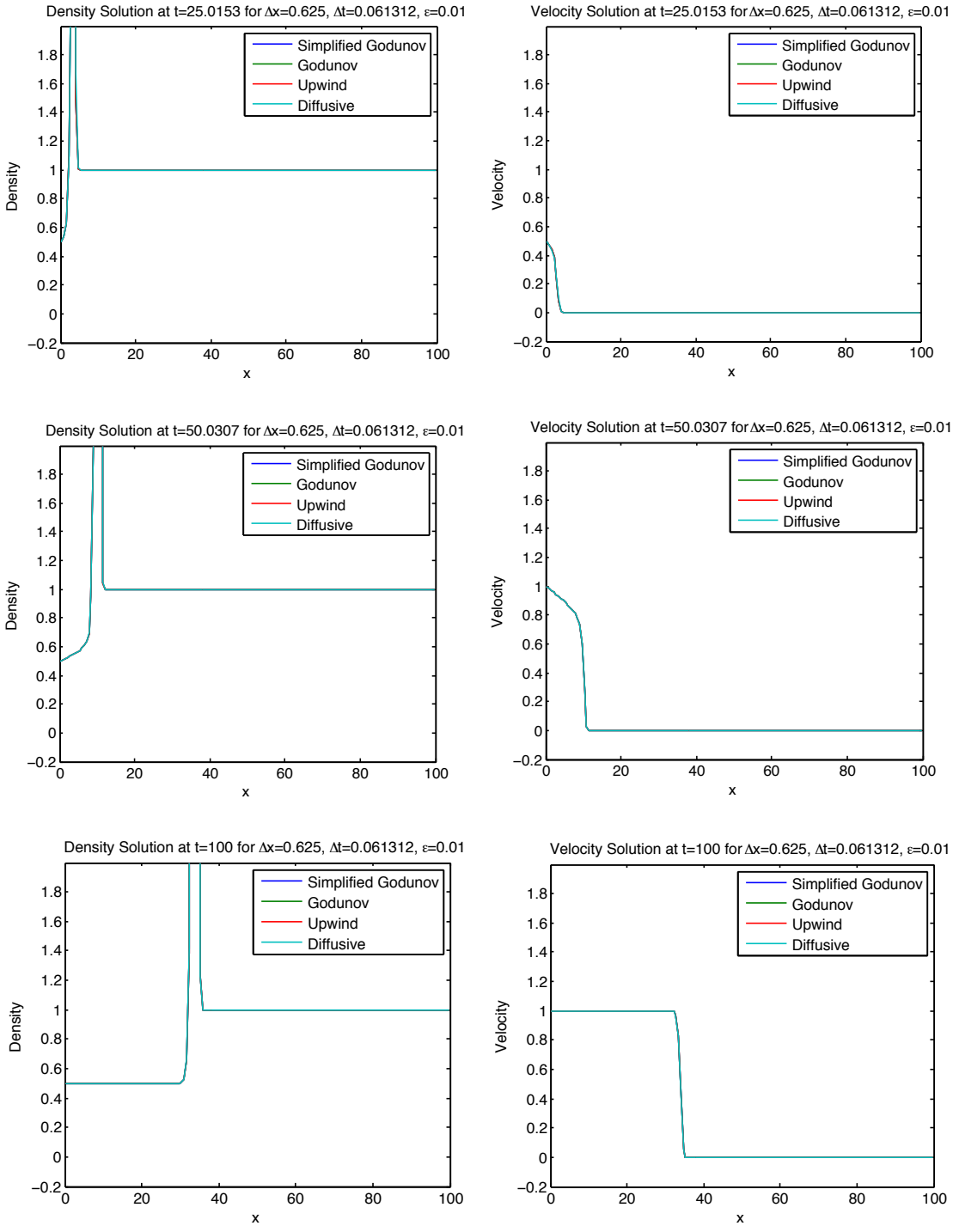

Figure B.10: Solution to Coupled System With Continuous in Time Data

B.4.2.3 Physically Conserved System

The system from Section B.3 is rerun with the new initial and boundary data and the results are shown in Figure B.11. As one might expect, the physically conserved system has the same qualities it had in the previous simulations. One can see that at $t = 25$, the first row in Figure B.11, the Godunov scheme is present, but its solution is far from what the solution should be. By $t = 50$, the second row in Figure B.11, the Godunov scheme has blown up and is no longer shown in the figure. The upwind scheme continues to smear the discontinuity and propagate the at a slower speed, which can be seen in the third row of figures in Figure B.11.

B.5 Non-Homogeneous Simplified System

Just as with the continuous initial data, a source term very similar to what is used in the full problem is added to the systems from Sections B.1, B.2 and B.3. With the addition of a source term that depends on space, time, and velocity, the exact solution is no longer known and intuition can no longer help. This makes an analytical solution nearly impossible. It is also worth noting that this problem is closest to the actual full problem being considered in this work. The source term is added to the systems above and the results are below.

B.5.0.4 Uncoupled Simple System

The system from Section B.1 is rerun again, this time with the original initial conditions and added non-homogeneous term. The numerical results are shown in Figure B.12. The solution profiles are radically different from each other, and as expected, the diffusive scheme smoothes the solution. The other schemes preserve the spike in the density solution that was present in the other simplified problems, although the amplitude is much lower due to the added source term. One should note that the plot at the final time (shown here), is a near steady-state solution of the system. If the simulation was run for longer times, the solution profile wouldn't change much from what is shown.

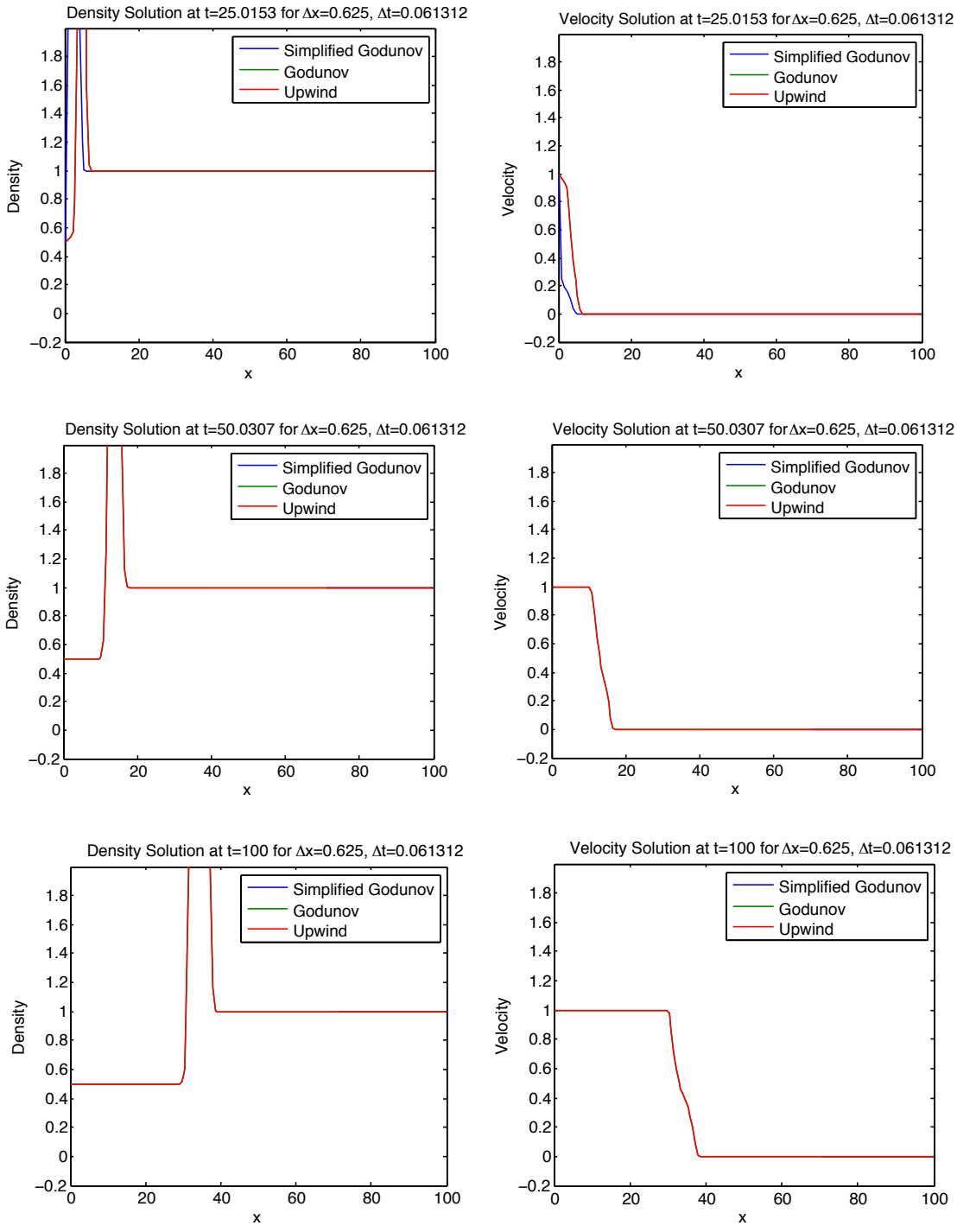

Figure B.11: Solution to Physically Conserved System With Continuous in Time Data

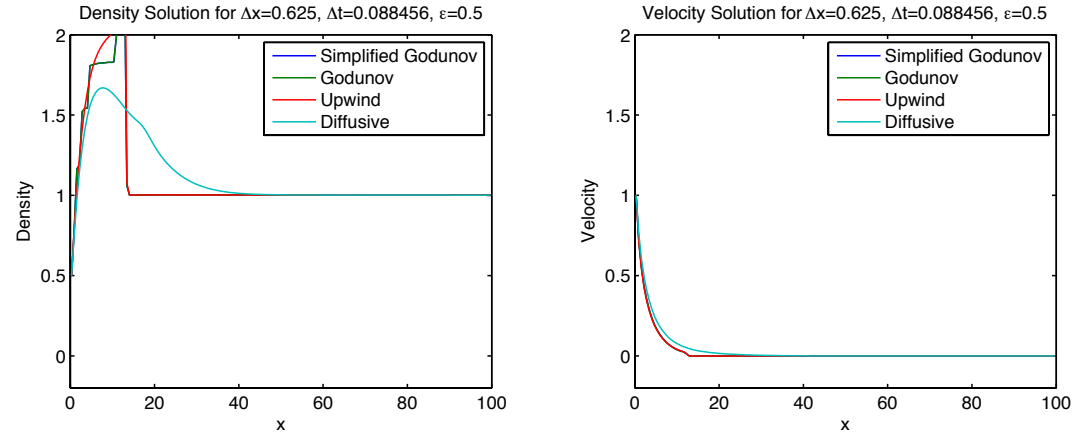

(a) Density Solution **(b) Velocity Solution**

Figure B.12: Solution to Uncoupled System With Source Term Added

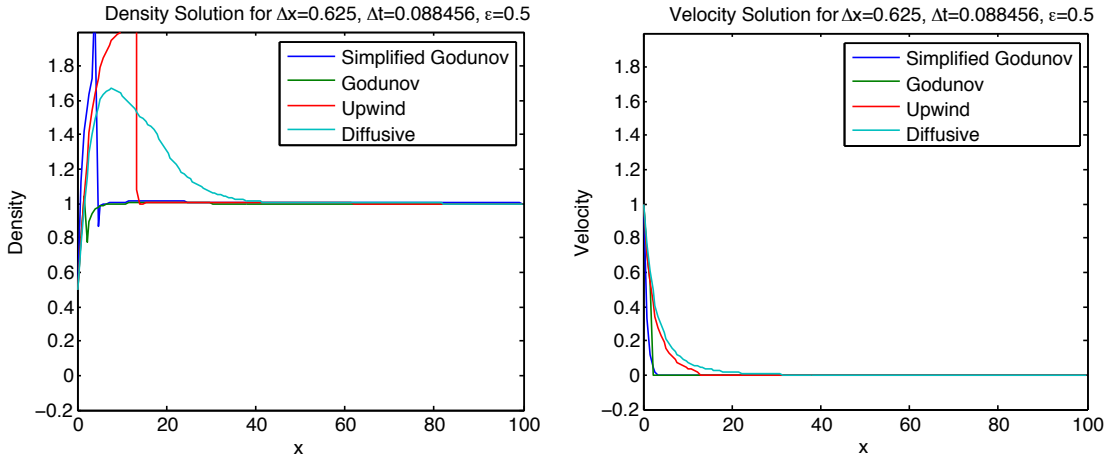

(a) Density Solution **(b) Velocity Solution**

Figure B.13: Solution to Coupled System With Source Term Added

B.5.0.5 Coupled Simple System

The system from Section B.2 is rerun again with the original initial conditions and added non-homogeneous term. The numerical results are shown in Figure B.13. The solution profiles of the upwind and diffusive schemes are the same as they are for the non-homogeneous uncoupled systems. This was expected considering all of the other numerical results obtained. In this simulation it is seen that the Godunov scheme results changed from the uncoupled problem, although both Godunov solutions given are much different than the upwind or diffusive scheme.

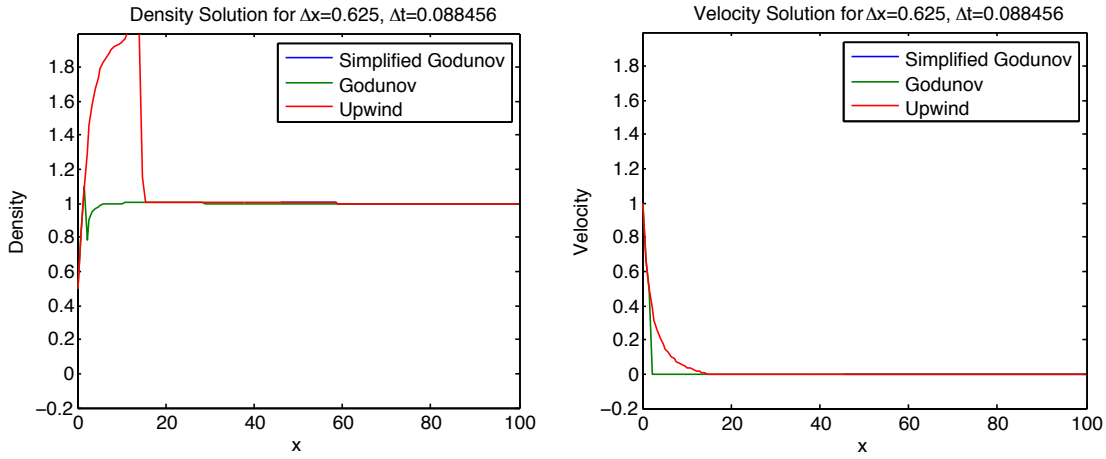

(a) Density Solution **(b) Velocity Solution**

Figure B.14: Solution to Physically Conserved System With Source Term Added

B.5.0.6 Physically Conserved System

The system from Section B.3 is rerun again with the original initial conditions and added non-homogeneous term. The numerical results are shown in Figure B.14. The upwind solution is the same shape as the other systems, except the density solution has a slightly larger amplitude than the other simulations. The Godunov scheme has blown up and is not present on the plot, just like the other simplified problems.

B.6 Twilight Method Verification

As one will have noticed by now, all of the previous simplified problems have not been verified with the exact solution and a convergence and error analysis has not been performed. As explained above, this is due to the fact that finding the exact solutions is difficult and impossible in some situations. The simplified problems were used in conjunction with intuition to see which schemes could handle the problem at hand.

In this section, a method will be used to compare the numerical solutions with a prescribed exact solutions. Both the linear and quadratic exact solutions will be

considered in the solution of the problem:

$$\rho_t + (\rho v)_x = f_\rho \tag{B.6.1}$$

$$v_t + (\frac{1}{2}v^2)_x = f_v, \tag{B.6.2}$$

where the right-hand side is a prescribed forcing function. The same four schemes (upwind, Godunov, simplified Godunov, and diffusive) will be used to solve this problem.

B.6.1 Linear Exact Solution

For the linear exact solution, it is chosen that:

$$\bar{v} = 1 + t + x \tag{B.6.3}$$

$$\bar{\rho} = 1 + 2x + 3t. \tag{B.6.4}$$

These exact solutions are substituted into (B.6.1) and (B.6.2) respectively to obtain the expressions for the forcing functions:

$$f_v = 2 + t + x \tag{B.6.5}$$

$$f_\rho = 6 + 4x + 5t. \tag{B.6.6}$$

With this, (B.6.1) and (B.6.2) are solved numerically and compared to the exact solution above. The relative errors, measured in the L_2 norm, are shown in Figure B.15 for various values of Δx. In addition, convergence rates are given for each scheme, which correspond to the known convergence rates of such schemes.

B.6.2 Quadratic Exact Solution

For the quadratic exact solution, it is chosen that:

$$\bar{v} = 1 + x + t + x^2 + xt + t^2 \tag{B.6.7}$$

$$\bar{\rho} = 1 + 2x + 3t + x^2 + xt + t^2. \tag{B.6.8}$$

Error

del_x=2.500000e+00

v_upwind	v_diffusive	v_godunov	v_s_godunov	r_upwind	r_diffusive	r_godunov	r_s_godunov
1.184569e-01	1.184569e-01	1.184569e-01	1.184569e-01	8.435856e-02	8.435856e-02	8.435856e-02	8.435856e-02

del_x=1.250000e+00

v_upwind	v_diffusive	v_godunov	v_s_godunov	r_upwind	r_diffusive	r_godunov	r_s_godunov
5.955255e-02	5.955255e-02	5.955255e-02	5.955255e-02	4.236627e-02	4.236627e-02	4.236627e-02	4.236627e-02

del_x=6.250000e-01

v_upwind	v_diffusive	v_godunov	v_s_godunov	r_upwind	r_diffusive	r_godunov	r_s_godunov
2.989300e-02	2.989300e-02	2.989300e-02	2.989300e-02	2.124019e-02	2.124019e-02	2.124019e-02	2.124019e-02

del_x=3.125000e-01

v_upwind	v_diffusive	v_godunov	v_s_godunov	r_upwind	r_diffusive	r_godunov	r_s_godunov
1.501152e-02	1.501152e-02	1.501152e-02	1.501152e-02	1.064456e-02	1.064456e-02	1.064456e-02	1.064456e-02

del_x=1.562500e-01

v_upwind	v_diffusive	v_godunov	v_s_godunov	r_upwind	r_diffusive	r_godunov	r_s_godunov
7.557859e-03	7.557858e-03	7.557859e-03	7.557859e-03	5.338587e-03	5.338587e-03	5.338587e-03	5.338587e-03

Convergence

v_upwind	v_diffusive	v_godunov	v_s_godunov	r_upwind	r_diffusive	r_godunov	r_s_godunov
0.992127	0.992127	0.992127	0.992127	0.993618	0.993618	0.993618	0.993618
0.994356	0.994356	0.994356	0.994356	0.996119	0.996119	0.996119	0.996119
0.993737	0.993737	0.993737	0.993737	0.996680	0.996680	0.996680	0.996680
0.990021	0.990021	0.990021	0.990021	0.995587	0.995587	0.995587	0.995587

Figure B.15: Relative Error and Convergence Rate for Linear Exact Solution

These exact solutions are substituted into (B.6.1) and (B.6.2) respectively to obtain the expressions for the forcing functions:

$$f_v = 2 + 4x + 3x^2 + 2x^3 + 4t + 4tx + 3tx^2 + 2t^2 + 3t^2x + t^3 \tag{B.6.9}$$

$$f_{v\,\text{diffusive}} = 2 + 4x + 3x^2 + 2x^3 + 4t + 4tx + 3tx^2 + 2t^2 + 3t^2x + t^3 - 2\epsilon \tag{B.6.10}$$

$$f_\rho = 6 + 9x + 9x^2 + 4x^3 + 9t + 14tx + 6tx^2 + 7t^2 + 6t^2x + 2t^3. \tag{B.6.11}$$

One will notice that the forcing function for the diffusive scheme requires an additional term. This is because the diffusive scheme actually solves the PDE:

$$v_t + (\frac{1}{2}v^2)_x = \epsilon v_{xx} + f_{v\,\text{diffusive}}. \tag{B.6.12}$$

The extra diffusive term is reflected in the forcing function. With this, (B.6.1) and (B.6.2) are solved numerically and compared to the exact solution above. The relative errors, measured in the L_2 norm, are shown in Figure B.16 for various values of Δx. In addition, convergence rates are given for each scheme, which correspond to the known convergence rates of such schemes.

Throughout this section, results make it easy to see that all schemes are first

```
Error

del_x=2.500000e+00
v_upwind        v_diffusive     v_godunov       v_s_godunov     r_upwind        r_diffusive     r_godunov       r_s_godunov
3.821490e-01    3.821489e-01    3.821490e-01    3.821490e-01    3.706054e-01    3.706055e-01    3.706054e-01    3.706054e-01

del_x=1.666667e+00
v_upwind        v_diffusive     v_godunov       v_s_godunov     r_upwind        r_diffusive     r_godunov       r_s_godunov
2.546934e-01    2.546933e-01    2.546934e-01    2.546934e-01    2.470058e-01    2.470059e-01    2.470058e-01    2.470058e-01

del_x=1.250000e+00
v_upwind        v_diffusive     v_godunov       v_s_godunov     r_upwind        r_diffusive     r_godunov       r_s_godunov
1.909931e-01    1.909930e-01    1.909931e-01    1.909931e-01    1.852277e-01    1.852278e-01    1.852277e-01    1.852277e-01

del_x=1.000000e+00
v_upwind        v_diffusive     v_godunov       v_s_godunov     r_upwind        r_diffusive     r_godunov       r_s_godunov
1.527829e-01    1.527827e-01    1.527829e-01    1.527829e-01    1.481687e-01    1.481688e-01    1.481687e-01    1.481687e-01

del_x=8.333333e-01
v_upwind        v_diffusive     v_godunov       v_s_godunov     r_upwind        r_diffusive     r_godunov       r_s_godunov
1.273138e-01    1.273136e-01    1.273138e-01    1.273138e-01    1.234663e-01    1.234664e-01    1.234663e-01    1.234663e-01

Convergence
v_upwind        v_diffusive     v_godunov       v_s_godunov     r_upwind        r_diffusive     r_godunov       r_s_godunov
1.000703        1.000703        1.000703        1.000703        1.000644        1.000643        1.000644        1.000644
1.000490        1.000491        1.000490        1.000490        1.000501        1.000500        1.000501        1.000501
1.000341        1.000342        1.000341        1.000341        1.000406        1.000405        1.000406        1.000406
1.000229        1.000230        1.000229        1.000229        1.000340        1.000340        1.000340        1.000340
```

Figure B.16: Relative Error and Convergence Rate for Quadratic Exact Solution

order, convergent, and accurate. In theory, this means any of the considered schemes can be used in the full problems without issue. However, this is not the case. When taking this and the solutions to the simplified problems above into consideration, the following conclusions can be drawn.

B.7 Conclusions

The process of deciding which scheme to use for the full problem has been outlined in Figure B.17. The full problem was reduced to simpler problems, which isolated physically conserved quantities from elementary variables. From the results of all of the simplified problems examined in this exercise, it can easily be seen that the focus should be on the elementary variables. Finally, it needed to be decided upon which scheme to use in the full problem. Clearly the correct choice from the above simplified problems suggests that the diffusive scheme should be used in the full problem. This choice is reinforced by the fact that even though this scheme is first order, it correctly captures the features of the known simple solutions. Even though the analytic solution for the simplified problem with the source terms is not known, it is taken that the diffusive scheme can capture those features correctly as

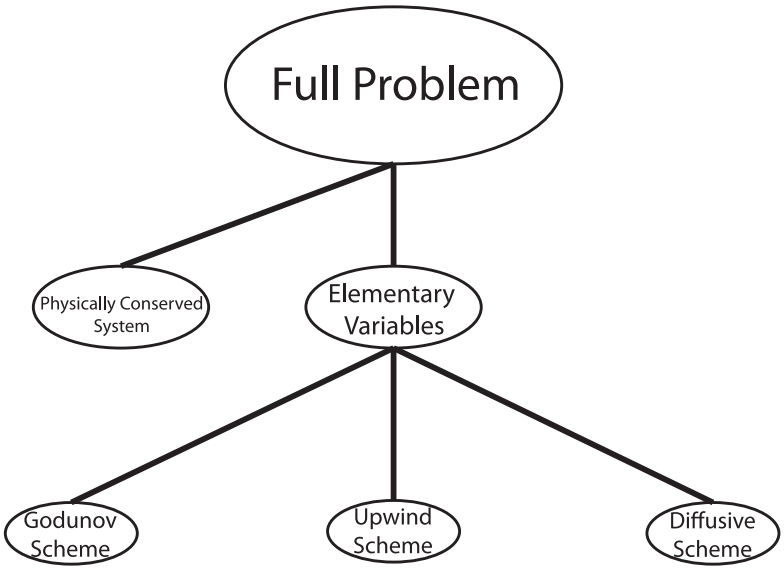

Figure B.17: Decision Tree to Find Scheme for Full Problem

well.

An appropriate value of ϵ is something that needed to be determined through numerical experiments. A relatively low value is needed to damp oscillations that form in the full problem, while preserving the behavior of the solution. The scheme is implemented using the coupled simplified system solution method. The dependence of the numerical solution on ϵ was investigated, although these results are not presented here. A reasonable value of $\epsilon = .005$ has been determined to be appropriate for this model.

It is also worth mentioning that using the calculations leading to the decision procedure, following LeVeque's exercises [38], one might expect the velocity across the contact discontinuity in the problem to be constant. Although this solution has been shown to satisfy the jump conditions, it also shows that a discontinuous velocity is inherent given the nature of the fire plume problem. The discontinuity in the velocity stems from the fact that the velocity toward the bottom of the plume is faster than the velocity toward the top of the plume. From Burgers' equation, the characteristics in this situation will clearly cross, indicating a discontinuity. This jump in the velocity creates the jump, and results in the collection of mass in the spike present in the density.